

# Spatiotemporal Brain Imaging and Modeling

by

Fa-Hsuan Lin

Submitted to the Harvard-M.I.T. Division of Health Sciences and  
Technology

in partial fulfillment of the requirements for the degree of

Doctor of Philosophy in Medical and Electrical Engineering

at the

MASSACHUSETTS INSTITUTE OF TECHNOLOGY

December 2003

© Fa-Hsuan Lin, MMIII. All rights reserved.

The author hereby grants to MIT permission to reproduce and  
distribute publicly paper and electronic copies of this thesis document  
in whole or in part.

Author .....

Harvard-M.I.T. Division of Health Sciences and Technology

December 11, 2003

Certified by .....

John W. Belliveau Ph. D.

Associate Professor of Radiology

Thesis Supervisor

Accepted by .....

Martha L. Gray Ph. D.

Edward Hood Taplin Professor of Medical and Electrical Engineering

Co-director, Harvard-M.I.T. Division of Health Sciences and

Technology



# Spatiotemporal Brain Imaging and Modeling

by

Fa-Hsuan Lin

Submitted to the Harvard-M.I.T. Division of Health Sciences and Technology  
on December 11, 2003, in partial fulfillment of the  
requirements for the degree of  
Doctor of Philosophy in Medical and Electrical Engineering

## Abstract

This thesis integrates hardware development, data analysis, and mathematical modeling to facilitate our understanding of brain cognition. Exploration of these brain mechanisms requires both structural and functional knowledge to (i) reconstruct the spatial distribution of the activity, (ii) to estimate when these areas are activated and what is the temporal sequence of activations, and (iii) to determine how the information flows in the large-scale neural network during the execution of cognitive and/or behavioral tasks. Advanced noninvasive medical imaging modalities are able to locate brain activities at high spatial and temporal resolutions. Quantitative modeling of these data is needed to understand how large-scale distributed neuronal interactions underlying perceptual, cognitive, and behavioral functions emerge and change over time.

This thesis explores hardware enhancement and novel analytical approaches to improve the spatiotemporal resolution of single (MRI) or combined (MRI/fMRI and MEG/EEG) imaging modalities. In addition, mathematical approaches for identifying large-scale neural networks and their correlation to behavioral measurements are investigated. Part I of the thesis investigates parallel MRI. New hardware and image reconstruction techniques are introduced to improve spatiotemporal resolution and to reduce image distortion in structural and functional MRI. Part II discusses the localization of MEG/EEG signals on the cortical surface using anatomical information from MRI, and takes advantage of the high temporal resolution of MEG/EEG measurements to study cortical oscillations in the human auditory system. Part III introduces a multivariate modeling technique to identify “nodes” and “connectivity” in a large-scale neural network and its correlation to behavior measurements in the human motor system.

Thesis Supervisor: John W. Belliveau Ph. D.  
Title: Associate Professor of Radiology



## Acknowledgments

I would first like to express my sincere gratitude to my research advisor John W. Belliveau. Over the last five years, Jack has been a mentor and a friend and has provided me his unreserved support in academics and life. I am indebted to my thesis committee: Drs. Bruce Rosen, Larry Wald, Randy McIntosh, Matti Hämäläinen, Steve Stufflebeam and Anders Dale. Their feedback helped me to improve my thesis work continuously. I would like to thank my colleagues in the Athinoula A. Martinos Center for Biomedical Imaging, including Kenneth K. Kwong, Seppo Ahlfors, Dave Tuch, Thomas Witzel, Iiro Jääskeläinen, Tommi Raij, Jyrki Ahveninen, Sunao Iwaki, Ing-Jye Huang, Teng-Yi Huang and Fu-Nien Wang. Also thanks go to my colleagues outside the lab: Tom Zeffiro, John Agnew, Eden Guinevere, Ying-Jui Chen, Hung-Jen Wang and Nan-Kuei Chen. Without them, it would not have been possible to complete this thesis.

Finally, I thank my family and Fanya. They ultimately made my journey to the exploration of human brain possible.

## **Support**

I would like to thank the generous financial support from the organizations which made this work possible. The work presented in this thesis was supported by the National Center for Research Resources (P41RR14075) and the Mental Illness and Neuroscience Discovery (MIND) Institute. I also thank the Martinos Scholarships from Harvard-MIT Division of Health Sciences and Technology, and the Government Scholarship for Biomedical Engineering from the Ministry of Education, Taiwan.

# Contents

<b>1</b>	<b>Introduction</b>	<b>21</b>
1.1	Motivation . . . . .	21
1.1.1	Neuroimaging using functional magnetic resonance imaging . .	21
1.1.2	Neuroimaging using magnetoencephalography . . . . .	22
1.1.3	Brain modeling using data from MRI, fMRI and MEG . . . .	23
1.2	Thesis goals and novel contributions . . . . .	25
1.2.1	Enhancement of spatiotemporal resolution of magnetic resonance imaging using parallel MRI . . . . .	25
1.2.2	Localization of brain activity using multiple modalities with priors . . . . .	26
1.2.3	Spatiotemporal studies of functional and effective connectivity of large-scale neuronal interactions . . . . .	27
<b>2</b>	<b>Enhancement of spatiotemporal resolution by parallel MRI</b>	<b>33</b>
2.1	INTRODUCTION . . . . .	34
2.2	THEORY . . . . .	35
2.2.1	Tikhonov regularization . . . . .	37
2.2.2	Estimating the optimal regularization parameter using the L-curve . . . . .	39
2.3	METHOD . . . . .	39
2.4	RESULTS . . . . .	44
2.5	DISCUSSION . . . . .	52

<b>3 Distributed Current Estimates with a Cortical Orientation Constraint</b>	<b>63</b>
3.1 INTRODUCTION . . . . .	64
3.2 DISTRIBUTED INVERSE SOLUTIONS . . . . .	66
3.2.1 Spatial whitening . . . . .	67
3.2.2 Depth weighting . . . . .	67
3.2.3 Noise-normalization . . . . .	68
3.2.4 Cortical patch statistics (CPS) . . . . .	69
3.2.5 The Loose Orientation Constraint (LOC) . . . . .	70
3.2.6 Minimum-current estimates . . . . .	71
3.3 METHODS . . . . .	72
3.3.1 Anatomical information from high resolution MRI for MNE and MCE . . . . .	72
3.3.2 Simulations . . . . .	75
3.3.3 Auditory and somatosensory MEG experiments . . . . .	76
3.4 RESULTS . . . . .	78
3.4.1 Patch statistics . . . . .	78
3.4.2 Simulations . . . . .	80
3.4.3 Auditory and somatosensory MEG experiments . . . . .	85
3.5 DISCUSSION . . . . .	88
<b>4 Wavelet-based Spectral Spatiotemporal Mapping in the Human Brain</b>	<b>97</b>
4.1 INTRODUCTION . . . . .	98
4.2 MATERIALS AND METHODS . . . . .	99
4.2.1 Spectral dynamic statistical parametric mapping . . . . .	99
4.2.2 The Wavelet transform . . . . .	100
4.2.3 Source estimation . . . . .	102
4.2.4 Spectral power and phase locking value calculation . . . . .	103
4.2.5 Noise normalized spectral power using MNE and statistical inference of PLV . . . . .	104

4.2.6	Simulation . . . . .	105
4.2.7	Subject . . . . .	109
4.2.8	MEG acquisition . . . . .	109
4.2.9	Structural MRI . . . . .	110
4.3	RESULTS . . . . .	112
4.3.1	Simulation . . . . .	112
4.3.2	Spontaneous MEG measurement and localization . . . . .	112
4.3.3	Auditory evoked MEG measurement and localization . . . . .	114
4.4	DISCUSSION . . . . .	116
4.4.1	Limitations . . . . .	121
4.4.2	Future Applications . . . . .	122

<b>5</b>	<b>Multivariate Analysis of Neuronal Interactions in the Generalized Partial Least Squares Framework: Simulations and Empirical Studies</b>	<b>129</b>
5.1	INTRODUCTION . . . . .	130
5.2	THEORY . . . . .	133
5.2.1	Multivariate approach to reveal the functional connectivity: PCA	133
5.2.2	Multivariate approach to reveal the functional connectivity: ICA	135
5.2.3	Functional connectivity analysis by generalized Partial Least Squares . . . . .	136
5.3	METHODS . . . . .	140
5.3.1	Quantifying results from PCA and ICA by Receiver Operating Curve Analysis . . . . .	140
5.3.2	Simulation . . . . .	142
5.3.3	fMRI experiments of voluntary finger movement . . . . .	144
5.4	RESULTS . . . . .	145
5.4.1	Simulation studies . . . . .	145
5.4.2	fMRI motor system study . . . . .	152
5.4.3	Multiple comparisons between finger tapping rates . . . . .	158

5.5	DISCUSSION . . . . .	159
<b>6</b>	<b>Differential Spatiotemporal Visuomotor Neural Network for Dominant and Non-dominant Voluntary Hand Movement</b>	<b>171</b>
6.1	INTRODUCTION . . . . .	172
6.2	METHODS . . . . .	174
6.2.1	FMRI experiments and image acquisition . . . . .	174
6.2.2	Preprocessing of data . . . . .	175
6.2.3	Identification of nodes of large-scale neural network by generalized Partial Least Squares . . . . .	175
6.2.4	Network analysis by Structural Equation Modeling . . . . .	177
6.3	RESULTS . . . . .	178
6.3.1	Functional connectivity revealed by gPLS . . . . .	178
6.3.2	Effective connectivity revealed by SEM . . . . .	180
6.4	DISCUSSION . . . . .	187
<b>7</b>	<b>Conclusion</b>	<b>201</b>
7.1	SUMMARY . . . . .	201
7.2	FUTURE WORKS . . . . .	206
<b>A</b>	<b>A degenerate mode birdcage volume coil for sensitivity encoded imaging</b>	<b>209</b>
A.1	INTRODUCTION . . . . .	210
A.2	METHOD . . . . .	211
A.3	RESULTS . . . . .	214
A.4	DISCUSSIONS . . . . .	216
<b>B</b>	<b>A wavelet based approximation of surface coil sensitivity profiles for correction of image intensity inhomogeneity and parallel imaging reconstruction</b>	<b>223</b>
B.1	INTRODUCTION . . . . .	224
B.2	METHOD . . . . .	227

B.2.1	Multi-resolution analysis . . . . .	228
B.2.2	Application to coil sensitivity profile estimation . . . . .	229
B.2.3	Automatic selection of optimal reconstruction level . . . . .	230
B.2.4	Image acquisition for image intensity inhomogeneity removal .	232
B.2.5	Parallel MRI acquisition and reconstruction . . . . .	233
B.3	RESULTS . . . . .	233
B.4	DISCUSSIONS . . . . .	239
<b>C</b>	<b>Multivariate linear modeling of brain images</b>	<b>251</b>
C.1	Multivariate linear modeling . . . . .	251
C.2	Robust modeling by cross validation for optimal model selection and statistical inferences . . . . .	255



# List of Figures

1-1	The spatial and temporal resolution of MEG/EEG and fMRI/MRI . . . . .	24
2-1	An L-curve illustrates the two costs during reconstruction the aliased images from an array . . . . .	40
2-2	The reconstructed phantom images and g-factor maps using un-regularized or regularized reconstruction . . . . .	45
2-3	The reconstructed in vivo images and g-factor maps using un-regularized or regularized reconstruction . . . . .	47
2-4	The selected temporal lobe area and the detailed anatomy from unregularized and regularized SENSE reconstructions . . . . .	49
2-5	Detailed temporal lobe anatomy from unregularized and regularized SENSE reconstructions . . . . .	50
2-6	The fMRI t statistics maps of full k-space acquisition, 2.00-, 2.67- and 4.00-fold SENSE accelerations . . . . .	51
2-7	ROC curves for 2.00-, 2.67- and 4.00-fold SENSE accelerations . . . .	52
2-8	ROC areas for 2.00-, 2.67- and 4.00-fold SENSE accelerations . . . .	53
3-1	White matter brain anatomical mesh derived from high-resolution T1-weighted MRI . . . . .	73
3-2	A local cortical patch . . . . .	73
3-3	The division of a cortical surface triangulation . . . . .	74
3-4	Simulated sources locations . . . . .	77
3-5	Cortical patch statistics . . . . .	79

3-6	MNE, noise normalized MNE and MCE from a single ECD placed in Sylvian fissure . . . . .	81
3-7	MNE, noise normalized MNE and MCE source localization simulations from a single ECD placed on somatosensory cortex . . . . .	82
3-8	The average shift of center of mass from the simulated sources using MNE, noise normalized MNE and MCE in both auditory area and somatosensory (SI) areas. . . . .	84
3-9	Simulated two ECD simultaneous sources and the associated MNE, noise normalized MNE and MCE inverse. . . . .	85
3-10	MNE, noise normalized MNE, and MCE source localizations at 100 msec after the onset of the auditory stimuli. . . . .	87
3-11	MNE, noise normalized MNE and MCE source localizations at 50 msec after the onset of the median nerve stimulation. . . . .	88
4-1	A wavelet filter centered at 40 Hz with 5 cycles. . . . .	101
4-2	The schematic diagram illustrating the process of using raw MEG data to calculate the phase locking value (PLV) and the frequency specific power, as well as the noise normalized power, of the evoked response.	106
4-3	The locations of the simulated current sources around Heschl's gyrus (HG) and the superior temporal gyrus (STG). . . . .	108
4-4	The experimental paradigm of auditory stimuli and MEG acquisition.	110
4-5	The fMRI experimental paradigm for auditory stimuli. . . . .	111
4-6	Estimated 40Hz activity along Heschl's gyrus and ROC curves in the simulation study. . . . .	113
4-7	The most prominent spontaneous responses at 10Hz during the "eye-closed" condition (A), and the auditory stimuli evoked responses (B).	114
4-8	Medial aspects of the 10Hz power and the noise normalized 10Hz power on the inflated cortical surface during subject's "eye-closed" condition.	115
4-9	The <i>t</i> -statistics from 3 runs of fMRI experiments . . . . .	117

4-10 Wavelet-based spectral and phase locking value spatiotemporal maps using no fMRI prior and 90% fMRI priors . . . . .	118
5-1 The ROCs and their area metrics from varying thresholds to distinguish two Gaussian distributions with unit variance and various mean differences. . . . .	141
5-2 The weighted ROC area by PCA and ICA using gPLS from Gaussian background noise at various SNRs and the ROC area from the most correlated latent variable by PCA and ICA. . . . .	146
5-3 The weighted ROC area (upper panel) and the most correlated LV (lower panel) by PCA and ICA using gPLS and TD with Gaussian background noise at various SNR. . . . .	148
5-4 The most correlated LV by PCA and ICA using gPLS and TD on super-Gaussian and sub-Gaussian background noise at various SNR. .	149
5-5 The most correlated LV by PCA and ICA using gPLS on Gaussian background noise at various SNRs. . . . .	151
5-6 The total weighted ROC area in gPLS and TD using PCA and ICA for various temporal sampling rates (TSRs) at different SNR in the Gaussian background with 5 orthogonal activations. . . . .	153
5-7 The first brain LV of PCA and ICA decomposition from an event-related fMRI simulation data. . . . .	154
5-8 The design scores of 6 random groupings on different epochs of the left-hand tapping data. . . . .	155
5-9 <i>T</i> -test brain activity statistical maps and brain latent variables from gPLS using PCA and ICA decomposition of the effect space with 6 random groups in the contrast matrix. . . . .	157
5-10 Design scores of the first 3 latent variables in gPLS using PCA and ICA for multiple comparisons. . . . .	158
5-11 The first brain latent variable from PCA decomposition of the effect space. . . . .	160

6-1	The sigmoid basis functions with different shifts and transitions employed in the gPLS analysis. . . . .	177
6-2	Relationship between the manual repetitive rates and the global brain BOLD signal. . . . .	181
6-3	The active brain areas from first Brain LV by generalized Partial Least Square analysis and correlation coefficients for left hand movement and right hand movement. . . . .	182
6-4	The regional BOLD signals revealed by PLS for left hand and right hand movements at 0.3 Hz, 1Hz and 3Hz. . . . .	184
6-5	The anatomical model for structural equation modeling (SEM) . . . . .	185
6-6	The path coefficients for non-dominant (left column) and dominant (right column) hand in repetitive finger flexion. . . . .	189
A-1	The geometry and the coupling circuits for the dual mode birdcage coil.	213
A-2	Phantom images from homogenous mode (right) and gradient mode (left). SNR plots from the cross section depicted by the blue dashed line. . . . .	215
A-3	The g-factor map of the dual mode birdcage coil at 1.33, 1.67 and 2.00 fold SENSE acceleration. . . . .	217
A-4	<i>In vivo</i> brain magnitude images from the quadrature homogeneous mode and the gradient mode in full-FOV reference scan and the reconstructed image from 1.3 and 2.0 fold accelerated SENSE. . . . .	218
B-1	Schematic diagram of the iterative estimation of coil sensitivity profile at a specific level $l$ . . . . .	230
B-2	Simulation of one-dimensional data with superimposed slowly varying trend and signal from anatomical contrast. . . . .	231
B-3	The raw image acquired from bilateral phased array. White bar shows the location of the elements of the array. . . . .	234
B-4	Estimated sensitivity profiles and inhomogeneity indices for each of the 6 levels of wavelet decomposition and reconstruction. . . . .	235

B-5 Six levels of correction by Daub97 filter bank. . . . .	236
B-6 A cross-section from the unprocessed image data at the location of the 3rd ventricle overlaid with the sensitivity profile estimate without maximum intensity projection (MVP), and the sensitivity profile with MVP. . . . .	237
B-7 Comparison of corrected phased array image and volume head coil image. . . . .	238
B-8 The detail of the temporal lobe from the corrected phased array surface coil image and the birdcage head coil image. . . . .	238
B-9 Application of the DWT estimation of coil sensitivity profile and MVP to a T2-weighted image for inhomogeneity correction. . . . .	239
B-10 The full-FOV reference images from an 8-channel array coil and their optimal sensitivity profile estimates using DWT and MVP. . . . .	240
B-11 Reconstructed full-FOV image from an 8-channel array coil using root-mean-square of individual channels and SENSE acquisition with acceleration of 2.0 . . . . .	241



# List of Tables

2.1	G-factors in unregularized and regularized SENSE reconstructions from phantom images. . . . .	44
2.2	G-factors in unregularized and regularized SENSE reconstructions from <i>in vivo</i> images. . . . .	46
2.3	G-factors in unregularized and regularized SENSE reconstructions from <i>in vivo</i> images. . . . .	48
3.1	Shifts of the center of mass ( $S_{cm}$ ) and the maximum of the estimate ( $S_{max}$ ) from the ECD in MNE, noise normalized MNE and MCE using free orientation (FO), strict orientation constraint (SOC) and loose orientation constraint (LOC) in the somatosensory experiment at 100 msec after the onset of the median nerve stimulation. . . . .	86
3.2	Shifts of the center of mass ( $S_{cm}$ ) and the maximum of the estimate ( $S_{max}$ ) from the ECD in MNE, noise normalized MNE and MCE using free orientation (FO), strict orientation constraint (SOC) and loose orientation constraint (LOC) in the auditory experiment at 50 msec after the onset of the auditory stimulation. . . . .	89
5.1	The inner product of the first latent variable revealed by PCA and ICA at various numbers of randomized grouping. . . . .	156
6.1	Talairach coordinates, anatomical labels and Brodmann's Areas of brain regions showing high sensitivity to the repetitive motor rate dependency revealed by gPLS. . . . .	183

6.2 Path coefficient averages and standard deviations from 50 iterative Structural Equation Modeling calculation. . . . .	188
A.1 The g-factors of the accelerated SENSE acquisitions at 1.33, 1.60, and 2.00 fold SENSE accelerations. . . . .	216

# Chapter 1

## Introduction

Complex behavior and cognitive functions of the human brain have been suggested to be "mapped at the level of multi-focal neural systems rather than specific anatomical sites, giving rise to brain-behavior relationships that are both localized and distributed" [1]. Thus, for the study of the brain mechanisms, both structural and functional knowledge is required to answer (i) what is the spatial distribution of the activity, (ii) what is the temporal sequence of activations, and (iii) how does the information flow in the large-scale neural network during the execution of the cognitive and/or behavioral tasks. Advanced non-invasive medical imaging techniques are able to locate brain activities with fine spatial and temporal resolutions. In addition, quantitative modeling to interpret the data is needed to understand how the large-scale distributed neuronal interactions underlying perceptual, cognitive, and behavioral functions emerge.

### 1.1 Motivation

#### 1.1.1 Neuroimaging using functional magnetic resonance imaging

Over the last few decades, functional brain imaging has become a vivid discipline. Positron Emission Tomography (PET) was first introduced to map activated brain

areas by metabolic measurements using isotope-labeled marker agents. Later, functional magnetic resonance imaging (fMRI) was introduced [1, 3, 4]. The high spatial resolution (down to millimeters), the capability to utilize cerebral blood as an endogenous contrast agent [2, 4], and the ease of imaging underlying anatomy soon made functional MRI (fMRI) a popular tool to map brain functions. Typically, the echo-planar imaging (EPI) technique [7] is used in fMRI to achieve a fine spatiotemporal resolution. Owing to advances in magnetic resonance imaging techniques, including high slew-rate gradients, high quality radio-frequency coils, tailored pulse sequence designs and image reconstruction algorithms, a temporal resolution of 1-2 seconds and a spatial resolution of 3-5 millimeter can be achieved for whole brain fMRI. Besides technological challenges, the temporal resolution of fMRI is constrained by the safety concerns on acoustic noise, peripheral nerve stimulation, and tissue specific absorption rate (SAR) [8]. Furthermore, physiology constrains the fMRI: the hemodynamic measures are secondary to the neural activity and lasts for tens of seconds [9].

### 1.1.2 Neuroimaging using magnetoencephalography

Single-unit neurophysiological recordings in monkeys have suggested that communication among brain areas occur on the order of tens to hundreds of milliseconds [10]. Recordings of scalp potentials and extracranial fields using electroencephalography (EEG) or magnetoencephalography (MEG) provide noninvasive means to study human brain activity at a high temporal resolution [1, 24]. In contrast to PET and fMRI, MEG and EEG record neural activity directly and have a millisecond temporal resolution. MEG and EEG originate mainly from postsynaptic currents in pyramidal cells, which have an organized cytoarchitecture with orientations of cell apical dendrite perpendicular to the local cortical surface [9]. To utilize the temporal resolution of MEG for human brain mapping, we need to map the extracranial recordings back into the brain. Unfortunately, this inverse problem of MEG is ill-posed [14]: for a given MEG measurement, there exists an infinite set of current distributions inside the brain that can fully account for the observed signal, even if the electric potential and magnetic field were perfectly known everywhere outside the region containing

the currents. Thus, the solution of the MEG inverse problem, i.e., the estimation of the underlying current sources, requires additional constraints. Two main approaches to solving the MEG inverse problem are available. In the equivalent current dipole (ECD) fitting approach, the MEG measurements are modeled by a small set (usually less than 10) of focal current sources, whose locations, amplitudes and/or orientations are determined by non-linear optimization [15]. The distributed estimation approaches [21, 19] assume the probability distribution function of current amplitudes and estimates the current distributions across the whole brain (up to tens of thousands of sources) at once. Disadvantages of the ECD approach include the difficulty of determining the number of dipoles and the dependency of the solution on the initial values for iterative optimization techniques. With distributed current estimates, these problems are avoided. Furthermore, distributed estimates may be more realistic in many physiological conditions. However, in special cases, such as epileptic spike or very focal brain activations (such as elicited by median nerve stimulation), distributed source models may be too diffuse to accurately identify brain neural sources.

The relative spatiotemporal resolution of fMRI and MEG/EEG is shown schematically in Figure 1. fMRI and MEG have distinct, yet complementary advantages in spatial (in fMRI) and temporal (in MEG) resolution. The combination of these non-invasive whole-brain imaging modalities holds the promise of achieving accurate spatiotemporal characterization of brain function. Specifically, fMRI has been proposed to be used as an aid for manual placement of ECDs (Ahlfors, Simpson et al. 1999; Korvenoja, Huttunen et al. 1999). Minimum-norm estimates (MNE) [21], which is a distributed source model assuming Gaussian distribution of source amplitudes, have also been extended to incorporate fMRI information [26, 20]. Combining MEG and EEG can also help to achieve higher spatiotemporal resolution [19, 25].

### 1.1.3 Brain modeling using data from MRI, fMRI and MEG

In addition to mapping brain activity to answer the "where" and "when" questions, comprehensive understanding of brain functions requires additional modeling tech-

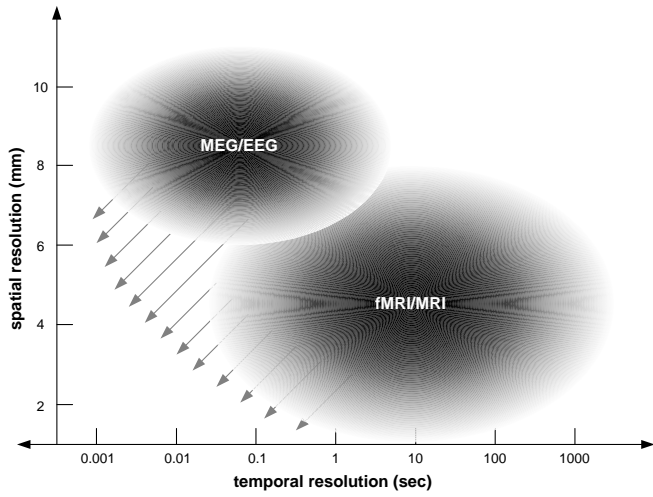


Figure 1-1: The spatial and temporal resolution of MEG/EEG and fMRI/MRI. The goal of the thesis is to push the spatiotemporal resolution toward finer scale as indicated by the gray arrows.

niques to reveal the mechanisms of information flow inside the neural network during perception, cognition and behavior. Traditionally, univariate techniques, such as correlation coefficient, t-test and F-test [5, 22], have been used to correlate the experimental paradigm with the spatiotemporal functional brain imaging data to reveal the activated brain foci. Nevertheless, under the fundamental assumption that both focal and distributed functional activities across the whole brain, in both time and space, underlie the complex perception, cognition and behavior [1], we need to take into account spatial correlations without treating the data as isolated temporal observations. The identification of an integrated neural network subserving the tasks of interest requires not only the identification of the “nodes” among the network, but also the estimation of the connectivity among these nodes. In addition, the data from multiple modalities contain information across time, frequency and space. Systematic classification of this large amount of data can help us to reveal the underlying processes consisting brain functions.

## 1.2 Thesis goals and novel contributions

This thesis introduces both hardware improvements and novel analysis methods to enhance the spatiotemporal resolution of single (MRI, fMRI or MEG) or combined (MRI/fMRI and MEG/EEG) modalities. In addition, mathematical approaches of identifying large-scale neural network and its correlation to behavioral measurements are investigated. The specific goals and novel contributions of the individual projects are:

### 1.2.1 Enhancement of spatiotemporal resolution of magnetic resonance imaging using parallel MRI

Typical whole-head fMRI techniques utilize Echo-Planar Imaging (EPI) with a temporal resolution of  $\approx 1$  second and in-plane resolution down to 3 mm by 3 mm. We further improve the spatiotemporal resolution of fMRI by making use of multiple receiver coils. The radio-frequency (RF) coil array was introduced to achieve higher signal-to-noise ratio (SNR) images [2]. The multiple copies of data from each channel in the RF coil array consist of distinct observations of MRI signals, modulated by individual coil sensitivity profiles. Instead of combining individual coil elements for higher SNR or larger field-of-view (FOV) MRI, parallel imaging was proposed to use multiple receivers in the array to reconstruct the full FOV images from aliased images due to incomplete k-space acquisition. Approaches in both the k-space domain (SMASH) [20] and the image domain (SENSE) [22] have been proposed to unfold the aliased images.

In this thesis, the possibility of applying the parallel MRI principles to both structural and functional imaging of the human brain was studied. In addition to using traditional surface RF coil arrays, I investigated the possibility of using a volume coil in parallel MRI. Specifically, the birdcage coil, which previously has been mostly adopted for its homogeneous first mode, has multiple modes with distinct sensitivity profiles. The combination of homogenous mode and higher order gradient modes enables the application of the parallel MRI principles to volume coils. Parallel MRI can

provide reduction in scanning time and, thus, higher temporal resolution. Alternatively, it can be used to increase the spatial resolution of the functional images within the same amount of acquisition time. Additional benefits of the parallel MRI technique include the lower susceptibility artifact due to reduced scanning time (shorter TE), and the lower EPI acoustic noise due to lowered gradient switching. This approach holds great potential for high field studies (for example, the 7 Tesla whole body scanner in the MIT-MGH-HMS Athinoula A. Martinos Center for Biomedical Imaging). In addition, I investigated algorithms for image reconstruction in parallel MRI. To reconstruct full FOV images without aliasing, the sensitivity profile of the individual coil elements in the array must be known. We have devised a multi-resolution approach, based on a discrete time wavelet transform, to estimate the coil sensitivity profiles from full FOV array reference images. Additionally, we improved the quality of reconstructed image by regularizing the observation with appropriate prior information for robust reconstructions. Regularized parallel MRI reconstruction is particularly beneficial in experiments where the RF coils in the array are not fully uncorrelated in order to improve the spatiotemporal resolution. In dynamic imaging, such as fMRI, the applicability of regularization to unfold aliased images in time series was studied to see if BOLD contrast-to-noise ratio (CNR), which is usually less than 10% in fMRI experiments, could be preserved in parallel MRI acquisitions.

### **1.2.2 Localization of brain activity using multiple modalities with priors**

EEG and MEG have a high temporal resolution (milliseconds), but the spatial resolution is lower (typically 7-10 mm) compared with fMRI ( 3 mm). Approaches have been proposed to combine EEG, MEG and fMRI to achieve a higher spatial and temporal resolution simultaneously. In our laboratory, previous research has developed a linear estimation scheme for distributed current dipole estimates with the L2-norm prior. More focal current estimate is obtained with the L1-norm prior. For distributed current models, with either L1- or L2-norm priors, an accurate anatomical

model is a critical factor in localization accuracy. Furthermore, MEG and EEG data can be analyzed in the time-frequency domain to assess the spatial distribution of both the magnitude and phase of the signals as a function of time in frequency bands of interest.

In this thesis, I developed a framework for using more accurate anatomical information in MEG/EEG source modeling. High spatial resolution MRI was used to calculate cortical patch statistics. Characterizations of cortical patch size, surface normal orientations, and the distribution of surface normals within the individual patch were used for both better visualization and more accurate localization in distributed source models using either the L<sub>2</sub>-norm or the L<sub>1</sub>-norm priors.

MEG source localization was also used to investigate cortical oscillations, measured with MEG and filtered at specific frequencies. I used the continuous wavelet transform to study 40 Hz power and 40 Hz phase locking in the auditory cortex in response to the external acoustic 40 Hz clicks. Three inverse methods (MNE, noise normalized MNE and fMRI weighted MNE) were compared in order to optimize spatial precision using both synthetic and empirical data.

### **1.2.3 Spatiotemporal studies of functional and effective connectivity of large-scale neuronal interactions**

The fundamental challenges in functional brain imaging include the identification and estimation of spatial brain loci responsive to specific cognitive experiment designs and their associated temporal dynamics. To investigate this spatiotemporal orchestration, we applied the analysis of functional connectivity (defined as the temporal coherence among brain areas) and effective connectivity (quantifying the causal effects among distributed regions) to functional magnetic resonance imaging experiments. Previously, Partial Least Squares (PLS) [24] has been proposed as a multivariate tool to reveal distributed brain systems. The benefits of PLS include computational efficiency, multiple contrasts/models detection, and simplification of the interpretation of decomposed components. For effective connectivity analysis, Structural Equation

Modeling (SEM) has been used with PET data to understand the human memory system by quantitative modeling of a distributed network in the human brain [27, 28].

This thesis work extended the PLS algorithm into a generalized multivariate framework not only to inherit advantages from PLS, but also to provide the flexibility to utilize Principle Component Analysis (PCA) or Independent Component Analysis (ICA) [30] as the decomposition tool. The generalized framework was tested with synthetic data to determine the optimal algorithm for various experimental scenarios. Further exploration of this generalized PLS framework also provided robust modeling of the mapping between neuroimaging data and behavioral measurements. Specifically, I explored quantitative models to correlate between the brain energy consumption as inferred by fMRI and the voluntary movement rates in either the dominant or non-dominant hand. Using PLS and SEM, I studied the distributed motor neural systems in both cerebrum and cerebellum to reveal their distinct communications during repetitive finger movement at different rates.

# References

- [1] M. M. Mesulam. Large-scale neurocognitive networks and distributed processing for attention, language, and memory. *Ann Neurol*, 28(5):597–613, 1990. 91083309 0364-5134 Journal Article Review Review, Tutorial.
- [2] John William Belliveau. *Functional NMR Imaging of the Brain*. Ph.d. thesis, Harvard University, 1990.
- [3] J.W. Belliveau, D.N. Kennedy, R.C. McKinstry, B.R. Buchbinder, R.M. Weisskoff, M.S. Cohen, J.M. Vevea, T.J. Brady, and B.R. Rosen. Functional mapping of the human visual cortex by magnetic resonance imaging. *Science*, 254:716–719, 1991.
- [4] J.W. Belliveau, D.N. Kennedy, R.C. McKinstry, B.R. Buchbinder, R.M. Weisskoff, J.M. Vevea, K. Nadeau, M.S. Cohen, T.J. Brady, and B.R. Rosen. Functional mapping of the human visual cortex with susceptibility-contrast mr imaging. *J. Magn. Reson. Imaging*, 1(2)(2):202, 1991.
- [5] S. Ogawa, T.M. Lee, A.R. Kay, and D.W. Tank. Brain magnetic resonance imaging with contrast dependent on blood oxygenation. *Proc. Natl. Acad. Sci. USA*, 87:9868–9872, 1990.
- [6] K.K. Kwong, J.W. Belliveau, D.A. Chesler, I.E. Goldberg, R.M. Weisskoff, B.P. Poncelet, D.N. Kennedy, B.E. Hoppel, M.S. Cohen, R. Turner, H.M. Cheng, T.J. Brady, and B.R. Rosen. Dynamic magnetic resonance imaging of human brain activity during primary sensory stimulation. *Proc. Natl. Acad. Sci. USA*, 89:5675–5679, 1992.

- [7] P. Mansfield. Multi-planar image formation using nmr spin echos. *J. Physics*, C10:L55–L58, 1977.
- [8] F. Schmitt, M. K. Stehling, R. Turner, and P. A. Bandettini. *Echo-planar imaging : theory, technique, and application*. Springer, Berlin ; New York, 1998. [edited by] F. Schmitt, M.K. Stehling, R. Turner ; with contributions by P.A. Bandettini ... [et al.] ; foreword by Peter Mansfield. ill. ; 24 cm.
- [9] A. M. Blamire, S. Ogawa, K. Ugurbil, D. Rothman, G. McCarthy, J. M. Ellermann, F. Hyder, Z. Rattner, and R. G. Shulman. Dynamic mapping of the human visual cortex by high-speed magnetic resonance imaging. *Proc Natl Acad Sci U S A*, 89(22):11069–73, 1992. 93066386 0027-8424 Journal Article.
- [10] D. L. Robinson and M. D. Rugg. Latencies of visually responsive neurons in various regions of the rhesus monkey brain and their relation to human visual responses. [review]. *Biological Psychology*, 26(1-3):111–116, 1988.
- [11] D. Cohen. Magnetoencephalography: evidence of magnetic fields produced by alpha-rhythm currents. *Science*, 161(843):784–6, 1968. 68350989 0036-8075 Journal Article.
- [12] MS Hamalainen, R Hari, RJ Ilmoniemi, J Knuutila, and OV Lounasmaa. Magnetoencephalography-theory, instrumentation, and application to noninvasive studies of the working human brain. *Review of Modern Physics*, 65:413–497, 1993.
- [13] Y. C. Okada, J. Wu, and S. Kyuhou. Genesis of meg signals in a mammalian cns structure. *Electroencephalogr Clin Neurophysiol*, 103(4):474–85, 1997. 98034867 0013-4694 Journal Article.
- [14] H. Helmholtz. Ueber einige gesetze der vertheilung elektrischer strome in korperlichen leitern, mit anwendung auf die thierisch-elektrischen versuche. *Ann. Phys. Chem.*, 89:211–233, 353–377, 1853.

- [15] M. Scherg. Functional imaging and localization of electromagnetic brain activity. *Brain Topogr*, 5(2):103–11, 1992. 93144068 0896-0267 Journal Article.
- [16] MS Hamalainen and RJ Ilmoniemi. Interpreting measured magnetic fields of the brain: estimates of current distributions. Technical report, Helsinki University of Technology, 1984.
- [17] AM Dale and MI Sereno. Improved localization of cortical activity by combining eeg and meg with mri cortical surface reconstruction: A linear approach. *J. Cog. Neurosci*, 5:162–176, 1993.
- [18] A. K. Liu, J. W. Belliveau, and A. M. Dale. Spatiotemporal imaging of human brain activity using functional mri constrained magnetoencephalography data: Monte carlo simulations. *Proc Natl Acad Sci U S A*, 95(15):8945–50., 1998.
- [19] A. M. Dale, A. K. Liu, B. R. Fischl, R. L. Buckner, J. W. Belliveau, J. D. Lewine, and E. Halgren. Dynamic statistical parametric mapping: combining fmri and meg for high-resolution imaging of cortical activity. *Neuron*, 26(1):55–67, 2000. 20256250 0896-6273 Journal Article.
- [20] A. K. Liu, A. M. Dale, and J. W. Belliveau. Monte carlo simulation studies of eeg and meg localization accuracy. *Hum Brain Mapp*, 16(1):47–62, 2002. 21859140 1065-9471 Journal Article.
- [21] P. A. Bandettini, A. Jesmanowicz, E. C. Wong, and J. S. Hyde. Processing strategies for time-course data sets in functional mri of the human brain. *Magn Reson Med*, 30(2):161–73., 1993.
- [22] K. J. Friston, A. P. Holmes, J. B. Poline, P. J. Grasby, S. C. Williams, R. S. Frackowiak, and R. Turner. Analysis of fmri time-series revisited. *Neuroimage*, 2(1):45–53., 1995.
- [23] P. B. Roemer, W. A. Edelstein, C. E. Hayes, S. P. Souza, and O. M. Mueller. The nmr phased array. *Magn Reson Med*, 16(2):192–225, 1990. 91094620 0740-3194 Journal Article.

- [24] D. K. Sodickson and W. J. Manning. Simultaneous acquisition of spatial harmonics (smash): fast imaging with radiofrequency coil arrays. *Magn Reson Med*, 38(4):591–603., 1997.
- [25] K. P. Pruessmann, M. Weiger, M. B. Scheidegger, and P. Boesiger. Sense: sensitivity encoding for fast mri. *Magn Reson Med*, 42(5):952–62., 1999.
- [26] A. R. McIntosh, F. L. Bookstein, J. V. Haxby, and C. L. Grady. Spatial pattern analysis of functional brain images using partial least squares. *Neuroimage*, 3(3 Pt 1):143–57., 1996.
- [27] A. R. McIntosh and F. Gonzalez-Lima. Structural modeling of functional neural pathways mapped with 2-deoxyglucose: effects of acoustic startle habituation on the auditory system. *Brain Res*, 547(2):295–302, 1991. 91356285 0006-8993 Journal Article.
- [28] A. R. McIntosh and F. Gonzalez-Lima. Network interactions among limbic cortices, basal forebrain, and cerebellum differentiate a tone conditioned as a pavlovian excitor or inhibitor: fluorodeoxyglucose mapping and covariance structural modeling. *J Neurophysiol*, 72(4):1717–33., 1994.
- [29] A. J. Bell and T. J. Sejnowski. An information-maximization approach to blind separation and blind deconvolution. *Neural Comput*, 7(6):1129–59., 1995.

# Chapter 2

## Enhancement of spatiotemporal resolution by parallel MRI

Increased spatiotemporal resolution in MRI can be achieved using parallel acquisition strategies, which simultaneously sample reduced k-space data using the information from multiple receivers to reconstruct full FOV images. The price for the increased spatiotemporal resolution in parallel MRI is the degradation of signal-to-noise ratio (SNR) of the final reconstructed images. Part of the SNR reduction results if the spatially correlated nature of the information from the multiple receivers destabilizes the matrix inversion used in the reconstruction of the full FOV image. In this chapter, a reconstruction algorithm based on Tikhonov regularization is presented to reduce the SNR loss due to geometric correlations in the spatial information from the array coil elements. In this method, reference scans are utilized as a priori information about the final reconstructed image to provide regularized estimates for the reconstruction using the L-curve technique. This automatic regularization method was found to reduce the average g-factors in phantom images from a 2-channel array from 1.47 to 0.80 in two fold SENSE acceleration. In vivo anatomical images from 8-channel system show averaged g-factor reduction from 1.22 to 0.84 in 2.67 fold acceleration. In a simulated fMRI experiment, SENSE EPI using regularization in image reconstruction can benefit the detection power at 2.67- and 4.00-fold accelerations.

## 2.1 INTRODUCTION

The utilization of multiple receivers in MRI can be exploited for the enhancement of spatiotemporal resolution by reducing the number of k-space acquisitions. The folded image that would result with conventional reconstruction is avoided by using spatial information from multiple coils. Several methods for using this information have been proposed including the k-space based SMASH method [20, 2] and the image domain based SENSE approach [22]. By reducing sampling time, these parallel MRI techniques can be used to reduce image distortion in EPI [4] or diminish acoustic noise by lowering gradient switching rates [5]. A major price for these advantages is the decreased image SNR. The reduction in SNR comes from two sources; the reduced number of data samples, and the instability in reconstruction due to correlations in the spatial information as determined by the geometrical arrangement of the array coil. The first is an inevitable result of reducing the number of samples. The second might be affected by optimizing coil geometry [6, 7] or improving the stability of the reconstruction algorithm. The increased noise originating from correlated spatial information from the array elements can be estimated based on knowledge of the array geometry and is quantified by the geometric factor map (g-factor map) [22].

The reconstruction of parallel MRI can be formulated as linear equations [23] which must be inverted to obtain an unfolded image from the reduced k-space data set. If the matrix is well conditioned, the inversion can be achieved with minimal amplification of noise. While the encoding matrix can still be inverted even if it is nearly singular, in this ill-conditioned case small noise perturbations in the measured data (aliased image) can produce large variations in the full FOV reconstruction. This effect causes noise amplifications in regions of the image where the encoding matrix is ill conditioned. The restoration of full-FOV images requires the use of additional information such as the coil sensitivity maps provided by a low spatial resolution full FOV reference scan. In addition to being required to determine the coil sensitivity profile that becomes part of the linear equations to be inverted, the reference scan might also provide a priori information useful for regularizing the inversion process.

In this chapter, we present a framework to mitigate the noise amplification effect in SENSE reconstruction by utilizing Tikhonov regularization [8]. The advantage of regularized parallel MRI reconstructions was previously reported [2] on cardiac imaging using an empirical formula of a fixed fraction (0.05) of the first eigen value, Similarly, regularized SENSE reconstruction using an empirical regularization parameter was described by King et. al. [9]. The benefits of incorporating prior information to reduce the noise level of reconstructed images were reported in [9, 30, 11]. Furthermore, it has been reported that regularization can potentially used to unfold aliased images from an under-determined system, i.e., the aliased pixel number exceed the RF channels in the array [12]. Nevertheless, no systematic approach has been described to provide regularization parameter for SENSE image reconstruction. And spatial distribution of noise arising from unfolding SENSE images has not been well characterized when regularization is employed. In this chapter, we employ a full FOV reference scan and the L-curve algorithm [13] to determine the optimal regularization parameter. Also, we demonstrate the effect of regularization on the noise of the unfolded images by g-factor maps using both phantom and in vivo experimental data.

## 2.2 THEORY

The formation of aliased images from multiple receivers in parallel MRI can be formulated as a linear operation to “fold” the full-FOV spin density images[29].

$$\vec{y} = A\vec{x} \tag{2.1}$$

Here  $\vec{y}$  is the vector formed from the pixel intensities recorded by each receiver (folded image) and  $\vec{x}$  is the vector formed from the full FOV image. The encoding matrix  $A$  consists of the product of the aliasing operation due to sub-sampling of the k-space data and coil-specific sensitivity modulation over the image. The goal of the image reconstruction is to solve for  $\vec{x}$  given our knowledge of  $A$  derived from understanding the folding process and an estimate of the coil sensitivity maps. While Eq. (2.1) is expressed in the image domain SENSE approach [22], similar linear

relationships are formed in the k-space based SMASH [20, 2] method. Furthermore, the same basic formalism is used in either the in-vivo sensitivity method (Sodickson 2000), or conventional SENSE/SMASH methods requiring coil sensitivity estimation. In general, Eq. (2.1) is an over-determined linear system, i.e., the number of array coils, which is the row dimension of  $\vec{y}$ , exceeds the number of the pixels which fold into the measured pixel; the row dimension of  $\vec{x}$ . To solve for  $\vec{x}$  (the full FOV image) the over-determined matrix is inverted utilizing least-square estimation [22].

$$\begin{aligned}\vec{x} &= U\vec{y} \\ &= (A^H \Psi^{-1} A)^{-1} A^H \Psi^{-1} \vec{y}\end{aligned}\quad (2.2)$$

where the  $H$  superscript denotes the transposed complex conjugate and  $\Psi$  is the receiver noise covariance [22]. When  $\Psi$  is positive semi-definite, the eigen decomposition of the receiver noise covariance leads to the unfolding matrix,  $U$ , using the whitened aliasing operator  $\tilde{A}$  and the whitened observation  $\tilde{y}$ .

$$\begin{aligned}\Psi &= V \Lambda V^H \\ \tilde{A} &= \Lambda^{-1/2} V^H A \\ \tilde{y} &= \Lambda^{-1/2} V^H \vec{y} \\ \vec{x} &= U \tilde{y} \\ &= (\tilde{A}^H \tilde{A})^{-1} \tilde{A}^H \tilde{y}\end{aligned}\quad (2.3)$$

The whitening of the aliasing operator will be used in the regularization formulation introduced in the next section. The whitening incorporates the receiver noise covariance matrix implicitly allowing optimal SNR reconstruction within the regularization formulation. The noise sensitivity of the parallel imaging reconstruction is thus quantified by the amplification of the noise power due to the geometry of the array. This g-factor is thus written [22]

$$g_{\rho\rho} = \frac{\sqrt{X_{\rho\rho}^{\text{parallel imaging}}}}{\sqrt{R}\sqrt{X_{\rho\rho}^{\text{full}}}} = \sqrt{[(\tilde{A}^H \tilde{A})^{-1}]_{\rho\rho} (\tilde{A}^H \tilde{A})_{\rho\rho}} \quad (2.4)$$

The subscript  $\rho$  indicates the voxels to be “unfolded” in the full FOV image, and  $X$  denotes the covariance of the reconstruction image vector  $\hat{\vec{x}}$ . Here  $R$  denotes the factor by which the number of samples is reduced (the acceleration rate).

### 2.2.1 Tikhonov regularization

Tikhonov regularization [8] provides a framework to stabilize the solution of ill-conditioned linear equations. The solution of Eq. (2.1) using Tikhonov regularization can be written

$$\vec{x}^\lambda = \arg \min_{\vec{x}} \left\{ \left\| \tilde{A} \vec{x} - \vec{y} \right\|_2^2 + \lambda^2 \left\| L(\vec{x} - \vec{x}^0) \right\|_2^2 \right\} \quad (2.5)$$

Here  $\lambda^2$  is the regularization parameter.  $L$  is a positive semi-definite linear transformation, and  $\vec{x}^0$  denotes the prior information about the solution  $\vec{x}$ . And  $\|\bullet\|_2$  represents the L-2 norm. Thus the second term in Eq. (2.5), defined as the prior error, is the deviation of the solution image from the prior knowledge. The first term, defined as the model error, represents the deviation of the observed aliased image from the model observation. The model observation is a folded version solution image. The regularization parameter determines the relative weights with which these two estimates of error combine to form a cost function. Consider the extreme case when  $\lambda^2$  is zero and we attempt to minimize only the first term. This is equivalent to solving the original equation,  $\vec{y} = A \vec{w} c x$ , without conditioning (conventional SENSE reconstruction.) On the other extreme, when  $\lambda^2$  is large, the solution will be a copy of the prior information . Thus, the regularization parameter  $\lambda^2$  quantifies the trade-off between the error from prior knowledge not describing the current image and the error from noise amplification from unconditioned matrix inversion. An appropriate choice of  $\lambda^2$  (regularization) decreases the otherwise complete dependency on the

whitened model ( $\tilde{A}$ ) and the whitened observation ( $\tilde{y}$ ) to constraint the solution to within a reasonable “distance” from the prior knowledge ( $\vec{x}^0$ ). Thus the regularization increases the influence of prior knowledge full-FOV image information during the unfolding of the aliased images. Given the regularization parameter  $\lambda^2$  and letting  $L$  be an identity matrix, the solution of Eq. (2.4) is written [13]:

$$\begin{aligned}\vec{x}^\lambda &= \sum_{j=1}^n \left( f_j \frac{\vec{u}_j^H \tilde{y}}{s_{jj}} + (1 - f_j) \vec{v}_j^H \vec{x}^0 \right) \vec{v}_j \\ f_j &= \frac{s_{jj}^2}{s_{jj}^2 + \lambda^2} \cong \begin{cases} 1, s_{jj} >> \lambda \\ s_{jj}^2 / \lambda^2, s_{jj} << \lambda \end{cases}\end{aligned}\quad (2.6)$$

Here  $\vec{u}_j$ ,  $\vec{v}_j$ , and  $s_{jj}$  are the left singular vectors, right singular vectors and singular values of  $\tilde{A}$  generated by singular value decomposition (SVD) with singular values and singular vectors indexed by  $j$ . This leads to the following matrix presentations:

$$\begin{aligned}\vec{x}^\lambda &= V\Gamma U^H \tilde{y} + V\Phi V^H \vec{x}^0 \\ VAR(\vec{x}^\lambda) &= V\Gamma^2 V^H \\ \Gamma_{ii} &= \frac{f_i}{s_{ii}} = \frac{s_{ii}}{s_{ii}^2 + \lambda^2} \\ \Phi_{ii} &= 1 - f_i = \frac{\lambda^2}{s_{ii}^2 + \lambda^2}\end{aligned}\quad (2.7)$$

Using regularization and Eq. (2.4), the ratio of the noise levels between the regularized parallel MRI reconstruction and the original full-FOV image normalized by the factor of acceleration gives the local geometry factor for noise amplification.

$$g_{\rho\rho} = \sqrt{[(V\Gamma^2 V^H)^{-1}]_{\rho\rho} (V S^2 V^H)_{\rho\rho}} \quad (2.8)$$

Inside the square root of Eq. (2.8), the first square bracket term denotes the variance of the unfolding using regularization from Eq. (2.7), and the second square

bracket term denotes the variance of full FOV reference image.

### 2.2.2 Estimating the optimal regularization parameter using the L-curve

To determine the appropriate regularization parameter  $\lambda^2$ , we utilized the L-curve approach [13]. Qualitatively, we expect that as regularization increases, more dependency on the prior information leads to a smaller discrepancy between the prior information and the solution at the cost of a larger difference between model prediction and observation. Similarly, a small regularization parameter decreases the difference between model prediction and observation at the cost of a larger discrepancy between the prior information and the solution. The L-2 norm is used to quantify the difference between these vectors. The model error and prior error can then be calculated [13] using:

$$\begin{aligned}\rho &\equiv \|\tilde{y} - \tilde{A}\vec{x}\|_2 = \sum_{j=1}^n ((1 - f_j)u_j^H \tilde{y})^2 \\ \eta &\equiv \|\vec{x} - \vec{x}^0\|_2 = \sum_{j=1}^n (f_j(\frac{u_j^H \tilde{y}}{s_{jj}} - \vec{x}_j^0))^2\end{aligned}\tag{2.9}$$

$\vec{x}_0^j$  is the j-th element of prior  $\vec{x}_0$ . Plotting model error versus prior error for a range of shows the available tradeoffs between the two types of error. A representation of this plot, termed the L-curve, is shown in Figure 2.1. The optimal regularization parameter is defined as that which strives to minimize and balance the two error terms. This occurs in the elbow of the L-curve. Mathematically this is where its curvature is minimum. The analytic formula [13] for the L-curve's curvature enables a computationally efficient search for the  $\lambda^2$  at the point of minimal curvature.

## 2.3 METHOD

Phantom studies were performed on a 1.5T clinical MRI scanner (Siemens Medical Solutions, Inseln, NJ) using a homemade 2-element array. Each element is a circular

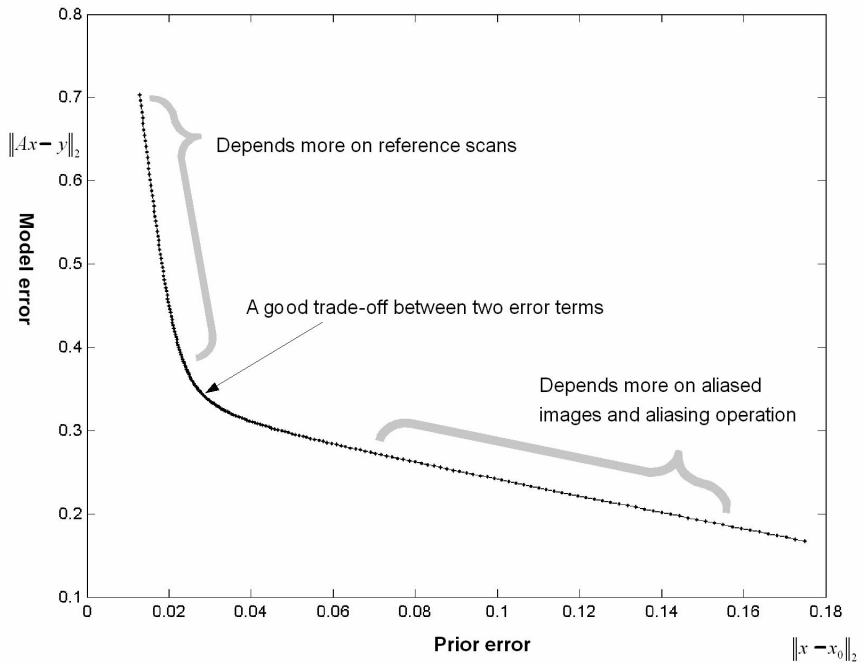


Figure 2-1: An L-curve illustrates the two costs during reconstruction the aliased images from an array. Using distinct regularization, the reconstruction biases toward either minimizing the prior error or minimizing the model error. A trade-off between these two error metrics is using the regularization at the "corner" of the L-curve.

surface coil with diameter of 5.5 cm tuned to the Larmor frequency of the scanner. The two element coils have a 1.5 cm overlap to minimize inductive coupling. The array was mounted on curved plastic with curvature radius of 20 cm to conform the phantom and subjects. A 2D gradient echo sequence was used to image the homogenous spherical (11.6cm dia.) saline phantom. The imaging parameters are: TR=100 msec, TE=10 msec, flip angle=10 deg, slice thickness=3 mm, FOV=120 mm x 120 mm, image matrix=256 x 256. The same scan was repeated with the number of phase encode lines reduced to 75%, 62.5% and 50%.

The in vivo anatomical images were acquired using a 3T scanner (Siemens Medical Solution, Inseln, NJ) with an 8-channel linear phased array coil wrapping around the whole brain circumferentially. Each circular surface coil element was of 9cm diameter and tuned to the proton Larmor frequency at 3T. Appropriate overlapping between neighboring coils minimized mutual inductance between coil elements. We used a FLASH 3D sequence to acquire in vivo brain images from a healthy subject after approval from the Institutional Review Board and informed consent. Parameters of FLASH sequence are TR=500 msec, TE=3.9 msec, flip angle=20 deg, slice thickness=3 mm with 1.5 mm gap, 48 slices, FOV=210 mm x 210 mm, image matrix=256 x 256. The same scan was repeated with the number of phase encode lines reduced to 50%, 37.5% and 25%. We adopted in vivo sensitivity reconstructions for both phantom and in vivo experiments to avoid the potential increases in g-factor due to the mis-estimation of the coil sensitivity maps [2]. Also to illustrate the validity of utilizing prior information without involving complications from different spatial resolutions, we employed identical spatial resolution for both reference scans and accelerated acquisitions. While using a full resolution reference scan defeats the purpose of the SENSE acceleration for standard radiographic imaging, it is useful for time-series imaging applications such as fMRI. However, to demonstrate the effect of regularization when only a low-resolution full-FOV reference scan is available, we also apply the regularization method to a reconstruction using lower resolution full-FOV reference images. For this demonstration, we downsampled the full-FOV reference images by two or four fold (from 256 X 256 matrix to 128 X 128 and 64 X 64 matrix)

and employed the lower resolution reference images as priors in 2-fold and 2.67 fold accelerated acquisitions. Using regularization allows a smooth tradeoff between replication of the reference information and noise introduced in the poorly conditioned inversion that may result from reliance on the measured data alone. It is important, therefore to have some indication that there is not an over reliance on the reference data (i.e. that the regularization parameter is not extremely high). For the fMRI application, the time series data should not simply replicate the reference data, in which case subtle temporal changes in the time-series will not be detected (functional CNR will be lowered). To test the degree to which regularization might reduce the CNR in an fMRI study we simulated a 2-fold accelerated SENSE fMRI scan consisting of 50 time points for the baseline (resting) condition and 50 time points for the active condition. An image from the 8 channel array was used as a template to construct the 100 image series. Model activation was added to half of the images by increasing the pixel value by 10% in a 4 pixel ROI in the occipital lobe of the left hemisphere. White Gaussian noise of zero mean was added to the time-series and the images were reconstructed with and without the regularization method. A two-sample t-test between the active and baseline conditions was used to measure fMRI sensitivity. In practice, we calculate the L-curve by iteratively calculating the two terms in the cost function (Eq. (2.9)) after performing SVD on the whitened encoding matrix. The search range of the regularization parameter was restricted in range to between the largest and smallest singular values. The search was done in a 200-sample geometric sequence, each term of which is given by a multiple of the previous one. The curvature associated with each sample was computed. Subsequently the minimal curvature was found within this search range. Image reconstruction, matrix regularization and computation of the g-factor maps were performed on a Pentium-III 1GB dual processor Linux system with code written in MATLAB (Mathworks, Natick, MA). The *in vivo* functional MRIs were acquired from a 3T scanner (Siemens Medical Solution, Inseln, NJ) with an 8-channel linear phased array coil wrapping around the whole brain circumferentially (Siemens Medical Solution, Inseln, NJ). A healthy subject was recruited to the study after the approval from the Institutional Review Board and

informed consent. Visual stimulus of 4-Hz checkerboard flashing was presented using E-PRIME software (Psychology Software Tools, Inc. Pittsburgh, PA). The visual stimulus was designed to display either continuous checkerboards flashing for 30 seconds (“on” block), or a 30-second fixation (“off” block). Three “off” blocks and two “on” blocks were alternatively presented to the subject starting with the “off” blocks. Imaging acquisition used a 2D gradient echo echo-planar imaging (EPI) sequence with parameters as: TR=2000 msec, TE=40 msec, flip angle=90 deg, slice thickness=3 mm with 1.5 mm gap, 10 slices, FOV=200 mm x 200 mm, image matrix=64 x 64. 75 volumes of the brain were acquired. The total imaging time is 2 min. and 30 sec. Parallel imaging acceleration was performed on the phase encoding (PE) direction. We sub-sampled the full k-space of each EPI volume by skipping every other PE line, selecting 3 PE lines from a contiguous 8-PE line k-space data, and skipping every 4 PE lines in the full k-space trajectory to simulate 2.00-fold, 2.67-fold and 4.00 fold acceleration respectively. The reconstruction of SENSE EPI images used the *in vivo* sensitivity reconstructions to avoid the potential increases in g-factor due to the mis-estimation of the coil sensitivity maps. In addition, we also calculated regularized SENSE image reconstruction in order to decrease g-factors due to the correlations among array channels. Given the visual stimulus paradigm, t-tests were performed on the reconstructed SENSE fMRI to contrast “on” and “off” blocks. The detection powers of the regularized and the non-regularized SENSE reconstructions were computed using the receiver-operating characteristic (ROC) curves. In simulations, due to the lack of the gold standard of cortical areas selectively sensitive to the present visual stimulus, we operationally defined the true positive rate as the ratio between the areas where both SENSE fMRI and full-FOV fMRI showed significant activations, given a significance level. Also, the false positive rate was calculated as the ratio between the areas where SENSE fMRI statistics were significant but full-FOV fMRI were insignificant. At each chosen significance level of full-FOV fMRI statistical map, ROC curves for both regularized and non-regularized SENSE fMRI were calculated separately by varying the significance level of the SENSE fMRI statistical map. The areas under each ROC curve were used to quantify the detection power.

acceleration	Unregularized			Regularized		
	mean	std.	median	mean	std.	median
2.00	1.47	1.56	1.17	0.80	0.52	0.67
1.60	1.43	1.96	1.07	0.76	0.65	0.60
1.33	1.31	1.27	1.00	0.70	0.58	0.50

Table 2.1: G-factors in unregularized and regularized SENSE reconstructions from phantom images using an 2-channel phased array coil at 50%, 62.5% and 75% phase encoding.

## 2.4 RESULTS

Figure 2.2 shows the reconstructed full-FOV phantom images and the associated g-factor maps from the 1.5T scanner using the spherical saline phantom and 2-element surface coil array using 1.33-fold (192 lines), 1.60-fold (160 lines), and 2.00-fold (128 lines) accelerations. Although the overall image SNR in this acquisition was relatively high near the surface coils, SENSE reconstruction noise arising from matrix inversion was significantly improved by the regularization step for all of the accelerated acquisitions (1.33-fold, 1.60-fold and 2.00-fold accelerations). The effect of the regularization step was greatest for SENSE reconstruction at 2.00-fold acceleration. The largest reductions in noise were observed near the coil. The bottom panel of Figure 2.2 shows the g-factor maps for regularized and non-regularized reconstructions. All the g-factor maps are scaled by the same factor to facilitate comparison. The regularized reconstructions allow g-factors less than one since prior knowledge is used. In contrast, the conventional non-regularized reconstructions always have a minimum g-factor of one. Table 2.1 summarizes the g-factors average, standard deviation, and the median in 1.33-fold, 1.60-fold, and 2.00-fold accelerations. For the 1.33-fold acceleration case, the regularization provided an average 87% reduction in the added reconstruction noise. For the 2.00-fold acceleration case, the regularization provided an average 1.84 fold reduction.

Figure 2.3 shows the regularized and non-regularized reconstructed *in vivo* images and g-factor maps from the 3T scanner using the 8-channel array coil with 2.67-fold

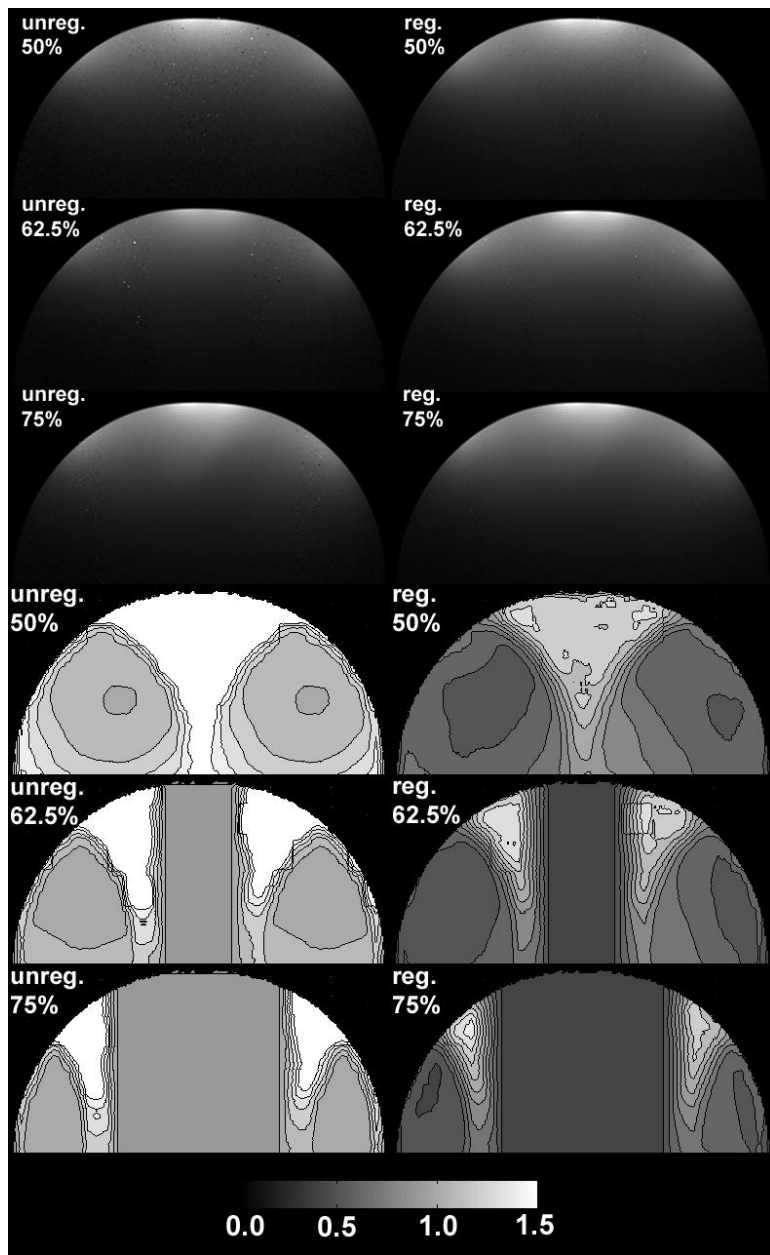


Figure 2-2: The reconstructed phantom images and g-factor maps using unregularized or regularized reconstruction in 50%, 62.5% and 75% phase encoding.

acceleration	Unregularized			Regularized		
	mean	std.	median	mean	std.	median
2.00	1.07	0.12	1.02	0.72	0.25	0.66
2.67	1.22	0.23	1.14	0.84	0.31	0.98
4.00	2.04	0.58	1.94	1.52	0.53	1.52

Table 2.2: G-factors in unregularized and regularized SENSE reconstructions from *in vivo* images using an 8-channel phased array coil at 25%, 37.5% and 50% phase encoding.

acceleration, and 2.00 -fold acceleration. The g-factor maps showed noticeable local decreases in the added noise levels of the regularized reconstructed images. Similarly, regularization helped reduce noise in the temporal lobe in 2.67-fold acceleration (middle panel). In 4.00-fold acceleration, regularized reconstruction demonstrated decreased noise in the deep temporal lobe inside insular cortex. Table 2.2 summarizes the g-factor average, standard deviation, and median in the reconstructed anatomical images. As expected, more accelerated acquisitions resulted in higher g-factors in either regularized or non-regularized reconstructions. In 2.00-fold acceleration, g-factor average was suppressed from 1.07 to 0.72 by regularization (49% reduction). In 4.00-fold acceleration, g-factor associated noise reduction by regularization is 31% (non-regularized: 2.04, regularized: 1.52). Here, the advantages in SNR due to regularized reconstruction can be appreciated in the temporal lobe of the anatomical images (Figure 2.4). In 2.00-fold acceleration, a banded noise region in the non-regularized reconstruction was minimized (Figure 2.3 and 2.4). The calculated L-curve is shown in Fig. 2.1 for a representative set of aliased pixels for the 2.0-fold accelerated case.

The SENSE reconstructions using lowered spatial resolution reference scans are shown in Figure 2.5 and Table 2.3. In 2.00-fold acceleration using a reference scan at 50% of the spatial resolution of the accelerated acquisition, the average g-factor was reduced by the regularization method from 1.08 to 0.73. When employing the reference scan with 25% of the spatial resolution of the 2.00-fold accelerated acquisition, the average g-factor was reduced from 1.10 to 0.73. For the higher acceleration

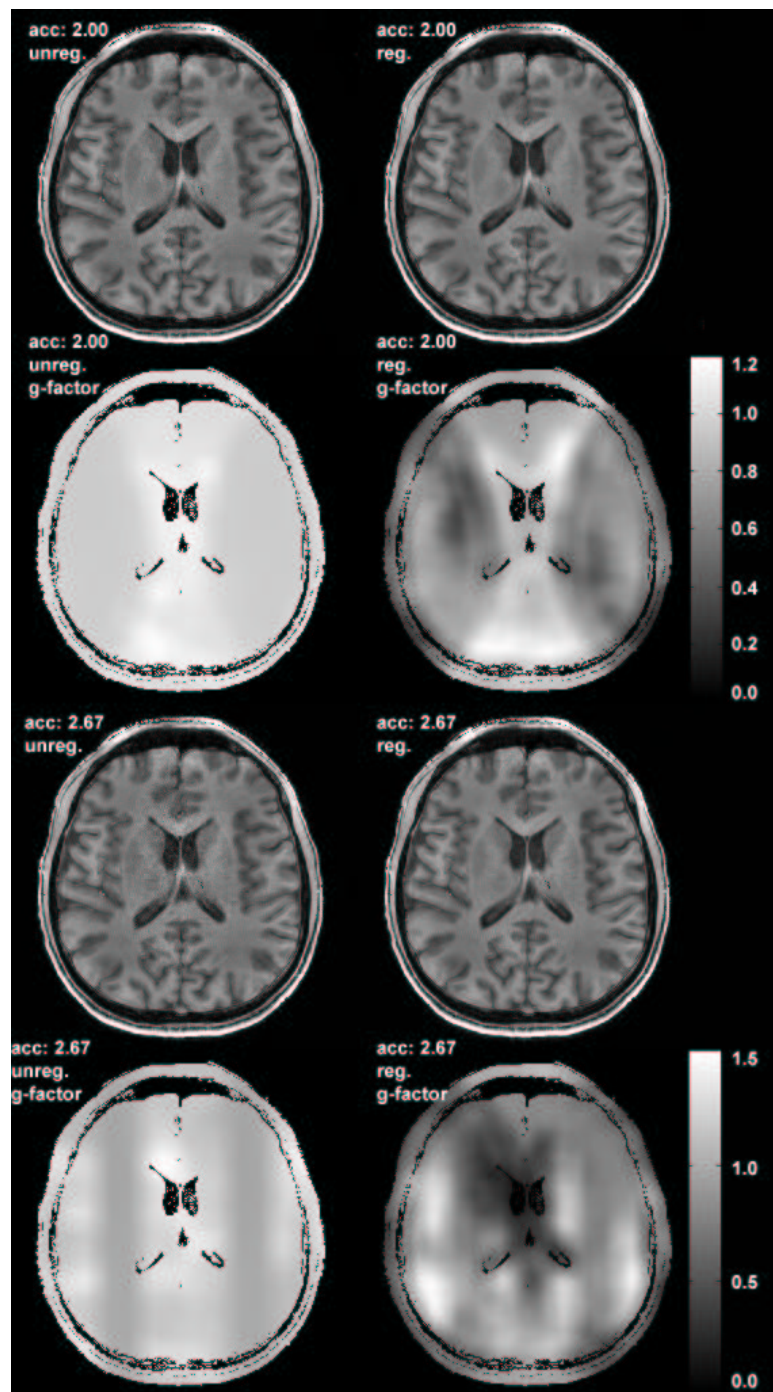


Figure 2-3: The reconstructed *in vivo* images and g-factor maps using un-regularized or regularized reconstruction in 37.5% (top panel) and 50% (bottom panel) phase encoding.

acceleration	reference image resolution	Unregularized			Regularized		
		mean	std.	median	mean	std.	median
2.00	100%	1.07	0.12	1.02	0.72	0.25	0.66
	50%	1.08	0.15	1.02	0.73	0.26	0.66
	25%	1.10	0.20	1.01	0.73	0.27	0.67
	100%	1.22	0.23	1.14	0.84	0.31	0.98
	50%	1.21	0.23	1.14	0.86	0.31	1.01

Table 2.3: G-factors in unregularized and regularized SENSE reconstructions from *in vivo* images using an 8-channel phased array coil at 2-fold and 2.67-fold acceleration using reference image of lower spatial resolutions.

(2.67-fold) case a reference scan of 50% of the spatial resolution resulted in an average g-factor of 1.21. Regularization reduced this to 0.86. In this simple fMRI model data, the contrast reduction resulting from replication of the reference image was compensated by the lower noise in the regularized reconstruction. A two-sample t-test between the active and baseline conditions showed that using regularization increased the t-statistics from 5.93 to 6.77. For a full-FOV image with matrix size of 256 X 256, the computation time in estimating the regularization parameters are 72 min., 45 min. and 26 min. for 2.00-fold, 2.67-fold and 4.00-fold accelerations respectively. After the estimation of the regularization parameters, it takes 44 min, 34 min, and 24 min to reconstruct a single-slice single-measurement aliased image at 2.00-fold, 2.67-fold and 4.00-fold accelerations respectively, including calculating both regularized and non-regularized unfolded images and their associated g-factor maps.

Figure 2.6 shows the t-statistics of the fMRI data using full k-space, regularized and unregularized SENSE fMRI acquisitions at 2.00-, 2.67-, and 4.00-fold accelerations. Note that at the same t-statistics level, less activation areas were revealed. The loss of BOLD contrast-to-noise ratio (CNR) were potentially due to reduced data samples in SENSE accelerations. Comparing between regularized and unregularized SENSE reconstructions shows qualitatively similar activations maps.

Figure 2.7 shows the ROC curves of regularized and unregularized SENSE fMRI detection at 2.00-, 2.67-, and 4.00-fold accelerations. Compared to the t-statistics of

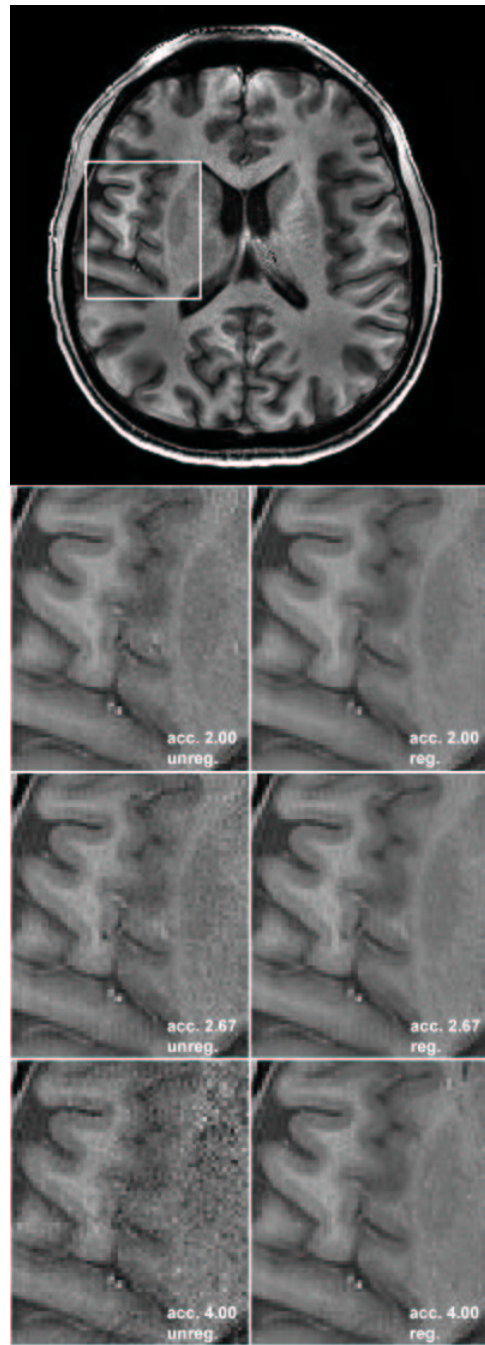


Figure 2-4: The selected temporal lobe area from the whole brain image as shown by the white box (top panel). Detailed anatomy from unregularized and regularized SENSE reconstructions of 2.00, 2.67 and 4.00 fold accelerations.

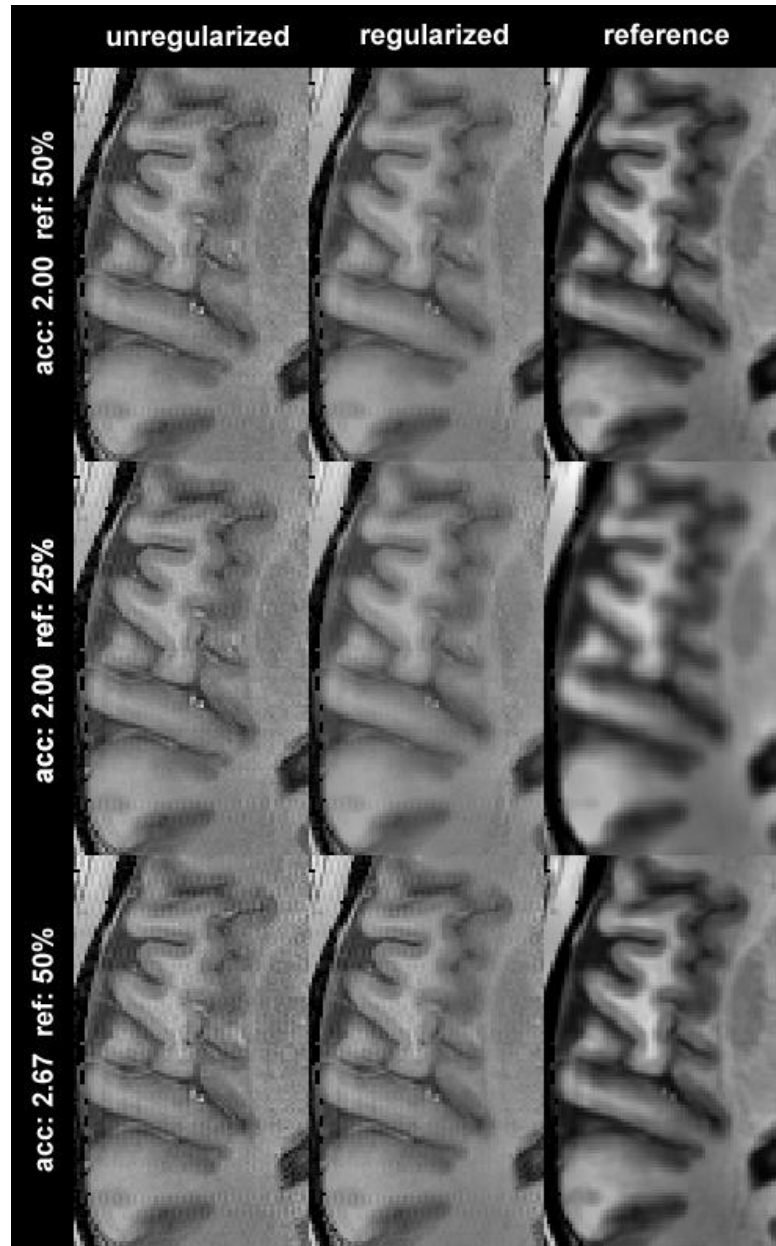


Figure 2-5: Detailed temporal lobe anatomy from unregularized and regularized SENSE reconstructions of 2.00 and 2.67 fold accelerations using reference scans at 50% and 25% spatial resolution of the accelerated acquisitions.

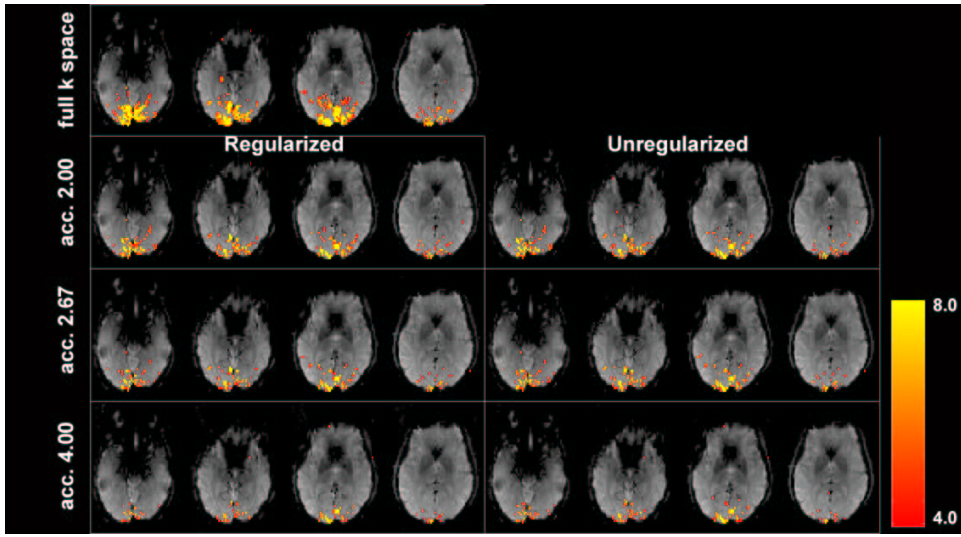


Figure 2-6: The t statistics maps of full k-space acquisition, 2.00-, 2.67- and 4.00-fold SENSE accelerations with/without regularization.

4.0 of the unaccelerated fMRI data, 2.00-fold accelerations using regularization or not does not show significant difference in the ROC curves. In 2.67-fold acceleration, regularized SENSE reconstruction outperforms unregularized reconstructions when false positive rate is controlled below 0.12. In 4.00-fold acceleration, regularized SENSE reconstructions have higher sensitivity and specificity than unregularized reconstructions. Note that in general the detection decreases when the SENSE acceleration increases by shifting the ROC curves toward lower right corner. This is potentially due to the decreased SNR in SENSE acquisitions when more k-space data are skipped.

The ROC areas corresponding to SENSE fMRI reconstruction using regularization and without regularization at acceleration of 2.00, 2.67 and 4.00 were shown in Figure 2.8. In 2.00-fold acceleration, the ROC areas for fMRI using regularized SENSE reconstruction are larger than those of unregularized SENSE reconstruction when the t statistics from data without acceleration varies between 8 and 11. When the t-statistics from data without acceleration vary between 0 and 7, we found that the ROC area not using regularization is larger than regularized reconstructions at t statistics of 2.0, 3.0, 5.0, 6.0, and 7.0. In 2.67-fold acceleration, regularized SENSE fMRI have larger ROC areas than unregularized SENSE fMRI when the t-statistics

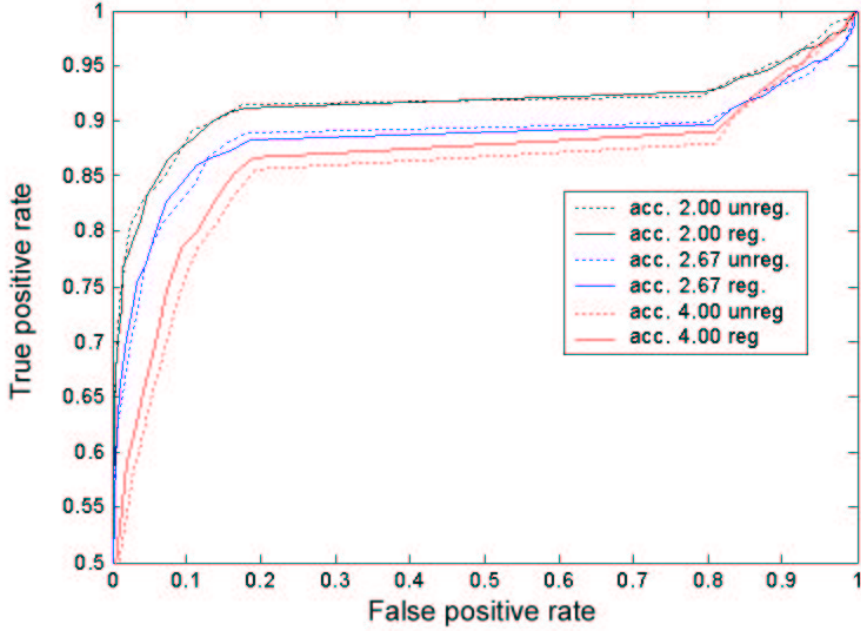


Figure 2-7: ROC curves for 2.00-, 2.67- and 4.00-fold SENSE accelerations with/without regularization.

varies between 0 and 12, except t-statistics at 6.0 and 8.0. In 4.00-fold acceleration, regularized SENSE fMRI has larger ROC area than the unregularized reconstructions when the t statistics of the unaccelerated SENSE vary from 0 to 11.

## 2.5 DISCUSSION

The regularization approach introduced in this work was intended to minimize the SNR loss by constraining the matrix inversion. Mathematically, this is equivalent to obtaining a compromise between an expected a priori result and the noisy result from inversion with no conditioning. Such an approach is equivalent to the maximal a posteriori (MAP) estimation in stochastic Bayesian modeling. The "optimal" solution in this scenario thus implies the simultaneous minimizations of model errors and prior errors, which is graphically represented in the L-curve. The proposed regularized parallel MRI reconstruction algorithm is expected to be universally workable independent of the k-space sampling scheme, the array coil configuration and the imaging

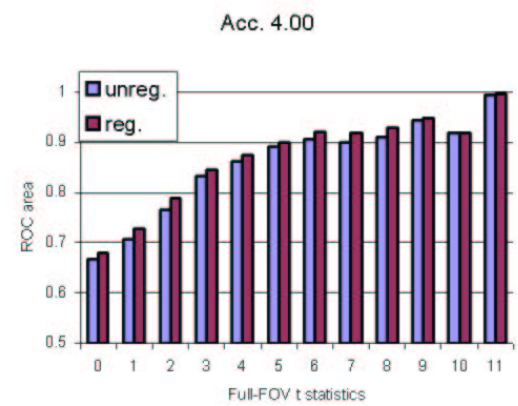
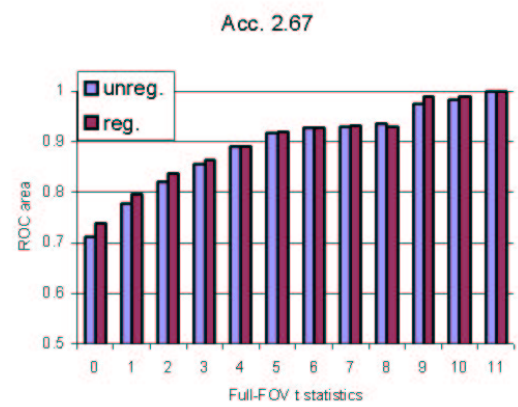
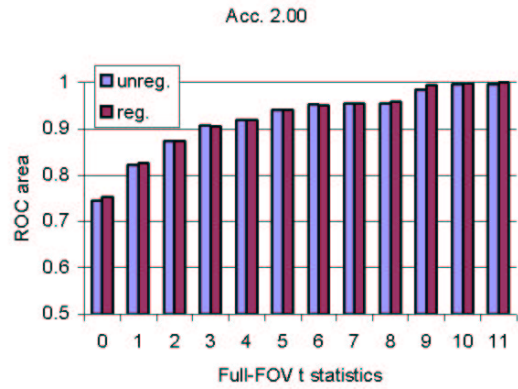


Figure 2-8: ROC areas for 2.00-, 2.67- and 4.00-fold SENSE accelerations with/without regularization when the full FOV t statistics are thresholded between 0 and 11 to determine true positive rates and false positive rates.

anatomy. In the regularized SENSE reconstruction, we found that g-factors can be smaller than 1. A g-factor of 1 indicates that the reconstruction added no additional noise due to the operation of unfolding the aliased image alone. A g-factor less than 1, which can occur when regularization is employed, indicates that the unfolding operation itself decreases the stochastic variability of the estimated spin density compared to the full FOV reference scans. This reduction in noise results from the prior knowledge used in the regularization process. From the original definition of g-factor, when excluding the effect of number of samples (or the acceleration factor, R) in the denominator of the first term in Eq (2.4), the g-factor is the ratio of the variance of the estimated spin density from parallel acquisitions over the variance of the spin density from the full-FOV reference scan. Since prior information is employed in the regularized parallel MRI reconstruction, less variability of the estimated spin density from parallel acquisitions is expected. Thus using regularization can partially compensate the SNR loss due to the reduced samples in the accelerated acquisition. It is important to note that the reduction reflects the use of prior knowledge, which may lead to a biased result. A potential concern of employing regularization is thus the replication of image features of the reference scan in the reconstructed image. This bias is seen as imparted image blurring in Fig. 2.5 for the high acceleration rate reconstruction using four fold lower spatial resolution reference images. For an fMRI time series experiment, later time-points might be biased toward the first reference image reducing the contrast between the activated and resting state. The model fMRI data set analyzed here suggests, however, that the CNR of the time series is improved by the regularization procedure. Thus the contrast reduction is less important than the noise reduction due to regularization. Another concern of using regularization in parallel MRI reconstruction is that the noise in the prior reference itself could at some point be introduced into the reconstruction, thereby limiting the visible SNR improvements. However, the quality of full-FOV prior image can be improved either by multiple averages if parallel MRI is used for dynamic imaging applications, or by spatial smoothing using kernels with dimensions similar to the signal based on matched filter theory. The advantage of regularized parallel MRI reconstruc-

tions was previously reported by Sodickson et. al. [2] on cardiac imaging using an empirical formula of a fraction (0.05) of the first eigen value, Similarly, regularized SENSE reconstruction using an empirical regularization parameter was described by King et. al. [9]. Subsequently other studies have demonstrated the benefits of prior information in parallel MRI reconstructions [12, 15, 30, 11]. In contrast to fixed regularization strategies, we have utilized an automatic regularization implemented by the mathematically and computationally convenient algorithms to stabilize the image reconstruction. This is expected to be more adaptive to different anatomy and coil configurations. We utilize the so-called "in vivo SENSE" reconstruction approach described by Sodickson et al [2]. This method substitutes an a priori information in place of the detailed estimate of the coil profile used by SENSE [22]. In the uniform phantom, the two methods are identical since the full FOV a priori image is identical to a coil profile map. We chose the in vivo sensitivity reconstruction approach to demonstrate the with/without regularization in unfolding effects in "in vivo SENSE" so that, i) we could demonstrate the g-factor gains independent of issues incurred from miss-estimation of the coil sensitivity profiles, ii) the inclusion of the phantom study demonstrates regularization in both "traditional" SENSE and in vivo SENSE since in vivo SENSE reduces to a form of tradition SENSE in this case, iii) the in vivo SENSE method has an intrinsic appeal for time series measurements (such as fMRI) where only small intensity changes are expected relative to the baseline image. Here we also present the simulated fMRI experiments using SENSE EPI to achieve 2.00-, 2.67- and 4.00-fold accelerations. The concerns for the reduced SNR and contrast-to-noise ratio (CNR) in BOLD images using SENSE acquisition were observed and quantified by the ROC analysis. Note that in fMRI, SENSE image reconstruction using regularization has two competing factors determining the BOLD contrast: signal level is lowered in SENSE acquisition due to the dependence on the prior information; and noise level is lowered if regularization is used to reduce the unfolding associated noise amplification. In high accelerations, the benefits of reduced noise amplification (measured by g-factors) may compensate the loss of contrast to yield SNR and CNR increment. This is shown in the 2.67-, and 4.00-fold accelerations. But such compensation for

SNR and CNR from regularization is compared to the SENSE reconstructions at the same acceleration. Compared to the full-encoded data, SENSE accelerated EPI has lowered SNR and CNR due to reduced data samples. In the experiments presented in this chapter, our regularization approach worked robustly in different field strengths and array coil configurations and the benefits of reduced g-factor associated SNR loss were consistently observed. Once the regularization parameters are determined, the computational reconstruction time is identical to the reconstruction without regularization. Thus the additional computational demand for the proposed technique is the total time needed to estimate the regularization parameters. The long computational time required even for un-regularized inversion using MATLAB shows that this environment is useful only for testing the method. Note that our unfolding of aliased SENSE images includes calculation of both regularized and non-regularized reconstructions and their associated g-factor maps. The computation time can be reduced to 1/4 if only one set of the unfolded full-FOV image is estimated. Computational speed may be further improved by optimizing code platform. Even given the closed form model errors and prior errors in Eq. (2.9), searching through different is necessary to locate the minimal curvature. This could be made more efficient by using a direct regularization estimation method. In dynamic imaging, the impact on the increased image reconstruction time due to regularization estimation can be minimized by estimating regularizations only once and then using identical regularization parameters for the repeated time points. This is particularly attractive for function brain activation studies where the changes with time are quite small. In addition to the proposed L-curve technique, other automatic regularization estimation methods, such as generalized cross validation (GCV) [16, 17], can be potentially used for appropriate regularization estimation. In this work we present an approach to employ regularization in reconstructing parallel MRI data in order to reduce the noise amplification of the reconstruction (g-factor). The proposed L-curve algorithm was fully automatic and showed a significant reduction in average g factors in phantom and in vivo data at 1.5T and 3T. For some pixels the g factor was reduced below 1 indicating that the a priori knowledge in the reconstruction reduced the variability below that

of the full-FOV reference scan. The reliance on a priori knowledge did not, however, reduce functional imaging CNR in a model fMRI experiment. Although the method was demonstrated using the *in vivo* SENSE method, the regularization method for reduction of noise amplification might potentially benefit most variants of parallel MR reconstruction.



# References

- [1] D. K. Sodickson and W. J. Manning. Simultaneous acquisition of spatial harmonics (smash): fast imaging with radiofrequency coil arrays. *Magn Reson Med*, 38(4):591–603., 1997.
- [2] D. K. Sodickson. Tailored smash image reconstructions for robust in vivo parallel mr imaging. *Magn Reson Med*, 44(2):243–51., 2000.
- [3] K. P. Pruessmann, M. Weiger, M. B. Scheidegger, and P. Boesiger. Sense: sensitivity encoding for fast mri. *Magn Reson Med*, 42(5):952–62., 1999.
- [4] P. Kellman and E. R. McVeigh. Ghost artifact cancellation using phased array processing. *Magn Reson Med*, 46(2):335–43., 2001.
- [5] J. A. de Zwart, P. van Gelderen, P. Kellman, and J. H. Duyn. Reduction of gradient acoustic noise in mri using sense-epi. *Neuroimage*, 16(4):1151–5, 2002. 22191965 1053-8119 Journal Article.
- [6] M. Weiger, K. P. Pruessmann, C. Leussler, P. Roschmann, and P. Boesiger. Specific coil design for sense: a six-element cardiac array. *Magn Reson Med*, 45(3):495–504, 2001. 0740-3194 Journal Article.
- [7] J. A. de Zwart, P. J. Ledden, P. Kellman, P. van Gelderen, and J. H. Duyn. Design of a sense-optimized high-sensitivity mri receive coil for brain imaging. *Magn Reson Med*, 47(6):1218–27, 2002. 22106786 0740-3194 Journal Article.
- [8] A. N. Tikhonov and V. Ia Arsenin. *Solutions of ill-posed problems*. Scripta series in mathematics. Winston ; distributed solely by Halsted Press, Washington New

York, 1977. Andrey N. Tikhonov and Vasiliy Y. Arsenin ; translation editor, Fritz John. ill. ; 23 cm. Translation of Metody resheniiia nekorrektnykh zadach. Includes index.

- [9] K. King. Sense image quality improvement using matrix regularization. In *Proceedings of the 9th Annual Meeting of ISMRM*, page 1771, Glasgow, Scotland, 2001. International Society of Magnetic Resonance in Medicine.
- [10] Fa-Hsuan Lin, Kenneth K Kwong, Ying-Jui Chen, John W. Belliveau, and Lawrence L. Wald. Reconstruction of sensitivity encoded images using regularization and discrete time wavelet transform estimates of the coil maps. In *International Society for Magnetic Resonance in Medicine Tenth Scientific Meeting and Exhibition*, page 2389, Honolulu, Hawaii, USA, 2002. International Society for Magnetic Resonance in Medicine.
- [11] J. Tsao, K. Pruessmann, and P. Boesiger. Prior-information-enhanced dynamic imaging using single or multiple coils with k-t blast and k-t sense. In *International Society for Magnetic Resonance in Medicine Tenth Scientific Meeting and Exhibition*, page 2369, Honolulu, Hawaii, USA, 2002. International Society of Magnetic Resonance in Medicine.
- [12] Ulrich Katscher and Dirk Manke. Underdetermined sense using a-priori knowledge. In *International Society for Magnetic Resonance in Medicine Tenth Scientific Meeting and Exhibition*, page 2396, Honolulu, Hawaii, USA, 2002. International Society for Magnetic Resonance in Medicine.
- [13] Per Christian Hansen. *Rank-deficient and discrete ill-posed problems : numerical aspects of linear inversion*. SIAM monographs on mathematical modeling and computation. SIAM, Philadelphia, 1998. Per Christian Hansen. ill. ; 26 cm.
- [14] D. K. Sodickson and C. A. McKenzie. A generalized approach to parallel magnetic resonance imaging. *Med Phys*, 28(8):1629–43., 2001.

- [15] Z-P. Liang, R. Bammer, J. Ji, N. Pelc, and G. Glover. Making better sense: wavelet de-noising, tikhonov regularization, and total-least squares. In *International Society for Magnetic Resonance in Medicine Tenth Scientific Meeting and Exhibition*, page 2388, Honolulu, Hawaii, USA, 2002. International Society of Magnetic Resonance in Medicine.
- [16] G Wahba. Practical approximate solutions to linear operator equations when the data are noisy. *SIAM J. Numer. Anal.*, 14:651–667, 1977.
- [17] G. H. Golub, M. T. Heath, and G. Wahba. Generalized cross-validation as a method fo choosing a good ridge parameter. *Technometrics*, 21:215–223, 1979.



# Chapter 3

## Distributed Current Estimates with a Cortical Orientation Constraint

In contrast to overdetermined source models with a small number of equivalent current dipoles (ECD), distributed source modeling of magnetoencephalogram (MEG) and electroencephalogram (EEG) employs a dense distribution of thousands of current sources. Previously, anatomical MRI data has been used to constrain the locations and orientations of the sources on the basis of the cortical geometry, extracted from anatomical MRI data. Here, this approach is extended by calculating Cortical Patch Statistics (CPS), which is incorporated into the source models as a Loose Orientation Constraint (LOC). The proposed approach allows us to take into account the variation of the cortical surface normal within the cortical patch corresponding to each current source location. Simulations with single ECDs, 10 mm diameter cortical patches, and 20 mm diameter patches show that applying the LOC can improve localization accuracy from 9 mm down to 7 mm in  $l_2$  minimum norm estimate (MNE), and from 12 mm to 3 mm in  $l_1$  minimum norm estimate, also called minimum current estimates, (MCE). The refined cortical constraints were applied to *in vivo* data from auditory and somatosensory evoked fields.

### 3.1 INTRODUCTION

Magnetoencephalography (MEG) is a non-invasive tool to investigate the human brain function with a high temporal resolution of milliseconds [1, 24] by measuring magnetic fields ensuing from neural currents in the brain. MEG is closely related to electroencephalography (EEG), which measures the electric potential distributions on the scalp. MEG is selectively sensitive to source currents flowing tangentially with respect to the surface of the head, whereas EEG detects both the tangential and radial source components. Localization of the sources with these methods is complicated by the non-uniqueness of the electromagnetic inverse problem. To render the solution unique several source models with different constraints have been proposed.

The most popular MEG and EEG source modeling approach is to assume the measured fields can be accounted for by modeling the source by a small number of focal sources modeled by equivalent current dipoles (ECDs). If multiple sources are simultaneously active, reliable estimation of the source parameters becomes difficult due to the non-linear relationship between the source locations and the measured signals. Whereas global optimization algorithms have been tailored to accomplish this task [3], the most feasible solutions combine optimization algorithms with partly heuristic interactive approaches, motivated by prior physiological and anatomical information. In addition, the dipole maybe an oversimplification as a model for spatially extended source activity.

As an alternative approach, distributed current solutions have been proposed. A widely employed distributed source localization approach in MEG and EEG is based on the  $l_2$ -norm prior, resulting in diffuse minimum-norm estimates (MNE), [19, 20, 21]. More focal estimates can be obtained by using an  $l_1$ -norm prior; the corresponding minimum-norm solution is often called the minimum-current estimate (MCE) [36, 37].

Previously, it has been proposed that individual anatomical information, acquired with structural magnetic resonance imaging (MRI), can be incorporated into the source localization with -norm constraint. In particular, the locations of the sources

can be constrained to the cortical mantle and their orientations perpendicular to the local cortical surface [19]. Such a modeling constraint is motivated by the physiological information that the main sources of MEG and EEG signals are postsynaptic currents in the pyramidal cells on the cortex and that the principal net direction of the current is perpendicular to the cortical surface [24, 9]. Importantly, in MCE, the optimization algorithm becomes more straightforward if the orientations of the sources are known and the source amplitudes are subsequently estimated subject to constraint. To this end, the MCE implementation described in [37] used the current-source orientations provided by MNE.

To maintain computational efficiency, distributed source models usually employ a spacing of 5 - 10 mm between neighboring sources in the discrete source space. In our previous work with the minimum  $\ell_1$ -norm estimate [20] we employed the cortical location constraint, with current orientations either unconstrained or strictly constrained to the orientation of the cortical normal at each source space point. Because the preferred net current direction on the cortex is known, omitting the orientation information available from MRI is obviously a suboptimal way to use the anatomical constraints. On the other hand, using a strict orientation constraint is sensitive to slight errors in the MEG-MRI alignment and does not take into account the fact that the orientation may vary considerably within each cortical patch corresponding to the source space points. To overcome these problems we have devised methods to calculate cortical patch statistics (CPS) and incorporated these data as the loose orientation constraint (LOC). In this chapter, we employ this new approach in the calculation of both  $\ell_1$  and  $\ell_2$ -norm distributed solutions. We will present the theoretical and technical details of our approach as well as simulations with different source configurations. Analysis of auditory and somatosensory MEG data will be presented to demonstrate the utility of the approach.

## 3.2 DISTRIBUTED INVERSE SOLUTIONS

Anatomically constrained minimum-norm estimates The measured MEG/EEG signals and the underlying current source strengths are related:

$$Y = AX + N \quad (3.1)$$

where  $Y$  is an  $m$ -by- $t$  matrix containing measurements from  $m$  sensors over  $t$  distinct time instants,  $X$  is a  $3n$ -by- $t$  matrix denoting the unknown time-dependent amplitudes of the three components of  $n$  current sources,  $A$  is the gain matrix representing the mapping from the currents to MEG/EEG signals, i.e., the solution of the forward problem, and  $N$  denotes noise in the measured data. The most feasible assumption is that  $N$  is Gaussian with a spatial covariance matrix  $C$ , to be estimated from the data. If we further assume that the source amplitudes are also Gaussian with a covariance matrix  $R$ , we obtain the regularized  $l_2$  minimum-norm solution, linearly related to the source currents, as [19]

$$X^{MNE} = RA^T(ARA^T + \lambda^2 C)^{-1}Y = WY \quad (3.2)$$

where  $\lambda^2$  is a regularization parameter to avoid magnification of errors in data in the current solution and the superscript  $T$  indicates the matrix transpose. This result can be also interpreted as the Bayesian maximum a posteriori (MAP) estimate, if one assumes that the signals are Gaussian with mean  $AX$  and covariance matrix  $C$  and that the *a priori* distribution of the currents is Gaussian with zero mean and covariance matrix  $R/\lambda^2$ . However, in the present approach, there is no physiological information justifying this choice of the prior for currents; the choice is rather motivated by the simple computational realization of the estimation procedure. Consequently, we prefer not to emphasize here the Bayesian interpretation of the MNE.

In Eq. (3.2), the current orientations have not been constrained. *A priori* orientation information can be easily incorporated by replacing the gain matrix by

$$A_{fixed} = A\Theta \quad (3.3)$$

where  $\Theta$  is a  $3n$ -by- $n$  matrix containing the unit vectors pointing to the directions of the currents. If the direction cosines of the  $k$ th dipole are  $c_{kx}$ ,  $c_{ky}$ , and  $c_{kz}$ , the  $k$ th column of  $\Theta$  reads

$$\Theta_k = (\underbrace{0\dots 0}_{3(k-1)} \ c_{kx}c_{ky}c_{kz} \underbrace{0\dots 0}_{n-3k})^T \quad (3.4)$$

### 3.2.1 Spatial whitening

Instead of applying Eq. (3.2) directly, it is convenient to use an equivalent formulation

$$X^{MNE} = R\tilde{A}^T(\tilde{A}R\tilde{A}^T + \lambda^2 I)^{-1}\tilde{Y} = \tilde{W}\tilde{Y} \quad (3.5)$$

where

$$\begin{aligned} \tilde{Y} &= C^{-1/2}Y \\ \tilde{A} &= C^{-1/2}A \end{aligned} \quad (3.6)$$

are the spatially whitened data and spatially whitened gain matrix, respectively. This step allows us to simplify the subsequent calculations, since the noise-covariance matrix of the whitened data is a unit matrix, as indicated by the comparison of Eqs. (3.2) and (3.5).

### 3.2.2 Depth weighting

The MNE is known to have a bias towards superficial currents, caused by the attenuation of the MEG and EEG lead fields with increasing source depth. It is possible to compensate for this tendency by scaling the columns of  $A$  with a function, denoted here by  $f_k$  for the  $k$ th dipole, increasing monotonically with the source depth. A commonly used choice is

$$f_k = 1/(a_{3k-2}^T a_{3k-2} + a_{3k-1}^T a_{3k-1} + a_{3k}^T a_{3k})^\gamma \quad (3.7)$$

where  $a_p$  is the  $p$ th column of  $A$  and  $\gamma$  is a tunable parameter. Whereas [27] suggest  $\gamma = 0.5$ , we have found in our simulations that this does not provide sufficient compensation. Our preferred value is slightly bigger ( $\gamma = 0.6$ ). The alternative Bayesian interpretation of the depth weighting is that the variance of currents increases with depth, again hardly justifiable physiologically.

### 3.2.3 Noise-normalization

In the above, Eqs. (3.2) and (3.5) provide the best-fitting value for the current amplitudes or, in the Bayesian view, the maximum *a posteriori* (MAP) estimate. To make the resulting maps conceptually similar with those calculated in other functional imaging modalities, Dale et. al [20] proposed that the current values should be converted into dynamic statistical parametric maps. To this end, we need to consider the variances of the currents

$$w_k = (WCW^T)_{kk} = (\tilde{W}\tilde{W}^T)_{kk} \quad (3.8)$$

For fixed-orientation sources we now obtain the noise-normalized activity estimate for the  $k$ th dipole and  $p$ th time point as

$$z_{kp} = \frac{X_{kp}^{MNE}}{w_k} \quad (3.9)$$

which is  $t$ -distributed under the null hypothesis of no activity at the current location  $k$ . Since the number of time samples used to calculate the noise-covariance matrix  $C$  is quite large, more than 100, the  $t$  distribution approaches a unit normal distribution (i.e., a  $z$ -score). If the orientation is not constrained, the noise-normalized solution is calculated as

$$F_{kp} = \frac{\sum_{q=1}^3 (X_{3(k-1)+q}^{MNE})^2}{\sum_{q=1}^3 w_{3(k-1)+q}^2} \quad (3.10)$$

Note that under the null hypothesis,  $F_{kp}$  is  $F$  distributed, with three degrees of freedom for the numerator. The degree of freedom for the denominator is typically large, again depending on the number of time samples used to calculate the noise-covariance matrix. As discussed in [20], the noise-normalized estimates resulting from the transformations given in Eqs. (3.9) and (3.10) have a smaller depth bias than the MNEs obtained without depth weighting. Furthermore, the point-spread function, i.e., the image of a point current source, is more uniform in space in the noise-normalized estimate than in the MNE.

### 3.2.4 Cortical patch statistics (CPS)

As stated above, the most feasible anatomical constraint for MEG and EEG source localization is to restrict the source locations to the cortical mantle, extracted from the individual's MRI. With modern segmentation methods, the geometry of the cortex can be automatically triangulated from high-resolution 3D MRI data sets. We employed the FreeSurfer software [31, 12, 13] to build a triangular cortical surface mesh from T1-weighted anatomical MRI data (MPRAGE sequence) with a 1-mm isotropic spatial resolution. In addition to the folded surface, FreeSurfer also computes inflated and flattened views of the cortex. These views expose the parts of the cortex embedded in the sulci and are thus particularly useful for visualizing MEG data, which is mainly sensitive to fissural activity. We used the gray-white matter boundary to generate the cortically constrained source space. To achieve sufficient anatomical detail, the triangular tessellation typically consists of 130 000 - 150 000 vertices per hemisphere, corresponding to an approximate triangle size of 1 mm. For source modeling, this dense triangulation is subsequently decimated to a grid spacing of 5 - 10 mm. This is motivated by the limited spatial resolution intrinsic to the source localization using MEG/EEG and practical computational efficiency concerns. However, this simplified

source geometry may yield inaccurate dipole orientations, which do not take into account the orientation variation over the patch belonging to each decimated current source location. Furthermore, the actual areas of the patches have to be taken into account in the calculations to correctly estimate the current density on the cortex. To acquire more representative cortical information, we use the original dense cortical mesh to obtain a stochastic characterization of the cortical patches. We employ the Dijkstra [14] along the edges of the cortical mesh to calculate the distance from all vertices to each of the decimated source points. For each vertex of the original cortical mesh, the closest decimated dipole can be thus determined. Vertices in a given cortical patch share the same nearest decimated dipole location, as shown in Fig. 3.1. Given the cortical patch definitions across the whole cortical mantle, we can calculate the area associated with each decimated dipole source by assigning the area of each triangle to the associated cortical patch. At the boundary of the cortical patch, the area of the triangle is divided proportional to the number of vertices belonging to the same cortical patch, as shown in Figure 3.2. The individual columns of the forward matrix  $\tilde{A}$  are then weighted by the areas of the cortical patches, i.e.,

$$\tilde{A}^\Delta = \tilde{A} \text{diag}(\Delta) \quad (3.11)$$

where  $\text{diag}(\Delta)$  is a diagonal matrix with the areas of the patches as its elements. This transformation means that instead of net current dipole amplitudes at each source location we now estimate the current density on the patch in units of [Am/m<sup>2</sup>].

### 3.2.5 The Loose Orientation Constraint (LOC)

Given the structure of the cortical patches, we estimate the averaged cortical orientation associated with each patch and the associated standard deviation. Rather than assigning a fixed orientation to decimated dipole directly, we employ the averaged orientation within a patch to reduce the effect of sparse sampling of the original tessellation. To further accommodate the deviation around the averaged normal direction in each cortical patch, we use a Loose Orientation Constraint (LOC) as follows:

$$\begin{aligned}
R_{\{d,d\}} &= [\sin \theta_d \sin \theta_d 1], \\
\tilde{A}_{\{d\}} &= \tilde{A}_{\{d\}}^\Delta [\hat{e}_{x,d} \hat{e}_{y,d} \hat{e}_{z,d}], \\
X &= R \tilde{A}^T (\tilde{A} R \tilde{A}^T + \lambda^2 I)^{-1} \tilde{Y}
\end{aligned} \tag{3.12}$$

where  $R_{\{d,d\}}$  are the three diagonal elements of  $R$  corresponding to one dipole and  $\{d\}$  denotes the column indices for one dipole in the forward matrix.  $[\hat{e}_{x,d} \hat{e}_{y,d} \hat{e}_{z,d}]$  is a rotation matrix with  $\hat{e}_{z,d}$  pointing to the cortical normal direction,  $\hat{e}_{x,d}$  and  $\hat{e}_{y,d}$  being normal to it in the tangential plane. We used three alternatives for computing the cortically constrained source estimates: without an orientation constraint, with fixed orientation constraint taken as samples from the complete cortical triangulation, and the loose orientation constraint. Below, we refer to the three methods as free orientations (FO), the strict orientation constraint (SOC), and the loose orientation constraint (LOC), respectively.

### 3.2.6 Minimum-current estimates

The minimum-current estimate (MCE) [36, 37] can be formulated as the solution of the optimization problem:

$$\begin{aligned}
&\text{minimize} \sum_{i=1}^n w_i |X_i| \\
&\text{subject to } \tilde{Y}_r = B_r X
\end{aligned} \tag{3.13}$$

where  $w_i$  are the weights for dipole sources while  $\tilde{Y}_r$  and  $B_r$  are the regularized measurement and forward solution for fixed-orientation sources, respectively. As before, let  $\Theta$  be the  $n$ -by-3 matrix containing the source orientations and compute the singular-value decomposition

$$\tilde{A}^\Delta \Theta = U \Lambda V^T \tag{3.14}$$

Then

$$\begin{aligned} B_r &= U_r^T \tilde{A}^\Delta \Theta, \\ \tilde{Y}_r &= U_r^T \tilde{Y} \end{aligned} \quad (3.15)$$

where  $U_r$  is composed of the first  $r$  columns of  $U$ . This method of eigenvalue truncation in regularization is closely related to the use of the regularization parameter  $\lambda^2$  in Eqs. (3.2) and (3.5). It is easy to show that the latter corresponds to weighting of the eigenvalues with a smooth transition function instead of the step function implied by Eq. (3.15).

The above implementation of MCE requires the knowledge of the orientations of sources. It was previously suggested to employ MNE to estimate the dipole orientations, and subsequently using Linear Programming (LP) to solve Eqs. (3.13). [37]. In Uutela's approach, cortical location or orientation constraint was not used; the source space consisted of an even 3D grid of source locations. We propose to use the LOC together with the cortical source space in the computation of the initial MNE. The incorporation of brain anatomy from the high-resolution MRI with cortical patch definitions is expected to give a better approximation for the dipole orientations than the unconstrained MNE used in [37]. The subsequent anatomically-informed MCE is then computed given the measurement data, the forward solution, and dipole orientation estimates from the initial anatomy-informed MNE. Another possibility is to use a strict orientation constraint in the MCE calculations directly without computing a MNE first.

### 3.3 METHODS

#### 3.3.1 Anatomical information from high resolution MRI for MNE and MCE

The brain anatomy was imaged by high-resolution T1-weighted 3D volume MRI using MPRAGE sequence (TR/TE/flip = 2530ms/3.49ms/7°, partition thickness =

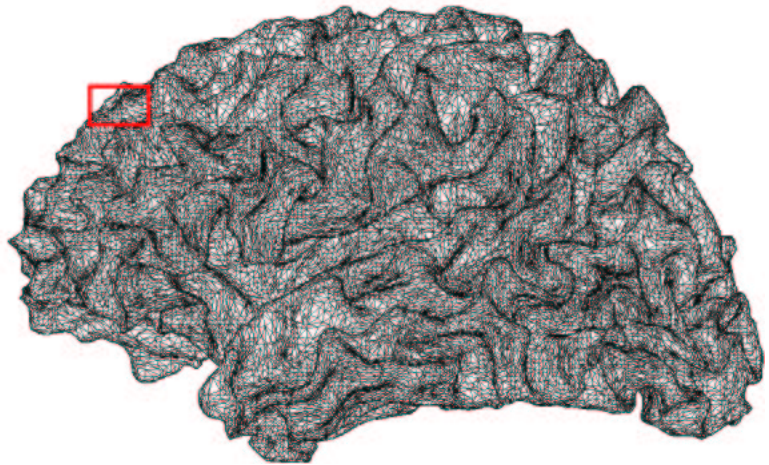


Figure 3-1: The 3 dimensional left hemisphere white matter brain anatomical mesh derived from high-resolution T1-weighted MRI. The red box indicates the region to introduce the definition of local cortical patch (see Fig. 3.2).

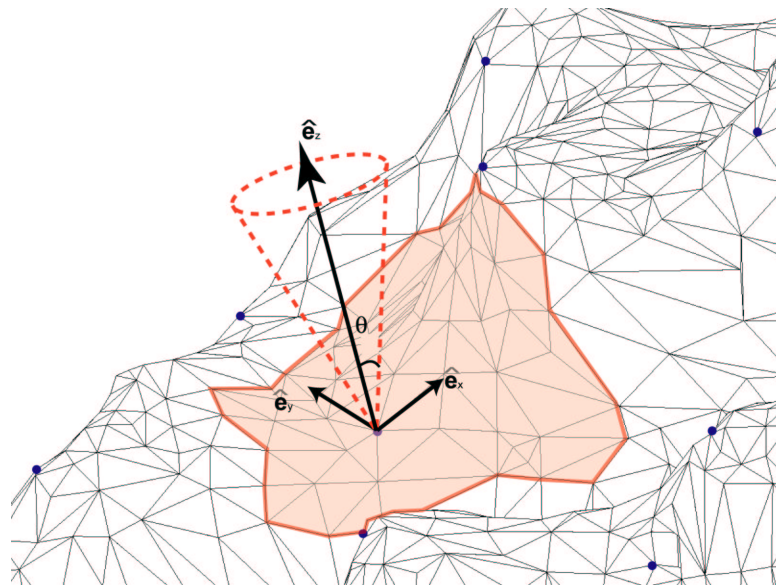


Figure 3-2: A local cortical patch defined by the thick red lines with average orientation in the red arrow. Blue spots denote the location of the selected dipole after 10-mm decimation. The loose orientation constraint (the 3D dashed cone) is defined by the average orientation and two tangential directions.

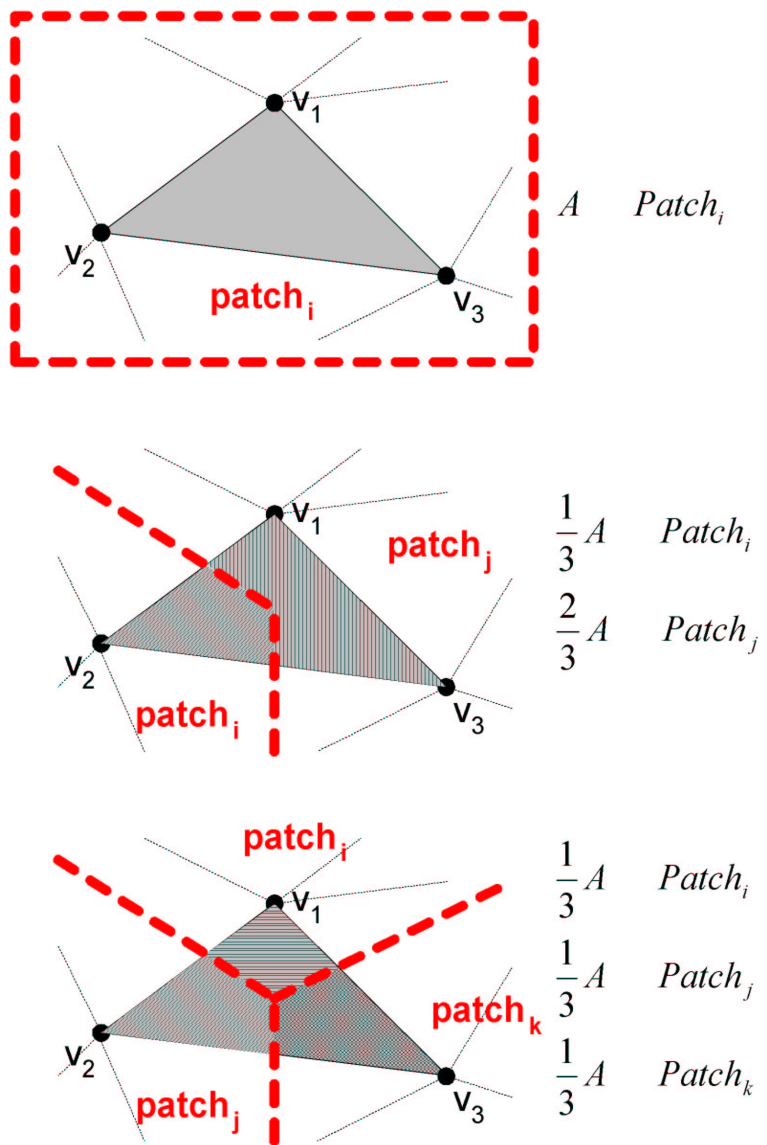


Figure 3-3: The division of a cortical surface triangulation with vertices V1, V2 and V3 to different cortical patches. The red dashed line indicates the boundary between cortical patches. A: the area of the single cortical triangulation.

1.33mm, matrix = 256 x 256, 128 partitions, Field of View = 21 cm x 21 cm) in a 1.5-T MRI scanner (SIEMENS Medical Solutions, Erlangen, Germany). The geometry of the gray-white matter surface in the cortex was subsequently derived from an automatic segmentation algorithm to yield a triangulated model with approximate 340,000 vertices [31, 12, 13]. The original triangulation was decimated to a source space of approximately 7,500 dipoles with 7-mm distance between the nearest two dipoles (Dale and Sereno, 1993). Subsequently, CPS were calculated using the methods described above, resulting in the average normal directions, their standard deviations, and approximate patch areas. In the MCE calculation, the value of  $r$  in Eq. (3.15) was selected to maintain 99% of the power of the singular values. The weights for currents, in Eq. (3.13), were the Euclidean norms of the columns of . The orientation matrix was obtained either from an initial MNE using the LOC or from the average patch normals. In line with [37] we employed Linear Programming [15] to estimate the magnitudes of dipole sources.

### 3.3.2 Simulations

In our simulations, we focused our interest to two brain regions, the primary somatosensory area and the temporal lobe near the primary auditory cortex. To this end, we placed sources around the central sulcus on the left hemisphere and around the Sylvian fissure on the right hemisphere, respectively. Figure 3.4 shows the locations of 73 simulated sources at somatosensory cortex and 90 simulated sources at auditory cortex. We employed three source configurations: current dipoles, 10-mm diameter patches, and 20-mm diameter patches. The orientations of these simulated sources were adjusted to be perpendicular to the local cortical surface as informed by anatomical MRI. The ideal sensor measurements on MEG sensors were thus calculated using the forward matrix ( $A$ ) and the dipole source amplitudes ( $X$ ). For the patches, we calculated the forward solution in the complete dense cortical grid and placed a dipole source of equal amplitude at every vertex within the patch. To approximate realistic situations where contaminating noise is present, we superimposed Gaussian noise of zero mean and unit variance on the ideal sensor measurements.

The amplitudes of the simulated brain signals were scaled such that the power signal-to-noise ratio (SNR) was 100. The SNR here was defined as the ratio between the instantaneous power of the ideal MEG sensor measurements over that of the MEG sensor noises.

Distributed source estimates were calculated using MNE, noise-normalized MNE [20, 25], and MCE. The orientations of source models were unconstrained, strictly constrained to the average normal within the cortical patch, or loosely constrained. Specifically, for LOC, Eq. (3.12)  $\theta_d$  was varied from 0.5 to 5.0 times standard deviations of the distribution of local cortical normal directions ( $\sigma_\theta$ ) within each cortical patch. The precision of localization was evaluated by the distance between the center of mass of the distributed source estimates and the center of mass of the simulated sources. We define this metric as *shift of center of mass*,  $S_{cm}$ . To avoid influence from the background insignificant dipole estimates, we used only the dipoles whose amplitudes exceeded 50% of the maximum amplitude. To demonstrate the behavior of the solutions when multiple sources are simultaneously active, we simulated two simultaneously active dipole sources at somatosensory cortex with separation of 21 mm (shown in Figure 3.4C) and subsequently localizing the synthetic MEG sensor data with free, strict cortical or loose cortical orientation constraints using MNE, noise normalized MNE and MCE.

### 3.3.3 Auditory and somatosensory MEG experiments

We also employed data from an auditory and a somatosensory MEG experiments to test our methods in realistic situations. The experiments were conducted with a healthy subject with the approval of the Institutional Review Board. Prior to the experiments an informed consent was obtained from the subjects. In the auditory experiment the stimuli were 60-ms wide-band noise bursts (2 kHz central frequency with 4 kHz bandwidth, 70 ms duration) presented binaurally. A 306-channel MEG system (Neuromag, Helsinki, Finland) was used to record the neuromagnetic responses. The measurement bandwidth was 0.1 to 172 Hz and the data were digitized at 600 Hz. About 200 responses were averaged. In the somatosensory study, the right median

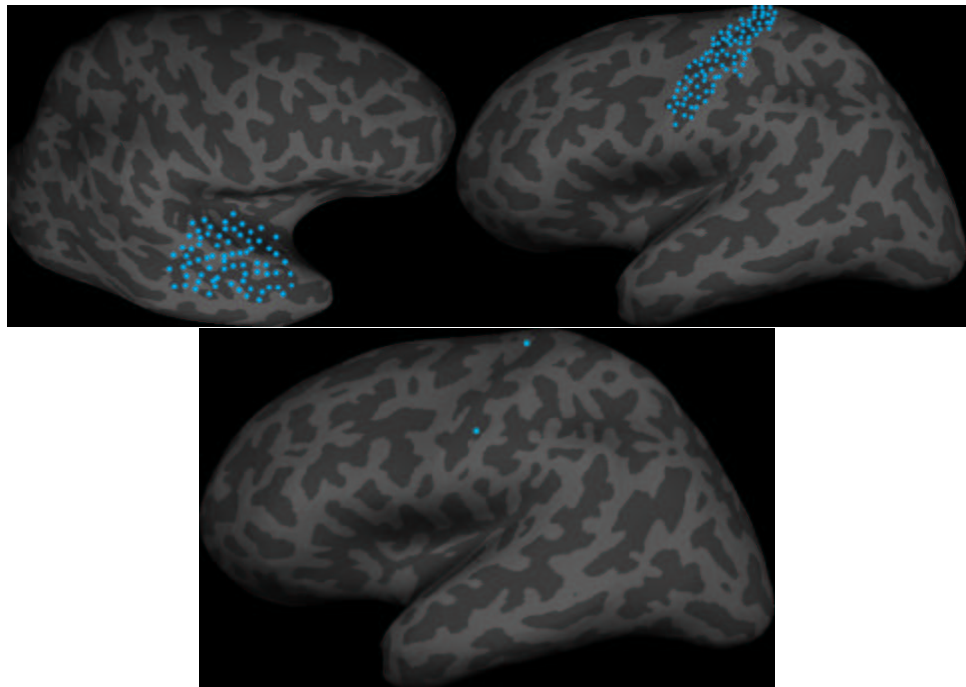


Figure 3-4: The locations of the simulated current sources at the auditory cortex at right hemisphere (A) and the somatosensory area at left hemisphere (B). Each blue dot represents an individually active current source of either single equivalent current dipole, or a 10-mm diameter cortical patch. (C) The locations of two equivalent current dipole sources at somatosensory area used to generate simulation to distinguish two simultaneously active sources. For visualization, cortical surface was inflated and with dark gray indicating sulci and light gray indicating gyri.

nerve was stimulated at the wrist with 0.5-ms constant current pulses whose amplitude was clearly above the motor threshold. The inter-stimulus-interval between the pulses was 4 s. The measurement bandwidth was 0.03 to 250 Hz and the data were digitized at 1004 Hz. About 100 responses were averaged.

The results were compared with equivalent current dipole (ECD) modeling. We used the Xfit program (Neuromag, Helsinki, Finland) to localize one ECD for both the auditory and somatosensory evoked field experiments. The location of the estimated single equivalent dipole was then exported to the high-resolution MRI data and projected to the nearest point on the inflated cortical surface.

## 3.4 RESULTS

### 3.4.1 Patch statistics

Figure 3.5a shows the distribution of the standard deviations ( $\sigma_d$ ) of the angles between all dipoles within a cortical patch and their averaged normal vector. In 99% of the patches this standard deviation was less than 25 degrees. The median of this distribution was 10 degrees. Figure 3.5b shows the distribution of the deviate between the averaged normal vectors within a cortical patch and the normal vector of the decimated source location associated with the cortical patch. Mostly such a deviate was between 5 to 10 degrees with the median of 8 degree. In about 3% of the decimated sources the average normal deviated from the source location normal as much as 30 degrees. Figure 3.5c shows the distribution of the number of sources in a cortical patch. On the average, a cortical patch contains 40 dipole sources with the 7-mm decimation. Cortical patches with dipole sources less than 20 and more than 60 constituted only approximately 5% of the total number of patches. The distribution of the patch areas is shown in Figure 3.5d. With 7 mm decimation, the patches had an averaged area of 22.76 mm<sup>2</sup>. The standard deviation of the distribution was 7.4 mm<sup>2</sup>.

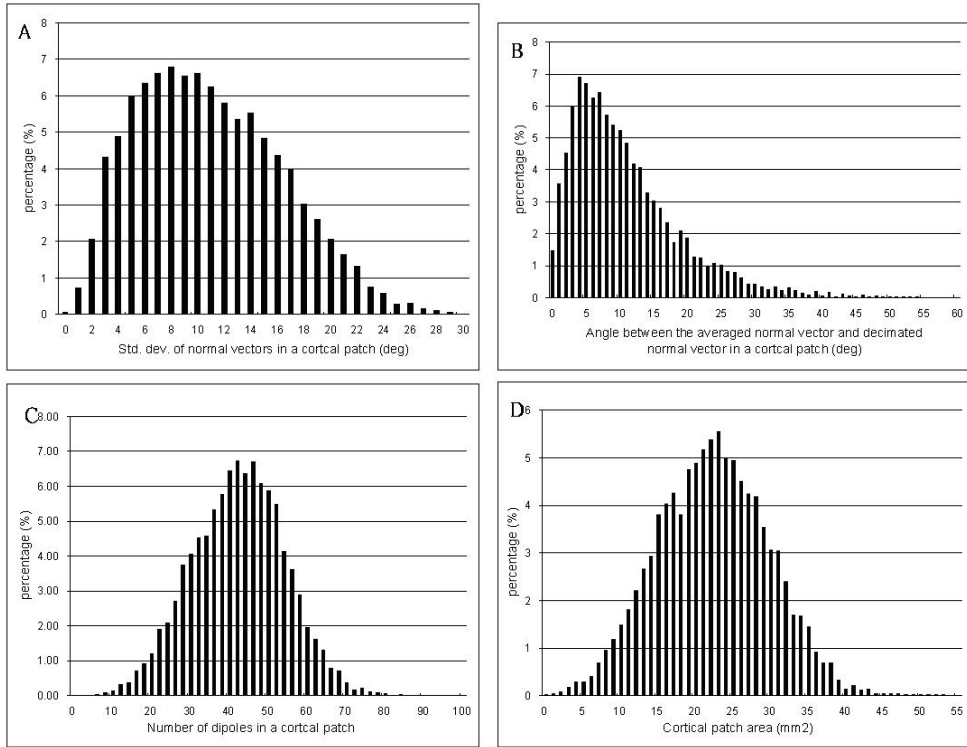


Figure 3-5: (a): The distribution of the standard deviation of the angle between dipole normals and the averaged dipole normal in each cortical patch. (b): The distribution of the angle between averaged dipole normal and the decimated dipole's normal. (c): The distribution of the number of dipoles in a cortical patch. (d): The distribution of the area of the cortical patch

### 3.4.2 Simulations

Figures 3.6 and 3.7 show simulation results of MNE, noise normalized MNE, and MCE using FO, SOC, and LOC with an ECD source at auditory cortex or somatosensory cortex. In simulations with a simulated ECD source in Sylvian fissure, MNE with free orientation constraint produced a distance between the ECD and the center of mass of the estimate of 10.8 mm. Using SOC and LOC with  $\theta_d = 3.5\sigma_\theta$ ,  $S_{cm}$  was 14.4 mm and 13.8 mm, respectively. Noise normalized MNEs with FO, SOC, and LOC with  $\theta_d = 3.5\sigma_\theta$  correspond to  $S_{cm} = 12.6$  mm, 12.3 mm, and 12.5 mm, respectively. In MCE, using dipole orientations estimated by MNE with FO led to  $S_{cm} = 12.0$  mm. Using MCE with SOC and LOC with  $\theta_d = 2.5\sigma_\theta$  reduced  $S_{cm}$  to 6.9 mm and 5.9 mm, respectively.

Figure 3.7 shows simulations of MNE, noise normalized MNE, and MCE with FO, SOC, and LOC for a dipole source at left hemisphere somatosensory area. MNEs using FO, SOC, and LOC with  $\theta_d = 4.5\sigma_\theta$  correspond to  $S_{cm} = 10.3$  mm, 9.6 mm, and 9.5 mm respectively. Note that the MNE with FO and that with SOC were distributed more around post central gyrus whereas MNE with LOC shifted the source estimates more anterior and thus corrected this error partially. In the noise-normalized MNE, these shifts are 7.0 mm, 4.4 mm and 5.3 mm (for FO, SOC, and LOC with  $\theta_d = 0.5\sigma_d$ ). MCE using free orientation constraint has  $S_{cm} = 6.5$  mm. Applying the SOC and the  $\theta_d = 2.0\sigma_\theta$  LOC reduced  $S_{cm}$  to 3.0 mm and 1.8 mm, respectively.

The simulation results on shift in the center of mass on the auditory area and somatosensory areas are shown in Figure 3.8. MNE utilizing LOC on single-dipole synthetic data yields the smallest average  $S_{cm}$  (11.3 mm in auditory area and 5.8 mm in somatosensory area), compared to MNE using either FO or SOC in both auditory (FO: 11.6 mm, SOC: 12.8 mm) and somatosensory area (FO: 8.5 mm, SOC: 15.2 mm). The medians of these LOC MNEs were  $\theta_d = 2.0\sigma_\theta$ . The effect of decreasing the shift of the center of mass by appropriate LOC was observed systematically with the more extended synthetic sources as well.

Using noise normalized MNE,  $S_{cm}$ 's using FO and SOC were on the average ap-

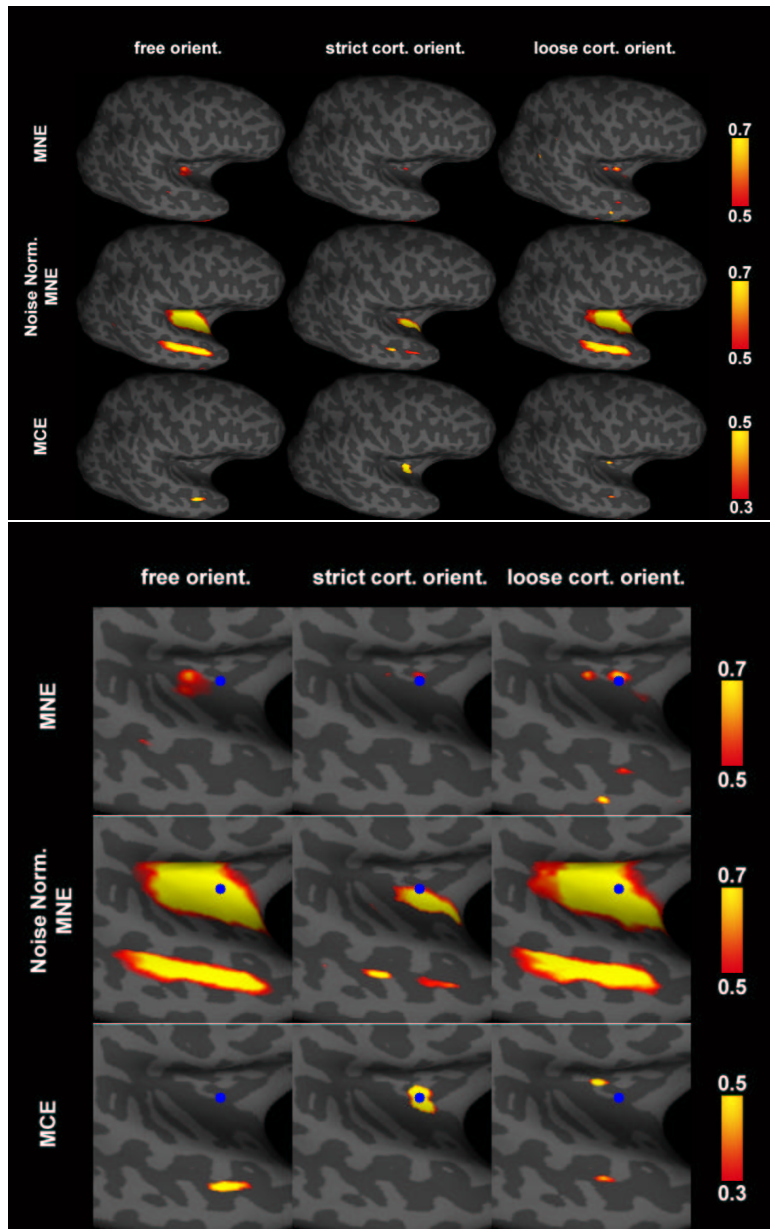


Figure 3-6: MNE, noise normalized MNE and MCE from a single ECD placed in Sylvian fissure, as indicated by blue dot.

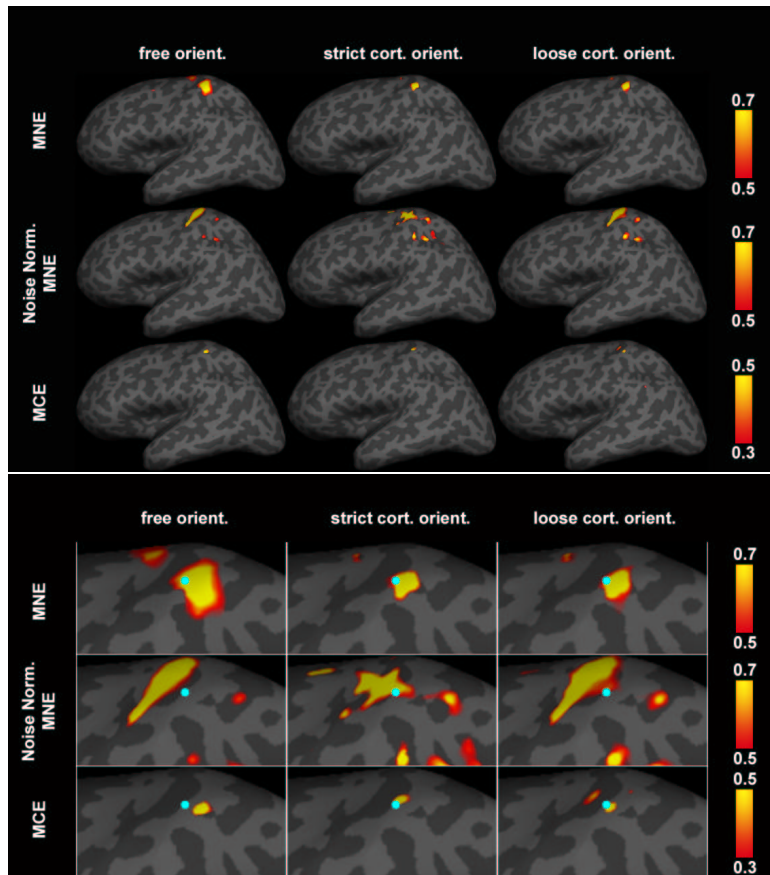


Figure 3-7: MNE, noise normalized MNE and MCE source localization simulations from a single ECD placed on somatosensory cortex, as indicated by blue dot.

proximately 9 mm, independent of both the location of the sources and their spatial extent. In auditory cortex, using LOC resulted in  $S_{cm} = 8.1$  mm, 8.1 mm, and 8.4 mm for dipoles, 10-mm, and 20-mm diameter cortical patches, respectively. In somatosensory cortex, with LOC,  $S_{cm} = 8.7$  mm, 8.5 mm, and 8.8 mm for dipoles , 10-mm, and 20-mm diameter extended sources, contrasted to  $S_{cm} = 9.5$  mm, 9.4 mm, and 10.0 mm with FO, and 8.5 mm, 8.0 mm, and 8.0 mm using SOC. Our simulations at somatosensory area indicated that using SOC could achieve the minimal  $S_{cm}$  compared to using FO or LOC. Nevertheless, this benefit is less 1 mm in average compared to loose cortical orientation constraint inverse. Finally, MCE with LOC in auditory cortex shows the least averaged  $S_{cm}$  (7.8 mm for dipoles, 7.8 mm for 10-mm diameter sources, 9.2 for 20-mm diameter sources). Using FO and SOC in MCE makes shifts in average approximately 12 mm and 14 mm in auditory area. In the somatosensory area, MCE with dipole orientations taken from the free-orientation MNE resulted in average  $S_{cm}$ 's of 2.9 mm, 4.0 mm and 5.0 mm with dipoles, 10-mm diameter, and 20-mm diameter extended sources. If the dipole orientations are taken from MNE with LOC, the  $S_{cm}$  was reduced to 2.6 mm, 3.2 mm and 3.6 mm with dipoles, 10-mm diameter and 20-mm diameter simulated sources. MCE using a preliminary MNE with SOC gave averaged  $S_{cm}$ 's 3.4 mm, 3.7 mm, and 8.6 mm with single ECD, 10-mm diameter and 20-mm diameter simulated sources, respectively.

Figure 3.9 shows the simulation results of MNE, noise normalized MNE, and MCE when two sources are simultaneously with 21 mm separation. In MNE, we found that using LOC with  $\theta_d = 2.0\sigma_\theta$  can reduce the spatial distribution of the source estimates at the same threshold, as compared to the free-orientation case. And two loci of simulated sources were indicated by separate dorsal and ventral MNEs. In the noise-normalized MNE, LOC and FO can both provide estimates around two active loci. However, the noise-normalized MNE with SOC failed to produce two separate source estimates at the threshold to show the most significant 50% estimates. MCE using free or strict orientation constraint generate estimates with false source locations, which are located either between two synthetic sources, or in incorrect locations in the post-central sulcus. Using LOC with  $\theta_d = 2.0\sigma_\theta$ , MCE can resolve two simultaneously

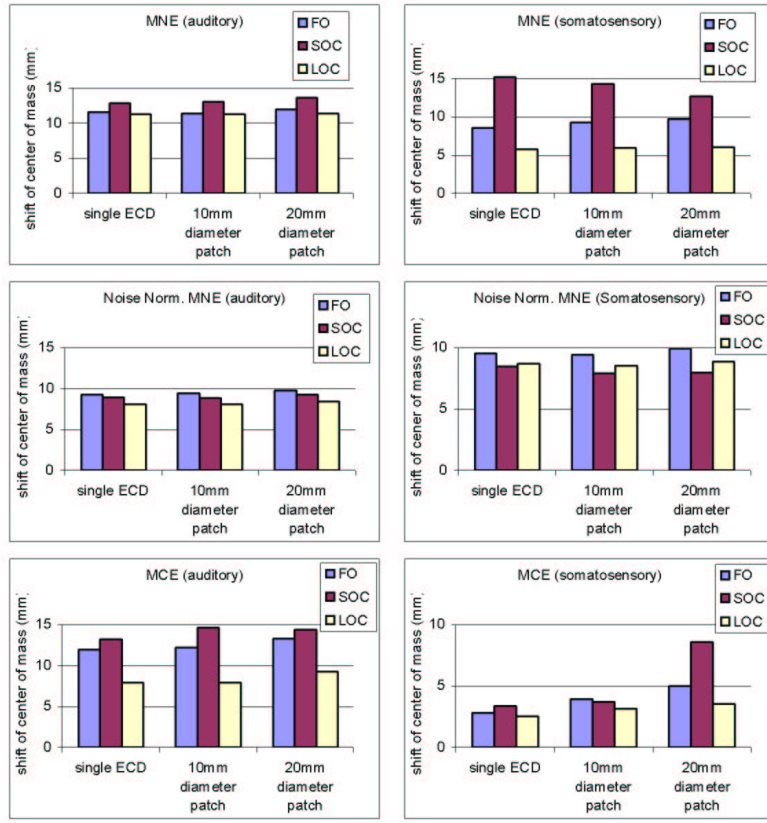


Figure 3-8: The average shift of center of mass from the simulated sources using MNE, noise normalized MNE and MCE in both auditory area and somatosensory (SI) areas. The spatial distributions of the sources were varied from single ECD to 10 mm diameter and 20 mm diameter cortical patches as shown in Figure 3.4.

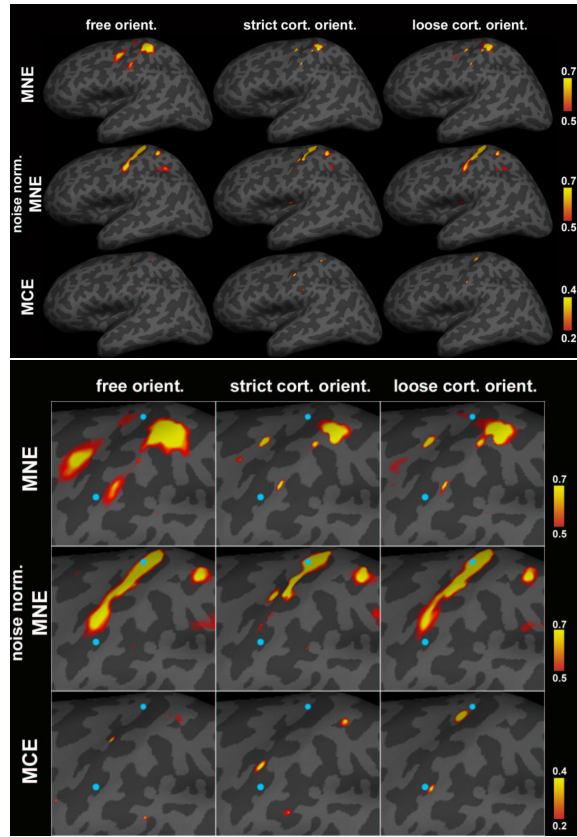


Figure 3-9: Simulated two ECD simultaneous sources and the associated MNE, noise normalized MNE and MCE inverse. Cortical current estimates were normalized between 0 and 1 to illustrate the spatial distributions.

active sources and localize them within 3 mm accuracy in the central sulcus.

### 3.4.3 Auditory and somatosensory MEG experiments

For the auditory experiment, Figure 3.10 shows the MNE, noise-normalized MNE, and MCE of MEG recordings at 100 ms after the onset of the stimulus. The blue spot indicates the location of single equivalent dipole fitting, which is localized to superior temporal gyrus. Compared to MCE, MNE and noise normalized MNE are more diffused. Note that in both MNE and noise-normalized MNE also showed estimated sources around medial temporal gyrus. The distance between the ECD and the center of mass of MNE with FO is 5.0 mm. Applying the SOC in MNE yields a distance of 11.4 mm. LOC with in MNE reduces the distance to 11.7 mm. However, examining

	FO		SOC		LOC	
	$S_{cm}$	$S_{max}$	$S_{cm}$	$S_{max}$	$S_{cm}$	$S_{max}$
MNE	3.1	6.2	4.0	7.0	3.2	7.0
Noise norm. MNE	11.0	15.0	10.9	12.5	11.6	15.0
MCE	7.8	7.8	2.2	7.5	6.5	7.0

Table 3.1: Shifts of the center of mass ( $S_{cm}$ ) and the maximum of the estimate ( $S_{max}$ ) from the ECD in MNE, noise normalized MNE and MCE using free orientation (FO), strict orientation constraint (SOC) and loose orientation constraint (LOC) in the somatosensory experiment at 100 msec after the onset of the median nerve stimulation.

the maximum of the MNE estimates revealed that the distances to the ECD locus were 11.5 mm, 6.8 mm and 6.8 mm using FO, SOC, and LOC, respectively. In MCE, using dipole orientations estimated from MNE with FO leads to the distance between ECD and the center of mass of the estimate 6.8 mm. MCE using dipole orientations estimated by MNE SOC and LOC with  $\theta_d = 2.0\sigma_\theta$  result in  $S_{cm} = 5.7$  mm. These are also values of the distance between ECD and the maximum of MCEs. Noise normalized MNEs with FO, SOC, and LC with  $\theta_d = 2.0\sigma_\theta$  lead to the distance between the ECD and estimates of 9.5 mm, 8.7 mm, and 8.7 mm, respectively. Table 3.1 summarizes these distance measurements.

Figure 3.11 shows MNE and MCE of the somatosensory MEG experiment at 50 msec after the onset of stimulation. The ECD was correctly located at the post-central gyrus. In MNE, it was found that the estimated activities were mostly from post-central gyrus with minor activation in pre-central gyrus. The distance between the center of mass of MNE and ECD with FO, SOC, and LOC with  $\theta_d = 2.0\sigma_\theta$  were 3.0 mm, 3.9 mm, and 3.2 mm, respectively. The maximums of MNE using SOC, FO, and LOC were 6.2 mm, 7.0 mm and 7.0 mm away from the ECD location. The distances between the center of mass of MCE with FO and SOC are 7.8 mm and 2.2 mm. Using LOC with this distance decreases to 6.5 mm. The maxima of MCE using FO, SOC, and LOC are located 7.7 mm, 7.5 mm and 7.0 mm off the ECD location. In the noise-normalized MNE, the distance between the estimate and ECD using FO and SOC are 11.0 mm and 10.9 mm. In noise-normalized MNE with LOC

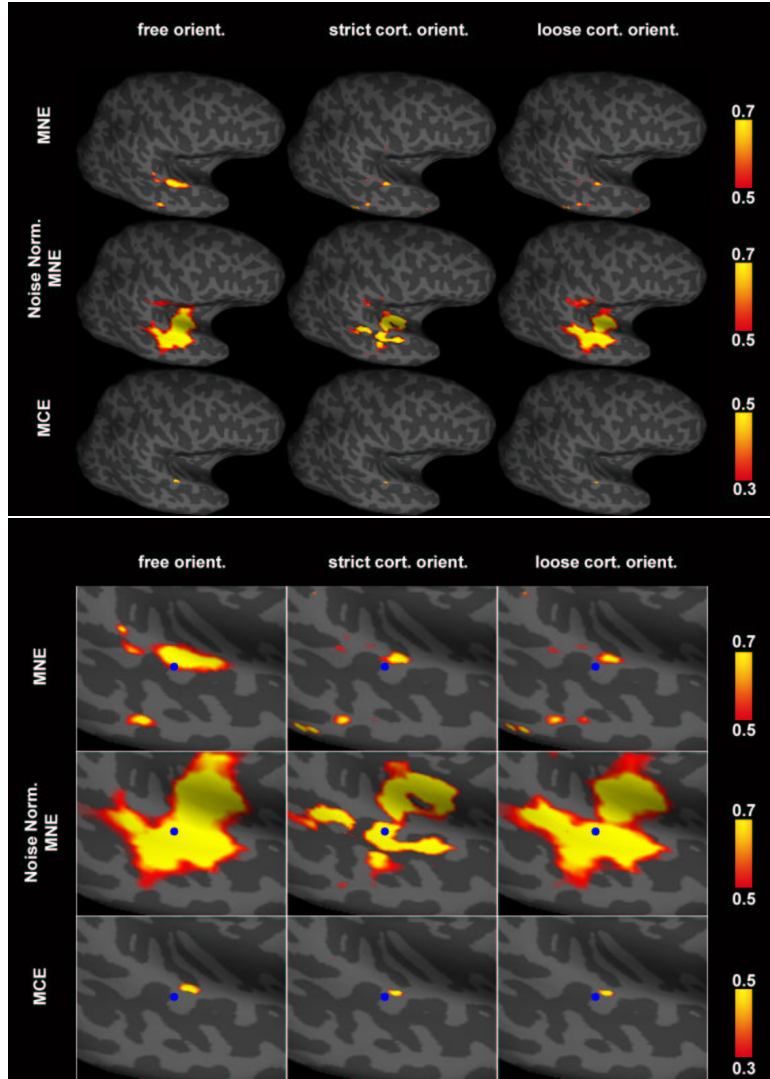


Figure 3-10: MNE, noise normalized MNE, and MCE source localizations at 100 msec after the onset of the auditory stimuli. The blue spot indicates the location of equivalent current dipole (ECD) by single dipole fitting.

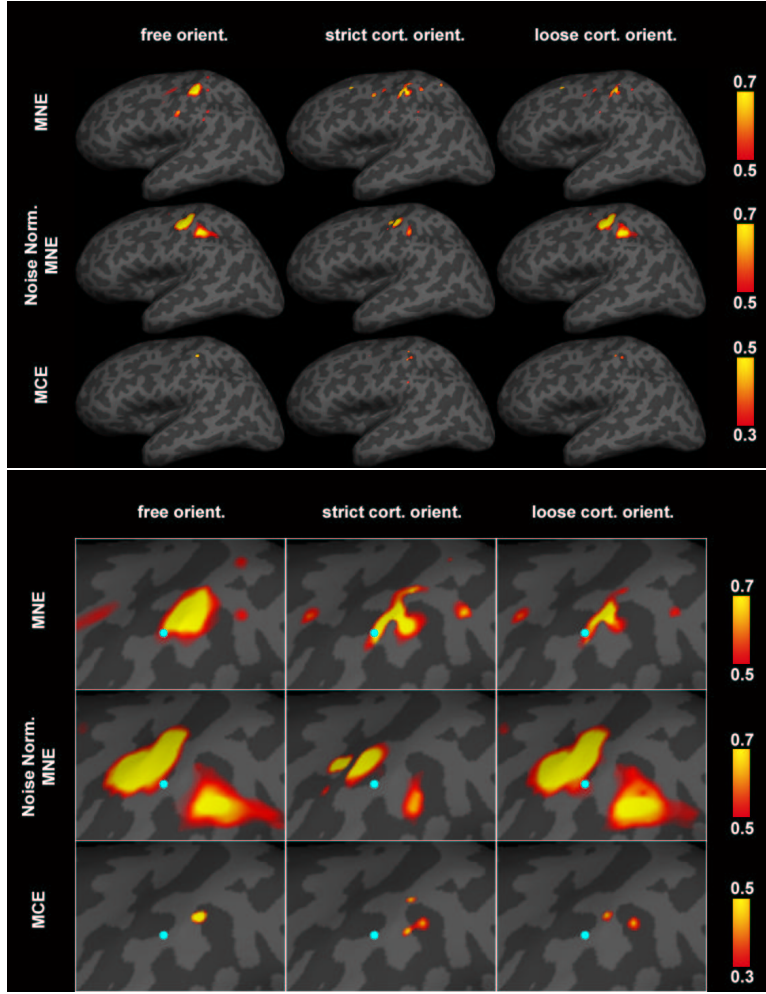


Figure 3-11: MNE, noise normalized MNE and MCE source localizations at 50 msec after the onset of the median nerve stimulation. The blue spot indicates the location of optimal fitting of a single equivalent current dipole.

$(\theta_d = 2.0\sigma_\theta)$  the maximum is 11.6 mm away from the ECD locus. Finally, the distance between ECD and the maximum of current estimates using FO, SOC, and LOC are 15.0 mm, 12.5 mm, and 15.0 mm respectively. Table 3.2 summarizes these distance measurements.

## 3.5 DISCUSSION

Structural MRI can provide precise anatomical features of the cortical geometry. This information can be utilized to derive CPS once the decimation is determined. The

	FO		SOC		LOC	
	$S_{cm}$	$S_{max}$	$S_{cm}$	$S_{max}$	$S_{cm}$	$S_{max}$
MNE	5.0	13.5	11.4	6.9	11.7	6.9
Noise norm. MNE	9.5	11.2	8.7	7.5	8.7	13.5
MCE	6.9	6.9	5.7	5.7	5.7	5.7

Table 3.2: Shifts of the center of mass ( $S_{cm}$ ) and the maximum of the estimate ( $S_{max}$ ) from the ECD in MNE, noise normalized MNE and MCE using free orientation (FO), strict orientation constraint (SOC) and loose orientation constraint (LOC) in the auditory experiment at 50 msec after the onset of the auditory stimulation.

reason to use CPS in MEG/EEG inverse is that CPS can provide more accurate description of the brain anatomy once the spatial resolution of forward model is determined. We demonstrated that using CPS in summary can improve the localization accuracy by posing a loose orientation constraint, as compared to free orientation or strict orientation constraint inverse. In this study, we found that source modeling with lead fields proportional to the size of the cortical patch provides qualitatively reasonable results. This qualitatively validates that (1) the cortical source space was constructed to achieve reasonable equal spatial sampling, and (2) the number of sources within each cortical patch, which equals to the product of the density of the current dipoles and the area of the cortical patch, is approximately uniform across the whole brain.

The incorporation of the loose orientation constraint with  $\theta_d = 2\sigma_\theta \dots 3\sigma_\theta$  increases the accuracy of the localization compared with localization with free orientation or strict orientation constraint, as shown in our simulation results in both auditory and somatosensory areas with dipolar or cortical patch synthetic sources. We used the standard deviations ( $\theta_d$ ), not angles in degrees, in loose orientation constraint, because the curvatures of cortical patches may vary significantly, depending on their anatomical locations. For example the cortical patch at the ridge of a gyrus has fairly flat cortex and small  $\theta_d$ , and the cortical patch at the junction between a gyrus and a sulcus is rather convoluted and thus large  $\theta_d$ . In this sense, the loose cortical constraint using standard deviations ( $\theta_d$ ) may less depend on the actual anatomical position as compared to using specific values of angles.

In our simulations, we found that there is no unique optimal number across the whole brain for the best utilization of loose cortical orientation constraint in MNE and MCE. Presumably this is due to the variations of cortical source space sampling and local anatomical curvature variations. However, in MNE, noise normalized MNE and MCE, we found that the utilization of LOC is especially critical to achieve both higher accuracy in localization and better resolution for simultaneously active sources. The LOC is different from the traditional implementation of MCE using MNE with free orientation to provide dipole orientation estimates [37] and the MNE with strict cortical constraint [26]. Here, the motivation of using loose cortical constraint is to provide more accurate cortical structure after the source space decimation. If the complete dense forward matrix could be employed in source estimation algorithms, such a loose cortical constraint may become unnecessary. In such a case, the price is the higher computational load in both L2 norm, and especially L1 norm prior source modeling. Nevertheless, the ill-posed nature of the MEG/EEG inverse with diffused point spread and cross talks does not encourage the utilization of full forward matrix down to millimeter resolution [25]. The proposed loose cortical constraint is thus a compromise for both computational resolution and sufficient anatomical features in MEG/EEG inverse.

The other benefit of loose cortical constraint in MNE is that it generates a less diffuse source estimate compared with localization using strict orientation constraint. This is because LOC allows a small source component tangential to the cortical surface to account for the MEG/EEG measurement. Even though not as focal as MCE, MNE with LOC can potentially help the interpretation of localization results by reducing the false source estimates in adjacent gyri or sulci, which were typical findings in our experience when applying strict orientation constraints.

The proposed method to include anatomical information in distributed source modeling for MEG/EEG was based on the physiological evidences that the orientations of pyramidal cells, which are responsible for dominant MEG signal genesis, are perpendicular to the cortical surface [24, 9]. This was especially documented in hippocampus in guinea pig model [9]. Further validations across the whole brain on

human can solidify the utilization of cortical orientation constraints, which would be of following-up research topic in the future. In this study, we only apply the proposed cortical constraints on MEG data. Due to the similarity of the formulation of the source localization and physiological nature for signal genesis, such cortical constraints are expected to provide similar benefits in EEG localization in distributed source modeling.



# References

- [1] D. Cohen. Magnetoencephalography: evidence of magnetic fields produced by alpha-rhythm currents. *Science*, 161(843):784–6, 1968. 68350989 0036-8075 Journal Article.
- [2] MS Hamalainen, R Hari, RJ Ilmoniemi, J Knuutila, and OV Lounasmaa. Magnetoencephalography-theory, instrumentation, and application to noninvasive studies of the working human brain. *Review of Modern Physics*, 65:413–497, 1993.
- [3] K. Uutela, M. Hamalainen, and R. Salmelin. Global optimization in the localization of neuromagnetic sources. *IEEE Trans Biomed Eng*, 45(6):716–23., 1998.
- [4] AM Dale and MI Sereno. Improved localization of cortical activity by combining eeg and meg with mri cortical surface reconstruction: A linear approach. *J. Cog. Neurosci*, 5:162–176, 1993.
- [5] A. M. Dale, A. K. Liu, B. R. Fischl, R. L. Buckner, J. W. Belliveau, J. D. Lewine, and E. Halgren. Dynamic statistical parametric mapping: combining fmri and meg for high-resolution imaging of cortical activity. *Neuron*, 26(1):55–67, 2000. 20256250 0896-6273 Journal Article.
- [6] MS Hamalainen and RJ Ilmoniemi. Interpreting measured magnetic fields of the brain: estimates of current distributions. Technical report, Helsinki University of Technology, 1984.

- [7] K. Matsuura and Y. Okabe. Selective minimum-norm solution of the biomagnetic inverse problem. *IEEE Trans Biomed Eng*, 42(6):608–15, 1995. 95309952 0018-9294 Journal Article.
- [8] K. Uutela, M. Hamalainen, and E. Somersalo. Visualization of magnetoencephalographic data using minimum current estimates. *Neuroimage*, 10(2):173–80., 1999.
- [9] Y. C. Okada, J. Wu, and S. Kyuhou. Genesis of meg signals in a mammalian cns structure. *Electroencephalogr Clin Neurophysiol*, 103(4):474–85, 1997. 98034867 0013-4694 Journal Article.
- [10] M. Fuchs, M. Wagner, T. Kohler, and H. A. Wischmann. Linear and non-linear current density reconstructions. *J Clin Neurophysiol*, 16(3):267–295, 1999. 99353451 0736-0258 Journal Article Review Review, Tutorial.
- [11] A. M. Dale, B. Fischl, and M. I. Sereno. Cortical surface-based analysis. i. segmentation and surface reconstruction. *Neuroimage*, 9(2):179–94., 1999.
- [12] B. Fischl, M. I. Sereno, and A. M. Dale. Cortical surface-based analysis. ii: Inflation, flattening, and a surface-based coordinate system. *Neuroimage*, 9(2):195–207., 1999.
- [13] B. Fischl, A. Liu, and A. M. Dale. Automated manifold surgery: constructing geometrically accurate and topologically correct models of the human cerebral cortex. *IEEE Trans Med Imaging*, 20(1):70–80, 2001. 0278-0062 Journal Article.
- [14] Dimitri P. Bertsekas. *Dynamic programming and optimal control*. Athena Scientific optimization and computation series. Athena Scientific, Belmont, Mass., 2nd edition, 2000. Dimitri P. Bertsekas.
- [15] Todd K. Moon and Wynn C. Stirling. Mathematical methods and algorithms for signal processing, 2000. Todd K. Moon, Wynn C. Stirling. 1 computer laser optical disc (4 3/4 in.).

- [16] A. K. Liu, A. M. Dale, and J. W. Belliveau. Monte carlo simulation studies of eeg and meg localization accuracy. *Hum Brain Mapp*, 16(1):47–62, 2002. 21859140  
1065-9471 Journal Article.
- [17] A. K. Liu, J. W. Belliveau, and A. M. Dale. Spatiotemporal imaging of human brain activity using functional mri constrained magnetoencephalography data: Monte carlo simulations. *Proc Natl Acad Sci U S A*, 95(15):8945–50., 1998.



# Chapter 4

## Wavelet-based Spectral Spatiotemporal Mapping in the Human Brain

This chapter presents a computationally efficient source estimation algorithm, which localizes cortical oscillations and their phase relationships. The present method employs wavelet-transformed MEG data and uses anatomical MRI to constrain the current locations to the cortical mantle. In addition, the locations of the sources can be further confined with help of functional MRI (fMRI) data. As a result, we obtain spatiotemporal maps of spectral power and phase relationships. As an example we show how the phase locking value (PLV), i.e., the trial-by-trial phase relationship between the stimulus and response, can be imaged on the cortex. We tested the method of combining MEG, structural MRI, and fMRI using simulated cortical oscillations along Heschl's gyrus. We also analyzed sustained auditory gamma-band neuromagnetic fields from MEG and fMRI measurements. The auditory source areas in the posterior superior temporal gyrus were chosen because they are difficult to access with any functional imaging modality. Our results showed that combining the MEG recoding with fMRI improves source localization for the non-noise normalized wavelet power. In contrast, it turned out that noise-normalized spectral power or PLV localization do not benefit from the fMRI constraint. We show that if the thresholds are

not properly chosen, noise-normalized spectral power or PLV estimates may contain false (phantom) sources, independent of the inclusion of the fMRI prior information. The proposed algorithm can be used for evoked MEG/EEG and block-designed or event-related fMRI paradigms, or for spontaneous MEG/EEG data sets.

## 4.1 INTRODUCTION

Oscillations and synchronization of oscillations (phase-locking) have become fundamental principles in physics and engineering since the first study by Huygens in 1673. In both MEG and EEG, the first signal measured was the alpha rhythm which is thought to be a cortical oscillation originating in the visual cortex and the parietal occipital junction. Due to advances in both source estimation and signal processing techniques, such as wavelet transforms, quantitative analysis of the synchronization of oscillations has recently attracted a lot of interest in order to understand how information is encoded and transmitted in the brain. A growing number of studies in both humans and animals suggest that cortical oscillations, or rhythmic activity at a variety of frequencies, might be involved in encoding information, and that synchronization (phase-locking) of cortical oscillations might bind and transmit disparate information across brain regions (see recent reviews [1, 2, 3]. Recent biologically realistic models, as well as *in vitro* and *in vivo* evidence, suggest that gamma-band oscillations ( $\approx 40\text{Hz}$ ) are vital in local information processing, while beta oscillations ( $\approx 20\text{Hz}$ ) are used to maintain synchrony over longer distances [4]. In the auditory system, cortical oscillations are well documented [5, 6] and are known to be abnormal in diseased states such as schizophrenia [7]. The phase relations in the gamma band have been shown to be important in understanding object perception [8, 9, 10, 11, 12, 2, 13] abnormal in schizophrenia [14].

Many methods of using spectral analysis on EEG and MEG data have been reported over the past several decades. Some propose wavelet-based techniques to measure neural synchrony between electrodes or between MEG sensors and an external signal, such as an electromyogram (EMG). However, sensors contain informa-

tion from a variety of brain sources, some of which might overlap. Further, a deep source oriented in the horizontal plane could produce a false apparent synchrony over anterior and posterior sensors. Because source estimates overcome many of these limitations, several methods of source localization of cortical oscillations have been proposed [15, 16, 17, 18]. Here, we propose a new method which provides the following new features: (1) It creates a map of the cortical oscillations on the cortical surface; (2) It is able to detect rapidly changing power and phase relations; 3) It can combine prior information from other functional imaging techniques such as fMRI.

The technique presented in this chapter is based on a combination of a cortically-constrained minimum norm estimate (MNE) [19, 20, 21] and wavelet-based spectral analysis employing a complex morlet a complex Morlet wavelet [10, 2, 3]. Wavelets preserve a high temporal resolution in the gamma band ( $\approx 40$  Hz) necessary to image rapidly time-varying oscillations [10, 2, 3]. We evaluated the new technique using both simulated and real MEG data. We validated the technique using a well-characterized simple paradigm: the 40-Hz steady-state evoked magnetic field. This paradigm was chosen because it produces a well-known periodically varying source in and around Heschl's gyrus, along the posterior superior temporal gyrus (STG). We can then quantify the accuracy of the localizations of this oscillation using our proposed methods. Further, since it is possible to control the magnitude and phase of the stimulus, we can produce a response with a driven phase relationship necessary to evaluate the method. We will also demonstrate that this technique reveals spontaneous oscillations, such as the alpha rhythm in the cortical space.

## 4.2 MATERIALS AND METHODS

### 4.2.1 Spectral dynamic statistical parametric mapping

Our method to analyze oscillatory activity is called Spectral Dynamic Statistical Parametric mapping (sdSPM). It involves the following computational steps: (1) wavelet transformation MEG sensor data, (2) calculation of the spectral-power minimum-

norm estimate (MNE) and the noise-normalized MNE (dSPM), and (3) calculation of the phase-locking values. In order to image the induced activity, these steps are repeated for each trial and the results are averaged across trials. If only the spectral power of the evoked response is desired, steps (1) and (2) can be calculated together using the signals averaged over epochs.

#### 4.2.2 The Wavelet transform

To reduce the computational burden, we performed a wavelet transformation of the MEG signals prior to performing the MNE. The MEG data were first filtered using a continuous wavelet transform (CWT). Temporal convolution of the MEG signal with the wavelet centering at center frequency and time produces a temporally localized frequency response:

$$w_i(t, f) = \int_{-\infty}^{\infty} y_i(\tau) \Psi_{f,t}^*(t - \tau) d\tau \quad (4.1)$$

where  $\Psi_{f,t}$  is the wavelet function and the superscript \* indicates a complex conjugate.  $y_i(\tau)$  represents the signal in one MEG sensor and  $w_i(t, f)$  are the wavelet coefficients of trial  $i$ . For multiple-channel MEG measurements, this convolution is performed for each individual channel of  $y_i(\tau)$  separately. In the transformation we employed the complex Morlet wavelet [22, 23]:

$$\Psi_{f,t}(\tau) = \frac{1}{\sqrt{2\pi f}} \exp\left(\frac{-(\tau - t)^2}{2\sigma^2}\right) \exp(i2\pi f\tau) \quad (4.2)$$

which is the product of a sinusoidal wave centered at  $f$  modulated by a Gaussian with  $\tau - t$  mean and  $\sigma^2$  variance. To select 40-Hz signals, we set  $f$  to be 40 Hz and  $\sigma^2$  to be  $7/2\pi f$ . Fig. 4.1 shows the wavelet function between -100 msec and 100 msec with central frequency of 40Hz and 5 cycles duration.

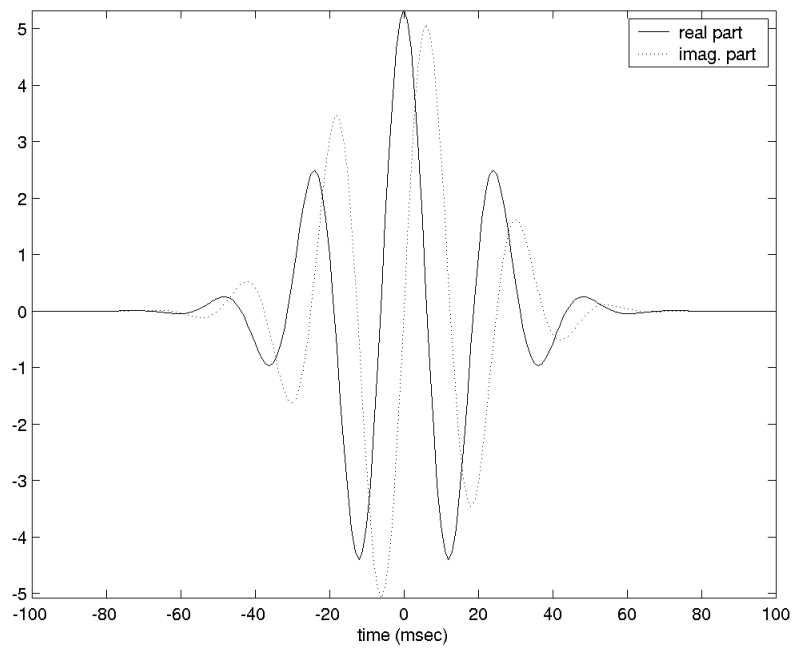


Figure 4-1: A wavelet filter centered at 40 Hz with 5 cycles. The solid line represents the real part and the dashed line represents the imaginary part of this linear filter in the temporal domain.

### 4.2.3 Source estimation

To localize the current sources underlying the MEG signals we employed the cortically-constrained minimum-norm estimate (MNE) [20, 24]. The minimum-norm estimate can be calculated by applying a linear inverse operator to the measured signals:

$$\hat{y}(t) = Wx(t) \quad (4.3)$$

where  $x(t)$  are the  $n$ -channel MEG data at time  $t$  and  $y(t)$  are the corresponding current values on the cortex. An expression for  $W$  is obtained in closed form, e.g., by minimizing

$$S = \|C^{-1/2}(x - Ay)\|_2 + \lambda^2 \|R^{-1/2}x\|_2 \quad (4.4)$$

where  $C$  and  $R$  denote covariance matrices of the noise and the sources, respectively,  $A$  is the gain matrix, i.e., the solution of the forward problem,  $\lambda$  is a regularization parameter [20, 25], and  $\|\bullet\|_2$  indicates the  $l_2$  norm. Minimization of Eq. (4.4) over  $y$  yields

$$W = RA^T(ARA^T + \lambda^2 C)^{-1} \quad (4.5)$$

The source covariance matrix incorporates *a priori* assumption on the spatial distribution of the source currents. It has been proposed that spatial information from fMRI can be incorporated into the MNE by employing a diagonal  $R$  with larger elements at the locations of significant fMRI activity [26]. The MNE is known to have a bias towards superficial currents, caused by the attenuation of the MEG lead fields with increasing source depth. It is possible to compensate for this tendency by scaling the columns of  $A$  with a function, denoted here by  $f_k$  for the  $k$ th dipole, increasing monotonically with the source depth. A commonly used choice is

$$f_k = 1/(a_{3k-2}^T a_{3k-2} + a_{3k-1}^T a_{3k-1} + a_{3k}^T a_{3k})^\gamma \quad (4.6)$$

Where  $a_p$  is the  $p$ th column of  $A$  and  $\gamma$  is a tunable parameter. Whereas [27]

suggest  $\gamma = 0.5$ , we have found in our simulations that this does not provide sufficient compensation. Our preferred value is slightly bigger ( $\gamma = 0.6$  ).

The noise covariance matrix,  $C$ , was calculated from the raw MEG data containing individual trials. We defined the interval of 100 msec before the onset of the trigger as the baseline period. The covariance matrix of the MEG sensors at each time point of the baseline were calculated separately:

$$C = E \left\langle \frac{\sum_{trial} (y_i(t) - \bar{y}_t)(y_i(t) - \bar{y}_t)^T}{M} \right\rangle \quad (4.7)$$

where  $M$  is the total number of trials, and temporal index  $t$  refers to the trigger of each trial.  $E < \bullet >$  is the mean of the measurements within trial  $i$ .  $E < \bullet >$  represents the mean operator over the temporal index  $t$ .

For spontaneous responses, the noise covariance was calculated from the 2-minute continuous MEG sensor measurements without the subject (the “empty room noise”) on the same day of the experiment. This is the reference baseline to exclude any activity other than the subject’s spontaneous responses. Mathematically, we can also utilize Eq. (4.7) to calculate the noise covariance matrix for spontaneous response estimation. However, in this case there is only 1 trial covering the whole duration of the empty room noise measurement.

#### 4.2.4 Spectral power and phase locking value calculation

After the wavelet transformation of the MEG sensor data, and subsequent linear transforming by the inverse operator  $W$  of each individual trial, we have

$$\vec{\Omega}(n) = W(\Psi_{f,t}(n) \otimes y_i(n)) \quad (4.8)$$

We use discrete time index  $n$  here to denote the implementation of the calculation in discrete time instants.  $\vec{\Omega}_i(n)$  denotes the frequency-specific source signal in the source space at time  $n$  of trial  $i$ .  $\otimes$  is the 1-dimensional convolution on the temporal domain. The convolution is calculated for each channel of  $y_i(n)$  separately. After

source localization, the time-varying power  $\vec{P}(t)$  and synchronization index  $\vec{\Theta}(t)$  were calculated

$$\begin{aligned}\vec{P}(n) &= \frac{1}{M} \sum_{i=1}^M \text{diag}(\vec{\Omega}_i(n) \vec{\Omega}_i^H(n)) \\ \vec{\Theta}(n) &= \frac{1}{M} \left| \sum_{i=1}^M \frac{\text{diag}(\vec{\Omega}_R(n) \vec{\Omega}_i^H(n))}{|\vec{\Omega}_R(n)| |\vec{\Omega}_i(n)|} \right|\end{aligned}\quad (4.9)$$

$\text{diag}(\bullet)$  indicates the operation to get diagonal entries from the operand to generate a column vector, and the superscript  $H$  denotes the Hermitian transpose.  $\vec{\Omega}_R(n)$  is the wavelet coefficient from the convolution of filtering matrix and reference time course.  $\vec{\Theta}_R(n)$  is the phase locking value (PLV) [22] describing the consistent phase locking between the measurement and the testing time series. In the perfect synchronized case, PLV will be 1, and PLV will be zero if the phase relationship is purely random. In our experiment,  $\vec{\Omega}_R(n)$  is the 40 Hz sinusoidal oscillation calculated from the complex Morlet wavelet. Note that the power and synchronization index was averaged across trials, not across different time instants.

#### 4.2.5 Noise normalized spectral power using MNE and statistical inference of PLV

Power estimates on the cortical surface were contrasted with the baseline power averages. Note that here the baseline is calculated from the raw data with multiple trials in order to include the trial-to-trial variability, rather than an averaged baseline as is traditionally done with ERP analysis. We adopted the  $F$ -statistics, which is the ratio of the instantaneous power at the frequency of interest over the averaged baseline power of the same frequency, to test if statistical significant activities exist [20]:

$$\vec{S}_{\text{power}}(n) = \frac{\vec{P}(n)}{\text{diag}(WC_fW^T)}$$

$$C_f = COV(\Psi_{f,t}(n) \otimes y_{baseline}(n)) \quad (4.10)$$

$y_{baseline}(n)$  denotes the temporal concatenation of baseline measurements from the raw data on MEG sensors.  $COV(\bullet)$  is the covariance operator. In the source localization without *a priori* dipole orientations, under the null hypothesis  $S_{power}(n)$  will follow the  $F$  distribution with 3 degrees of freedom for the numerator and a very large number of degrees of freedom for the denominator (the number of trials multiplied by the samples within each trial).

The statistical significance of phase-locking value can also be derived from the Rayleigh test [28, 29, 30]. Specifically, when the number of trials in the calculation is large (exceeding 50), the cumulative distribution function of PLV can be approximated by the following:

$$\vec{P}_{PLV}(n) \approx \exp(-\vec{\Theta}(n)) \quad (4.11)$$

Figure 4.2 summarizes the computation of MNE, noise normalized MNE and PLV on the cortical surface combining MEG, anatomical MRI and/or functional MRI.

#### 4.2.6 Simulation

We performed a simulation of the sustained 40-Hz activity field emanating from the left superior temporal gyrus (STG), along Heschl’s gyrus (HG). The anatomic information was derived from the structural MRI acquired for the subject of the MEG experiment (see Structural MRI section below for further details). After identifying this region of interest, we placed a patch of current dipoles prependicular to the cortical surface at HG. The cortical surface geometry was provided from an automatic cortical surface segmentation algorithm [31, 32]. The temporal activity of the source was modeled as a 40 Hz oscillation, with the onset at 50 msec. Afterwards, a sustained 40Hz activity was maintained for 200msec. The complete epoch was simulated to be 600 msec with 100 msec baseline. We superimposed Gaussian noise of zero

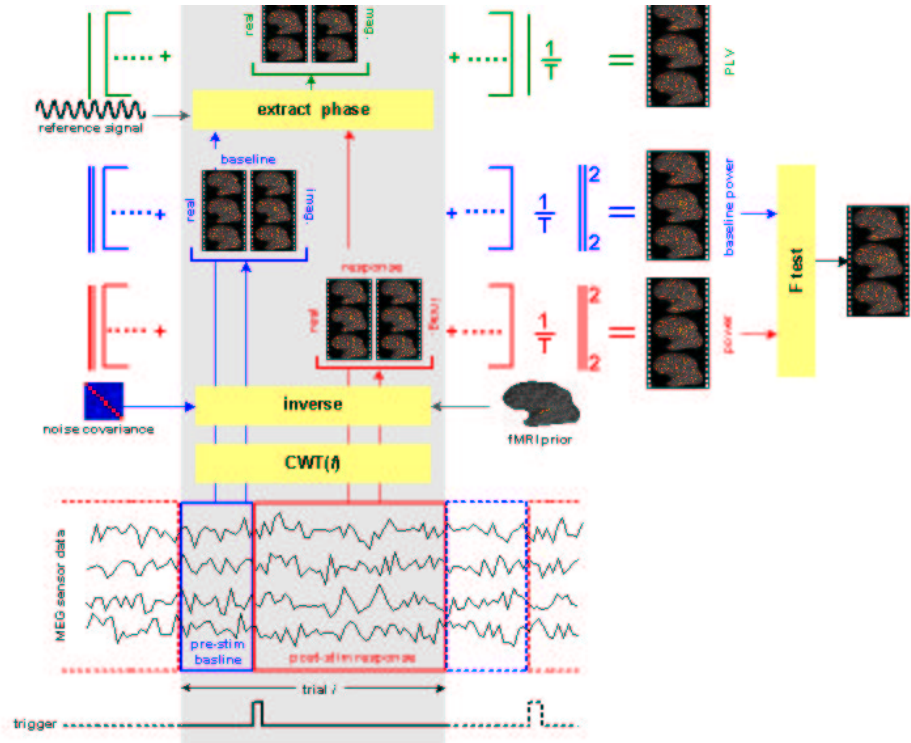


Figure 4-2: The schematic diagram illustrating the process of using raw MEG data to calculate the phase locking value (PLV) and the frequency specific power, as well as the noise normalized power, of the evoked response on the cortical space with temporal resolution in milliseconds. The blue lines indicate the pre-stimulus interval, which contains baseline activities. The red lines indicate the post-stimulus interval for the calculation of the evoked responses. The green color represents the calculation of the PLV, which is across both the pre-stimulus and post-stimulus interval. The noise-normalized power was calculated from the F-test of instantaneous power estimates and the baseline activities. Note that in the process of inverse, appropriate noise covariance and spatial prior (fMRI) are necessary for higher accuracy of localization.

mean and unit variance on each sensor to create a signal-to-noise ratio (SNR) for each trial of 0.01. 100 trials were produced to resemble a typical MEG experiment condition. Prior knowledge of neural activation sites was incorporated by manipulating the  $R$  matrix in Eq. (4.5) below for either no fMRI weighting or 90% fMRI weighting, The 90% weighting of the fMRI was chosen to provide the best compromise between separation of activity from correctly localized sources and minimization of error caused by missing sources [26]. In the case without fMRI weighting,  $R$  is an identity matrix, whereas with 90% fMRI weighting, entries corresponding to simulated source were adjusted to be 0.9 and all other entries were adjusted to be 0.1. The MEG signals were calculated with a boundary element model (BEM) [24, 33] without spatial decimation, which yields a source space of approximately 340,000 source locations. The inverse operator in the simulation was computed with a spatially decimated forward operator at 7-mm resolution on the cortical surface. The fMRI prior was mapped onto a 7-mm decimated BEM of the gray matter segmented using FreeSurfer (<http://surfer.nmr.mgh.harvard.edu>). The location of the simulated source and the associated fMRI priors are shown in Figure 4.3. We used the receiver operating characteristic (ROC) curves to quantify the detection power of the inverse operators. Specifically, true positive rate and false positive rate of and inverse detection thresholded at level were calculated as

$$\begin{aligned} TPR(\alpha) &= \frac{\text{area}(X_{sim}) \wedge \text{area}(X > \alpha)}{\text{area}(X_{sim})} \\ FPR(\alpha) &= \frac{(\text{area}(wholebrain) - \text{area}(X_{sim})) \wedge \text{area}(X > \alpha)}{\text{area}(wholebrain) - \text{area}(X_{sim})} \end{aligned} \quad (4.12)$$

Here  $\text{area}(X_{sim})$  indicates the area of the simulated sources,  $\text{area}(wholebrain)$  indicates the area of the whole brain, and  $\text{area}(X > \alpha)$  indications the area where the inverse solution has value greater than  $\alpha$ .  $\wedge$  is the boolean AND operator respectively.

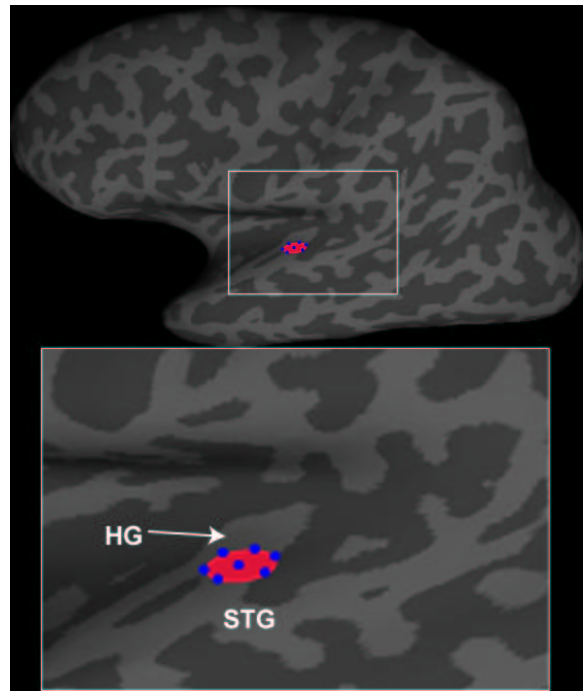


Figure 4-3: The locations of the simulated current sources around Heschl's gyrus (HG) and the superior temporal gyrus (STG) at the temporal lobe of the left hemisphere are rendered on the inflated cortical surface. The sources are spatially distributed on the cortical patch of 10 mm diameter (the red patch). 7 fMRI priors (blue spots) were used for the fMRI-weighted inverse. Here light gray denotes gyri and dark gray denotes sulci. This color scheme is used throughout the chapter.

#### **4.2.7 Subject**

For the MEG and fMRI measurements a single healthy male volunteer aged 30 was studied. He had no previous history of hearing loss and tested within the normal range with our screening audiogram. All research procedures were performed in accordance with the Institutional Review Board on human research. Written and oral informed consent were both obtained from the volunteer.

#### **4.2.8 MEG acquisition**

Neuromagnetic responses were recorded using a 306-channel MEG system (Elekta Neuromag OY, Espoo, Finland). During the MEG recording, the subject sat in the chair with his head inside the MEG dewar. Four head position indicator (HPI) coils were placed on the subject's head in order to coregister the anatomical MRI and the MEG sensors. A measurement of the room without a subject was made for 4 minutes that was later used for estimating the noise covariance matrix (see below). After the subject was seated inside the dewar, a 2-minute measurement was obtained while the subject was instructed to rest with eyes open. Another 2-minute measurement with the subject's eyes closed was also made. Auditory stimuli were delivered by an HP PC driving a Digidesign sound card to Eartone ER3A transducers (Etymotic, Elk Grove, IL, USA). The hearing threshold was defined as the stimulus intensity where the subject responded correctly approximately 70% of the time. Stimuli consisted of a series of 1 msec auditory clicks at 25msec intervals (40Hz). Stimuli were presented at 60dB sensation level (SL). Click trains were generated using Matlab (Mathworks, Natick, MA) and presented independently, with each click burst occurring 90 times. Monaural stimuli were presented alternatively to the left and right ear with 1 second duration and 1 second of silent gap, yielding 4-second trial including 2 seconds for left ear stimuli (1 second auditory click and 1 second silence) and 2 seconds for right ear stimuli. The experimental paradigm is shown in Figure 4.4.

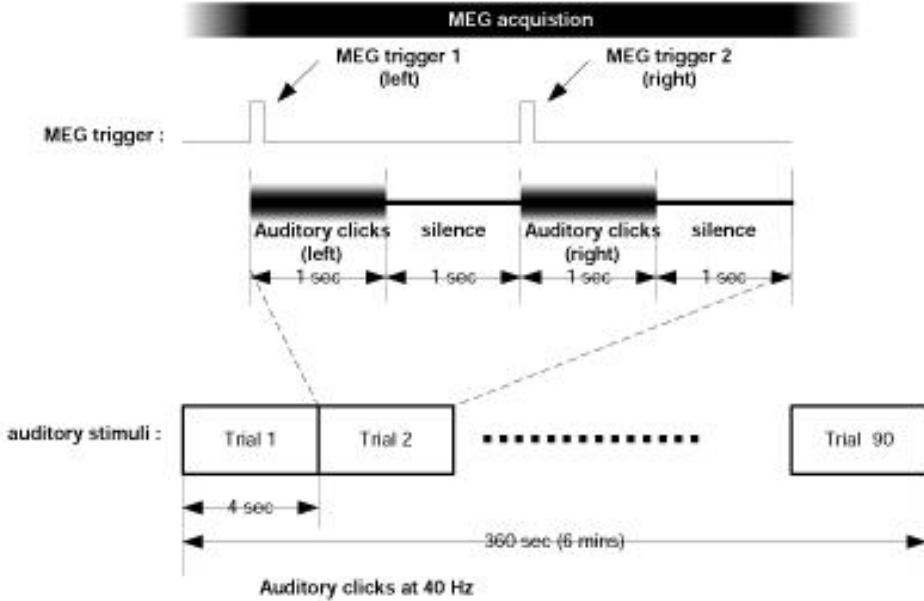


Figure 4-4: The experimental paradigm of auditory stimuli and MEG acquisition. Right and left aural clicks at 40 Hz were sent alternatively every 4 seconds. Total 90 trials (6 min) were collected for each subject.

#### 4.2.9 Structural MRI

Anatomical information was acquired by a high-resolution T1-weighted 3D volume MRI using an MPRAGE sequence (TI/TR/TE/flip = 1100ms/2530ms/3.49ms/70, partition thickness = 1.33mm, matrix = 256 x 256, 128 partitions, Field of View = 21cm x 21 cm) using a 1.5T MRI scanner (SIEMENS Medical Solutions, Erlangen, Germany). The geometry of the gray-white matter surface in the cortex was subsequently derived from an automatic segmentation algorithm to yield a triangulated model with approximate 340,000 vertices [31, 32]. Subsequently, forward matrices were separately calculated using either (1) a decimated a source space of approximate 7,000 dipoles with a 7 mm distance between the nearest two dipoles, or (2) using all the vertices in the cortical surface triangulation. The geometry of the inner skull required for the boundary-element model was derived from the segmented MRI data with a resolution of approximately 5000 triangular elements. [24, 33]. Functional MRI The fMRI experimental paradigm is illustrated in Figure 4.5. We employed a sparse imaging paradigm [34, 35], where auditory clicks were presented during the

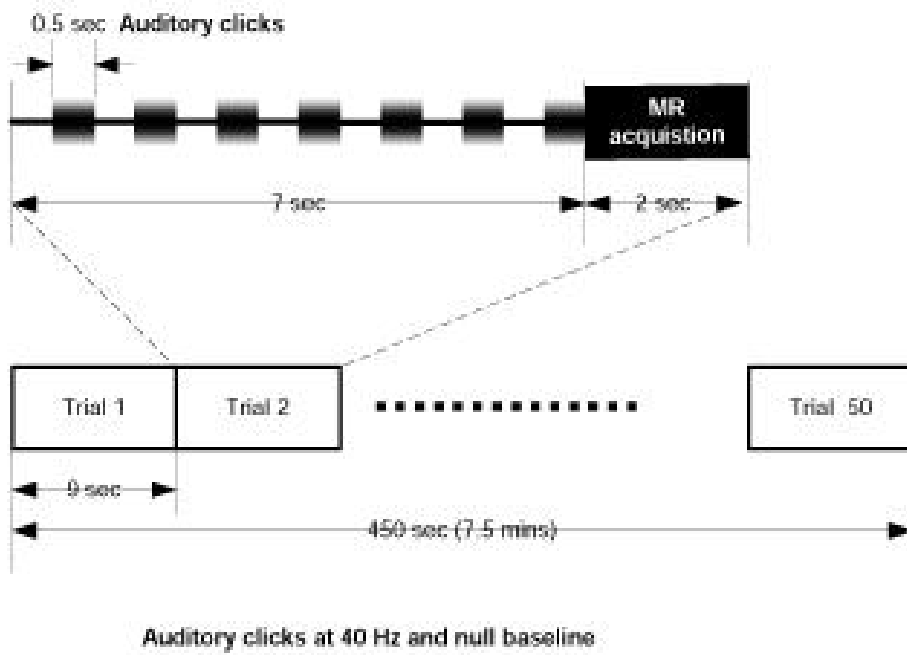


Figure 4-5: The fMRI experimental paradigm for auditory stimuli. In each trial, 7 auditory clicks were present during the 7-second inter-EPI silence period, followed by the 2-second EPI acquisition. Total 50 trials were collected for the subject.

7 seconds silent period between consecutive MRI acquisitions to mitigate the acoustic noise generated by gradient switching during the image acquisitions. We used a gradient echo BOLD pulse sequence on a 3T scanner (SIEMENS Medical Solutions, Erlangen, Germany) with imaging parameters of TR: 9sec, TE: 30 msec, flip angle: 90 deg., FOV: 200 mm x 200 mm, matrix, 64 x 64, slice thickness: 5 mm with 10% gap, 24 slices. The analysis of the fMRI data included motion artifact correction using a 12-parameter rigid-body transformation and spatial smoothing with a 3D Gaussian kernel with full-width-half-maximum (FWHM) of 6 mm. The experimental data was subsequently analyzed by the Student t-test to estimate the statistical significant image voxels between the trials of auditory clicks and the trials of null baseline condition.

## 4.3 RESULTS

### 4.3.1 Simulation

The simulation results are shown in Figure 4.6A. We averaged the responses of the 200 msec sustained oscillation period to generate snapshots of the power, noise normalized power, and the PLV on cortical surface. The power estimates were normalized between 0 and 1 to illustrate the relative spatial distribution of the dipole estimates. Noise-normalized power estimates were kept the original scale to reflect the averaged F-statistics [20]. After 100 trials, all three metrics localized to the correct hemisphere near the temporal lobe region. Without fMRI prior, the power estimate split at the Heschl's gyrus into two separate activation loci. The 90% fMRI weighted power estimates provided a well-matched spatial distribution to the location of the simulated cortical patch. The noise normalized power estimates cover the location of the simulated cortical patch but extend to the insula. However, the 90% fMRI weighted noise-normalized power estimates generate a phantom activation at the inferolateral aspect of the central sulcus. Phase locking values with and without fMRI priors both cover the location of the simulated patch. Like noise-normalized power estimates, both PLV simulations also show phantom insular activity and even 90% fMRI-weighted PLV shows phantom activation along the inferolateral central sulcus. Figure 4.6B shows the receiver operating characteristic (ROC) curves for the spatial sensitivity and specificity of power, noise normalized power and PLV using either no fMRI prior or 90% fMRI prior. Note that without fMRI prior, noise normalization can increase sensitivity and specificity of the detection, compared to MNE. Nevertheless, with 90% fMRI weighting, fMRI weighted MNE outperforms noise normalized power estimates by shifting ROC curve to the left.

### 4.3.2 Spontaneous MEG measurement and localization

Spontaneous signals were measured in the MEG sensors covering the whole brain including the parietal lobe. Time-frequency analysis using complex Morlet wavelets

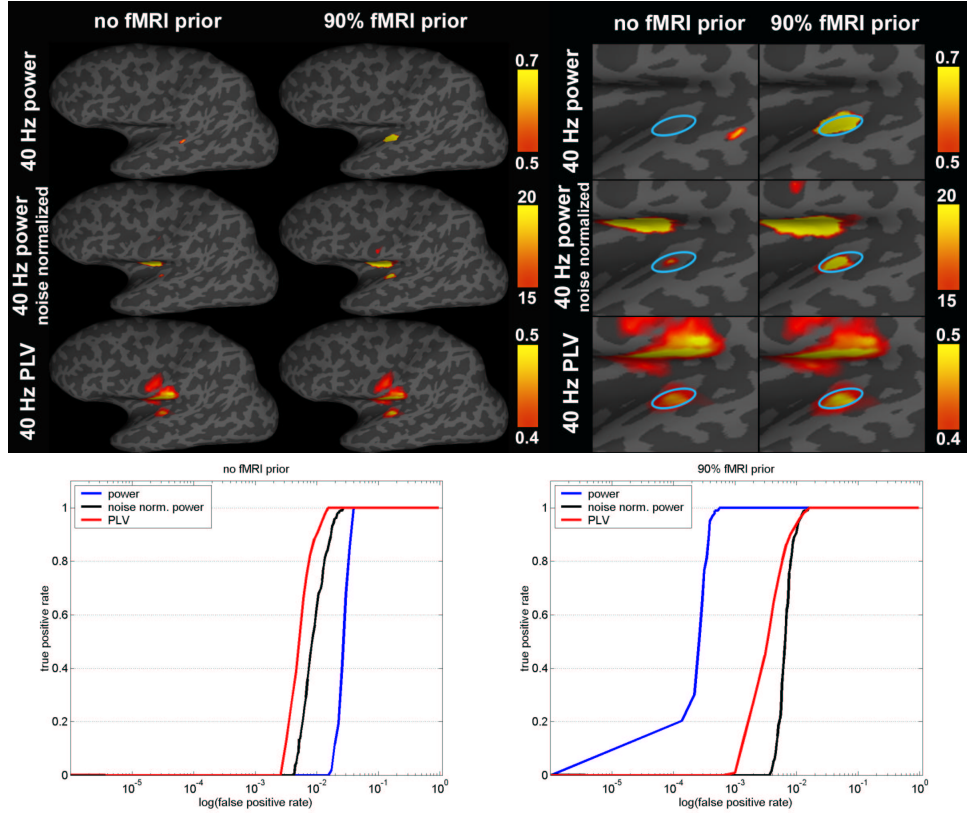


Figure 4-6: Estimated 40Hz activity along Heschl's gyrus in the simulation study. The three rows show the MNE 40 Hz wavelet power, noise-normalized MNE 40 Hz wavelet power, and 40 Hz PLV. The images are temporal averages of the 200 msec oscillation period. Left panels are the lateral views of the whole inflated left hemisphere. Right panels are the enlarged views at the temporal lobe. The light blue circle indicates the location of the simulated 10 mm diameter cortical patch. Receiver operating characteristic curves for the spatial sensitivity/specificity of 3 cortical space inverse methods (power, noise normalized power, and PLV) based on the simulations of a synthetic 10 mm diameter dipole patch at the Heschl's gyrus in the left hemisphere.

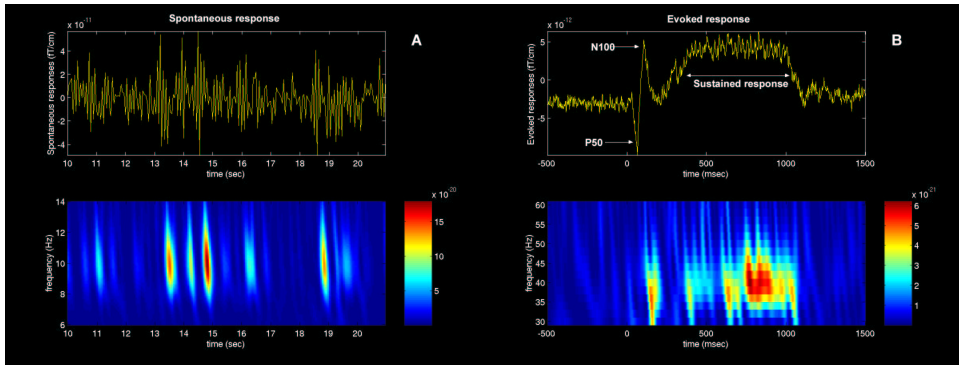


Figure 4-7: The most prominent spontaneous responses at 10Hz during the "eye-closed" condition (A), and the auditory stimuli evoked responses (B). The top graphs are the signal strength in the time domain. The associated time-frequency representations between 6-14 Hz for the spontaneous response and 30-60 Hz for the evoked responses are also rendered in the bottom graphs. Note that the spontaneous response is spectrally centered at 10 Hz with temporal bursts. For the auditory evoked response, the unfiltered magnetic field strength ( $\text{fT}/\text{cm}$ ) vs. time (stimulus presented at time 0, lasting 900msec) from a single channel over the temporal lobe shows the middle latency evoked responses (P50m and N100m) as well as the overriding sustained field.

centered at 6Hz to 14 Hz revealed that the maximal spectral power detected was approximately 10Hz. Note that the 10Hz spontaneous oscillation was not sustained but rather occurred in bursts (see Figure. 4.7A). Spontaneous 10Hz oscillation was localized predominately to the right hemisphere. Before noise normalization, the 10Hz power was localized to the superficial parietal gyrus around the occipital parietal junction. Using the noise covariance matrix from 2-minute empty room raw data, the noise normalized 10 Hz power localized the spontaneous activities to retrosplenial cortex at the occipital parietal junction (Figure 4.8).

### 4.3.3 Auditory evoked MEG measurement and localization

The auditory response evoked by the 40 Hz clicks is shown in Figure 4.7B, including both initial primary evoked response and sustained responses around the temporal lobe. Specifically, a P50 deflection followed by a N100 deflection was recorded at around 50 msec and 100 msec after the onset of the auditory stimuli. Subsequently, a sustained oscillation response began approximately 400 msec after the stimulus

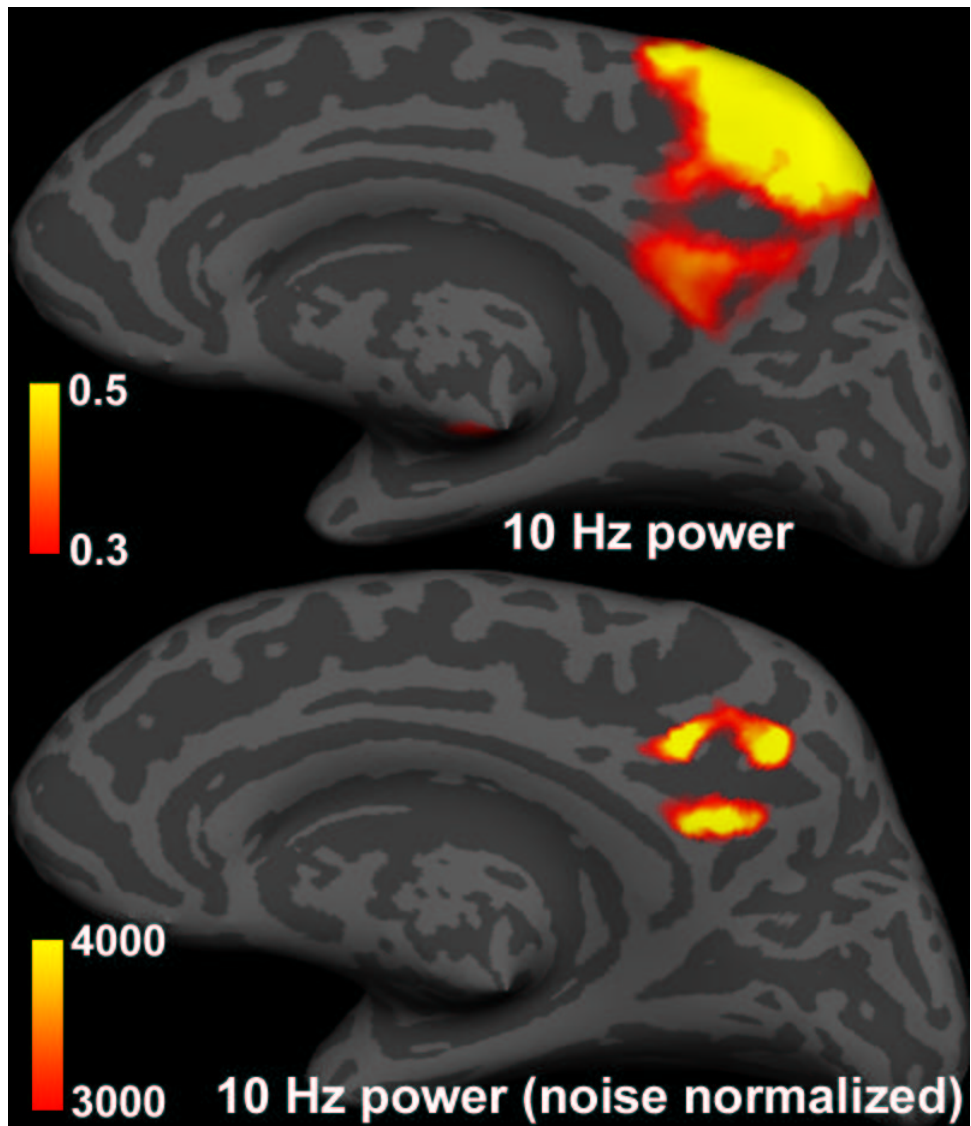


Figure 4-8: Medial aspects of the 10Hz power and the noise normalized 10Hz power on the inflated cortical surface during subject's "eye-closed" condition. These snapshots are temporally averaged across 20 seconds. Note that the noise normalization power estimates correct the superficial estimation by MNE from superficial parietal lobe around the parietal occipital junction to the retrosplenial cortex at the parietal occipital junction.

onset and lasted for approximately 400 msec. The MEG channel with the most prominent evoked fields was shown in Figure. 4.7B. Using auditory clicks, fMRI revealed that BOLD activation along the left Heschl's gyrus and the superior temporal gyrus, contrasted with the silent baseline. This is illustrated in Figure 4.9A at a *t*-statistics threshold of 12 (uncorrected  $p < 10^{-10}$ ). The decimated dipoles (with 7 mm spacing) coincided with the fMRI active region were recruited as the priors for MNE. The source localization of 40Hz power, noise-normalized 40Hz power and phase-locking values with 90% or without fMRI priors were shown in Figure 4.9B. In the power illustrations, we average the power between 500 msec and 900 msec, (see Figure 4.7B), and subsequently normalized between 0 and 1 to illustrate the brain areas with power exceeding 30% of the maximum. Similar temporal averaging and source estimate scaling were done for noise normalized power and PLV calculation. Note that without fMRI weighting, the estimation of source power shifted towards the superior temporal gyrus (STG). Using fMRI weighting of 90%, significant power was centered in and around Heschl's gyrus as indicated by fMRI priors. For PLV localizations, inverse estimates with or without fMRI priors do not differ significantly. Comparing power and PLV localizations, we found that PLVs with/without fMRI priors can detect stimulus-sensitive regions including Heschl's gyrus.

## 4.4 DISCUSSION

Here we demonstrated a computationally efficient method of a wavelet-based, anatomically constrained MNE to create an image of signal frequency-power and phase on the cortical surface. In particular, we used the individual anatomy in the forward model and as a constraint for the location of the sources. The technique allows the calculation of both the spectral power over some frequency band and the phase relationships, either between brain regions or between a brain region and the stimulus. The use of the wavelet transformation allows us to confine the analysis to a desired short segment of the response.

We emphasize the importance of choosing and calculating the appropriate noise

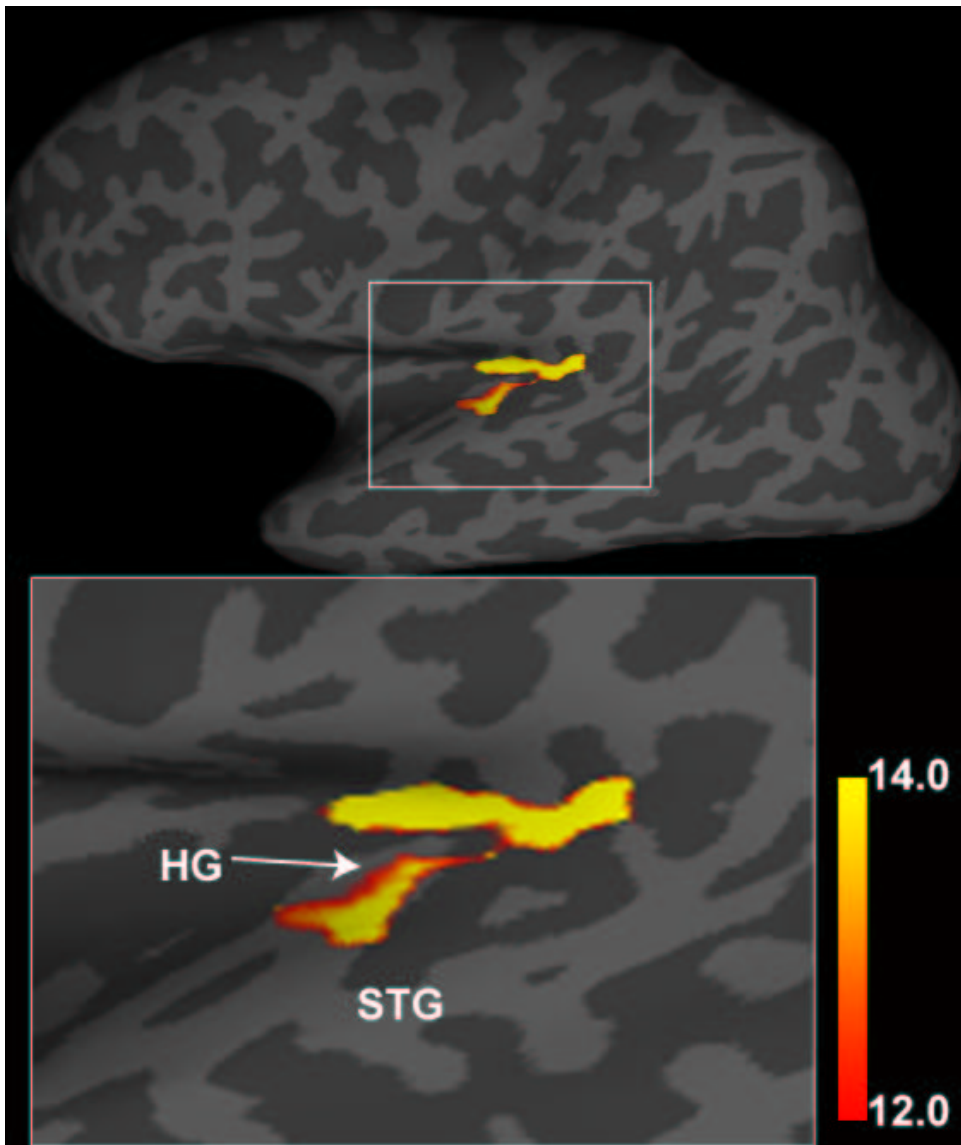


Figure 4-9: The  $t$ -statistics from 3 runs of fMRI experiments with paradigm shown in Figure 4.2. The  $t$ -statistics were calculated between the auditory click conditions and the silence conditions. The areas with negative 10-based logarithm of the p-values (uncorrected  $p < 10^{-10}$ ) were color-coded and distributed around Heschl's gyrus (HG), superior temporal gyrus (STG) and insula.

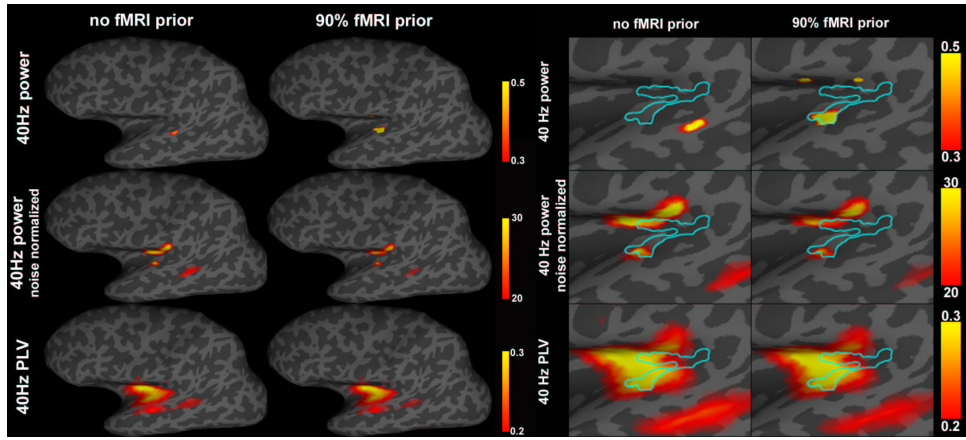


Figure 4-10: Wavelet-based spectral and phase locking value spatiotemporal maps using no fMRI prior and 90% fMRI priors separately.

covariance matrix. For spontaneous activities, such as 10Hz alpha rhythm in our results, the noise refers to the noise observed extraneous from the subject's brain activity. Therefore empty room recordings were used to calculate this noise covariance matrix. For the auditory evoked responses, the noise refers to all activity other than that elicited by the acoustic stimuli. In this scenario, noise covariance matrix should be derived from the pre-stimulus interval. Incorrect choice of the noise covariance causes either over or under estimation of the activity as well as the possibility of mis-localization of activity. In addition, the noise covariance should always be computed from the "raw data" before any averaging, even for the evoked responses estimation. Noise covariance matrix from averaged data always under characterizes the variability of the measurement and thus leads to over significance in the statistical tests. This is true because the (co)variance of the averaged data does not account for trial-to-trial variations. Therefore, raw data in appropriate "baseline" conditions have to be chosen wisely for accurate noise normalization.

Comparing our simulations and the results from real data, we validated that the reported technique can be used to detect frequency specific responses at signal to noise ratio (SNR) as small as 0.01, if up to 100 trials of measurements are available and the activity is phase-locked to the stimulus (evoked). However, if the activity is not phase locked to the stimulus (induced) the SNR must be greater than 1, a

limitation which is true for measuring induced spectral power Nevertheless, the magnitude of the F statistics and PLV differed in the simulations and the actual MEG measurements. Potentially this may be due to anatomical variations in the neural sources (not precisely perpendicular orientations of dipole sources to the local cortical surface), anatomical information errors from MRI and time varying activities in real brain responses (changes of spatial distribution and temporal duration of the oscillations). In the Bayesian estimation theory framework, this can be further improved by providing more accurate prior information regarding both the spatial and temporal properties of the brain activations, such as more accurate quantitative description between BOLD fMRI and MEG measurements. This is a current research topic we are actively investigating. Further, the relationships between the MEG oscillations and BOLD fMRI responses have yet to be explored. This relationship could be exploited in the Bayesian framework as well. It is hoped that this method will make such research possible. Although not explicitly tested here, this method should work well for detecting interaction of brain regions. Comparison with other source estimation methods

Currently, several methods have been proposed to map cortical oscillations, each of which has a particular strength for their application, but none of which meet all the requirements proposed here. Minimum current estimate (MCE), for example, [36, 37], assumes sources with exponential probability distribution function. Specifically, [18] proposed to use MCE to measure simultaneous cortical oscillations, based on the minimum  $\ell$ -norm estimate, using complex Fourier components from sections of raw MEG signals. Although it is limited to the analysis of spontaneous cortical oscillations, the method could be extended to include measurements of synchronization based on the phase of the Fourier components. It is, however, limited in that it does not have a high-temporal resolution to measure fast changing oscillations, and requires a high SNR. Source localizations using beamformer techniques [38, 39] have been also applied to study neural synchrony, such as Dynamic imaging of coherent sources (DICS) [16]. This innovative technique is a promising method of detecting synchronizations between neural networks in the brain, based on source estimation

using a spatial filter of coherence. Like the MCE technique it is limited, however, in that it requires a relatively high SNR and makes the assumption of stationary data, and consequently does not measure short lasting synchronizations. Sekihara et al [40, 41, 42] recently demonstrated that the stationary data assumption is not necessarily strict.

The use of the MNE to image cortical oscillations has also been proposed by others [15, 17]. Hauk et al [17] compared the MNE to a current source density method using EEG data sets with a wavelet-based frequency domain analysis. Others [15, 43] have recently performed simulations on various versions of the MNE. They concluded that MNE is a preferred method, if the regularization is optimized for the region of interest of the neural source. Compared to these other minimum  $l_2$  norm inverse approaches, our method differs in several ways. First, our solution computes single trial epochs, or uses clips of spontaneous activity, to create an averaged power spatiotemporal map. Second, we use a BEM to use the features of the actual head of the individual subject's MRI to create a power sources estimate directly on the cortical surface, utilizing a cortical constraint. Third, we also include the ability to create a phase synchronization map of the brain on the cortical surface. In this case, we show how the phase relation of the stimulus to the response can be created, but the same principle can be used to create maps showing synchronization between brain regions, once provided the reference temporal course from one specific brain region. And last, the utilization of prior neural activation information from fMRI can essentially help for correct power localization. This is especially important during the localization of the evoked responses of auditory responses, because of highly convoluted cortical surface at the temporal lobe. The anatomy challenges the traditional MNE to give focal and precise source estimations. Without fMRI priors, it is easy to lead to superficial source estimates away from Heschl's gyrus.

Our method is very similar to the that proposed by David et al [15] in that both source estimation methods use a wavelet based spectral analysis and a MNE. Our method differs in that we calculate the wavelet-based spectral power based on the power in source space (on the brain surface) across trials, instead of calculating the

single trial power and single trial phase locking maps as used by David et al. We have also proposed a method of producing a spectral dSPM with noise normalization of the MNE.

#### 4.4.1 Limitations

Several limitations of this technique are illustrated in this report. The algorithm's localizing ability is often limited, especially with activity in and around the Sylvian fissure, a common problem with imaging peri-Sylvian activity generally and auditory activity specifically. We can see in our results that probable 'phantom' sources are seen in the posterior inferior frontal lob, insula, and the middle temporal gyrus. These sources, even with actual measurements, are likely phantom as they are seen in the simulations as well, due to the close anatomical proximity to Heschl's gyrus. Due to the anatomical convolution of cortical surface, traditional MNE without *a priori* activation loci may lead to mis-localization of auditory neural activities. Using fMRI, which provides higher spatial resolution brain activation estimates, it is possible to constrain the localization process to avoid over-estimation of the power of neuromagnetic sources in traditional MNE. For phase-locking value and noise normalized power estimates, it appears that *a priori* information could be less essential. This is because of the intrinsic normalization of PLV calculation by disregarding the amplitude of dipole estimates in an individual trial. The noise normalization also tries to compensate the biases on the magnitude of the estimates. Therefore PLV and noise normalized power localization shows similar sensitivity for either superficial sources on the gyri or deep sources in the sulci. Although mostly both PLV and noise normalized power can correct biases toward superficial cortical activities, potential over correction may occur, as we found in both the simulations and real data that the insula were possibly false activated. So for simultaneous high sensitivity and specificity, fMRI weighted MNE can be a candidate tool for auditory response localization. Another limitation of our approach at this moment is that there exists no deep gray nuclei activity. Thalamocortical interaction is probably responsible for the generation and maintenance of oscillations in the neocortex. Our group is actively

investigating and will be a focus for an upcoming study.

#### **4.4.2 Future Applications**

The new method detailed here is a general framework and can be extended to include other imaging technologies including PET, optical imaging, and transcranial Doppler. Any functional information that can be localized can be included in the source covariance matrix and used as prior information and thus improve the localizing ability of the MEG or EEG data.

# References

- [1] W. Singer. Neuronal synchrony: a versatile code for the definition of relations? *Neuron*, 24(1):49–65, 111–25, 1999. 0896-6273 Journal Article Review Review, Academic.
- [2] C. Tallon-Baudry and O. Bertrand. Oscillatory gamma activity in humans and its role in object representation. *Trends Cogn Sci*, 3(4):151–162, 1999. 1364-6613 Journal article.
- [3] F. Varela, J. P. Lachaux, E. Rodriguez, and J. Martinerie. The brainweb: phase synchronization and large-scale integration. *Nat Rev Neurosci*, 2(4):229–39, 2001. 1471-0048 Journal Article Review Review, Tutorial.
- [4] N. Kopell, G. B. Ermentrout, M. A. Whittington, and R. D. Traub. Gamma rhythms and beta rhythms have different synchronization properties. *Proc Natl Acad Sci U S A*, 97(4):1867–72, 2000. 20144133 0027-8424 Journal Article.
- [5] C. Pantev, S. Makeig, M. Hoke, R. Galambos, S. Hampson, and C. Gallen. Human auditory evoked gamma-band magnetic fields. *Proc Natl Acad Sci U S A*, 88(20):8996–9000, 1991. 92020978 0027-8424 Journal Article.
- [6] C. Pantev, O. Bertrand, C. Eulitz, C. Verkindt, S. Hampson, G. Schuierer, and T. Elbert. Specific tonotopic organizations of different areas of the human auditory cortex revealed by simultaneous magnetic and electric recordings. *Electroencephalogr Clin Neurophysiol*, 94:26–40, 1995.

- [7] R. W. McCarley, C. G. Wible, M. Frumin, Y. Hirayasu, J. J. Levitt, I. A. Fischer, and M. E. Shenton. Mri anatomy of schizophrenia. *Biol Psychiatry*, 45(9):1099–119, 1999. 0006-3223 Journal Article Review Review, Academic.
- [8] E. Rodriguez, N. George, J. P. Lachaux, J. Martinerie, B. Renault, and F. J. Varela. Perception's shadow: long-distance synchronization of human brain activity. *Nature*, 397(6718):430–3, 1999. 99142514 0028-0836 Clinical Trial Journal Article Randomized Controlled Trial.
- [9] C. Tallon-Baudry, O. Bertrand, C. Delpuech, and J. Pernier. Stimulus specificity of phase-locked and non-phase-locked 40 hz visual responses in human. *J Neurosci*, 16(13):4240–9, 1996. 0270-6474 Journal Article.
- [10] C. Tallon-Baudry, O. Bertrand, C. Delpuech, and J. Pernier. Oscillatory gamma-band (30-70 hz) activity induced by a visual search task in humans. *J Neurosci*, 17(2):722–34, 1997. 0270-6474 Journal Article.
- [11] C. Tallon-Baudry, O. Bertrand, C. Wienbruch, B. Ross, and C. Pantev. Combined eeg and meg recordings of visual 40 hz responses to illusory triangles in human. *Neuroreport*, 8(5):1103–7, 1997. 0959-4965 Clinical Trial Journal Article.
- [12] C. Tallon-Baudry, O. Bertrand, F. Peronnet, and J. Pernier. Induced gamma-band activity during the delay of a visual short-term memory task in humans. *J Neurosci*, 18(11):4244–54, 1998. 0270-6474 Journal Article.
- [13] C. Tallon-Baudry, O. Bertrand, and C. Fischer. Oscillatory synchrony between human extrastriate areas during visual short-term memory maintenance. *J Neurosci*, 21(20):RC177, 2001. 1529-2401 Clinical Trial Journal Article.
- [14] J. S. Kwon, B. F. O'Donnell, G. V. Wallenstein, R. W. Greene, Y. Hirayasu, P. G. Nestor, M. E. Hasselmo, G. F. Potts, M. E. Shenton, and R. W. McCarley. Gamma frequency-range abnormalities to auditory stimulation in schizophrenia. *Arch Gen Psychiatry*, 56(11):1001–5, 1999. 0003-990x Journal Article.

- [15] O. David, L. Garnero, D. Cosmelli, and F. J. Varela. Estimation of neural dynamics from meg/eeg cortical current density maps: application to the reconstruction of large-scale cortical synchrony. *IEEE Trans Biomed Eng*, 49(9):975–87, 2002. 22203223 0018-9294 Journal Article Validation Studies.
- [16] J. Gross, J. Kujala, M. Hamalainen, L. Timmermann, A. Schnitzler, and R. Salmelin. Dynamic imaging of coherent sources: Studying neural interactions in the human brain. *Proc Natl Acad Sci U S A*, 98(2):694–9, 2001. 21143371 0027-8424 Journal Article.
- [17] O. Hauk, A. Keil, T. Elbert, and M. M. Muller. Comparison of data transformation procedures to enhance topographical accuracy in time-series analysis of the human eeg. *J Neurosci Methods*, 113(2):111–22, 2002. 21635346 0165-0270 Journal Article.
- [18] O. Jensen and S. Vanni. A new method to identify multiple sources of oscillatory activity from magnetoencephalographic data. *Neuroimage*, 15(3):568–74, 2002. 21839696 1053-8119 Journal Article.
- [19] A.M. Dale and M.I. Sereno. Improved localization of cortical activity by combining eeg and meg with mri cortical surface reconstruction: A linear approach. *J. Cog. Neurosci.*, 5(2):162–176, 1993.
- [20] A.M. Dale, A.K. Liu, B.R. Fischl, R.L. Buckner, J.W. Belliveau, J.D. Lewine, and E. Halgren. Dynamic statistical parametric mapping: Combining fmri and meg for high-resolution imaging of cortical activity. *Neuron*, 26:55–67, 2000.
- [21] MS Hamalainen and RJ Ilmoniemi. Interpreting measured magnetic fields of the brain: estimates of current distributions. Technical report, Helsinki University of Technology, 1984.
- [22] J. P. Lachaux, E. Rodriguez, J. Martinerie, and F. J. Varela. Measuring phase synchrony in brain signals. *Hum Brain Mapp*, 8(4):194–208, 1999. 20084432 1065-9471 Journal Article.

- [23] M. Le Van Quyen, J. Foucher, J. Lachaux, E. Rodriguez, A. Lutz, J. Martinerie, and F. J. Varela. Comparison of hilbert transform and wavelet methods for the analysis of neuronal synchrony. *J Neurosci Methods*, 111(2):83–98, 2001. 21479679 0165-0270 Journal Article Review Review, Tutorial.
- [24] MS Hamalainen, R Hari, RJ Ilmoniemi, J Knuutila, and OV Lounasmaa. Magnetoencephalography-theory, instrumentation, and application to noninvasive studies of the working human brain. *Review of Modern Physics*, 65:413–497, 1993.
- [25] A. K. Liu, A. M. Dale, and J. W. Belliveau. Monte carlo simulation studies of eeg and meg localization accuracy. *Hum Brain Mapp*, 16(1):47–62, 2002. 21859140 1065-9471 Journal Article.
- [26] A. K. Liu, J. W. Belliveau, and A. M. Dale. Spatiotemporal imaging of human brain activity using functional mri constrained magnetoencephalography data: Monte carlo simulations. *Proc Natl Acad Sci U S A*, 95(15):8945–50., 1998.
- [27] M. Fuchs, M. Wagner, T. Kohler, and H. A. Wischmann. Linear and nonlinear current density reconstructions. *J Clin Neurophysiol*, 16(3):267–295, 1999. 99353451 0736-0258 Journal Article Review Review, Tutorial.
- [28] C. Babiloni, F. Babiloni, F. Carducci, F. Cincotti, F. Rosciarelli, L. Arendt-Nielsen, A. C. Chen, and P. M. Rossini. Human brain oscillatory activity phase-locked to painful electrical stimulations: a multi-channel eeg study. *Hum Brain Mapp*, 15(2):112–23, 2002. 21823847 1065-9471 Journal Article.
- [29] N. I. Fisher. *Statistical analysis of circular data*. Cambridge University Press, Cambridge [England] ; New York, NY, 1993. N.I. Fisher.
- [30] C. Simoes, O. Jensen, L. Parkkonen, and R. Hari. Phase locking between human primary and secondary somatosensory cortices. *Proc Natl Acad Sci U S A*, 100(5):2691–4, 2003. 22506329 0027-8424 Journal Article.

- [31] A. M. Dale, B. Fischl, and M. I. Sereno. Cortical surface-based analysis. i. segmentation and surface reconstruction. *Neuroimage*, 9(2):179–94., 1999.
- [32] B. Fischl, M. I. Sereno, and A. M. Dale. Cortical surface-based analysis. ii: Inflation, flattening, and a surface-based coordinate system. *Neuroimage*, 9(2):195–207., 1999.
- [33] T. F. Oostendorp and A. van Oosterom. Source parameter estimation in inhomogeneous volume conductors of arbitrary shape. *IEEE Trans Biomed Eng*, 36(3):382–91., 1989.
- [34] W.B. Edmister, T.M. Talavage, P.J. Ledden, and R.M. Weisskoff. Improved auditory cortex imaging using clustered volume acquisitions. *Human Brain Mapping*, 7:89–97, 1999.
- [35] D.A. Hall, M.P. Haggard, M.A. Akeroyd, A.R. Palmer, A.Q. Summerfield, M.R. Elliott, E.M. Gurney, and R.W. Bowtell. "sparse" temporal sampling in auditory fmri. *Human Brain Mapping*, 7:213–223, 1999.
- [36] K. Matsuura and Y. Okabe. Selective minimum-norm solution of the biomagnetic inverse problem. *IEEE Trans Biomed Eng*, 42(6):608–15, 1995. 95309952 0018-9294 Journal Article.
- [37] K. Uutela, M. Hamalainen, and E. Somersalo. Visualization of magnetoencephalographic data using minimum current estimates. *Neuroimage*, 10(2):173–80., 1999.
- [38] B. D. Van Veen, W. van Drongelen, M. Yuchtman, and A. Suzuki. Localization of brain electrical activity via linearly constrained minimum variance spatial filtering. *IEEE Trans Biomed Eng*, 44(9):867–80, 1997. 97427576 0018-9294 Journal Article.
- [39] J Vrba, G Anderson, K Betts, MB Burbank, T Cheung, D Cheyne, AA Fife, S Govorkov, F Habib, G Haid, V Haid, T Hoang, C Hunter, PR Kubik, S Lee,

J McCubbin, J McKay, D McKenzie, D Nonis, J Paz, E Reihl, D Ressel, SE Robinson, C Schroyen, I Sekatchev, P Spear, B Taylor, M Tillotson, and W Sutherlilng. 151-channel whoel cortex meg system for seated or supine positions. In *11th International Conference on Biomagnetism*, Recent advances in biomagnetism., Sendai, 1999. Tohoku Univ. Press.

- [40] I. Hashimoto, T. Kimura, Y. Iguchi, R. Takino, and K. Sekihara. Dynamic activation of distinct cytoarchitectonic areas of the human si cortex after median nerve stimulation. *Neuroreport*, 12(9):1891–7, 2001. 21329635 0959-4965 Journal Article.
- [41] K. Sekihara, S. S. Nagarajan, D. Poeppel, A. Marantz, and Y. Miyashita. Reconstructing spatio-temporal activities of neural sources using an meg vector beamformer technique. *IEEE Trans Biomed Eng*, 48(7):760–71, 2001. 21335277 0018-9294 Journal Article.
- [42] K. Sekihara, S. S. Nagarajan, D. Poeppel, A. Marantz, and Y. Miyashita. Application of an meg eigenspace beamformer to reconstructing spatio-temporal activities of neural sources. *Hum Brain Mapp*, 15(4):199–215, 2002. 21823854 1065-9471 Journal Article.
- [43] J. P. Lachaux, A. Lutz, D. Rudrauf, D. Cosmelli, M. Le Van Quyen, J. Martinerie, and F. Varela. Estimating the time-course of coherence between single-trial brain signals: an introduction to wavelet coherence. *Neurophysiol Clin*, 32(3):157–74, 2002. 22152701 0987-7053 Journal Article Review Review, Tutorial.

# Chapter 5

## Multivariate Analysis of Neuronal Interactions in the Generalized Partial Least Squares Framework: Simulations and Empirical Studies

Identification of spatiotemporal interactions within/between neuron populations is critical for detection and characterization of large-scale neuronal interactions underlying perception, cognition and behavior. Univariate analysis has been employed successfully in many neuroimaging studies. However, univariate analysis does not explicitly test for interactions between distributed areas of activity and is not sensitive to distributed responses across the brain. Multivariate analysis can explicitly test for multiple statistical models, including the designed paradigm, and allows for spatial and temporal model detection. Here, I investigate multivariate analysis approaches that take into consideration the 4-D (time and space) covariance structure of the data. Principal Component Analysis (PCA) and Independent Component Analysis (ICA) are two popular multivariate approaches with distinct mathematical constraints. Common difficulties in using these two different decompositions include: classification of the revealed components (task-related signal versus noise); overall

signal-to-noise sensitivity; and the relatively low computational efficiency (multivariate analysis requires the entire raw data set and more time for model identification analysis). Using both Monte Carlo simulations and empirical data, I derived and tested the generalized Partial Least Squares (gPLS) framework which can incorporate both PCA and ICA decompositions with computational efficiency. The gPLS method explicitly incorporates the experimental design to simplify the identification of characteristic spatiotemporal patterns. I performed parametric modeling studies of a blocked-design experiment under various conditions, including background noise distribution, sampling rate and hemodynamic response delay. I used a randomized grouping approach to manipulate the degrees of freedom of PCA and ICA in gPLS to characterize both paradigm coherent and transient brain responses. Simulation data suggest that in the gPLS framework, PCA mostly outperforms ICA as measured by the Receiver Operating Curves (ROCs) in SNR from 0.01 to 100, the hemodynamic response delays from 0 to 3 TR in fMRI, background noise models of Guassian, sub-Gaussian and super-Gaussian distributions, and the number of observations from 5, 10 to 20 in each block of a 6-block experiment. Further, due to selective averaging, the gPLS method performs robustly in low signal-to-noise ratio ( $\downarrow 1$ ) experiments. I also tested PCA and ICA using PLS in a simulated event-related fMRI data to show their similar detection. Finally, I tested our gPLS approach on empirical fMRI motor data. Using the randomized grouping method, both transient responses, and consistent paradigm/model coherent components in the 10-epoch block design motor fMRI experiment can be identified. Overall, studies of synthetic and empirical data suggest that PLS analysis, using PCA decomposition, provides a stable and powerful tool for exploration of fMRI/behavior data.

## 5.1 INTRODUCTION

The analysis of functional magnetic resonance imaging data (fMRI) [1, 2, 3, 4] is intended to reveal the underlying spatiotemporal interactions of neuronal populations. This includes the identification and characterization of orchestrated brain areas in

both spatial and temporal domains. Traditionally, univariate statistical methods [5, 22, 7, 23], such as the t-test or non-parametric Kolmogorov-Smirnov test and their associated statistical parametric maps, have been used quite often to detect cognitive task-related components. A reference temporal profile, which usually is associated with the experiment stimulus paradigm, is required for hypothesis testing. Such univariate approaches test brain voxels distributed over the brain independently, and they ignore the anatomical connections among brain loci. This lack of consideration of spatial interactions inspired the utilization of multivariate methods for detection and estimation of spatial activation and temporal dynamics of the brain [9, 10, 24, 32, 13]. Multivariate statistics regard the whole spatiotemporal data as an entity during estimation of active brain areas. We investigated two different approaches (PCA and ICA) for data decomposition within our generalized Partial Least Squares framework.

Principal component analysis (PCA) and associated eigen-image [14, 15, 22, 10] are examples of multivariate methods to decompose the data into subspaces. These subspaces account for the total spatiotemporal variance in the order of explained variance. The first eigen-image in PCA represents the spatial brain patterns and their associated timing which explains the most of the variance. The subsequent eigen-images explain the residual variance using the constraint of orthonormality to the preceding eigen-images. PCA is thus, a successive variance decomposition process with an orthonormality constraint among eigen-images.

Independent Component Analysis (ICA) [30, 32, 13] is an alternative approach. Unlike PCA, which assumes an orthonormality constraint, ICA assumes statistical independence among a collection of spatial patterns. ICA uses a linear mixture assumption to decompose the original data into spatially statistically independent components. Both PCA and ICA are model-free methods (independent of task paradigm design) to explore the structure of the data without a priori information. This data-driven property excludes biases and enables the detection of transient responses and artifacts inside the data.

The difficulties of applying PCA and ICA to fMRI analysis include the need to identify separated components and computational requirements. Owing to the size

of collected fMRI data, PCA and ICA both identify a large collection of intrinsic structures, which makes it difficult for researchers to establish direct correspondence between the identified components and the experiment hypotheses. Both PCA and ICA require high computational power to decompose the data matrix. ICA is especially computationally expensive compared to PCA, even when utilizing an advanced algorithm [17].

Regardless of the analysis approach used to explore the data matrix, prior information about the design of the experiment is valuable for detection and estimation of brain activity. The univariate General Linear Model (GLM) framework [22] utilizes experimental paradigms and presumed basis functions to encode multiple null-hypotheses and confounds in the design matrix as regressors. On the other hand, PCA and ICA make use of the information about the experimental design after the decomposition [9, 32], instead of incorporating such information before the decomposition, like GLM. Thus, PCA and ICA are more data-driven methods due to the post-hoc identification of decomposed components.

Partial Least Squares (PLS) [24] is a compromise between hypothesis-driven and data-driven approaches. PLS uses an intermediate step of selective averaging of the experimental design to incorporate hypotheses explicitly. PCA is then used to decompose the collapsed data to reveal intrinsic structures. PLS provides advantages of dimensional reduction of the data, and signal-to-noise enhancement due to the selective averaging. The dimension reduction process relieves the difficulties of posterior interpretation for numerous components resulting from direct multivariate decomposition by PCA.

Traditionally PLS has utilized PCA for decomposition. Here, we extended the original Partial Least Square framework [24] to incorporate both PCA and ICA as data decomposition alternatives. Furthermore, a randomized grouping/selective averaging approach was used to generalize the a priori contrast matrix to investigate possible transient and time-locked activities in both simulations and empirical studies. To quantitatively evaluate the use of either PCA or ICA in this generalized PLS (gPLS) framework, we performed parametric simulations for a blocked-design

fMRI experiment at conditions of various SNR, time of repetition (TR), background noise models, experimental paradigms, and hemodynamic response delays. Also we presented the simulation results for an event-related fMRI experiments to test the differences when PCA or ICA is utilized as the decomposition in PLS. In addition to modeling studies, we analyzed an empirical blocked-design fMRI experiment of voluntary finger tapping. We examined the capability of gPLS to detect consistently task-related components and transient responses, in both task-control single contrast and parametrically designed multiple contrast experiments. Our generalized Partial Least Squares approach proposed here, takes advantage of the a priori task paradigm design, yet allows for detection of potential brain activity un-associated with the a priori contrast matrix. The pros and cons of using either PCA or ICA decomposition schemes to optimize fMRI signal detection are discussed.

## 5.2 THEORY

### 5.2.1 Multivariate approach to reveal the functional connectivity: PCA

The collected data in functional brain imaging studies can be collapsed into a two-dimensional matrix,  $D$ , which includes both spatial and temporal information and is referred to the data matrix. Without loss of generality, we assume here that each row encodes one time-point/condition acquisition for the whole brain, and each column represents one voxel's time series or voxel's recording across different subjects and different conditions. For example,  $D_{ij}$  represents the value of voxel  $j$  in time point  $i$  acquisition.

Different decomposition procedures can be applied to the data matrix to reveal the internal structures. Here we refer to "Total Decomposition" (TD) as the approach that directly decomposes the spatiotemporal data matrix,  $D$ , by multivariate tools. PCA decomposes the two-dimensional matrix into orthogonal subspaces, which are termed latent variables (LV) in the gPLS framework. The outer product of the left

singular vector and the right singular vector, weighted by the corresponding singular value, results in each latent variable expressed as:

$$D = {}_{PCA}U \times {}_{PCA}S \times {}_{PCA}V^T \quad (5.1)$$

$$\begin{aligned} {}_{PCA}U^T {}_{PCA}U &= {}_{PCA}U {}_{PCA}U^T = I \\ {}_{PCA}V^T {}_{PCA}V &= {}_{PCA}V {}_{PCA}V^T = I \end{aligned} \quad (5.2)$$

Here  $I$  denotes the identity matrix. Each LV consists of a singular value (a diagonal entry of  ${}_{PCA}S$ ), one left singular vector (a column of  ${}_{PCA}U$ ) and one right singular vector (a row of  ${}_{PCA}V$ ). The left singular vector in each LV ( ${}_{PCA}U$ ), which is termed the "design LV" in the following application of PCA in gPLS, gives the loading of different time-points/conditions to maximize the explained variance in the associated LV under the orthonormality constraint to the remaining design LVs. In addition, the right singular vector ( ${}_{PCA}V$ ), which is named "brain LV" in the following application of PCA in gPLS, gives the loading of each voxel to maximize the explained variance in the associated LV subjected to the orthonormality constraint to other right singular vectors. Singular values,  ${}_{PCA}S$ , are metrics to quantify the significance of each LV. Larger singular values represent a more dominant contribution from the corresponding LV to the total variance in the data matrix. The proportion of the square of one singular value over the sum of squares of singular values provides the quantitative significance of the latent variable. Each design LV provides the physiological inference of the latent variable, and the brain LV represents the spatial loading of the effect on different voxels.

The data matrix can be reconstructed from the latent variables created by the outer product of the corresponding left singular vector and the right singular vector, weighted by the singular value. The sequential sum of all latent variables constitutes the least square fit of the data matrix in terms of minimizing the mean square error. The spectrum theorem describes the reconstruction procedure from the decomposed

components,

$$D = \sum_i {}_{PCA}S_{ii}({}_{PCA}\vec{U}_{\bullet i} \times {}_{PCA}\vec{V}_{i\bullet}^T) \quad (5.3)$$

where  ${}_{PCA}\vec{U}_{\bullet i}$  denotes the  $i$ th column of matrix  ${}_{PCA}U$ , and  ${}_{PCA}\vec{V}_{i\bullet}$  denotes the  $i$ th row of matrix  ${}_{PCA}V$ .

PCA is the mathematical process to re-organize the total variance in the new coordinate system by orthogonal rotation. PCA provides such a rotation subject to the constraints on orthonormality among coordinate axes and maximal variance of the projected raw data on the new coordinate system after rotation.

### 5.2.2 Multivariate approach to reveal the functional connectivity: ICA

Independent Component Analysis (ICA) is an alternative multivariate brain imaging data analysis tool. Instead of decomposing the data into orthogonal subspaces, ICA minimizes the mutual information among "channels", which refers to rows in the data matrix [32, 13]. The critical assumption of ICA is that the recorded signal is the linear time-invariant mixture of several statistically independent components. The ICA algorithm estimates the mixture matrix and it searches an "un-mixing" linear operator to restore these spatially independent components. This is formulated as:

$$D = W \times X \quad (5.4)$$

Each row of  $X$  represents one spatially independent component (IC). Observed data matrix,  $D$ , is generated by the linear mixture of these independent components via the linear mixing operator,  $W$ .

Independent components are found by reversing the mixture process.

$$\hat{X} = \hat{W}^{-1} \times D \quad (5.5)$$

The similarity between the independent components in ICA and the latent vari-

ables in PCA can be compared by Eq. (5.1) and Eq. (5.5). This generates the following analogy between PCA and ICA brain latent variables and design latent variable.

$$\begin{aligned} {}_{ICA}\vec{U}_{\bullet i} &= \frac{\hat{W}_{\bullet i}}{\|\hat{W}_{\bullet i}\|} \\ {}_{ICA}\vec{V}_{\bullet i} &= \frac{\hat{X}_{\bullet i}}{\|\hat{X}_{\bullet i}\|} \\ {}_{ICA}S_{ii} &= \sqrt{\frac{\|\hat{W}_{\bullet i} \times \hat{X}_{\bullet i}\|}{\|{}_{ICA}\vec{U}_{\bullet i} \times {}_{ICA}\vec{V}_{\bullet i}^T\|}} \end{aligned} \quad (5.6)$$

where the  $\|\bullet\|$  operator denotes the root-mean-square of the vector. The defined design LV,  ${}_{ICA}\vec{U}$ , and brain LV,  ${}_{ICA}\vec{V}$ , are normalized to unit power as they are in PCA. A diagonal singular matrix can also be constructed by placing defined ICA singular values in Eq. 5.6c at diagonal entries. Similar to the spectrum theorem in PCA, the derived design and brain latent variables in ICA reconstruct the original data matrix by summing up the subspaces by cross product of ICA design and brain LV weighted by the ICA singular value.

$$D = \sum_i {}_{ICA}S_{ii}({}_{ICA}\vec{U}_i \times {}_{ICA}\vec{V}_i^T) \quad (5.7)$$

### 5.2.3 Functional connectivity analysis by generalized Partial Least Squares

Partial Least Squares (PLS) [24] is an alternative multivariate approach for analyzing the functional neuroimaging matrices within the new space of proposed contrasts (or hypotheses) of interest. The goal here is to generalize the PLS algorithm (gPLS) to utilize both PCA and ICA as decomposition tools. Like the original PLS approach, generalized PLS constructs an effect space of reduced dimension via the interaction of the data matrix  $D$ , and the contrast matrix  $C$ , which encodes multiple comparisons

mathematically.

For a data matrix  $D$  of  $n$  time-points (or conditions) and  $m$  voxels, a contrast matrix  $C$  of size  $c$  by  $n$  can be constructed to incorporate  $c$  contrasts, each of which represents one null hypothesis. The cross-product of these two matrices creates the effect space  $E$ .

$$E = C^T \times D \quad (5.8)$$

By use of the contrast matrix, the dimensionality of the original spatiotemporal neuroimaging recordings is decreased dramatically compared to the total decomposition of the data matrix in most fMRI experiment scenarios. This leads to the advantages of gPLS for increased power for signal detection and estimation, resulting from the weighted averaging provided by the contrast matrix, and for decreased complexity in interpreting the revealed structures within the data due to the reduction of dimension.

One would like to contrast effects in the temporal domain without temporal overlapping. In a task-control experiment to detect baseline-activation differences or in parametrically designed experiments to reveal condition-related effects, orthonormal Helmert contrasts [24] can be used as the contrast matrix for multiple conditions comparison. A Helmert contrast matrix of temporal dimension  $n$  is written explicitly as

$$H_{ij} = \begin{cases} 0, & \text{when } i < j \\ \frac{1}{\sqrt{1+1/(n-j)}}, & \text{when } i = j \\ -\frac{1}{(n-j)\sqrt{1+1/(n-j)}}, & \text{when } i > j \end{cases} \quad (5.9)$$

Each column of the Helmert contrast matrix can be used to represent one null hypothesis. Two properties of the Helmert basis function are useful for detecting activation: first, the fact that each basis with sum of entries equal to zero explicitly implements a matched filter by providing weightings to various temporal observations.

Each basis tests one single null hypothesis in the selective averaging process by correlating the contrast matrix and the data matrix. Second, all Helmert bases are of unit variance and orthogonal among each other such that no bias toward any comparison encoded by an individual basis is generated in the subsequent decomposition.

To perform multiple comparisons, observations are temporally segregated into groups, and the associated Helmert bases are created to encode the differences among them. The following decomposition algorithm identifies the coefficients for these bases by maximizing the total effect created by individual comparison using either PCA or ICA. For a blocked-design experiment, groups can be either different epochs for a single subject experiment, or different condition/subject indices for a cross-subject, parametrically designed study.

In the case of testing a single hypothesis (e.g., detection of baseline-activation contrast in blocked-design experiment) only one associated contrast vector is created and traditional PLS fails in this degenerated case, because of the rank deficiency of the effect space. To resolve this problem, we propose "randomized grouping," which is essentially making use of the repeated observations by posing multiple null hypotheses to test differences between partitioned groups. In practice, we may assume there are  $g$  groups in a  $t$ -epoch blocked-design experiment, where  $g \leq t$ . A supplementary contrast matrix encoding the difference of  $g$  groups can be created by randomly partitioning epochs using Helmert bases. The new contrast matrix, consisting of the baseline-activation contrast vector as well as the epoch difference encoded in the supplementary contrast matrix, enriches the content of the effect space. The dimension of the effect space after randomized grouping is still dramatically smaller than that of the data matrix in conventional experiment setups. This property can be exploited for iterations of randomized grouping to estimate the errors in the grouping process.

Using the total decomposition, the dimension of the matrix fed into the multivariate decomposition is often the number of temporal observations, because an fMRI experiment generates many more spatial voxels than temporal scans. In contrast, the PLS and gPLS frameworks create the effect space with dimension equal to the num-

ber of contrasts to be tested. This reduction in dimension provides the advantages of not only increased power for signal detection/estimation (due to the explicit selective averaging by columns of the contrast matrix) but also decreased computational complexity due to the reduced row dimension of the effect space. Randomized grouping further provides the flexibility to manipulate the size and the rank of the effect space. Various dimension-reduced effect spaces constitute the sampling pool to estimate the robustness of the subsequent decomposition.

Either PCA or ICA can be applied to the effect space to explore the intrinsic structures associated with the proposed contrasts. In PCA, revealed latent variables sequentially account for the total variances in the effect space  $E$ , subject to the orthonormality constraint. In ICA, however, the mutual information among spatial patterns of different effects and comparisons is minimized among rows of  $E$ . Latent variables are generated by either PCA or ICA decomposition. Each design LV represents the loadings of the proposed contrasts, and each brain LV summarizes the spatial loading of different voxels in the associated LV, which imply the characteristic brain activity patterns. For both PCA and ICA, the loading at different time-points/conditions can be obtained by calculating the design score ( $S_{design}$ ), which is defined as the product of the contrast matrix and the design LV:

$$S_{design} = C \times U \quad (5.10)$$

Design scores indicate the physiological implications of the latent variables since the temporal loadings can be covaried with either the experiment paradigm or the temporal confounds. The loading of all voxels for each revealed latent variable can be represented by the brain score ( $S_{brain}$ ), which is defined as the product of the data matrix and the brain LV:

$$S_{brain} = D \times V \quad (5.11)$$

Each column of the brain score constitutes the loading of single brain LV's at different time points/conditions.

The name "generalized Partial Least Squares" (gPLS) is derived from the process to decompose the effect space, which is the temporal covariance between the contrast designs and the observed data. In total decomposition, people deal with the complete covariance matrix of data, and thus it is computationally expensive. The effect space is a subset of the complete covariance matrix, correlating all spatiotemporal observations and null hypotheses encoded in the contrast matrix. gPLS deals with only a fraction of the complete covariance, enabling the fast computation of latent variables by reducing the dimension of the matrix to be decomposed. Note that the generalized Partial Least Squares and total decomposition are equivalent when the contrast matrix is identity.

## 5.3 METHODS

### 5.3.1 Quantifying results from PCA and ICA by Receiver Operating Curve Analysis

Using simulation data, quantitative comparison of PCA and ICA decomposition was performed by using Receiver Operating Curves (ROC) to access the detection-cost characteristics of these two decomposition approaches in the gPLS and TD framework. The ROC area index is defined as the area under each ROC. An ROC area around 0.5 represents an inferior separation of signal from noise by the testing procedure, while an area close to 1 implies a good differentiation. Figure 5-1 illustrates the ROCs and their underlying areas when various thresholds are set to distinguish two Gaussian distributions of identical unit variance and separated at different means ( $D$ ).

Given a single revealed brain latent variable and the activated voxel indices, an ROC area metric (the ROC index) can be obtained. To characterize all latent variables for detection, a "weighted ROC index" for brain latent variables is defined as the weighted sum of all ROC areas from all LVs. One possible choice of the weighting factor for the latent variable  $i$ ,  $W_i$ , is the latent variable specific "power fraction" equal to the fraction of the sum-of-squares of singular values.

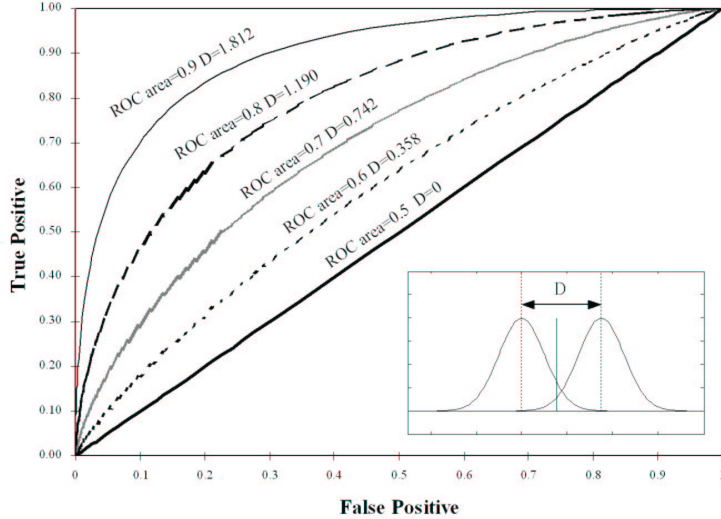


Figure 5-1: The ROCs and their area metrics from varying thresholds to distinguish two Gaussian distributions with unit variance and various mean differences. When the distance of the mean of two Gaussians is more than 1.8, the ROC area is higher than 0.9.

$$W_i = \frac{S_{ii}^2}{\sum_k S_{kk}^2} \quad (5.12)$$

These two ROC area metrics enable the assessment of detection power by either an individual latent variable or the ensemble of LVs. Ideally, a perfect detection without either Type-I or Type-II error makes both the ROC index and the weighted ROC index equal to 1.

The brain LV from either PCA or ICA can be regarded as a multi-dimensional vector. Due to the normalization in Eq. 5.2 and Eq. 5.6, each brain LV has unit power, and we propose an angle metric to quantify the (dis)similarity between two brain LVs by the multidimensional inner-product.

$$\theta(\vec{V}_1, \vec{V}_2) = \vec{V}_1^T \vec{V}_2 \quad (5.13)$$

### 5.3.2 Simulation

Using a blocked-design experiment, a data matrix of dimension 120 rows and 10,000 columns was created to simulate the spatiotemporal observations of 6 epochs, each of which had a baseline of 10 time points and a stimuli of 10 time points. Values of the time series of each voxel consist of foreground signal and background noise at different signal-to-noise ratio (SNR), which is defined as the power ratio of the artificially created signal patterns and the background noise realizations. Two categories of signal patterns of activations were created: orthogonal activation patterns and non-orthogonal activation patterns. In a task-control blocked-design experiment, orthogonal patterns arise from the perfect alignment of a voxel's activating response to the timing of the experiment stimuli. Additionally, multiple subjects and/or multiple conditions in the experiments also create temporally, and individually, orthogonal time series when there is no interaction among conditions and subjects. Note that non-orthogonal activation delay (NOAD) can be present in the realistic fMRI data due to the hemodynamic delay of the onset of brain response to the stimuli. We varied NOAD between 0 to 3 TR in fMRI acquisition to simulate the delays of the activity relative to the orthogonal activation due to experimental paradigms. In the conventional TR=2 seconds setting, this is equivalent to accommodating 0.6 seconds hemodynamic response delay. The background noise for each voxel ( $i$ ) was assumed to follow three probability distribution functions (PDF): Gaussian distribution, super-Gaussian distribution, and sub-Gaussian distribution. The Gaussian background noise was created by the normal distribution with zero mean and  $\sigma_i^2$  variance, denoted by  $N(0, \sigma_i^2)$ , where the variance follows another normal distribution  $\sigma_i^2 \approx N(5, 1)$ . A super-Gaussian noise model was implemented using an exponential distribution with zero mean, which was equivalent to a kurtosis of 6. We also adjusted the variance of each voxel's time series to follow another exponential distribution, with the mean equal to 5 and the variance equal to 1. A sub-Gaussian noise model was created by uniform distribution between -0.5 and 0.5, with the variance of each voxel's time series following another uniform distribution between 3 and 7.

The duration of activation for each activated pattern may affect the signal detection. Thus, we varied the temporal sampling rate (TSR), which is defined as the number of scans in a fMRI experiment within each epoch/condition, to test the difference in the detection power. TSR changed from 5, 10, and 20, in the six-block simulations with corresponding changes of the number of rows in the data matrix. We performed iterative analyses by parametric variations over TSR, SNR, orthogonal and non-orthogonal patterns, noise models, as well as decomposition schemes by PCA or ICA. Each combination of simulation parameters was repeated for 30 iterations to evaluate the averaged performance. This also generated the error estimates for each set of the simulation parameters. For each gPLS simulation, a contrast matrix used the Helmert basis Eq. 5.9 to encode the orthogonal contrasts. Total decomposition of the data matrix by either PCA or ICA at the same parameter settings was also simulated to contrast the detection power of gPLS.

We compared the outcome of applying PCA versus ICA decompositions to a simulated event-related fMRI data set. The data were created by the same methods as outlined in [18]. Briefly, baseline fMRI time series data were extracted from actual EPI MRI. First, we generated the baseline activity of the simulated datasets by using a first-order autoregressive plus white-noise model derived empirically by [19]. Then, for defined epoch in the time series for five “subjects”, a 2% signal change was added to three voxel clusters ( $3 \times 3 \times 2$  voxels/cluster). This signal change was represented by a modeled hemodynamic response function [20]. Three tasks were modeled for each subject, one without any change in activation (baseline) and two tasks showing unique activation patterns.

These data were analyzed using the spatiotemporal variation of PLS [21]. Here the voxel time-series are expressed in the same dimension so that the resulting data matrix has space and time extending along the rows of the matrix and observations/subjects along the column dimension. This enables the same decompositon method to be used on the data matrix as for PLS on block-design fMRI, but idenifies both the timing and location of task-related differences. The first latent variables from both ICA and PCA decompositions are rendered to illustrate the most significant activation.

Independent component analysis was implemented by the FastICA algorithm [17]. We used the Matlab R11 (Waltham, MA) built-in function to calculate PCA. The Intel Pentium-III 450 MHz PC (Santa Clara, CA) was used as the hardware platform for the simulation and the data analysis.

### 5.3.3 fMRI experiments of voluntary finger movement

A Right-handed subject executed a button press using the left hand in response to a visual stimulus appearing at three different frequencies: 0.3 Hz, 1 Hz, and 3 Hz during the task conditions using a block design, which consisted of 6 task time points (TR) and 6 baseline time points per epoch in the 10 epochs. In baseline, a cross hair was shown at the center for visual fixation. Multislice echoplanar image (EPI) acquisition was used (1.5 Tesla scanner, SIEMENS, Erlangen Germany) (43 msec TE, 4.2 sec TR, 64x64 matrix, 230mm FOV, 46 axial slices, 3.6mm cubic voxels, 128 time points per run). The time series were processed using MEDx (Sensor Systems, Sterling, VA). To correct for within-run interscan head motion, each EPI volume was registered to the mean of its time series using a linear 6-parameter rigid-body transformation model employing a least-squares cost function. Image volumes were resampled using scanline chirp-z interpolation. Global intensity variations were corrected by global image intensity rescaling, performed by computing the ratio that relates the mean image intensity in a particular volume to an arbitrary value of 1000. Low-frequency temporal signal fluctuations were removed by the application of a high-pass filter with a cutoff of twice the period length. Next, a 3D Gaussian filter (FWHM 6 mm in all dimensions) was applied to each volume in the time series for spatial smoothing. Images were then spatially normalized with a 3D warp to an EPI template in Talairach space. The full time series of the subject's tapping at the rate of 1 Hz was used to demonstrate the capability of gPLS to identify task-related spatiotemporal structures. To illustrate the power of multiple comparisons using gPLS, the data of the same subject tapping the left hand at 3 different frequencies were analyzed to highlight the frequency-dependent activities. All baseline time points and all task time points in each tapping frequency were averaged to generate a single fixation mean and a task

mean, respectively, in order to reduce the dimension of the data, and to minimize the variability of different epochs.

Two gPLS analyses were separately computed to differentiate the task-control contrast and finger flexion rate-dependent effects. The first gPLS made use of a contrast matrix including a paradigm coherent vector representing the "on" time points, when the subject tapped his fingers at the rate cued by the visual stimuli, and the "off" time points, when the subject maintained visual fixation only. Additionally, we manipulated the degree of freedom of the contrast matrix by segregating different epochs of the experiment paradigm into 2 to 6 groups to differentiate the epoch-related effects. The second gPLS detected additional finger flexion rate-dependent effects by using Helmert basis to construct a contrast matrix for comparing three finger tapping frequencies. Also, we choose 8 randomized groups inside the contrast matrix to test the robustness of the revealed eigen-structures. Both gPLS analyses utilized PCA and ICA separately, using 100 iterations to generate error estimates.

## 5.4 RESULTS

### 5.4.1 Simulation studies

#### Signal-to-noise ratio

Fig. 5-2 shows the weighted ROC indices for Gaussian background noise with 5 orthogonal activations in gPLS. Generally, as the SNR increases, the weighted ROC area from all latent variables using either PCA or ICA increases monotonically. Given the same SNR, PCA decomposition always gives better detection than ICA in the simulation. Note the high variability of the ICA results at low SNR ( $\leq 0.1$ ).

When the SNR is equal to one, which corresponds to the same level of paradigm-coherent activation signal and background noise, PCA has a weighted ROC area more than 0.82, while the weighted ROC area of ICA is only 0.73. The discrepancy between PCA and ICA prevails across various SNRs. When the SNR is higher than 10, PCA always has weighted ROC areas of more than 0.95, and ICA has values of around

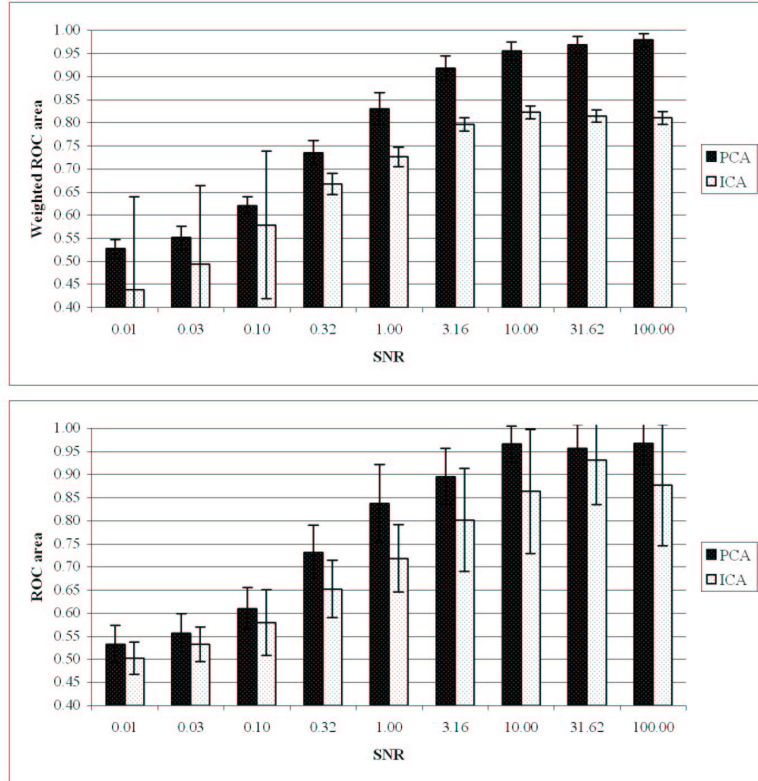


Figure 5-2: (Top panel) The weighted ROC area by PCA and ICA using gPLS from Gaussian background noise at various SNRs. (Bottom panel) The ROC area from the most correlated latent variable by PCA and ICA using gPLS from Gaussian background noise at various SNRs. Five orthogonal activation patterns with 6 epochs and 10 samples in each epoch were simulated here.

0.81. The plateau of ICA detection is about 0.8 when the SNR is greater than 3.16, while PCA stabilizes the detection power around 0.95 as the SNR is higher than 10.

### Most correlated latent variable

The bottom panel of Figure 5-2 also reports the ROC area detection metric of the "most correlated" latent variable, whose design score has the highest absolute value of correlation coefficient between the experimental paradigm and the revealed design score. The observation that higher SNRs correspond to higher ROC areas is still valid in the most correlated LV metrics for either PCA or ICA in the gPLS framework. When the SNR is higher than 10, the averaged ROC area by PCA is over 0.95, while ICA has variable ROC areas between 0.93 and 0.86. Low SNR decreases the

distinction between PCA and ICA decomposition. As the error bars show, there is no significant difference in the ROC area metric from PCA and ICA when the SNR is lower than 0.1. The similar detection power of the single most correlated LV to that of weighted ROC areas from all LVs at different SNR demonstrates that a single LV with the most correlated design score and experimental paradigm is capable of detecting underlying spatiotemporal patterns of activation.

### Total Decomposition versus Generalized Partial Least Squares

Figure 5-3 shows the comparison of the detection using gPLS and TD using Gaussian background noise and 5 synthetic orthogonal signals. The detection by the weighted ROC area in TD is lower than that in gPLS at SNRs ranging from 0.1 to 100. The gPLS approach performs better than TD when using either PCA and ICA decompositions. Presumably this advantage comes from the selective averaging step. When the SNR equals one, TD using PCA has a maximally weighted ROC area of 0.58, while TD using ICA is 0.54. gPLS at the same SNR (SNR = 1) has the weighted ROC area of 0.82 and 0.73 by PCA and ICA, respectively. This comparison quantitatively shows the advantage of gPLS over TD for higher signal detection. For the ROC area of the most correlated LV (bottom panel of Figure 5-3), PCA is of similar detection (ROC area over 0.95) using either gPLS or TD at high SNR ( $\geq 10$ ). ICA in gPLS demonstrates higher detection than in TD by a larger ROC area at high SNR. When SNR is lower than 0.03, gPLS or TD provides almost the same insufficient detection, no matter whether PCA or ICA is utilized. In general, the variability of the reported ROC metrics from the most correlated LV is smaller in PCA than ICA when SNR is higher than 1.

### Background noise

In addition to the Gaussian distribution, super-Gaussian and sub-Gaussian probability distribution functions were used to simulate background noises, as shown in Figure 5-4. With super-Gaussian background noise and using the most correlated latent variable metric, TD is slightly better than gPLS at high SNR regions (SNR  $\geq 10$ ).

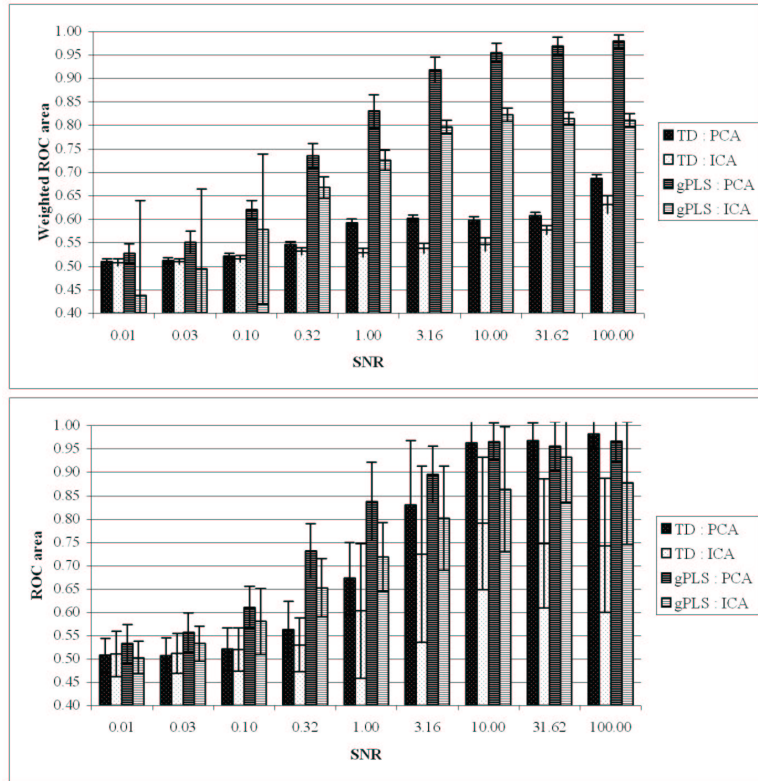


Figure 5-3: The weighted ROC area (upper panel) and the most correlated LV (lower panel) by PCA and ICA using gPLS and TD with Gaussian background noise at various SNR. Five orthogonal activation patterns with 6 epochs and 10 samples in each epoch were simulated here.

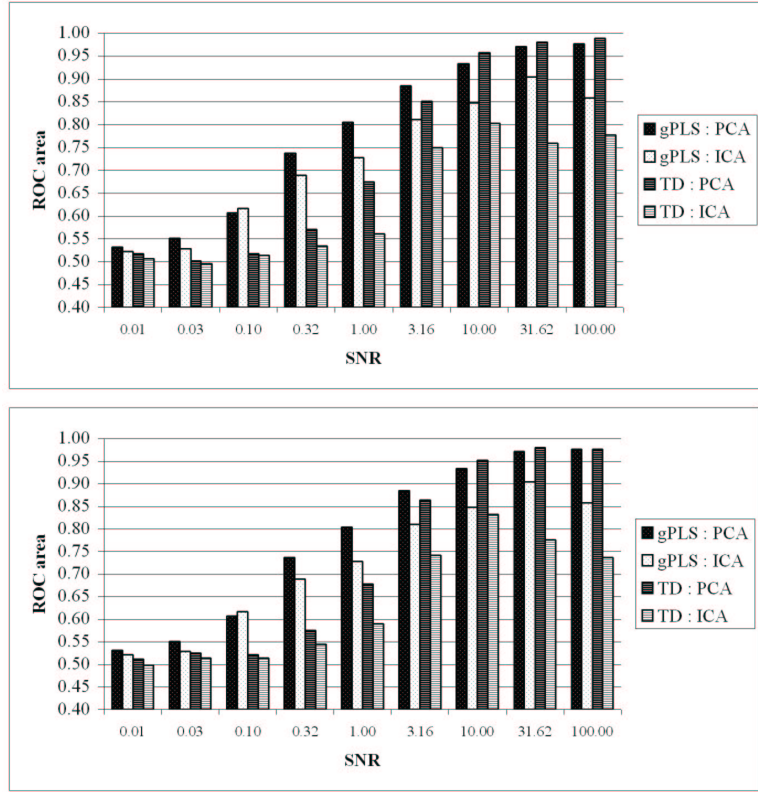


Figure 5-4: The most correlated LV by PCA and ICA using gPLS and TD on super-Gaussian (Top panel) and sub-Gaussian (bottom panel) background noise at various SNR. Five orthogonal activation patterns with 6 epochs and 10 samples in each epoch were simulated here.

10) when PCA is employed. In the lower SNR ( $\text{SNR} \leq 3$ ) contexts, gPLS is superior to TD using PCA. When ICA is adopted as the decomposition tool, gPLS always outperforms TD at all SNRs. The sub-Gaussian background noise study (bottom panel of Fig. 5-4) shows the higher detection using gPLS over TD and PCA over ICA when the SNR is lower than 1. With the sub-Gaussian background noise, the weighted ROC area metrics at SNR larger than 1 are slightly higher than the most correlated LV ROC index (not shown). This suggests that when the background noise follows a sub-Gaussian distribution, such as uniform distribution, the ensemble of multiple latent variables has higher detection power than the single most correlated LV.

## Effect of multiple contrasts and hemodynamic delays

The gPLS structure can be used for either multiple hypotheses/activations comparison/detection as well as a single contrast identification, as illustrated in Figures 5-5. In this Gaussian background test bed, when there is only one paradigm-related activation signal, detection using only the most paradigm correlated latent variable is quite efficient ( $\approx 0.99$ ) when the SNR is greater than 1. PCA outperforms ICA when the SNR is less than 1, except that ICA detects slightly better when SNR equals 0.3, and the delayed activations exist (NOAD = 3 TR). Simulation results show that when the number of contrasts is low, a single latent variable is adequate to examine the spatiotemporal structures associated with the posed null hypothesis encoded in the contrast matrix. Multiple contrasts detection by gPLS (bottom panel of Figure 5-5) is illustrated using 5 orthogonal activations and 0 to 3 TR delayed signals in the data (to model hemodynamic delays) at various SNRs. PCA has better detection than ICA for all SNR and time delays.

The hemodynamic responses in the realistic fMRI might contain voxels with different delays. Thus, we parametrically simulated the delayed activations between 0 and 3 time points, which are 0 to 3 TR delays in fMRI acquisition for the epoch length of 10 TR. If the data contain only a single paradigm-coherent component, such delays decrease the detection by PCA in low SNR contexts, but it enhances ICA detection at two simulation SNRs (SNR = 0.1 and SNR = 0.32). However, PCA provides higher detection power than ICA with or without hemodynamic delays in all conditions. In data containing multiple hypothesis-related signals, the delays hinder the PCA detection in low SNR regions (SNR  $< 1$ ), but they do not change significantly when SNR is greater than 10. ICA degrades the detection significantly when there are multiple delayed activations in higher SNR contexts (SNR  $> 3$ ). It is worth noticing that ICA has lower detection when delays exist in the multiple contrasts data. With sufficient SNR, gPLS using PCA is insensitive to the hemodynamic delays in the data, providing a higher detection power compared to ICA decomposition.

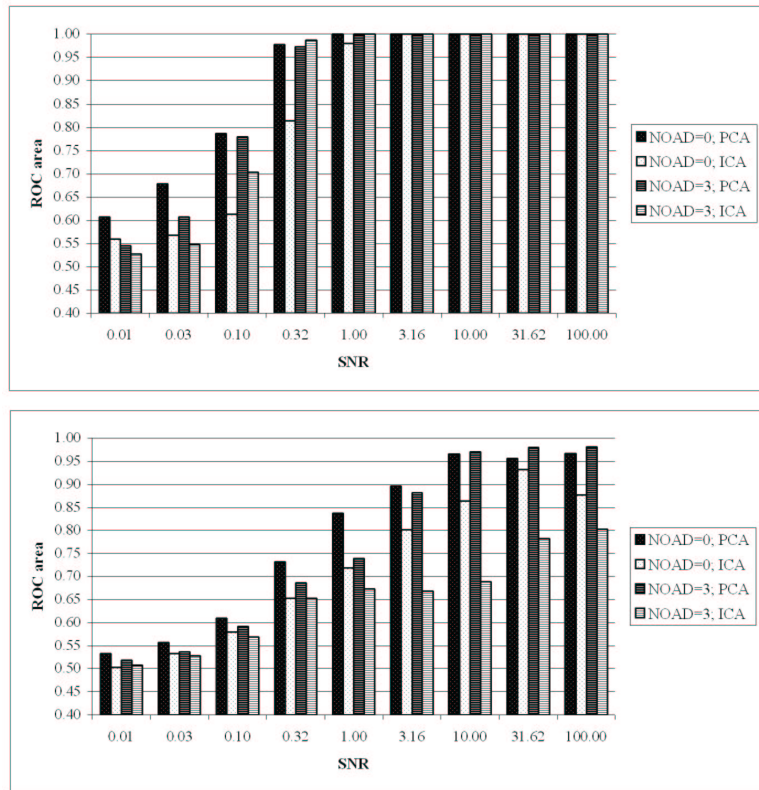


Figure 5-5: The most correlated LV by PCA and ICA using gPLS on Gaussian background noise at various SNRs. Single (top panel) or five (bottom panel) orthogonal activation patterns with 6 epochs and 10 samples in each epoch were simulated. Delays between the experimental paradigm and the onset of the voxel activity varied between 0 to 3 time points (NOAD=0 and NOAD=3).

## Temporal sampling rate

Various temporal sampling rates (TSR) were simulated for 5, 10, and 20 scans for each epoch in a blocked-design experiment. Results suggest that a higher TSR always has a higher ROC area metric in PCA decomposition at different SNRs, as shown in Figure 5-6. ICA has a similar tendency to have higher detection power as the TSR increases. When the SNR is higher than 3, more temporal samplings produce relatively fewer ROC increments. Increasing the TSR is only advantageous for gPLS, not for TD. The increased sampling does not enrich the content of data, and both PCA and ICA suffer from the increased degrees of freedom in the decomposition, as shown in the bottom panel of Fig. 5-6.

## Event-related fMRI simulation

Figure 5-7 shows the most significant 25% of the first brain latent variables in an event-related fMRI experiment when PCA and ICA were used to decompose the PLS effect space. Qualitatively, there was no appreciable difference in the results using PCA vs. ICA decomposition. Both show similar within-voxel activation duration and the location of the activation loci. This latent variable differentiated the two conditions with the added activations from each other, and the "baseline" condition.

### 5.4.2 fMRI motor system study

#### Movement contrast detection

We found from the singular values that the first LV using PCA and ICA accounts for 90% and 81%, respectively, of the total effect space variance. The variation of the singular value from ICA (8.5%) is higher, compared to the variation from PCA (0.5%) in the 100 iterative analyses.

Figure 5-8 shows the design scores of the most dominant (the 1st) latent variable in gPLS using PCA and ICA. The corresponding LVs are well correlated to the on-off experiment paradigm. Either PCA or ICA decomposition can robustly detect the contrast between the baseline and task conditions in the gPLS framework. Multiple

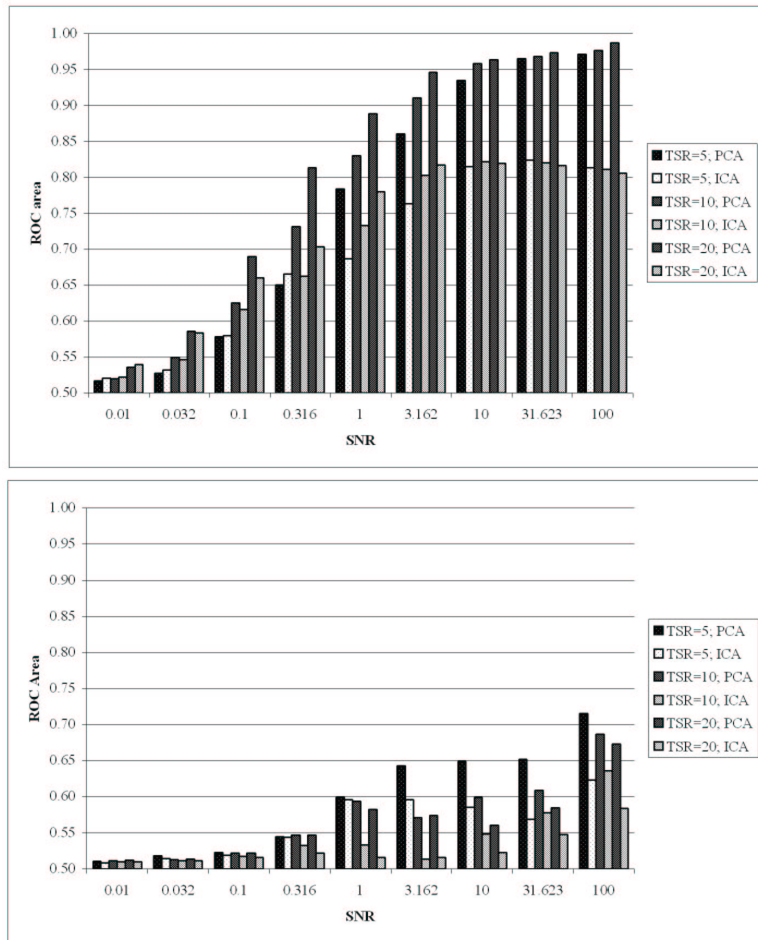


Figure 5-6: The total weighted ROC area in gPLS (top panel) and TD (bottom panel) using PCA and ICA for various temporal sampling rates (TSRs) at different SNR in the Gaussian background with 5 orthogonal activations.

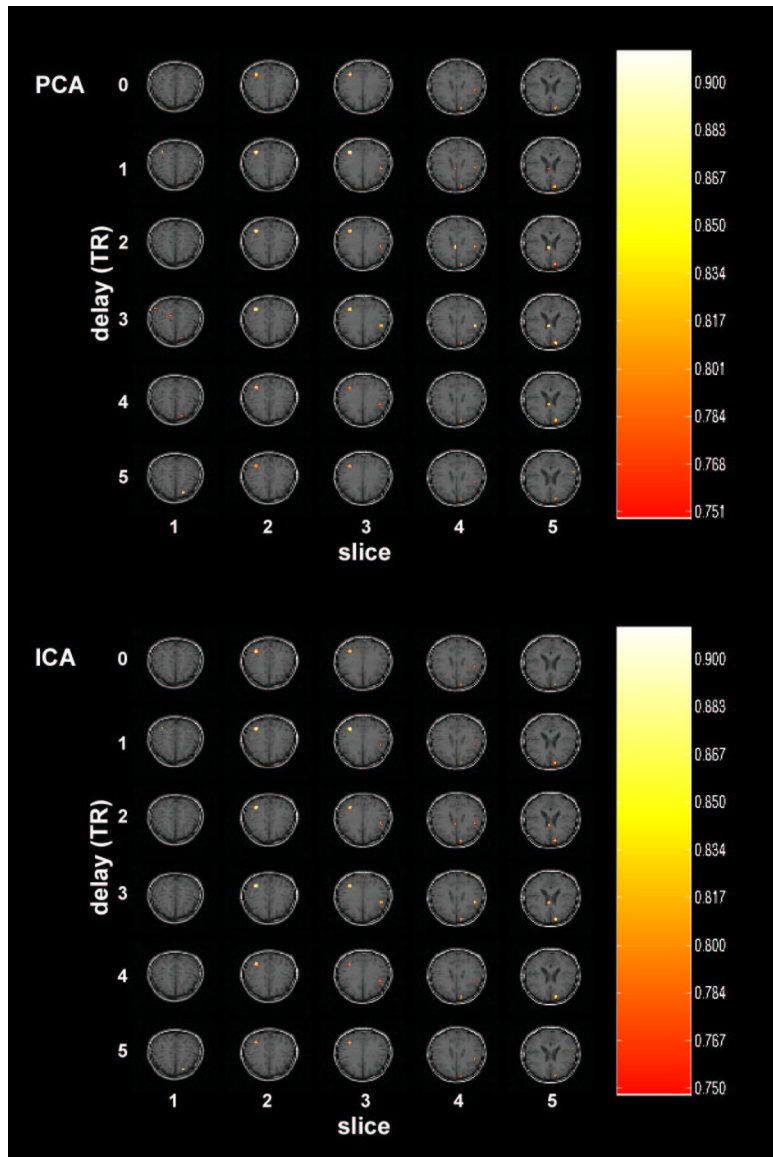


Figure 5-7: The first brain LV of PCA (top panel) and ICA (bottom panel) decomposition from an event-related fMRI simulation data.

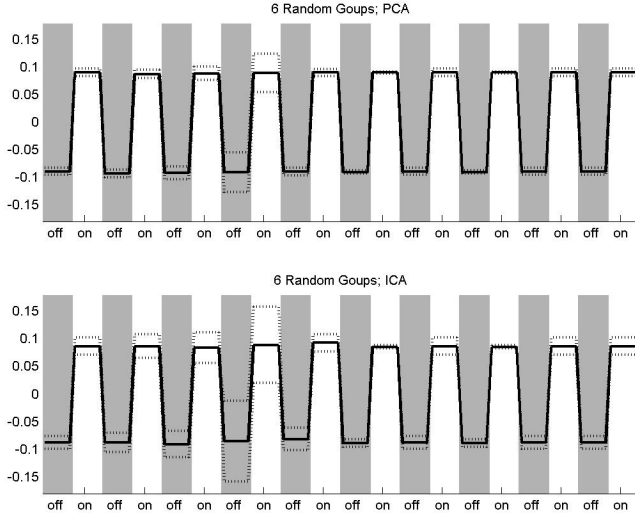


Figure 5-8: The design scores of 6 random groupings on different epochs of the left-hand tapping data. They reveal the task-related components as well as transient variation in these task-related components. Epoch 4 shows instability in identifying consistently task-related components.

(100) iterations were used to investigate the variability of the design scores in different epochs. Comparing PCA and ICA, the design scores show that gPLS is able to detect the consistently task-related structures inside the data matrix, as well as the transient responses. The 4th epoch of gPLS by both PCA and ICA using 6 randomized groups demonstrated higher variability, representing lower confidence during task-related component identification.

The spatial patterns of the first latent variable are shown in Figure 5-9. For comparison, T-test uncorrected p-values are also shown to contrast the detection by univariate and multivariate approaches. Thresholds are set to 3.5 for base 10 logarithm p-values for T-test, and 40% of latent variable maximum for gPLS. These values are chosen for optimal visual comparison between approaches. The cerebellum, visual cortex, primary motor area, cingulate gyrus, and the medial superior parietal lobule are shown activated in PCA and ICA decomposition using six random groups and the experiment paradigm to constitute the contrast matrix. A large amount of similarity and overlapping between PCA and ICA decompositions is observed. The differences

		PCA					ICA				
		2 groups	3 groups	4 groups	5 groups	6 groups	2 groups	3 groups	4 groups	5 groups	6 groups
<b>PCA</b>	2 groups	0.9992	0.9987	0.9982	0.9976	0.9973	0.8673	0.7589	0.7160	0.6749	0.6547
	3 groups		0.9984	0.9981	0.9978	0.9976	0.8678	0.7600	0.7168	0.6761	0.6557
	4 groups			0.9980	0.9979	0.9977	0.8675	0.7600	0.7163	0.6761	0.6547
	5 groups				0.9980	0.9979	0.8675	0.7605	0.7166	0.6768	0.6553
	6 groups					0.9979	0.8674	0.7602	0.7159	0.6756	0.6535
<b>ICA</b>	2 groups						0.7736	0.6812	0.6482	0.6103	0.5984
	3 groups							0.6085	0.5826	0.5568	0.5493
	4 groups								0.5663	0.5413	0.5390
	5 groups									0.5404	0.5467
	6 groups										0.5774

Table 5.1: The inner product of the first latent variable revealed by PCA and ICA at various numbers of randomized grouping. PCA shows consistent similarity at different randomized group numbers. ICA decomposition varies more greatly than PCA with a significant difference between 2-group and 6-group random grouping. Between PCA and ICA, the similarity is low and becomes lower when the number of random grouping increases.

between the T-test statistical map and gPLS brain LVs are most significant in spatial extension and distribution of estimated active areas in cerebellum, internal capsule and superior parietal lobule.

Different random groupings reveal similar significant latent variables in gPLS. Table 5-1 lists the angles between the most dominant brain LVs as multi-dimensional vectors. The inner product of two high-dimensional brain LVs quantifies the alignment and the similarity between them. PCA random grouping is more robust than ICA for the first LV because of the high inner product ( $\geq 0.999$ ). Brain LVs from ICA vary at different numbers of randomized grouping with a maximal similarity of inner product of 0.77, which is analogous to 39 degrees in two-dimensional space. In contrast, 0.992 inner-product is equivalent to 2.9 degrees in two-dimensional space.

Using total decomposition, PCA and ICA generate complex time courses for dif-

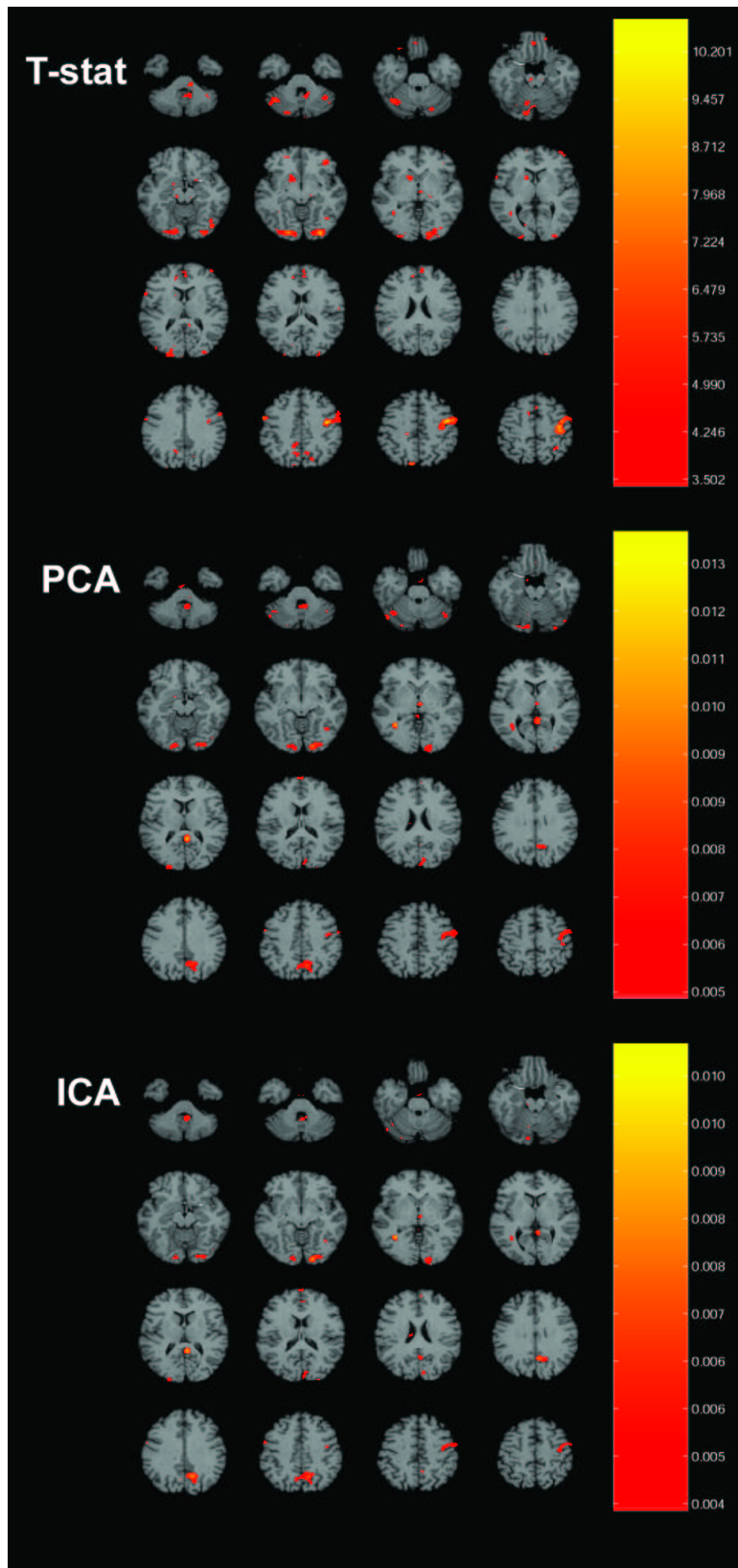


Figure 5-9: *T*-test brain activity statistical maps and brain latent variables from gPLS using PCA and ICA decomposition of the effect space with 6 random groups in the contrast matrix. In these maps, the right hemisphere is on the right.<sup>57</sup>

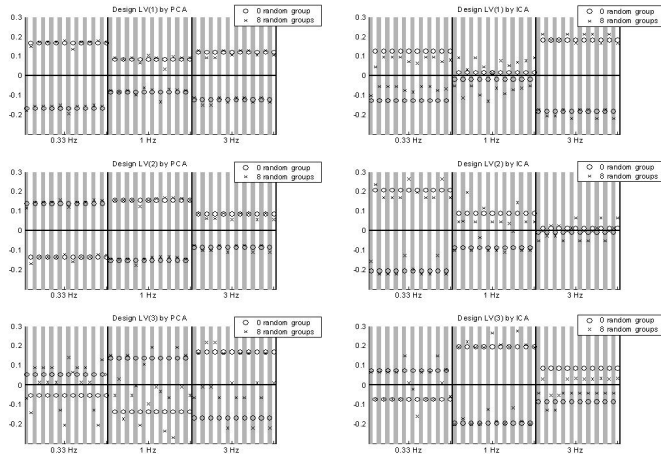


Figure 5-10: Design scores of the first 3 latent variables in gPLS using PCA and ICA for multiple comparisons including three different tapping frequencies and task-control contrast. The first 3 LVs account for the majority of the total variance in the effect space. And they represent the task-control contrast and tapping frequency-dependent brain maps.

ferent latent variables. The maximum of the correlation coefficient between the design score and the experiment paradigm is 0.5204 for PCA and 0.3441 for ICA. The associated spatial patterns are complicated by ventricle false alarms, distributed local activities, and motion artifacts (not shown), and therefore further processing, e.g. Canonical Variance Analysis [22], is necessary to make use of these eigen-structures.

#### 5.4.3 Multiple comparisons between finger tapping rates

The design score plots (Fig. 5-10) for the multiple comparisons of different tapping frequencies illustrate identification of both task-control contrast and tapping frequency contrast. The distance between the individual mark and zero is proportional to the contribution of that observation to the contrast revealed by the latent variable. Note that a design score may represent an interaction effects. For example, a design score with "on-off" contrast ("on" positive and "off" negative) and "off-on" contrast ("off" positive and "on" negative) at different frequencies, characterizes the differential "on-off" contrasts due to distinct motor frequencies.

To contrast the "on-off", the first LV revealed by both PCA and ICA using either no random groups or 8 random groups identifies the contrast between task and control states across three tapping frequencies. The 2nd LV of PCA decomposition represents the interaction of the generalized high tapping rate versus low tapping rate contrast (weighted average of 3 Hz and 1 Hz versus 0.3 Hz) and the task-control contrast. Similar results from ICA decompositions are also present but appeared in the 3rd LV. Interestingly, the 2nd LV from ICA also represents a contrast between task and control, which is consistent with the inference from the 1st LV. Note that the tapping frequency contrast is the interaction/modulation of task-control differences over blocks of different tapping frequencies.

The first three LVs explain all variances in the effect space when no random group is applied. And they account for 76.5% and 58.3% of total variance in 8 random grouping gPLS using PCA and ICA, respectively. Random grouping detects the transient responses and variations of different epochs in three tapping frequencies, as shown in Figure 5-11.

Examining spatial patterns of the brain LVs excludes ventricle activations in the 3rd LV in PCA and 2nd LV in ICA (not shown). The first LVs using PCA and ICA demonstrate the areas that are more active during task than control conditions regardless of finger tapping rates. These include the visual cortex, cerebellum hemispheres, and contralateral primary motor cortex. The contrast between the higher tapping rate and the lower rates revealed by the 2nd LV in PCA and the 3rd LV in ICA in gPLS suggests that the cerebellum hemisphere, visual cortex and medial superior parietal lobule are more activated at high-frequency finger tapping. Since areas indicated by LVs with PCA and ICA are visually similar, only PCA results are illustrated.

## 5.5 DISCUSSION

Univariate approaches, such as correlation coefficient analysis and statistical parametric mapping [5, 22, 7, 23], are model-driven. Reference functions are provided to

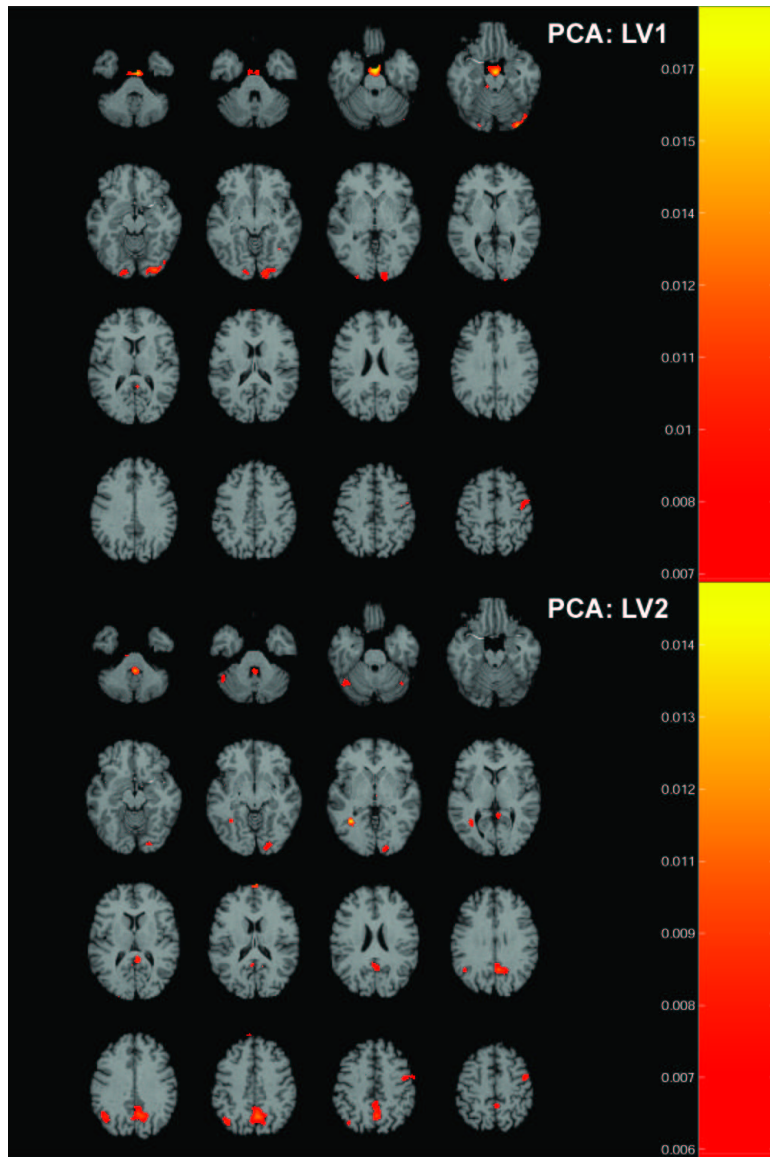


Figure 5-11: The first brain latent variable from PCA decomposition of the effect space, representing the areas that are more active during task than control conditions across all three tapping frequencies. The second brain latent variable from PCA (similar to the 3rd LV from ICA) highlights the areas that are more active during high frequency tapping (weighted average of 3 Hz and 1Hz) than low frequency tapping (0.1 Hz).

build models for the observed neuroimaging data. Since multiple null-hypotheses have been explicitly constructed inside the model, identification of components related to the questions of interest is straightforward. However, the segregation of image voxels during estimation is problematic because these methods ignore possible anatomically interconnected neurons and associated activation. It is also possible that voxels might correlate quite well to the reference function, but they are not significantly correlated with each other.

We have presented the theory and algorithms to use multivariate data analysis technique to explore brain mapping based on functional MRI data. Compared to univariate approaches, multivariate techniques facilitate the identification of interaction among neuronal populations in the data analysis. No additional clustering or corrected statistics for the estimated active regions are necessary. The multivariate approach has been verified and adopted for functional connectivity analysis to investigate temporal interactions among distributed regions in the brain during cognitive tasks, such as the orchestration of human memory and learning systems. A comparison study of the memory system even supports the assertion that more information is revealed by multivariate analysis than by univariate processing streams [22].

The conventional multivariate technique is a data-driven model subjected to different mathematical constraints. The data-driven characteristics make the identification of components of interest in the revealed structures difficult. This is especially discussed in Independent Component Analysis (ICA) [32, 13] because of the high variability of the correlation coefficient between the provided reference function and the temporal independent component, which is equivalent to the design score in the generalized Partial Least Squares (gPLS) formulation. The proposed gPLS framework moderates the difficulty of identifying task-related components by selective averaging to increase the SNR in the data. gPLS is an extension of Partial Least Squares in the sense of identical utilization of the contrast matrix. The rank-reduced effect space in gPLS has advantages of both increased SNR as well as decreased computation time. The higher power of detection in low SNR data derives from the construction of an effect space by explicit incorporation of columns of the contrast matrix as averaging

factors. The subsequent PCA/ICA decomposition allows the data itself to reorganize into separate components under distinct mathematical constraints, which are either orthogonality constraint in PCA or statistical independence in ICA. In gPLS, the size of effect space is dramatically smaller than the original data matrix. Dimension reduction in gPLS facilitates efficient calculation for latent variables. Without gPLS, the size of the matrix is huge for a multiple-subject multiple-task full time series analysis. In our simulation, even with the improved fast algorithm [17], ICA is much slower than PCA in the same computational environment. The difference in computational loading between PCA and ICA is many-fold (PCA is about 10 to 30 seconds depending on the size of the matrix; ICA takes more than 2 to 15 minutes for the data of the same size). Thus, generalized Partial Least Squares has the combined advantages of being model-driven from univariate statistical procedures by the essence of contrast matrix correlation, and data-driven characteristics via PCA/ICA decomposition to explore the interactions inside these data in an integrated way.

Another feature of gPLS is efficient multiple comparisons, which have been reported in studies of the memory system [24] and interactions of sensory systems [31, 24, 25]. In our simulations and realistic fMRI data, we observe that gPLS is capable of detecting effects of different conditions. This is essentially accomplished by providing different "contrast basis functions" in the contrast matrix. Subsequent PCA/ICA application is then used to estimate the relative contributions of these contrast bases. Without gPLS, multiple subjects and multiple conditions comparison is difficult, because of the large data size and unconstrained decomposition. gPLS is thus a convenient tool for experiments with parametric designs and those reporting multiple-subjects commonality.

Yet another advantage of gPLS is the simplified identification of latent variables. Since the data are constructed within hypotheses of interest, the revealed design latent variable explicitly gives the weighting factors of different hypotheses under the test. The associated design scores immediately show the temporal representation of the corresponding structure. A simple correlation coefficient can be applied to categorize latent variables as either task-related or task-independent as shown in our simulation

studies. The associated singular values quantify the significance of latent variables in terms of variance partitioning. Conventional Total Decomposition interpretation of the revealed latent variables suffers because the correlation coefficient between the reference function and LV associated temporal components is highly variable and small. A final complication of using total decomposition comes from the need to do another canonical variate analysis following the first multivariate decomposition.

In a full-rank effect space, the number of latent variables (or principal components in PCA and independent components in ICA) is determined by the minimum of the dimension of the effect space. This fixed-dimension property poses another constraint in addition to the mathematical requirements of the decomposition algorithm. The fixed number of decomposed components may consume the degrees of freedom by partitioning total variance in the data into either hypothesis-related components or confounds. Thus, the separation of confounds from pertinent contrasts is essential in analysis of functional imaging data, regardless of using either total decomposition or generalized Partial Least Squares. However, this problem can be partially alleviated by varying the number of groups, which collapses the non-paradigm related data components together. For example, we dealt with the single subject blocked-design fMRI experiment by randomly partitioning different epochs in the data into various numbers of groups. The flexible manipulation of randomized grouping in the construction of the contrast matrix enables the identification of not only constantly task-related responses, but also transiently varying responses, as shown in Figure 5-7 and Figure 5-9. This randomization releases the constraint on the fixed number of components by either PCA or ICA. Various numbers of random groups enable another statistical inference about the robustness of the detected neural activity structures. This randomization can be combined with the bootstrap and permutation tests in the Partial Least Squares approach to provide further confidence in the estimation of the revealed neuronal interaction.

Between PCA and ICA, it has been claimed that ICA is superior for task-related components, especially transient responses, and noise detection [32, 13]. And it is claimed that ICA identifies components following a super-Gaussian distribution more

efficiently than PCA. Recently, it has been reported that the BOLD fMRI follows a super-Gaussian distribution [26], which suggests an advantage of ICA over PCA. But in the gPLS framework, the selective averaging implemented by the contrast matrix over the raw data compromises such claims; because the Central Limit Theorem suggests that the mixture of independently identically distributed components appears to be Gaussian. Although the number of averaged samples might not be large enough to be Gaussian for all cases, and the observations of fMRI time series are not temporally independent, gPLS still generates a sufficient amount of averaging to increase detection power. This contributes to the better performance of PCA over ICA in our generalized Partial Least Squares framework. Such a statement is valid for blocked-design experiments and has been verified in our simulations of both blocked-design and event-related fMRI. From our fMRI data, it is evident that PCA is more robust for the estimation. The revealed most-significant latent variables at different numbers of random grouping are very similar (inner-product  $\geq 0.99$ ). Our simulation also shows a smaller standard deviation in PCA compared to ICA. ICA is sensitive to the number of components to be decomposed, which is equal to the minimum of the number of rows and columns of the matrix. The observed high variability between the most significant LVs at different numbers of random grouping decreases the confidence of estimated spatial patterns derived by ICA.

Realistic hemodynamic responses of voxels have various waveforms including different delays and shapes, as identified by previous studies [27, 28]. Versatile waveforms deviating from the box-car reference paradigm in blocked-design fMRI experiments have been modeled at different SNR in generalized Partial Least Squares. Different onset delays have also been simulated by assuming different numbers of non-orthogonal activation delays (NOADs). We simulated that delays may be up to 3 TR in our test bed of 10 TR, which is equivalent to 30% temporal incoherence. The results suggest that in most SNR contexts, a single LV from PCA has better detection power than one from ICA in the gPLS framework. In addition, the most correlated LV might be quite sufficient to detect task-related components, which include transient variations if random grouping is employed. Multiple-subjects multiple-conditions comparison

favors PCA over ICA.

The general conclusion that in the PLS framework, PCA and ICA are comparable to reveal the significant latent variables is also validated in our event-related fMRI simulations. This is entirely consistent with our findings in the block design simulation for the similarity of PCA and ICA detection power in the PLS framework. We suspect that part of the reason for the agreement comes from the constraint of the solution space to those spanned by task differences, rather than all dimensions in the data.

To evaluate the power of hypothesis testing under the Neyman-Pearson framework [29], we used receive operation curves (ROC) to assess the trade-off between Type-1 and Type-2 error. ROC has been adopted for assessment of fMRI signal detection [30, 31]. The ROC area and weighted ROC area for all LVs in our simulations are neither unique nor globally optimal methods for assessing the power of detection. However, singular values are good metrics for quantifying the amount of variance explained in the model. And, ROC areas correspond conveniently to the trade-off between Type-1 and Type-2 errors. However, if people are more concerned about one hypothesis testing error than the other, other metrics should be employed.

Here, we used a linear decomposition approach to reveal the structures in the data. Nonlinear decomposition can also be used in the gPLS framework as well. PCA has been extended for identifying nonlinear interactions in brain systems. The same approach could be applied to the nonlinear identification of different functional areas when it is applied on the effect space in the future.

In summary, adoption of the multivariate analysis tool depends on the spatiotemporal structure of the data and the experimental questions. We show gPLS provides computational efficiency and flexibility for testing hypotheses at different levels. And gPLS can be used for either single or multiple hypotheses testing by two alternative decompositions: PCA and ICA. While PCA seems to out perform ICA in several of our scenarios, a conservative conclusion would suggest that neither can be favored when applied in the PLS framework.



# References

- [1] J. W. Belliveau, B. R. Rosen, H. L. Kantor, R. R. Rzedzian, D. N. Kennedy, R. C. McKinstry, J. M. Vevea, M. S. Cohen, I. L. Pykett, and T. J. Brady. Functional cerebral imaging by susceptibility-contrast nmr. *Magn Reson Med*, 14(3):538–46, 1990. 90286887 0740-3194 Journal Article.
- [2] S. Ogawa, T. M. Lee, A. R. Kay, and D. W. Tank. Brain magnetic resonance imaging with contrast dependent on blood oxygenation. *Proc Natl Acad Sci U S A*, 87(24):9868–72., 1990.
- [3] J. W. Belliveau, Jr. Kennedy, D. N., R. C. McKinstry, B. R. Buchbinder, R. M. Weisskoff, M. S. Cohen, J. M. Vevea, T. J. Brady, and B. R. Rosen. Functional mapping of the human visual cortex by magnetic resonance imaging. *Science*, 254(5032):716–9., 1991.
- [4] K. K. Kwong, J. W. Belliveau, D. A. Chesler, I. E. Goldberg, R. M. Weisskoff, B. P. Poncelet, D. N. Kennedy, B. E. Hoppel, M. S. Cohen, R. Turner, and et al. Dynamic magnetic resonance imaging of human brain activity during primary sensory stimulation. *Proc Natl Acad Sci U S A*, 89(12):5675–9., 1992.
- [5] P. A. Bandettini, A. Jesmanowicz, E. C. Wong, and J. S. Hyde. Processing strategies for time-course data sets in functional mri of the human brain. *Magn Reson Med*, 30(2):161–73., 1993.
- [6] K. J. Friston, A. P. Holmes, J. B. Poline, P. J. Grasby, S. C. Williams, R. S. Frackowiak, and R. Turner. Analysis of fmri time-series revisited. *Neuroimage*, 2(1):45–53., 1995.

- [7] K. J. Friston, C. D. Frith, R. Turner, and R. S. Frackowiak. Characterizing evoked hemodynamics with fmri. *Neuroimage*, 2(2):157–65., 1995.
- [8] K. J. Worsley and K. J. Friston. Analysis of fmri time-series revisited—again. *Neuroimage*, 2(3):173–81., 1995.
- [9] K. J. Friston, C. D. Frith, R. S. Frackowiak, and R. Turner. Characterizing dynamic brain responses with fmri: a multivariate approach. *Neuroimage*, 2(2):166–72., 1995.
- [10] E. T. Bullmore, S. Rabe-Hesketh, R. G. Morris, S. C. Williams, L. Gregory, J. A. Gray, and M. J. Brammer. Functional magnetic resonance image analysis of a large-scale neurocognitive network. *Neuroimage*, 4(1):16–33., 1996.
- [11] A. R. McIntosh, F. L. Bookstein, J. V. Haxby, and C. L. Grady. Spatial pattern analysis of functional brain images using partial least squares. *Neuroimage*, 3(3 Pt 1):143–57., 1996.
- [12] M. J. McKeown, T. P. Jung, S. Makeig, G. Brown, S. S. Kindermann, T. W. Lee, and T. J. Sejnowski. Spatially independent activity patterns in functional mri data during the stroop color-naming task. *Proc Natl Acad Sci U S A*, 95(3):803–10., 1998.
- [13] M. J. McKeown, S. Makeig, G. G. Brown, T. P. Jung, S. S. Kindermann, A. J. Bell, and T. J. Sejnowski. Analysis of fmri data by blind separation into independent spatial components. *Hum Brain Mapp*, 6(3):160–88, 1998. Using Smart Source Parsing.
- [14] K. J. Friston, C. D. Frith, and R. S. Frackowiak. Principal component analysis learning algorithms: a neurobiological analysis. *Proc R Soc Lond B Biol Sci*, 254(1339):47–54., 1993.
- [15] K. J. Friston, C. D. Frith, P. F. Liddle, and R. S. Frackowiak. Functional connectivity: the principal-component analysis of large (pet) data sets. *J Cereb Blood Flow Metab*, 13(1):5–14., 1993.

- [16] A. J. Bell and T. J. Sejnowski. An information-maximization approach to blind separation and blind deconvolution. *Neural Comput*, 7(6):1129–59., 1995.
- [17] A. Hyvarinen. Fast and robust fixed-point algorithms for independent component analysis. *IEEE Transactions on Neural Networks*, 10(3):626–634, 1999.
- [18] V. Della-Maggiore, W. Chau, P. R. Peres-Neto, and A. R. McIntosh. An empirical comparison of spm preprocessing parameters to the analysis of fmri data. *Neuroimage*, 17(1):19–28, 2002. 22369583 1053-8119 Journal Article.
- [19] P. L. Purdon and R. M. Weisskoff. Effect of temporal autocorrelation due to physiological noise and stimulus paradigm on voxel-level false-positive rates in fmri. *Hum Brain Mapp*, 6(4):239–49, 1998. 98369886 1065-9471 Journal Article.
- [20] M. S. Cohen. Parametric analysis of fmri data using linear systems methods. *Neuroimage*, 6(2):93–103, 1997. 97479544 1053-8119 Clinical Trial Journal Article.
- [21] N. J. Lobaugh, R. West, and A. R. McIntosh. Spatiotemporal analysis of experimental differences in event-related potential data with partial least squares. *Psychophysiology*, 38(3):517–30., 2001.
- [22] P. C. Fletcher, R. J. Dolan, T. Shallice, C. D. Frith, R. S. Frackowiak, and K. J. Friston. Is multivariate analysis of pet data more revealing than the univariate approach? evidence from a study of episodic memory retrieval. *Neuroimage*, 3(3 Pt 1):209–15., 1996.
- [23] A. R. McIntosh, N. J. Lobaugh, R. Cabeza, F. L. Bookstein, and S. Houle. Convergence of neural systems processing stimulus associations and coordinating motor responses. *Cereb Cortex*, 8(7):648–59., 1998.
- [24] A. R. McIntosh, M. N. Rajah, and N. J. Lobaugh. Interactions of prefrontal cortex in relation to awareness in sensory learning. *Science*, 284(5419):1531–3., 1999.

- [25] V. Della-Maggiore, A. B. Sekuler, C. L. Grady, P. J. Bennett, R. Sekuler, and A. R. McIntosh. Corticolimbic interactions associated with performance on a short-term memory task are modified by age. *J Neurosci*, 20(22):8410–6., 2000.
- [26] S. J. Hanson and B. M. Bly. The distribution of bold susceptibility effects in the brain is non-gaussian. *Neuroreport*, 12(9):1971–7., 2001.
- [27] J. C. Rajapakse, F. Kruggel, J. M. Maisog, and D. Y. von Cramon. Modeling hemodynamic response for analysis of functional mri time-series. *Hum Brain Mapp*, 6(4):283–300, 1998. Using Smart Source Parsing.
- [28] F. Kruggel and D. Y. von Cramon. Modeling the hemodynamic response in single-trial functional mri experiments. *Magn Reson Med*, 42(4):787–97., 1999.
- [29] George Casella and Roger L. Berger. *Statistical inference*. Brooks/Cole, Pacific Grove, CA, 2nd edition, 2002. 2001025794 George Casella, Roger L. Berger. Includes bibliographical references and indexes.
- [30] R. T. Constable, P. Skudlarski, and J. C. Gore. An roc approach for evaluating functional brain mr imaging and postprocessing protocols. *Magn Reson Med*, 34(1):57–64., 1995.
- [31] P. Skudlarski, R. T. Constable, and J. C. Gore. Roc analysis of statistical methods used in functional mri: individual subjects. *Neuroimage*, 9(3):311–29., 1999.

# **Chapter 6**

## **Differential Spatiotemporal Visuomotor Neural Network for Dominant and Non-dominant Voluntary Hand Movement**

Here we present a robust multivariate modeling technique, based on the analysis of partial covariance between functional magnetic resonance imaging and behavior measurements, to disclose the quantitative relationship between whole-brain functional activation and repetitive manual movement rates. In an fMRI experiment of right-handed subjects ( $n=12$ ) executing thumb flexion at frequencies distributed around 0.3 Hz, 1 Hz and 3 Hz by dominant and non-dominant hands respectively, we revealed a distributed neural network that includes primary motor area, supplementary motor area, visual cortex, cerebellum, thalamus, and putamen/globus pallidus. We found that this network demonstrates differential BOLD signal dependency on the rate of voluntary manual movement by either hand, with the dominant hand activity more linearly rate dependent (between 0.3Hz and 2 Hz) and the non-dominant hand more non-linearly rate dependent. Subsequent effective connectivity analysis by Structural Equation Modeling of cortico-thalamic-cerebellar sub-circuits shows that both the

left and right cortico-cerebellar circuits exhibit rate-related modulations in relation to movement of the contralateral hand. The SMA-putamen-globus pallidus-thalamus loops in both hemispheres were estimated to be constantly active across movement frequencies and the hand employed in repetitive movement. The proposed approach can be applied to resolve spatiotemporal dynamics of large-scale brain networks.

## 6.1 INTRODUCTION

The control of voluntary movement requires integrated activity of distributed inter-hemispheric brain areas [1, 2]. Previous positron emission tomography (PET) [3, 4], and functional magnetic resonance imaging (fMRI) [5, 6] studies have suggested that motor coordination includes bi-hemispheric cerebral motor areas (primary motor (M1), lateral pre-motor areas and supplementary motor areas (SMA)), as well as sub-cortical areas, such as thalamus and cerebellum [7, 8]. To investigate the motor system using neuroimaging techniques, repetitive finger movement have been widely employed to study the somatotopic distribution [6, 9] of differential responses due to movement complexity [7, 5, 10], brain asymmetry [11, 12, 13, 14], and the correspondence between the movement and metabolic rate [8, 15, 16, 17]. During repetitive voluntary manual movements, previous PET results showed a linear dependency of the regional cerebral blood flow (rCBF) on the rate of simple repetitive finger movement in the primary sensorimotor area [8, 18]. Subsequent fMRI studies also confirmed the linear relationship between the primary motor area blood oxygen level dependency (BOLD) and movement repetition rate [15, 17, 19]. Nevertheless, secondary motor areas, including lateral premotor and supplementary motor area (SMA), showed nonlinear rate dependent responses using either PET [8, 16] or fMRI [17]. Concerning other brain areas in functional motor system, the responses of cerebellum during repetitive manual movement have remained a topic of speculation, as well as the recently observed "deactivation" patterns seen in motor areas [20, 21, 14].

In this study, we explore the motor system using a repetitive manual movement paradigm. Different from studies using univariate analysis, we chose a multivariate

method to characterize the whole brain pattern of functional activation, including areas subserving the visuomotor tasks and connections among these functional loci. The hypothesis is that there exists an interwoven functional network for motor coordination, potentially including not only motor system for planning and execution, but also sensory perception. Additionally, such a neural network would demonstrate differential regional activities modulated by the connections between functional areas across different conditions. To do this, we employed the multivariate approach to investigate the integrated network including "nodes" (functional active areas) and directional "paths" (the connection modulating functional areas), both of which consist of the "neural context" of the functional motor system. This is different from the traditional univariate approaches, which ignore the interconnectedness of areas in the characterization of functional responses [22, 23]. Here, we explored not only the "functional connectivity", the temporal correlations among loci in the brain during behavior/cognitive tasks, but also the "effective connectivity", the quantitative causal influence among brain regions during different conditions. Specifically, we interrogated the asymmetrical spatiotemporal responses elicited by dominant and non-dominant manual movement at different rates, the functional modulations between left and right hemisphere, as well as between cerebellum, subcortical structures and cerebrum.

Here, we utilized the multivariate robust modeling algorithm based on Partial Least Squares (PLS) framework [24, 25] to take advantage of computational efficiency and simultaneous multiple-contrast comparisons. We extended the PLS analysis by utilizing collections of basis functions to investigate the optimal spatiotemporal model correlating fMRI BOLD signal and repetitive movement rates. This novel modeling method enables the direct modeling between volumetric neuroimaging data and behavioral measurements across spatiotemporal scales, and is especially suitable for parametrically designed neuroimaging experiments. Results of both functional and effective connectivity are presented.

## 6.2 METHODS

### 6.2.1 FMRI experiments and image acquisition

Twelve subjects executed unimanual thumb flexions to a repeating visual stimulus. Before entering the MRI, subjects were trained on the task and asked to respond using the same response pad that they would use inside the MRI. They practiced the task until stable response rates were achieved. Stimuli consisted of a fixation cross and, during the task condition, a bright annulus that flashed around the fixation mark. The annulus subtended 2-degrees and was present for 100 ms. Subjects were instructed to execute a button press response upon stimulus presentation and their response time and accuracy were recorded using a fiber optic response pad (fORP; Current Designs, Inc., Philadelphia, PA). The experiment was designed to be a pacing task, in which the stimulus served to keep subjects entrained, rather than a stimulus-response task. Subjects were instructed at the beginning of each imaging run whether to respond with their right or left thumb. Each subject participated in six data acquisition runs during a single imaging session. Subjects executed movements with either the dominant (right) or non-dominant (left) thumb at three different rates: 0.3 Hz, 1 Hz and 3 Hz. The order of presentation was pseudo-randomized. During the course of the experiment, subjects lay supine in the MRI system and viewed the stimulus projected onto a rear-projection screen. For the task condition, they were instructed to move in time with the stimulus using only the thumb specified by the experimenter at the beginning of that run. During the control condition, subjects were instructed to lay still relax and focus on the fixation cross. Ten blocks of movement task and control alternated in each acquisition run. Kinematic data were recorded to assess task compliance. Multislice echo-planar image (EPI) acquisition was used (43 msec TE, 4.2 sec TR, 64x64 matrix, 230mm FOV, 46 axial slices, 3.6mm cubic voxels, 128 time points per run) in the 1.5 Tesla scanner (Sonata, SIEMENS Medical Solutions, Erlangen, Germany).

### **6.2.2 Preprocessing of data**

The fMRI time series were processed using MEDx (Sensor Systems, Sterling, VA). To correct for within-run interscan head motion each EPI volume was registered to the mean of its time series using a linear 6-parameter rigid-body transformation model employing a least-squares fit. Image volumes were resampled using scanline chirp-z interpolation. Global intensity variations were corrected with global image intensity rescaling, performed by computing the ratio that relates the mean image intensity in a particular volume to an arbitrary value of 1000. Low frequency temporal signal fluctuations were removed by application of a high-pass filter with a cutoff of twice the period length. Next, a 3D Gaussian filter (FWHM 6 mm in all dimensions) was applied to each volume in the time series. Images were then spatially normalized with a 3D warp to an EPI template in Talairach space.

We created two separate data matrices for dominant (right) hand and non-dominant (left) hand experiments respectively. To reduce the between-run variability, a difference image from each subject created by the difference between the mean of task conditions and the mean of control conditions were generated for each movement rate for both hands. The pre-processed whole-brain fMRI images at each time point were then reshaped into one row vector in the data matrix. The experiment consisted of 3 conditions (0.3 Hz, 1 Hz and 3 Hz tapping) and 12 subjects, making total 36 rows in the two data matrices for dominant (right) hand and non-dominant (left) hand respectively.

### **6.2.3 Identification of nodes of large-scale neural network by generalized Partial Least Squares**

We present the mathematical framework for identifying spatiotemporal characteristics of large-scale neural network using generalized Partial Least Square in the appendix. In summary, the robust gPLS modeling uses the basis functions parameterized by the behavioral measurements to correlate the spatiotemporal neuroimaging data. Subsequent employment of multivariate decomposition dissects the collapsed factors be-

tween brain images and behavior data, and thus it leads to the spatial distribution and temporal dynamics of functional systems. The robust gPLS analysis yields, first, design latent variables (design LVs) and temporal scores showing the quantitative relationship between the BOLD responses at sensitive regions and the employed basis function parameterized by the behavioral measurements, i.e. the repetitive movement rate. Secondly, the brain latent variables (brain LVs) that elucidate their spatial distribution of the sensitive regions to the revealed BOLD-behavior relationship. And finally, singular values quantify the relative power in multiple revealed spatiotemporal models.

During spatiotemporal gPLS modeling, we used the a constant and a linearly rate-dependent basis, as well as sigmoid functions with different transitions slope ( $\eta$ ) and shifts ( $\kappa$ ), to build basis  $b$  based on the repetitive manual movement rate  $r$  to model the fMRI data. Sigmoid functions are written explicitly as:

$$b = \frac{1}{1 + \exp(-\eta(r - \kappa))} \quad (6.1)$$

Transition slopes of sigmoidal functions were varied by 1, 2, 4 and 8. And shifts of sigmoid functions were varied by 0, 0.3 1, 2 and 3. These give to the corresponding bases rendered in Fig. 6.1.

In each gPLS analysis of either dominant (right) or non-dominant (left) hand data across 3 motor tapping frequencies, 100 iterations were calculated to reveal and to test the robustness of the spatiotemporal models. In each iteration, data from an individual subject at one tapping frequency was reserved for cross validation. The reduced data and the chosen basis functions were used to identify the spatiotemporal models. The cross-validation metrics was then calculated in 100 iterations, the average of which generated the cross-validity of the model. The spatiotemporal models with the minimal cross validation errors were considered to be optimal, in terms of robustness. Further details of gPLS were described in the Appendix 3.

To test if the spatiotemporal model is tapping-rate independent, linearly tapping rate-dependent, or nonlinearly tapping rate dependent, various Hotelling's  $\bar{z}$ -statistic

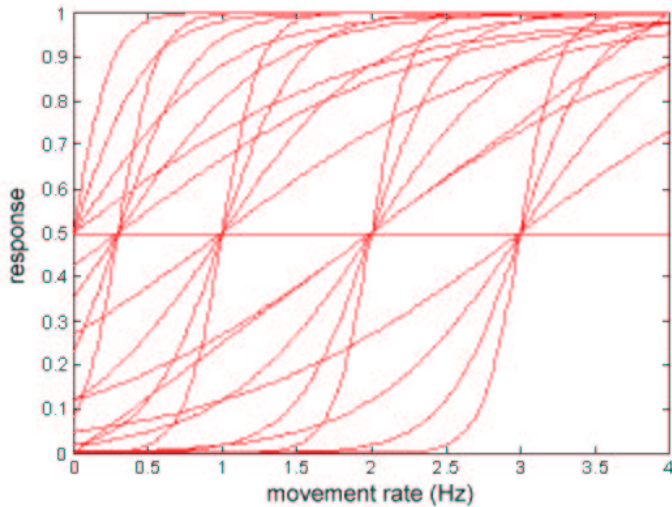


Figure 6-1: The sigmoid basis functions with different shifts and transitions employed in the gPLS analysis. Each analysis utilizes one sigmoid basis function in addition to a constant and a linear basis.

and associated p-values were calculated. The optimal model was compared to the constant basis (the zeroth-order model) and the constant basis plus linearly rate dependent basis (the first-order model) to test whether the spatiotemporal models are motor-rate independent or linearly dependent for dominant and non-dominant hand separately.

#### 6.2.4 Network analysis by Structural Equation Modeling

Using the first dominant brain LV with Z-scores thresholded at 45, we identified regional activated areas and recruited them into the network analysis. To construct the anatomical model for the effective connectivity analysis using Structural Equation Modeling (SEM), connections between nodes in the neural network were obtained by literature reviews to provide a directional interconnected anatomical model with unknown path coefficients. Variances of the nodes were calculated separately at a specific movement rate from dominant and non-dominant hand data to give the endogenous source variance of each node in the network.

The identification of the directional paths was implemented by SEM based on the

formulation by McArdle and McDonald [26]

$$C = (I - A)^{-1} S [(I - A)^{-1}]^T \quad (6.2)$$

where  $S$  denotes the endogenous source variance matrix between the nodes of the network,  $I$  is the identity matrix, and  $A$  is the path coefficient matrix with entry  $A_{i,j}$  at the  $i^{th}$  row and the  $j^{th}$  column quantifying the connection from node  $j$  to node  $i$ . The  $^H$  superscript represents the transpose of the matrix.  $C$  represents the observed covariance matrix among nodes in the network, which can be estimated from the time series as described above. To estimate the path coefficients, we adopted the maximal likelihood estimator, which minimizes the following cost function [27, 28]:

$$\frac{1}{2} \ln |\det(C)| - \ln |\det(\Phi)| + Tr[\Phi C^{-1}] - p \quad (6.3)$$

where  $Tr[\bullet]$  denotes the trace of a matrix, and  $\det(\bullet)$  denotes the determinant of a matrix.  $\Phi$  represents the sample covariance matrix, and  $p$  is the number of paths in the anatomical model.

We used the non-linear optimization tool from Matlab (Natick, MA) to search the minimum of the cost function. Repetitive estimation of path coefficients for each condition was computed for 50 times, each of which performed a 2-sample bootstrap from 12 subjects: namely 2 subjects' data were replaced by the other 2 subjects' at the same tapping frequencies using the same hand. The ratios between mean values and standard deviations for path coefficients among iterations with values smaller than 0.6745 (two-tails  $p$ -value=0.5 in  $N(0, 1)$ ) were considered insignificant paths.

## 6.3 RESULTS

### 6.3.1 Functional connectivity revealed by gPLS

Spatiotemporal models using combination of constant, linear and sigmoid functions of various shifts and transitions in leave-1-out cross validation chose the different optimal models for dominant and non-dominant hand movements: sigmoid at transition slope

$(\eta)$  8 and shift  $(\kappa)$  0 with constant and linear bases are optimal for non-dominant hand data; sigmoid at transition slope  $(\eta)$  1 and shift  $(\kappa)$  0 with constant and linear bases are optimal for dominant hand data. The cross validation error for these two are 107.9 and 113.2 for non-dominant hand and dominant hand respectively. The relative significance of LVs can be quantified by the total variance in the effect space explained by each LV, which is equivalent to the ratio of the square of the singular values. For the non-dominant (left) hand data, the first LV from optimal model accounts for 35% of total variance, and in dominant (right) hand data, the first LV from the optimal model accounts for 69% of the variance.

The temporal scores describe the mapping between the behavioral finger tapping rate and the normalized whole-brain fMRI BOLD responses. Figure 6.2 shows the temporal scores of the first LV in the identified optimal model. In the figure, the gray bars depict the actual finger tapping rates in 3 major frequency ranges around 0.3Hz, 1Hz and 3Hz. The dashed lines in both left and right hand models represent the standard deviation of the temporal model estimations from 100 iterative computations. The first LV of the optimal model for the dominant (right) hand indicates a more linear relationship between the rate of finger flexion and fMRI BOLD responses around 0.3 Hz to 2 Hz. The non-dominant (left) hand optimal model shows a more non-linear relationship between the figure flexion rate and the normalized fMRI signal. Note the plateau in the BOLD-behavioral relationship after 0.7 Hz when non-dominant hand was employed.

To identify if these responses are either frequency independent, linearly frequency-dependent or nonlinearly frequency-dependent, hypothesis tests using Hotelling's  $T^2$ -statistics were performed for both hands against the frequency independent model (constant) and against the linearly frequency-dependent model. The Hotelling's  $T^2$ -statistics comparing the non-dominant hand optimal model to the constant and the linear models are  $1.9 \times 10^8$  and  $8 \times 10^8$  respectively, both of which have p-value less than 0.01%. Comparing dominant hand's optimal model to the constant and the linear models gives the  $T^2$ -statistics of  $4 \times 10^8$  and  $1.8 \times 10^8$  ( $p < 0.01$ ). These results show that the dominant (right) hand 1st LV is linearly rate-dependent, while the

non-dominant (left) hand 1st LV is nonlinearly rate-dependent.

From 100 iterative cross-validations and the subsequent thresholding at Z-score of 45, the spatial distribution of the activation areas is shown in Brain LV. The first Brain LV of the dominant (right) hand tapping identified regions including ipsilateral cerebellum, bilateral visual areas in the occipital lobe, contralateral thalamus, putamen/globus pallidus, primary motor (M1) area and supplementary motor area (SMA). These regions represent the spatial distribution of the brain area whose BOLD fMRI signals are with motor-rate dependency on the first temporal scores, as shown in Figure 6.2. For the non-dominant (left) hand motor movements, the first Brain LV identified also the ipsilateral cerebellum, bilateral visual areas in the occipital lobe, contralateral thalamus, putamen/globus pallidus, M1, and SMA. These areas are shown in Figure 6.3A and 6.3B. The stereotaxis Talairach coordinates of local maxima in the first Brain LVs by dominant and non-dominant hands are reported in Table 6.1, with additional anatomical labels, Brodmann's Areas (BA) and the associated node names in the subsequent network analysis by SEM. To compare the detection of active brain areas between PLS and univariate methods, correlation coefficient maps using the BOLD-finger flexion rate were rendered in Figure 6.3C and 6.3D for left and right hand movements respectively. Note that univariate correlation coefficient detected more activation in cerebellums and visual cortex, while the basal ganglia and SMA activities were less active or missed.

The regional BOLD signals were shown in Figure 6.4, where we separated the brain activated area detected by PLS into two lateralized categories containing ipsilateral cerebellum and contralateral M1, globus pallidus/putamen, thalamus and SMA. Note that the activities were more activated in the cerebral areas contralateral and cerebellar areas ipsilateral to the hand employed for movement. And in general the BOLD signals increases at faster movement rates.

### 6.3.2 Effective connectivity revealed by SEM

To evaluate the modulation of connections in the functional neural network of voluntary movement between dominant and non-dominant hands at different frequen-

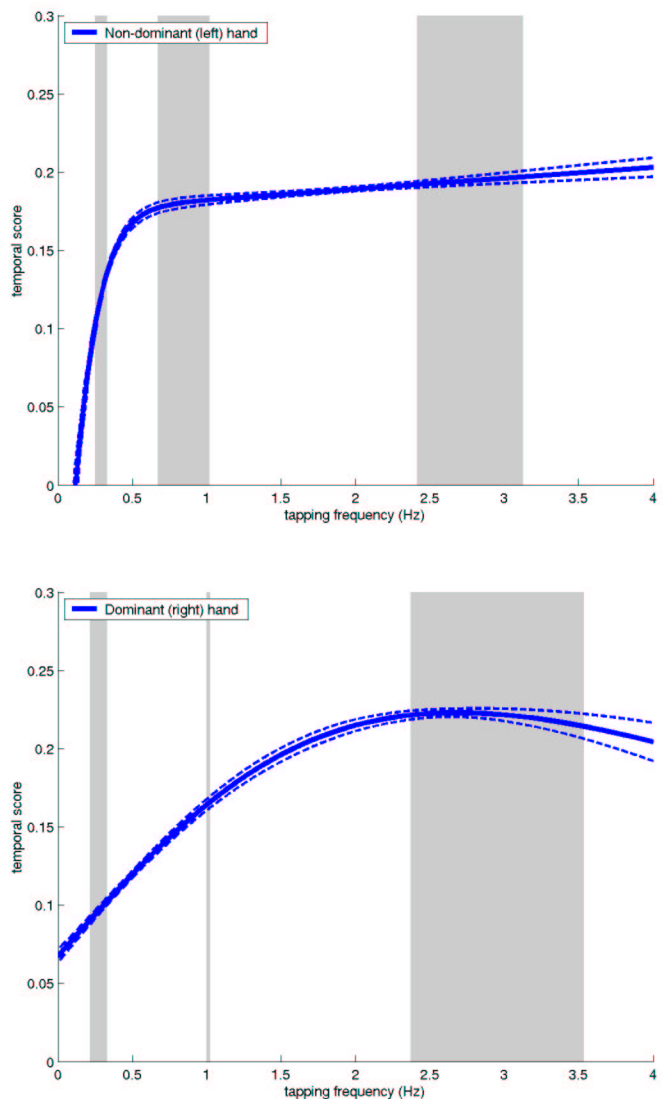


Figure 6-2: Relationship between the manual repetitive rates and the global brain BOLD signal. Gray bars depict the actual repetitive movement rates recorded from subjects. From right-handed subjects ( $n=12$ ), fMRI responses elicited by non-dominant hand movement demonstrates a more non-linearly rate dependence on the frequency of the motor tasks, while dominant hand shows more linear rate dependency. The dashed line illustrated the unit standard deviation estimated from 100 iterative analyses.

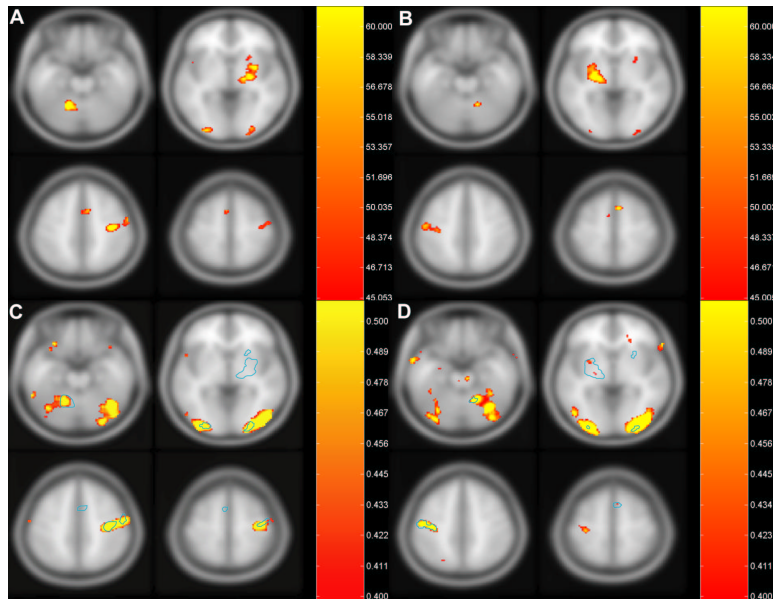


Figure 6-3: The active brain areas from first Brain LV by generalized Partial Least Square analysis for left hand movement (A) and right hand movement (B). The BOLD responses from these areas have differential sensitivity on the rate of the repetitive movement by dominant or non-dominant hand as shown in Figure 6.2. The unit in these figures are the Z-scores calculated from 100 iterative leave-1-out cross validations. The maps of correlation coefficients between repetitive movement rates and BOLD images were shown in (C) and (D) for left and right hand movements respectively. The blue traces in (C) and (D) denote the active regions detected by PLS.

SEM node	anatomical label	left hand movement					Right hand movement				
		x	y	z	volume (mm³)	BA	x	y	z	volume (mm³)	BA
cerebellum (LH)	Left Cerebellum,Anterior Lobe	-15	-54	-19	112						
	Left Cerebellum,Anterior Lobe,Culmen	-14	-53	-16	744						
	Left Cerebellum,Posterior Lobe,Declive	-13	-58	-14	688						
cerebellum (RH)	Right Cerebellum,Anterior Lobe						16	-52	-19	40	
	Right Cerebellum,Anterior Lobe,Culmen						14	-52	-16	328	
	Right Cerebellum,Posterior Lobe,Declive						13	-55	-13	72	
thalamus (LH)	Left Brainstem,Midbrain						-14	-18	-2	296	
	Left Cerebrum,Extra-Nuclear						-18	-15	2	48	
	Left Cerebrum,Thalamus						-14	-18	3	520	
	Left Cerebrum,Sub-lobar,Extra-Nuclear						-18	-15	-2	40	
thalamus (RH)	Right Brainstem,Midbrain	15	-18	-1	144						
	Right Cerebrum,Extra-Nuclear	18	-15	2	48						
	Right Cerebrum,Thalamus	14	-17	3	504						
	Right Cerebrum,Midbrain,Extra-Nuclear	18	-14	-1	8						
	Right Cerebrum,Sub-lobar,Thalamus	14	-17	6	168						
putamen/globus pallidus (LH)	Left Cerebrum,Extra-Nuclear						-19	-10	2	104	
	Left Cerebrum,Lentiform Nucleus						-25	-9	2	920	
	Left Cerebrum,Sub-lobar,Extra-Nuclear						-28	-2	-4	568	
	Left Cerebrum,Sub-lobar,Lentiform Nucleus						-24	-7	-2	816	
putamen/globus pallidus (RH)	Right Cerebrum,Extra-Nuclear	29	4	2	80						
	Right Cerebrum,Lentiform Nucleus	25	0	2	696						
	Right Cerebrum,Sub-lobar,Extra-Nuclear	27	9	-2	128						
	Right Cerebrum,Sub-lobar,Lentiform Nucleus	25	3	0	512						
M1 (LH)	Left Cerebrum,Frontal Lobe,Postcentral Gyrus						-44	-16	44	64	
	Left Cerebrum,Frontal Lobe,Precentral Gyrus						-44	-13	45	832	4
	Left Cerebrum,Frontal Lobe,Sub-Gyral						-33	-19	41	48	
	Left Cerebrum,Parietal Lobe,Postcentral Gyrus						-48	-15	45	488	[1 3]
	Left Cerebrum,Parietal Lobe,Precentral Gyrus						-50	-14	39	8	4
M1 (RH)	Right Cerebrum,Frontal Lobe,Postcentral Gyrus	53	-10	45	64						
	Right Cerebrum,Frontal Lobe,Precentral Gyrus	52	-7	43	448	[4 6]					
	Right Cerebrum,Parietal Lobe,Postcentral Gyrus	54	-11	45	24	3					
SMA (LH)	Left Cerebrum,Frontal Lobe,Medial Frontal Gyrus	-4	6	49	184	[6 32]	-5	3	50	136	6
	Left Cerebrum,Frontal Lobe,Superior Frontal Gyrus	-3	8	51	184	6	-4	6	51	80	6
	Left Cerebrum,Limbic Lobe,Cingulate Gyrus	-2	3	46	16	24					
SMA (RH)	Right Cerebrum,Frontal Lobe,Medial Frontal Gyrus	5	9	46	456	[6 32]	6	12	47	80	[6 32]
	Right Cerebrum,Frontal Lobe,Superior Frontal Gyrus	5	12	50	312	6	5	14	51	408	[6 8]
	Right Cerebrum,Limbic Lobe,Cingulate Gyrus	6	8	43	64	[24 32]					

Table 6.1: Talairach coordinates, anatomical labels and Brodmann's Areas of brain regions showing high sensitivity to the repetitive motor rate dependency shown in Figure 6.3.

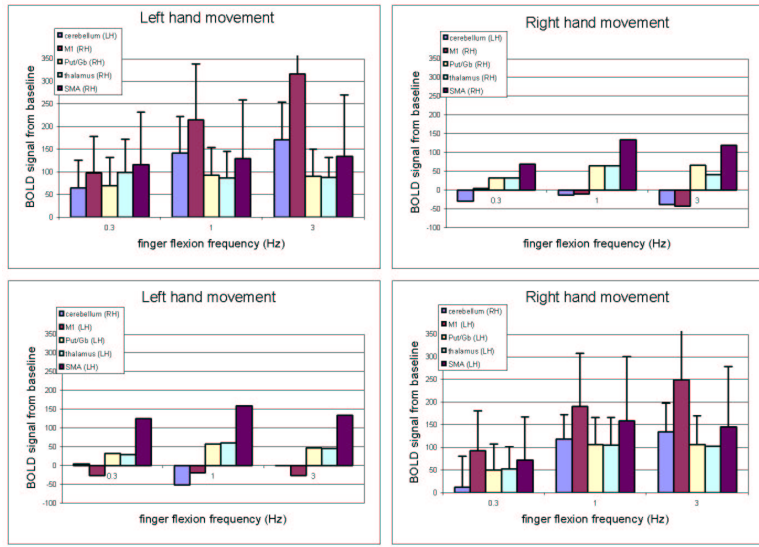


Figure 6-4: The regional BOLD signals revealed by PLS for left hand and right hand movements at 0.3 Hz, 1Hz and 3Hz. For each condition, the brain areas were separated two lateralized system containing ipsilateral cerebellum and contralateral M1, Putamen/Globus pallidus, SMA and thalamus.

cies, the previous behavior-data informed gPLS was used to identify "nodes" in the anatomical models. Functional areas include bilateral cerebellum hemispheres, thalamus, putamen/globus pallidus, supplementary motor area (SMA) and primary motor (M1) areas. The inter-connected anatomical model consists of three main loops: ipsilateral cerebellar- contralateral thalamus-contralateral M1 loop, contralateral SMA-putamen/globus pallidus-thalamus loop, and contralateral M1-putamen/globus pallidus-thalamus loop. In addition, bi-directional connections between the primary motor areas in both hemispheres and SMA-M1 connections are also included. Previous magnetoencephalography study in motor control proposed a similar cerebellar-striatal-cerebral connectivity [29]. These directional connections are illustrated in Fig. 6.5.

The values of effective connectivity estimated by SEM were reported in Table 6.2 for dominant (right) and non-dominant (left) hand at rate centered at 0.3 Hz, 1 Hz and 3 Hz respectively. Figure 6.6 illustrates the values of effective connectivity after thresholded by the Z-score of 0.6745 (two-tails p-value=0.5), where red arrows indicate positive path coefficients, and blue arrows represent negative path coefficients. The width of an arrow corresponds to the value of the path. The paths with absolute

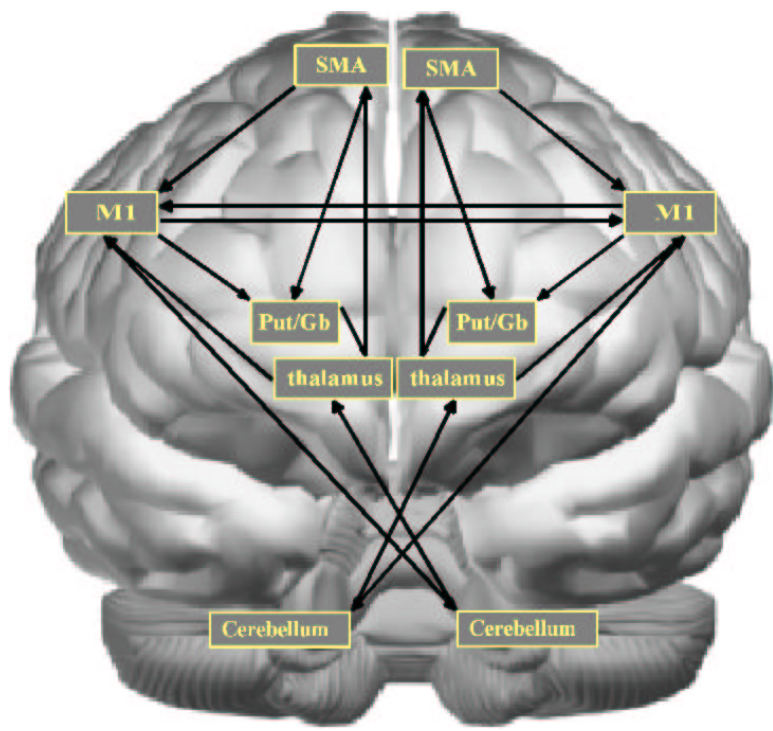


Figure 6-5: The anatomical model for structural equation modeling (SEM) to evaluate the modulation of the distributed neural network for voluntary motor movement. Nodes of the network included bilateral cerebellum, primary motor (M1), supplementary motor area (SMA), thalamus, and collapsed putamen and globus pallidus. The arrows indicate the direction of causal influence.

Z-scores less than 0.6745 were drawn by gray color to indicate the lack of statistical significance.

During low frequency ( 0.3 Hz) repetitive thumb-index finger flexion using non-dominant (left) hand, the major positive active connections were from left cerebellum to right thalamus with an estimated path coefficient of 0.61, as well as the connection from right M1 to left cerebellum with a path coefficient of 0.51. The path coefficients from in the SMA-putamen/globus pallidus-thalamus loop in both hemispheres were also positively prominent. The effective connectivity between M1 areas in both hemispheres failed to reach statistical significance. Note that a negative connectivity was observed from right cerebellum to left thalamus during the 0.3-Hz non-dominant hand finger flexion. For the dominant (right) hand tapping at the same 0.3 Hz, active connections were from right cerebellum to left thalamus and then to left M1 with estimated path coefficients of 0.23 and 0.70 respectively. The SMA-putamen/globus pallidus-thalamus loops in both hemispheres were found to be positive and of statistical significance. One statistically significant negative connection from thalamus to M1 of right hemisphere was observed.

During the 1-Hz voluntary non-dominant (left) hand movement, the effective connectivity in the ipsilateral cerebellum-contralateral thalamus-M1 loop was found to be positively active. We also estimated positive right SMA-right M1 effective connectivity and positive right SMA-right putamen/globus pallidus connectivity. The connectivity from right SMA to right M1 was also found statistically significant (path coefficient = 0.90). For dominant (right) hand 1Hz movement, we found that the ipsilateral cerebellum-contralateral thalamus connectivity was statistically insignificant, but the contralateral thalamus-M1 connectivity was positive and stronger than in the 0.3Hz. The connectivity from contralateral M1 to ipsilateral cerebellum was found significantly positive. The effective connectivity among contralateral thalamus to SMA, and from contralateral SMA to contralateral putamen/globus pallidus were both positive. The SMA-M1 connectivity was found significantly positive in both hemispheres.

3-Hz non-dominant (left) hand effective connectivity was remarkable for the fol-

lowing positive paths: left cerebellum to right thalamus (0.22), right thalamus to right M1 (3.04), right M1 to left cerebellum (0.49). The paths in the SMA-putamen/globus pallidus-thalamus loop on the both left and right hemispheres were all positive. Note that significant negative effective connectivity was estimated also from left thalamus to left M1 (-1.13). Dominant (right) hand finger tapping at 3Hz revealed positive effective connectivity paths: from right cerebellum to left thalamus (0.15; not statistically significant), from left thalamus to left M1 (1.45), and from right M1 to left cerebellum (0.48). Both hemispheres showed strong positive thalamus-SMA connectivity. The connectivity from SMA to M1 was found to be significantly positive in both hemispheres.

## 6.4 DISCUSSION

In this study, we utilized a network analysis to reveal brain and behavioral lateralization and conditional modulation in a large-scale neural network. In summary, the results showed the integration of the functional visual system and the motor system by using generalized Partial Least Squares (gPLS) framework [24, 25], which identifies nodes in the network, and subsequent Structural Equation Modeling (SEM), which quantifies the connections between functional areas. The gPLS approach successfully revealed the orchestration of human functional visual and motor systems, as well as within the motor system, during the passive voluntary manual movements. This indicates the capability of the proposed multivariate modeling technique to identify functional coherent activities without *a priori* anatomical constraints. Different from previous studies revealing the region-specific relationship between the rate of repetitive manual movement and brain imaging data, our approach considers the interaction among distributed regions of brain during spatiotemporal brain activity identification. The results from the combination of PLS and SEM provide the general spatiotemporal descriptions of brain functions at the system level.

The particular novelty in this research is the proposal of robust multivariate linear modeling to decompose the partial covariance matrix between the behavioral mea-

Path		From	To	Left hand; 0.3Hz		Right hand; 0.3Hz		Left hand; 1 Hz		Right hand; 1Hz		Left hand; 3 Hz		Right hand; 3Hz	
M1 (LH)	M1 (RH)			M1 (LH)	M1 (RH)	M1 (LH)	M1 (RH)	M1 (LH)	M1 (RH)	M1 (LH)	M1 (RH)	M1 (LH)	M1 (RH)	M1 (LH)	M1 (RH)
Cerebellum (LH)	Cerebellum (RH)		thalamus (RH)	0.61(0.78)	0.13(0.31)	0.68(0.33)	-0.06(0.68)	0.22(0.24)	0.43(0.60)						
Cerebellum (RH)	Cerebellum (LH)		thalamus (LH)	-0.21(0.20)	0.23(0.25)	-0.11(0.28)	-0.03(1.33)	0.12(0.44)	0.15(0.31)						
thalamus (RH)	thalamus (LH)		SMA (RH)	0.94(0.25)	1.20(0.59)	1.00(0.26)	1.20(0.70)	1.25(0.74)	1.62(0.96)						
thalamus (LH)	SMA (LH)		SMA (RH)	1.97(0.56)	0.87(0.59)	1.99(0.58)	1.30(0.61)	2.00(1.07)	1.29(0.49)						
M1 (LH)	M1 (RH)		M1 (LH)	-0.33(0.65)	0.13(0.42)	0.80(0.55)	-0.32(0.66)	1.09(1.83)	-0.52(0.58)						
M1 (RH)	M1 (LH)		M1 (RH)	0.15(0.68)	0.54(0.27)	0.15(0.36)	-0.39(0.75)	0.08(0.41)	0.27(0.76)						
SMA (RH)	SMA (LH)		M1 (RH)	-0.34(0.59)	0.53(0.24)	-0.06(0.43)	0.56(0.63)	0.09(0.75)	0.53(0.69)						
SMA (LH)	SMA (RH)		M1 (RH)	0.35(0.40)	0.01(0.38)	0.90(0.42)	0.49(0.69)	0.32(1.11)	0.95(0.85)						
M1 (RH)	M1 (LH)		Cerebellum (LH)	0.51(0.12)	-0.21(0.41)	0.50(0.12)	0.27(0.14)	0.49(0.03)	0.31(0.19)						
M1 (LH)	M1 (RH)		Cerebellum (RH)	0.03(0.36)	0.00(0.24)	0.46(0.24)	0.53(0.10)	0.88(0.51)	0.48(0.11)						
thalamus (LH)	thalamus (RH)		M1 (LH)	0.32(0.44)	0.70(0.33)	-0.61(0.51)	0.90(1.02)	-1.13(0.85)	1.45(1.10)						
thalamus (RH)	M1 (LH)		M1 (RH)	0.16(0.44)	-0.60(0.74)	0.95(0.74)	-0.00(0.52)	3.04(2.34)	-0.48(1.06)						
SMA (LH)	SMA (RH)		Putamen/ Globus pallidus (LH)	0.16(0.16)	0.31(0.21)	0.32(0.17)	0.25(0.20)	0.26(0.12)	0.06(0.17)						
SMA (RH)	SMA (LH)		Putamen/ Globus pallidus (RH)	0.33(0.25)	0.38(0.25)	0.41(0.14)	0.32(0.13)	0.21(0.17)	0.48(0.09)						
Putamen/ globus pallidus (RH)	Putamen/ globus pallidus (LH)		thalamus (RH)	1.16(0.46)	0.77(0.22)	0.93(0.33)	0.95(1.47)	1.02(0.43)	0.72(0.34)						
Putamen/ globus pallidus (LH)	Putamen/ globus pallidus (RH)		thalamus (LH)	0.74(0.77)	0.61(0.46)	-0.14(0.40)	0.99(0.41)	0.47(0.42)	0.41(0.52)						
M1 (LH)	M1 (RH)		Putamen/ globus pallidus (LH)	0.17(0.40)	0.12(0.28)	0.27(0.61)	0.28(0.19)	-0.17(0.29)	0.31(0.13)						
M1 (RH)	M1 (LH)		Putamen/ globus pallidus (RH)	0.27(0.19)	0.12(0.45)	0.20(0.08)	-0.15(0.28)	0.14(0.09)	-0.09(0.16)						

Table 6.2: Path coefficient averages and standard deviations from 50 iterative Structural Equation Modeling calculation

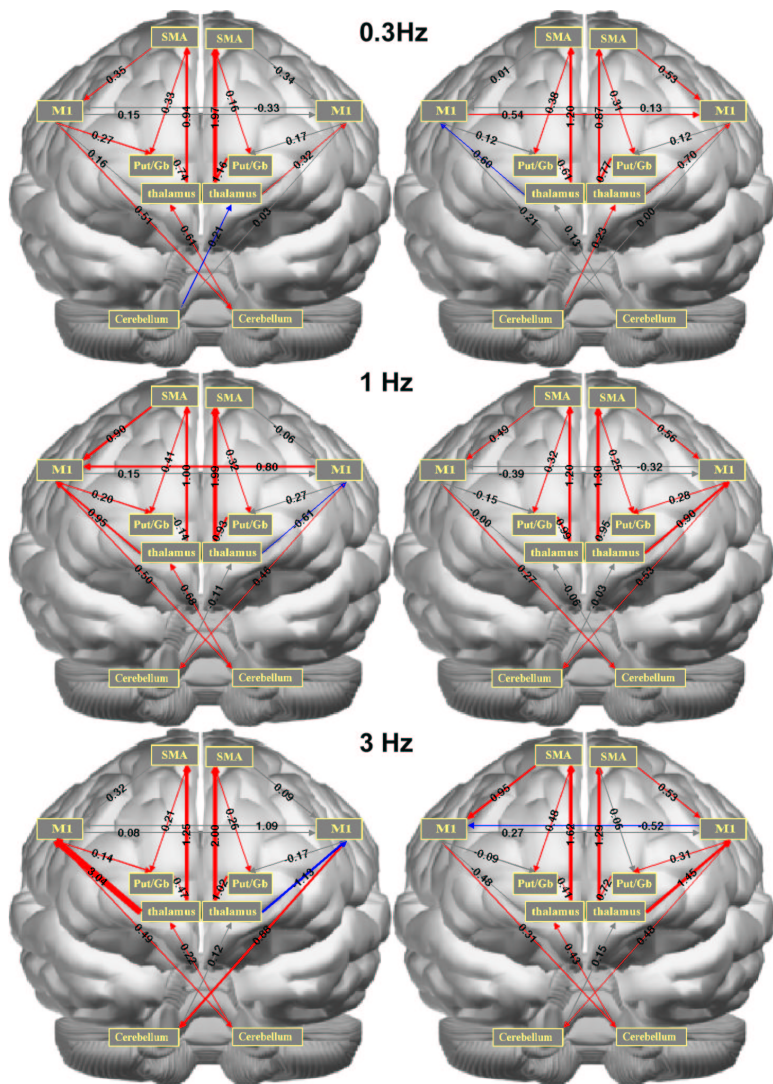


Figure 6-6: The path coefficients for non-dominant (left column) and dominant (right column) hand in repetitive finger flexion. Top: 0.3 Hz; Middle: 1 Hz; Bottom: 3 Hz. The widths of the arrows correspond to the estimated path coefficients, which are also reported on top of the arrows. Red arrows represent positive path coefficients and blue arrows represent negative path coefficients. Arrows with absolute Z-score less than 0.6745 (two-tail p-value  $> 0.5$ ) were considered insignificant and were plotted in gray. The right of the figure represents left hemisphere.

surements and neuroimaging data. Conventionally, multivariate analysis of functional images suggested the combined Principle Component Analysis (PCA) and Canonical Variate Analysis (CVA) [22] method for the analysis of PET data. Later Partial Least Squares (PLS) [24] uses PCA to dissect the projection of functional data to multiple contrasts of interest. Compared to the multivariate techniques analyzing the variance structure within functional images directly, the advantages of PLS include simultaneous multiple contrast comparisons, computational efficiency and the simplified procedures in the post-hoc interpretation of the decomposed data structures. These advantages are all derived from the decomposition of the collapsed effects into orthogonal subspaces mathematically constrained using PCA. Alternative constraint was also suggested to minimize mutual information among decomposed components using Independent Component Analysis [30, 31, 32]. Recently we proposed generalized Partial Least Squares (gPLS) to adopt PCA and ICA flexibly [25]. We suggested that gPLS is capable of detecting both transient and consistent activities by randomly categorizing repetitive observations into groups. Additionally, such a randomized grouping approach can assess the robustness of the decomposed components. However, the question about selecting the appropriate randomized grouping number is not resolved. In this paper, we propose using both cross-validation as well as data fitting to determine the "optimal" order of brain model. The identical principle can be applied to select the "optimal" randomized grouping number, since vectors encoding randomized grouping indices represent basis functions in the context of modeling transient and consistent responses. In general, data is modeled more accurately as assessed by smaller error between the original collection of observations and the modeled data, because more degrees of freedom are introduced in the modeling. This corresponds to more basis functions in the spatiotemporal multivariate modeling, and subsequently less model fitting error due to the richness of the bases to span the data space. The cost of the decreased model fitting error at higher orders of bases is the "robustness" of the model. An ideally robust model works stably across all observations. Stochastically, it is equivalent to small fluctuations between the predicted and the observed data. Given finite data samples, we tested the ro-

bustness of the model by "leave-one-out" cross validation. As shown in the results, higher order basis functions generate larger cross-validation error, because the model is sensitive to these. The contradiction between model accuracy, which is reflected in model fitting error, and model robustness, which is quantified in cross validation error, set a balanced point to trade off an optimal model compromising both essential error characteristics.

In gPLS where behavioral data is used to build spatiotemporal models, basis functions are required for the identification. In theory, we have no preferences toward any basis functions, as long as the basis functions in the model are capable of capturing features in the data, which implies that the span of the basis functions contains the effect space constructed by correlating neuroimaging data and behavioral measurements. Either discrete or continuous basis functions are feasible alternatives in experiment designs. Here we want to relate the continuous external behavior measurement (finger tapping rate) to the functional brain images. In the previous study of similar experimental design but with region-of-interest (ROI) analysis, it has been shown that either linearly rate dependent model or step-function like model are optimal for different areas in the brain [8]. The proposed sigmoid basis function with parametrically varying shifts and transitions is thus capable of exploring a model between linear rate dependency and a step function to better characterize the whole brain BOLD responses to the finger flexion rates. As shown in the gPLS results, differential behavior-BOLD responses were identified between dominant and non-dominant hand movements. This approach is especially suitable for parametrically designed fMRI experiments to interrogate the quantitative relationship between neural activity and behavior measurements.

Based on the gPLS and SEM, we successfully found that the anatomical components of functional rate-dependent motor system, including primary motor cortex, supplementary motor area, thalamus, putamen, globus pallidus and cerebellum. At different rates, such a large-scale neural network exert orchestration during dominant and non-dominant hand movement by the integrated modulation on the connectivity among these areas, as well as localized region-specific activity. In general, the gPLS

elucidated two distinct networks elicited by dominant and non-dominant hand active movement as cued by visual stimuli. The linearly rate-dependent characteristic of dominant hand movement between 0.3 Hz and 3 Hz corresponds to the previous findings from SPECT [33], PET [8, 16] or fMRI [15, 17, 19]. The non-dominant hand demonstrated a nonlinearly rate dependent activity: increasing responses from 0.3 Hz to about 1 Hz for repetitive manual movement, and then a plateau between 1 Hz and 3 Hz. Different from the traditional region-based univariate modeling, our gPLS approach highlighted the global whole brain activity to complete the integrated visiomotor tasks. The results indicate that bilateral primary motor, supplementary motor areas, thalamus, putamen, and globus pallidus as well as cerebellum hemispheres, were involved in the movement, while they exerted different weighting during dominant and non-dominant hand movement. The integrated functional motor system confirmed the previous neuroimaging studies' proposing the movement rate dependent system consisting of contralateral primary motor, contralateral thalamus and ipsilateral cerebellum [8, 34, 15, 19, 35, 36, 37]. The visual cortex was found to be active with rate dependency in this study, potentially because of the visual cues present in the experiment, which also matched the previous neuroimaging finding [38]. The differential rate dependency between dominant and non-dominant manual movement supports the brain asymmetry as evidenced by previous anatomical [11] and functional [12] findings.

Structural Equation Modeling in this study revealed several interesting findings: first, the lateralized motor loop consisting of paths from ipsilateral cerebellum to contralateral thalamus and then to contralateral M1 was found to demonstrate stronger positive modulation as the movement rate increases. This finding is well matched to previous ROI -based analyses [8, 18, 16] showing stronger M1 and cerebellum activities at faster movement rates. At slow repetitive rates, strong effective connectivity from ipsilateral cerebellum to contralateral thalamus was observed. While at faster repetitive rate, the effective connectivity from ipsilateral thalamus to ipsilateral M1 was found to be dominant. Secondly, the SMA-putamen/globus pallidus-thalamus loop is consistently active across 3 different rates in both dominant and

non-dominant hand movements. This showed that the significant involvement of this corticostriatal system in repetitive manual movement. Interestingly, the connectivity in this coritcostrial subcircuit is mostly positively modulated, except for the contralateral putamen/globus pallidus - thalamus connection at 1Hz condition in both dominant and non-dominant hand movement. Thirdly, the SMA to M1 modulation demonstrated differential connectivity in non-dominant and dominant hand repetitive movements: using non-dominant hand, contralateral SMA to contralateral M1 connectivity was only active during slow rate movement; while using dominant hand, SMA to M1 connectivity in both hemispheres was found almost active at all movement rates, except the ipsilateral SMA-ipsilatearl M1 connectivity during slow (0.3 Hz) repetitive movement. Lastly, the revealed negative modulation toward the ipsilateral M1 area corresponds to the recent deactivation patterns in the neuroimaging studies [20, 21, 14]. The suppression of ipsilateral primary motor area might be from either ipsilateral thalamus or from contralateral M1, as shown in the SEM results from both dominant and non-dominant hand movements in our experiment. These significant negative modulations confirmed the deactivation observations and the hypothesis of suppressing mirror movement [21, 14]. Using SEM, we found that cerebellum hemispheres participated in the repetitive manual movement with distinct patterns. First, we found cerebellum's activity is rate dependent, and therefore our gPLS is capable of including cerebellum hemisphere during functional connectivity exploration. Secondly, through effective connectivity analysis, we found both significant input and output projections to and from cerebellum. This corresponds to the previous finding that cerebellum has both significant sensory and motor functions [39].

The network analysis of human motor system has the implications to apply this to the categorization of left-handedness or right-handedness. Since the handiness is derived from long-term habitation on top of innate anatomical features, which is still under controversy [11, 40], we expect that learning might change both the functional connectivity and effective connectivity of the motor system. A specific example is the recent report about the modification of effective connectivity through visuomo-

tor learning [41]. Clinically, we expect this technique would reveal the differential responses for motor system, especially when contrasting the normal subjects and the neuro-degenerative diseases or stroke patients. Recently, the effective connectivity was applied to show that patients with Parkinson's Disease demonstrated characteristic enhancement of attentional modulation on the effective connectivity between SMA and pre-motor [42]. Such findings regarding the performance of the whole brain functional motor system may be further utilized to provide better management for motor rehabilitation and early diagnosis.

# References

- [1] John Nolte. *The human brain : an introduction to its functional anatomy*. Mosby, St. Louis, MO, 4th edition, 1998. John Nolte ; three-dimensional brain reconstructions by John Sundsten.
- [2] Eric R. Kandel, James H. Schwartz, and Thomas M. Jessell. *Principles of neural science*. McGraw-Hill Health Professions Division, New York, 4th edition, 2000. edited by Eric R. Kandel, James H. Schwartz, Thomas M. Jessell ; art direction by Sarah Mack and Jane Dodd.
- [3] P. T. Fox, J. M. Fox, M. E. Raichle, and R. M. Burde. The role of cerebral cortex in the generation of voluntary saccades: a positron emission tomographic study. *J Neurophysiol*, 54(2):348–69., 1985.
- [4] J. G. Colebatch, M. P. Deiber, R. E. Passingham, K. J. Friston, and R. S. Frackowiak. Regional cerebral blood flow during voluntary arm and hand movements in human subjects. *J Neurophysiol*, 65(6):1392–401, 1991. 91341567 0022-3077 Journal Article.
- [5] S. M. Rao, J. R. Binder, P. A. Bandettini, T. A. Hammeke, F. Z. Yetkin, A. Jesmanowicz, L. M. Lisk, G. L. Morris, W. M. Mueller, L. D. Estkowski, and et al. Functional magnetic resonance imaging of complex human movements. *Neurology*, 43(11):2311–8, 1993. 94050622 0028-3878 Journal Article.
- [6] D. Le Bihan and A. Karni. Applications of magnetic resonance imaging to the study of human brain function. *Curr Opin Neurobiol*, 5(2):231–7, 1995. 95345675 0959-4388 Journal Article Review Review, Tutorial.

- [7] S. T. Grafton, J. C. Mazziotta, R. P. Woods, and M. E. Phelps. Human functional anatomy of visually guided finger movements. *Brain*, 115 ( Pt 2):565–87, 1992. 92298191 0006-8950 Journal Article.
- [8] J. W. VanMeter, J. M. Maisog, T. A. Zeffiro, M. Hallett, P. Herscovitch, and S. I. Rapoport. Parametric analysis of functional neuroimages: application to a variable-rate motor task. *Neuroimage*, 2(4):273–83, 1995. 98003497 1053-8119 Journal Article.
- [9] S. M. Rao, J. R. Binder, T. A. Hammeke, P. A. Bandettini, J. A. Bobholz, J. A. Frost, B. M. Myklebust, R. D. Jacobson, and J. S. Hyde. Somatotopic mapping of the human primary motor cortex with functional magnetic resonance imaging. *Neurology*, 45(5):919–24, 1995. 95265196 0028-3878 Journal Article.
- [10] B. E. Wexler, R. K. Fulbright, C. M. Lacadie, P. Skudlarski, M. B. Kelz, R. T. Constable, and J. C. Gore. An fmri study of the human cortical motor system response to increasing functional demands. *Magn Reson Imaging*, 15(4):385–96, 1997. 97366229 0730-725x Journal Article.
- [11] K. Amunts, G. Schlaug, A. Schleicher, H. Steinmetz, A. Dabringhaus, P. E. Roland, and K. Zilles. Asymmetry in the human motor cortex and handedness. *Neuroimage*, 4(3 Pt 1):216–22, 1996. 98005372 1053-8119 Journal Article.
- [12] P. Dassonville, X. H. Zhu, K. Uurbil, S. G. Kim, and J. Ashe. Functional activation in motor cortex reflects the direction and the degree of handedness. *Proc Natl Acad Sci U S A*, 94(25):14015–8., 1997.
- [13] R. Kawashima, M. Matsumura, N. Sadato, E. Naito, A. Waki, S. Nakamura, K. Matsunami, H. Fukuda, and Y. Yonekura. Regional cerebral blood flow changes in human brain related to ipsilateral and contralateral complex hand movements—a pet study. *Eur J Neurosci*, 10(7):2254–60, 1998. 98420183 0953-816x Journal Article.

- [14] A. C. Nirkko, C. Ozdoba, S. M. Redmond, M. Burki, G. Schroth, C. W. Hess, and M. Wiesendanger. Different ipsilateral representations for distal and proximal movements in the sensorimotor cortex: activation and deactivation patterns. *Neuroimage*, 13(5):825–35, 2001. 21201489 1053-8119 Journal Article.
- [15] S. M. Rao, P. A. Bandettini, J. R. Binder, J. A. Bobholz, T. A. Hammeke, E. A. Stein, and J. S. Hyde. Relationship between finger movement rate and functional magnetic resonance signal change in human primary motor cortex. *J Cereb Blood Flow Metab*, 16(6):1250–4, 1996. 97054401 0271-678x Journal Article.
- [16] N. Sadato, V. Ibanez, M. P. Deiber, G. Campbell, M. Leonardo, and M. Hallett. Frequency-dependent changes of regional cerebral blood flow during finger movements. *J Cereb Blood Flow Metab*, 16(1):23–33, 1996. 96121047 0271-678x Journal Article.
- [17] G. Schlaug, J. N. Sanes, V. Thangaraj, D. G. Darby, L. Jancke, R. R. Edelman, and S. Warach. Cerebral activation covaries with movement rate. *Neuroreport*, 7(4):879–83, 1996. 96332949 0959-4965 Journal Article.
- [18] N. Sadato, G. Campbell, V. Ibanez, M. Deiber, and M. Hallett. Complexity affects regional cerebral blood flow change during sequential finger movements. *J Neurosci*, 16(8):2691–700, 1996. 96256705 0270-6474 Journal Article.
- [19] N. Sadato, V. Ibanez, G. Campbell, M. P. Deiber, D. Le Bihan, and M. Hallett. Frequency-dependent changes of regional cerebral blood flow during finger movements: functional mri compared to pet. *J Cereb Blood Flow Metab*, 17(6):670–9., 1997.
- [20] J. D. Allison, K. J. Meador, D. W. Loring, R. E. Figueroa, and J. C. Wright. Functional mri cerebral activation and deactivation during finger movement. *Neurology*, 54(1):135–42, 2000. 20100094 0028-3878 Journal Article.

- [21] H. Reddy, P. M. Matthews, and M. Lassonde. Functional mri cerebral activation and deactivation during finger movement. *Neurology*, 55(8):1244, 2000. 20521200 0028-3878 Comment Journal Article.
- [22] K. J. Friston, C. D. Frith, R. S. Frackowiak, and R. Turner. Characterizing dynamic brain responses with fmri: a multivariate approach. *Neuroimage*, 2(2):166–72., 1995.
- [23] K. J. Worsley and K. J. Friston. Analysis of fmri time-series revisited—again. *Neuroimage*, 2(3):173–81., 1995.
- [24] A. R. McIntosh, F. L. Bookstein, J. V. Haxby, and C. L. Grady. Spatial pattern analysis of functional brain images using partial least squares. *Neuroimage*, 3(3 Pt 1):143–57., 1996.
- [25] Fa-Hsuan Lin, Anthony R. McIntosh, John A. Agnew, Guinevere F. Eden, Thomas A. Zeffiro, and John W. Belliveau. Multivariate analysis of neuronal interactions in the generalized partial least squares framework: Simulations and empirical studies. *NeuroImage*, 20(2):625–42., 2003.
- [26] J. J. McArdle and R. P. McDonald. Some algebraic properties of the reticular action model for moment structures. *Br J Math Stat Psychol*, 37(Pt 2):234–51., 1984.
- [27] John C. Loehlin. *Latent variable models : an introduction to factor, path, and structural analysis*. Lawrence Erlbaum, Mahwah, N.J., 3rd edition, 1998. John C. Loehlin. Path models in factor, path, and structural equation analysis – Fitting path models – Varieties of path and structural models-I – Varieties of path and structural models-II – Exploratory factor analysis-I extracting the factors – Exploratory factors analysis-II transforming the factors to simpler structure – Elaborations and extensions of latent variable analysis.

- [28] Brian Everitt and G. Dunn. *Applied multivariate data analysis*. Arnold ; Oxford University Press, London New York, 2nd edition, 2001. Brian S. Everitt and Graham Dunn.
- [29] J. Gross, L. Timmermann, J. Kujala, M. Dirks, F. Schmitz, R. Salmelin, and A. Schnitzler. The neural basis of intermittent motor control in humans. *Proc Natl Acad Sci U S A*, 99(4):2299–302, 2002. 21843939 0027-8424 Journal Article.
- [30] A. J. Bell and T. J. Sejnowski. An information-maximization approach to blind separation and blind deconvolution. *Neural Comput*, 7(6):1129–59., 1995.
- [31] A. R. McIntosh, N. J. Lobaugh, R. Cabeza, F. L. Bookstein, and S. Houle. Convergence of neural systems processing stimulus associations and coordinating motor responses. *Cereb Cortex*, 8(7):648–59., 1998.
- [32] M. J. McKeown, T. P. Jung, S. Makeig, G. Brown, S. S. Kindermann, T. W. Lee, and T. J. Sejnowski. Spatially independent activity patterns in functional mri data during the stroop color-naming task. *Proc Natl Acad Sci U S A*, 95(3):803–10., 1998.
- [33] U. Sabatini, F. Chollet, O. Rascol, P. Celsis, A. Rascol, G. L. Lenzi, and J. P. Marc-Vergnes. Effect of side and rate of stimulation on cerebral blood flow changes in motor areas during finger movements in humans. *J Cereb Blood Flow Metab*, 13(4):639–45, 1993. 93301015 0271-678x Journal Article.
- [34] M. Blinkenberg, C. Bonde, S. Holm, C. Svarer, J. Andersen, O. B. Paulson, and I. Law. Rate dependence of regional cerebral activation during performance of a repetitive motor task: a pet study. *J Cereb Blood Flow Metab*, 16(5):794–803, 1996. 96378661 0271-678x Journal Article.
- [35] L. Jancke, K. Specht, S. Mirzazade, R. Loose, M. Himmelbach, K. Lutz, and N. J. Shah. A parametric analysis of the 'rate effect' in the sensorimotor cortex: a functional magnetic resonance imaging analysis in human subjects. *Neurosci Lett*, 252(1):37–40., 1998.

- [36] R. S. Turner, S. T. Grafton, J. R. Votaw, M. R. Delong, and J. M. Hoffman. Motor subcircuits mediating the control of movement velocity: a pet study. *J Neurophysiol*, 80(4):2162–76, 1998. 98447760 0022-3077 Journal Article.
- [37] S. Khushu, S. S. Kumaran, R. P. Tripathi, A. Gupta, P. C. Jain, and V. Jain. Functional magnetic resonance imaging of the primary motor cortex in humans: response to increased functional demands. *J Biosci*, 26(2):205–15, 2001. 21319095 0250-5991 Journal Article.
- [38] P. T. Fox and M. E. Raichle. Stimulus rate dependence of regional cerebral blood flow in human striate cortex, demonstrated by positron emission tomography. *J Neurophysiol*, 51(5):1109–20, 1984. 84215267 0022-3077 Journal Article.
- [39] J. H. Gao, L. M. Parsons, J. M. Bower, J. Xiong, J. Li, and P. T. Fox. Cerebellum implicated in sensory acquisition and discrimination rather than motor control. *Science*, 272(5261):545–7, 1996. 96194670 0036-8075 Journal Article.
- [40] L. E. White, T. J. Andrews, C. Hulette, A. Richards, M. Groelle, J. Paydarfar, and D. Purves. Structure of the human sensorimotor system. i: Morphology and cytoarchitecture of the central sulcus. *Cereb Cortex*, 7(1):18–30, 1997. 97175774 1047-3211 Journal Article.
- [41] I. Toni, J. Rowe, K. E. Stephan, and R. E. Passingham. Changes of cortico-striatal effective connectivity during visuomotor learning. *Cereb Cortex*, 12(10):1040–7, 2002. 22206082 1047-3211 Journal Article.
- [42] J. Rowe, K. Friston, R. Frackowiak, and R. Passingham. Attention to action: specific modulation of corticocortical interactions in humans. *Neuroimage*, 17(2):988, 2002. 22265923 1053-8119 Journal Article.

# Chapter 7

## Conclusion

### 7.1 SUMMARY

In this thesis, I investigated approaches to improve the spatiotemporal resolution of human brain imaging using either the magnetic resonance imaging (MRI) along, or the combined MRI/functional MRI (fMRI), and magnetoencephalogram (MEG). The goal to achieve high spatiotemporal resolution in millimeters and milliseconds were approached by hardware and software efforts. On top of the high spatiotemporal resolution brain imaging data, I also studied the approach to reveal large-scale neural networking, including both the nodes and the connectivity of the network, and its correlates to macroscopic behavior measurements. These developments were procedures to better understand human brain function during perception, cognition and motor behaviors. We wish to utilize the technique developed in this thesis to answer (i) where are the foci of brain activity, (ii) when are these areas activated and what is the temporal sequence of activations, and (iii) how does the information flow in the large-scale neural network during the execution of the cognitive and/or behavioral tasks.

In Chapter 2, I presented an approach to employ regularization in reconstructing parallel MRI data in order to reduce the noise amplification of the reconstruction (g-factor). The proposed L-curve algorithm was fully automatic and showed a significant reduction in average g factors in phantom and in vivo data at 1.5T and 3T. For some

pixels the g factor was reduced below 1 indicating that the a priori knowledge in the reconstruction reduced the variability below that of the full-FOV reference scan. The reliance on a priori knowledge did not, however, reduce functional imaging CNR in a model fMRI experiment. Although the method was demonstrated using the *in vivo* SENSE method, the regularization method for reduction of noise amplification might potentially benefit most variants of parallel MR reconstruction.

The parallel MRI study also included hardware building efforts. In Appendix 1, I demonstrated a volume birdcage coil for accelerated image encoding with parallel acquisition methods using SENSE principles. The coil is degenerately tuned with both the standard homogeneous modes and the first gradient mode of the birdcage coil resonant at the Larmor frequency. Conventional and anti-symmetric coupling structures allow imaging from each of these modes simultaneously. I demonstrated the coil for SENSE type reconstruction with acceleration factors of up to 2 fold. The maximal 2-fold acceleration in this dual-mode degenerate birdcage coil offers the potential to extend SENSE type image reconstruction methods to applications demanding uniform whole brain coverage.

Appendix 2 presented an automatic method to estimate the coil sensitivity profile and use it to correct the inhomogeneity of surface coil MRI using wavelet transforms as well as for parallel imaging reconstruction using SENSE. The Daubechies maximally flat filter bank was found to have good computational efficiency and approximation of coil sensitivity map. The optimum level could be automatically determined by the defined inhomogeneity index from the corrected image and estimated coil profile. Thus the method uses neither presumed digital filter specifications or the knowledge of the electromagnetic properties and the location of the RF coil. Reconstructed images showed both cortical and sub-cortical structures farther away from the surface coil with relatively constant contrast. The corrected surface coil images have both higher SNR than volume coil images and homogeneous contrast and brightness. Surface coil images corrected in this way were found to be usable with automated image segmentation software. The coil sensitivity profile estimation was applied to the accelerated parallel MRI of brain images using an 8-channel array coil to reduce the

image encoding time by a factor of 2 allowing either the reduction of susceptibility distortions or increased spatial resolution at given imaging time.

Chapter 3 presented an approach to utilizing anatomical MRI data to calculate Cortical Patch Statistics (CPS), which is incorporated into the source models as a Loose Orientation Constraint (LOC). The proposed approach allows us to take into account the variation of the cortical surface normal within the cortical patch corresponding to each current source location. Simulations with single ECDs, 10 mm diameter cortical patches, and 20 mm diameter patches showed that applying the LOC can improve localization accuracy from 9 mm down to 7 mm in minimum norm estimate (MNE), and from 12 mm to 3 mm in minimum norm estimate, also called minimum current estimates, MCE). The refined cortical constraints were applied to *in vivo* data from auditory and somatosensory evoked fields.

In Chapter 4, I presented a computationally efficient source estimation algorithm, which localizes cortical oscillations and their phase relationships. This method employs wavelet-transformed MEG data and uses anatomical MRI to constrain the current locations to the cortical mantle. In addition, the locations of the sources can be further confined with help of functional MRI (fMRI) data. As a result, I obtain spatiotemporal maps of spectral power and phase relationships. As an example I show how the phase locking value (PLV), the trial-by-trial phase relationship between the stimulus and response, can be imaged on the cortex. I tested the method of combining MEG, structural MRI, and fMRI using simulated cortical oscillations along Heschl's gyrus. I also analyzed sustained auditory gamma-band neuromagnetic fields from MEG/fMRI measurements. The auditory source areas in the posterior superior temporal gyrus were chosen because they are problematic to image with any functional imaging modality. Our results showed that combining the MEG recoding with fMRI improves source localization for non-noise normalized wavelet power. In contrast, it turned out that inclusion of fMRI data does not improve noise-normalized spectral power or PLV localization. I show that if the thresholds are not properly chosen, noise-normalized spectral power or PLV estimates may contain false (phantom) sources, independent of the inclusion of the fMRI prior information. The proposed

algorithm is appropriate for evoked MEG/EEG and block-designed or event-related fMRI paradigms, or for spontaneous MEG/EEG data sets.

In Chapter 5, I investigated multivariate analysis approaches that take into consideration the 4-D (time and space) covariance structure of the neuroimaging data in order to explicitly test for multiple statistical models, including the designed paradigm, and to allow for spatial and temporal model detection. In particular, Principal Component Analysis (PCA) and Independent Component Analysis (ICA), which are two popular multivariate approaches with distinct mathematical constraints, were studied in the proposed generalized Partial Least Square (gPLS) framework. Common difficulties in using these two different decompositions include: classification of the revealed components (task-related signal versus noise); overall signal-to-noise sensitivity; and the relatively low computational efficiency (multivariate analysis requires the entire raw data set and more time for model identification analysis). Using both Monte Carlo simulations and empirical data, I derived and tested the gPLS framework which can incorporate both PCA and ICA decompositions with computational efficiency. The gPLS method explicitly incorporates the experimental design to simplify the identification of characteristic spatiotemporal patterns. I performed parametric modeling studies of a blocked-design experiment under various conditions, including background noise distribution, sampling rate and hemodynamic response delay. I used a randomized grouping approach to manipulate the degrees of freedom of PCA and ICA in gPLS to characterize both paradigm coherent and transient brain responses. Simulation data suggested that in the gPLS framework, PCA mostly outperforms ICA as measured by the Receiver Operating Curves (ROCs) in SNR from 0.01 to 100, the hemodynamic response delays from 0 to 3 TR in fMRI, background noise models of Guassian, sub-Gaussian and super-Gaussian distributions, and the number of observations from 5, 10 to 20 in each block of a 6-block experiment. Further, due to selective averaging, the gPLS method performs robustly in low signal-to-noise ratio ( $\pm 1$ ) experiments. I also tested PCA and ICA using PLS in a simulated event-related fMRI data to show their similar detection. Finally, I tested our gPLS approach on empirical fMRI motor data. Using the randomized grouping method, both transient

responses, and consistent paradigm/model coherent components in the 10-epoch block design motor fMRI experiment can be identified. Overall, studies of synthetic and empirical data suggested that PLS analysis, using PCA decomposition, provides a stable and powerful tool for exploration of fMRI/behavior data. In summary, adoption of the multivariate analysis tool depends on the spatiotemporal structure of the data and the experimental questions. I showed that gPLS provides computational efficiency and flexibility for testing hypotheses at different levels. And gPLS can be used for either single or multiple hypotheses testing by two alternative decompositions: PCA and ICA. While PCA seems to out perform ICA in several of our scenarios, a conservative conclusion would suggest that neither can be favored when applied in the PLS framework.

Chapter 6 presented a robust multivariate modeling technique, based on the analysis of partial covariance between functional magnetic resonance imaging and behavior measurements, to disclose the quantitative relationship between whole-brain functional activation and repetitive manual movement rates. In an fMRI experiment of right-handed subjects ( $n=12$ ) executing thumb flexion at frequencies distributed around 0.3 Hz, 1 Hz and 3 Hz by dominant and non-dominant hands respectively, a distributed neural network that includes primary motor area, supplementary motor area, visual cortex, cerebellum, thalamus, and putamen/globus pallidus was identified. This network demonstrated differential BOLD signal dependency on the rate of voluntary manual movement by either hand, with the dominant hand activity more linearly rate dependent (between 0.3Hz and 2 Hz) and the non-dominant hand more non-linearly rate dependent. Subsequent effective connectivity analysis by Structural Equation Modeling of cortico-thalamic-cerebellar sub-circuits showed that both the left and right cortico-cerebellar circuits exhibit rate-related modulations in relation to movement of the contralateral hand. The SMA-putamen-globus pallidus-thalamus loops in both hemispheres were estimated to be constantly active across movement frequencies and the hand employed in repetitive movement. The proposed approach can be applied to resolve spatiotemporal dynamics of large-scale brain networks.

## 7.2 FUTURE WORKS

The parallel MRI principle was found to be capable of improving spatiotemporal resolution and reducing the artifacts during echo-planar imaging. However, people utilizing parallel MRI technique suffer from lowered image SNR due to two factors: the reduced number of data samples and the unfolding associated artifacts. This thesis presented an algorithm using L-curve technique to minimize the noise amplification from the latter factor. In the future, other regularization parameter estimation methods, such as Generalized Cross Validation (GCV) or direct regularization based on SNR of the linear system, are of potential advantages of reducing g-factors and improving the computation efficiency (reducing the time for regularization parameter estimation) respectively. Nevertheless, the former disadvantage (lowered image SNR due to reduced data samples) is not fully investigated. Other encoding schemes to improve the SNR efficiency in parallel MRI acquisition are worthwhile for further investigation. Using Fourier imaging principle, variable sampling in the phase-encoding direction with dense sampling around the low spatial frequency band and sparse sampling around the high spatial frequency band may improve the SNR efficiency during unfolding the aliased image from array elements. This is because that most energy of the Fourier encoded imaging has energy concentrated around the low spatial frequency region. Another possibility to mitigate the problem of SNR loss in parallel MRI is to use other encoding basis functions. Using encoding basis functions similar to the individual B1 field sensitivity profiles of the RF coils in the array may reduce the error derived from interpolating Fourier bases using measurements from individual array coils.

The spatiotemporal resolution of the MEG/EEG localization method can be improved by more accurate anatomical and physiological information. This thesis presented an approach to utilize high spatial resolution MRI to provide more accurate cortical surface information, including curvature and area, in MEG/EEG localization procedure. Nevertheless, we need more validation on the assumption that the genesis of MEG/EEG signal is originated from the pyramidal cells with primary orientation

perpendicular to local cortical surface. A description on the orientations and the density of the pyramidal cells in gray matter can be valuable information in improving the forward model of MEG/EEG inverse. This anatomical information (at approximately 5 mm – 7 mm resolution) could potentially obtain by modern MRI diffusion imaging technology. Other investigations on tuning parameters in the inverse process, such as depth weighting correction, regularization parameter estimation, and providing spatial prior information of the neural activity from other imaging modalities, can also be valuable for improving the localization precision.

This thesis also presented a study on the cortical oscillation using high temporal resolution MEG data. The study on the oscillatory properties of the neural activity may reveal the mechanisms of information processing within local cortical area and transmission across different loci. I combined the minimum norm inverse, phase locking value, and wavelet transform to provide temporally resolved brain dynamics on the cortical surface. Applying this technique to study large-scale neural network across cerebrum and cerebellum can reveal the structure and function of neural networks. Specifically, the oscillatory property can provide information for causal information flow from one cortical area to another. Therefore effective connectivity analysis can build a credible anatomical model. This is particularly useful in Structural Equation Modeling. Via the time-resolved measurements from MEG/EEG, dynamic Structural Equation Modeling can be implemented to show dynamic neural network at millisecond and millimeter scale.



# **Appendix A**

## **A degenerate mode birdcage volume coil for sensitivity encoded imaging**

We demonstrate a volume birdcage coil for accelerated image encoding with parallel acquisition methods such as SENSE. The coil is degenerately tuned with both the standard homogeneous modes and the first gradient mode of the birdcage coil resonant at the Larmor frequency. Conventional and anti-symmetric coupling structures allow imaging from each of these modes simultaneously. We demonstrate the coil for SENSE type reconstruction with acceleration factors of up to 2 fold.

The spatial distribution of the added noise from the SENSE reconstruction (g-factor map) due to geometrical arrangement of the two-channel system is estimated. The spatially averaged g-factors were found to be 1.21, 1.36 and 1.55 for 1.3, 1.6 and 2.0-fold accelerations respectively. The system was demonstrated *textit{in vivo}* using accelerated and non-accelerated anatomical brain images at 1.5T. The maximal 2-fold acceleration in this dual-mode degenerate birdcage coil offers the potential to extend SENSE type image reconstruction methods to applications demanding uniform whole brain coverage.

## A.1 INTRODUCTION

Although first proposed for increasing sensitivity and spatial coverage, simultaneous imaging from multiple surface coils has recently seen widespread use as a way of decreasing image encoding times utilizing either SENSE based or SMASH based techniques [20, 22]. These methods rely on the differing spatial profiles of the array elements to reconstruct the under-sampled image. Successful reconstruction favors spatially differing sensitivity profiles such as those derived from a non-overlapping (gapped) array of surface coils [20, 22, 29]. The surface coil array, especially those utilizing smaller surface coil elements, necessarily have a sensitivity profile which decreases with depth into the tissue. Clinical applications, however, often favor the homogeneous coverage of the birdcage coil. For this reason, volume birdcage head coils have become the standard for clinical brain imaging. Because of its excellent homogeneity and simple spatial relationship of its two orthogonal homogeneous modes, the uniform birdcage mode alone does not provide the additional spatial information needed for SENSE reconstruction. The higher order modes of the birdcage, however, have substantially differing spatial magnitude profiles from the uniform mode, and all of the modes differ from one another in phase profile. In this case, the benefits of parallel imaging encoding acceleration schemes can be achieved while preserving uniform image acquisition.

Detection of the MR signal from degenerate modes of the birdcage coil has been explored for both SNR enhancement [4, 5] and for decreased image encoding times [6]. In order to evaluate the potential for SENSE acceleration with uniform signal detection, we utilize a degenerate mode birdcage in which the homogeneous and gradient modes of the coil are simultaneously detected. The two homogeneous modes are combined in quadrature and detected in receiver 1 and the first gradient mode of the birdcage structure is also tuned to the Larmor frequency and detected in receiver 2. The spatially differing nature of the two modes makes them well suited to a maximum of 2-fold acceleration with the SENSE method. The uniform nature of the homogeneous mode provides image uniformity nearing that of traditional birdcage

coils.

## A.2 METHOD

An eight-rung low-pass quadrature birdcage volume coil (26.3 cm diameter and 33.5 cm length) tuned for a 1.5T scanner (Siemens Symphony Sonata, Siemens Medical Solutions, Iselin NJ) was constructed for this study. The birdcage was used in "receive-only" mode. The body coil was used for uniform excitation. The homogeneous (lowest frequency) mode of the low-pass birdcage was connected to the first receiver using a four-port ( $0^\circ$ ,  $90^\circ$ ,  $180^\circ$ ,  $270^\circ$ ) drive with conventional capacitive coupling. The  $0^\circ$ ,  $90^\circ$ ,  $180^\circ$ , and  $270^\circ$  legs were combined with a conventional  $90^\circ$  hybrid coupler driving two rungs  $90^\circ$  apart, in conjunction with two  $\lambda/2$  RG-58 coaxial cables connecting opposite rungs of the driving legs, as shown in Fig. A1-1B. This 4-port drive is necessary to ensure that only the uniform mode is coupled into the first receiver. The next highest mode of the birdcage (a gradient mode) shows a high sensitivity at the periphery of the coil and a decreasing sensitivity profile near the center of the birdcage. There is no  $B_1$  field at the center of the coil. In addition to the linear change in  $B_1$  magnitude across the diameter, opposite sides of the coil have a  $B_1$  field phase difference of  $180^\circ$ . Since the 2nd (gradient) mode of the conventional low-pass birdcage resonates at a higher frequency than the uniform mode it is necessary to selectively perturb the frequency of this mode to make it resonant at the Larmor frequency. For the coil geometry used, the gradient mode resonated at a frequency 11.5MHz above the uniform mode. In this work, we tuned the gradient mode to the Larmor frequency using a resonant anti-symmetric coupling structure around the coil, whose symmetry allows coupling only to the gradient mode [5]. This anti-symmetric coupling structure has a zigzag anti-Helmhotz configuration shown in Fig. A1-1C. Although not resonant at the Larmor frequency, adjusting the resonant frequency of the anti-symmetric coupling structure allows it to be used to pull the gradient mode of the birdcage to a lower frequency. Its anti-symmetric symmetry does not allow it to perturb the resonance frequency of the homogeneous mode. The

signal coupled out of the anti-symmetric structure via capacitive coupling was connected to the second receiver. The configuration of the dual-mode birdcage volume coil is illustrated in Figure A1-1. Active pin diode traps were placed on every other rung to actively detune the birdcage structure during RF transmission using the body coil. An active RF trap was also mounted on the gradient mode anti-symmetric coupling structure to avoid the coupling between body coil and this structure during RF transmission. Additionally, four passive RF cable traps were placed where the coaxial cables connected to the coil to block common-mode currents on the cables.

The birdcage coil was tested on the bench using a network analyzer (Hewlett-Packard model 4395A, Palo Alto, CA).  $S_{11}$  parameters were measured for both the homogeneous mode and gradient mode separately to ensure sufficient tuning and matching. Coil tuning and identification of the modes was also performed using  $S_{12}$  measures and appropriate shielded inductive probes. Isolation between the homogeneous and gradient modes was measured with an  $S_{12}$  measure between the two modes. To test the coil performance and noise amplification during SENSE acquisition, phantom images were acquired using a gradient echo sequence (TR/TE/flip = 100ms/5.4ms/90°, FOV = 170 mm x 170 mm; slice thickness = 5mm; Image matrix = 256 x 256). In addition to the full phase-encoded images (100% phase encoding (PE), 256 PE lines), we acquired aliased images of 75% (192 PE lines), 62.5% (160 PE lines) and 50% (128 PE lines) of full 256 phase encoding steps. Unfolding of the images to full FOV were reconstructed by textit{in vivo} sensitivity reconstruction [23]. Specifically, this is formulated by the following linear equation:

$$\vec{y} = A\vec{x} \quad (\text{A.1})$$

$\vec{y}$  is the under sampled data from the array coil,  $\vec{x}$  denotes the unknown spin density, and  $A$  is the encoding matrix representing the undersampling [29]. Noise amplification from parallel MRI was estimated by the g-factor [22]:

$$g = \sqrt{[(A^H \Psi A)^{-1}]_{\rho,\rho} (A^H \Psi A)_{\rho,\rho}} \quad (\text{A.2})$$

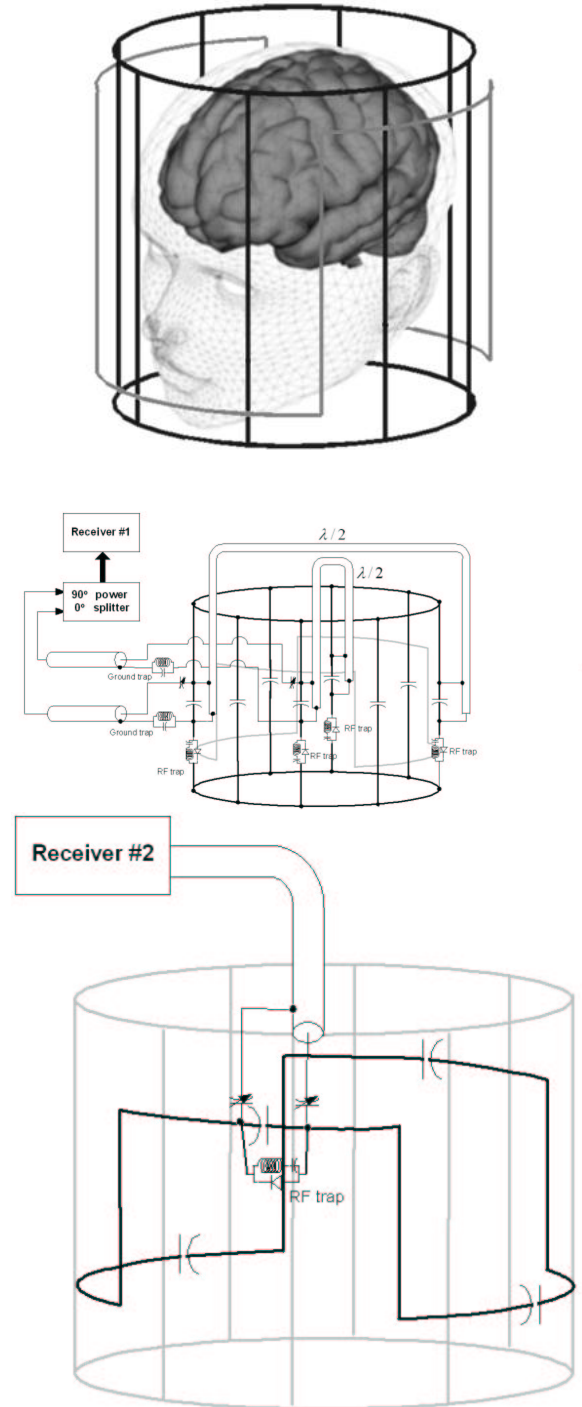


Figure A-1: (A) The geometry of the dual-mode degenerate birdcage. B) The coupling circuit for the coil. C) Detail of the anti-symmetric coupling structure to pull the frequency of the gradient mode to the Larmor frequency and to selectively couple to the gradient mode.

where  $A$  is the encoding matrix;  $\Psi$  is the noise covariance matrix; and  ${}^H$  denotes Hermitian operation. The noise covariance matrix was assumed to be diagonal (noise uncorrelated between the receivers). Noise levels were estimated from the signal variance in the airspace outside the head in raw complex images. The SNR of each mode was measured by region of interest measurement from the magnitude image produced by each receiver. The spatial profile of the reception field of each mode was visualized by plotting a line through the center of the phantom.

*In vivo* anatomical images were also collected from a healthy subject using the same 1.5T scanner using slab-excitation 3D FLASH sequence after the approval by the Institutional Review Board and informed consent. The imaging parameters for anatomical images were TR/TE/flip = 20ms/4ms/27°, FOV = 200 mm \* 200 mm \* 144 mm; slice thickness = 3.0 mm; 48 partitions; Image matrix = 256 (x) \* 256 (y) \* 48 (z). In addition to the full phase-encoded images (100% phase encoding (PE), 256 PE lines), we acquired aliased images of 75% (192 PE lines), 62.5% (160 PE lines) and 50% (128 PE lines) of full 256 phase encoding steps. To assess the uniformity in the reconstructed images, we computed the standard deviation as a percent of the mean value within the white matter region defined by manual segmentation.

## A.3 RESULTS

Prior to connecting the zig-zag structure to collapse the gradient mode and the homogenous mode, the splitting of the two modes was found to be 11.5 MHz. By starting with the tuning of the zig-zag structure far below resonance and adjusting its capacitance, the gradient mode can be steadily adjusted down in frequency until it superimposes on the uniform mode. The S12 parameter was measured between the gradient mode and the combined quadrature homogeneous modes of the coil. The isolation on the bench without loading was 30 dB, which decreased to 23 dB when loaded with a spherical saline phantom of 25 cm diameter. Figure A1-2 shows the individual phantom images from the homogenous mode and gradient mode as detected by the two independent receivers. Qualitatively, the phantom magnitude image of

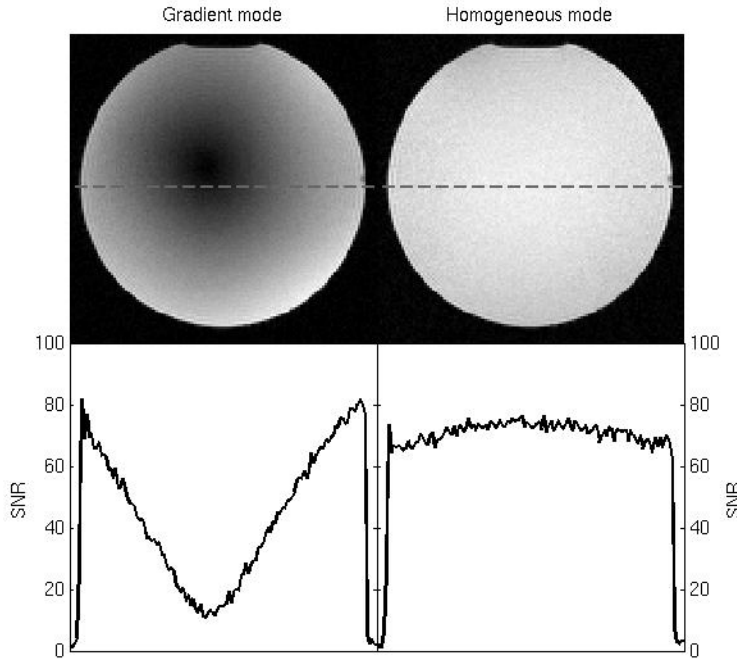


Figure A-2: Phantom images from homogenous mode (right) and gradient mode (left). SNR plots from the cross section depicted by the blue dashed line.

the homogeneous mode gives a relatively constant reception across the FOV. The gradient mode, however, shows the predicated sensitivity field pattern; almost null reception sensitivity at the center of the coil and high sensitivity near the periphery of the coil.

The phantom SNR of the homogenous mode of the quadrature-driven birdcage was found to be 68 with standard deviation of 3 across the FOV. The gradient mode produced an maximum SNR of 84 at the edges of the phantom and a minimum SNR of 0.2 near the center. The lower panel of Figure A1-2 shows the SNR plotted for each mode for the central line of pixels in a transverse slice through the phantom. For this line, the homogenous mode has maximal SNR of 76 and minimal SNR of 62 (average 71, standard deviation 3), while gradient mode has maximal SNR of 82 and minimal SNR of 10 (average 44, standard deviation 22). The noise amplification in the SENSE acquisition due to the geometrical arrangement of the array coil was assessed using

SENSE acceleration	Median	Average	Std. Dev.	Max	Min
1.33 (75%)	1.00	1.21	0.87	40.32	1.00
1.60 (62.5%)	1.09	1.36	1.53	160.51	1.00
2.00 (50%)	1.29	1.55	1.46	87.68	1.00

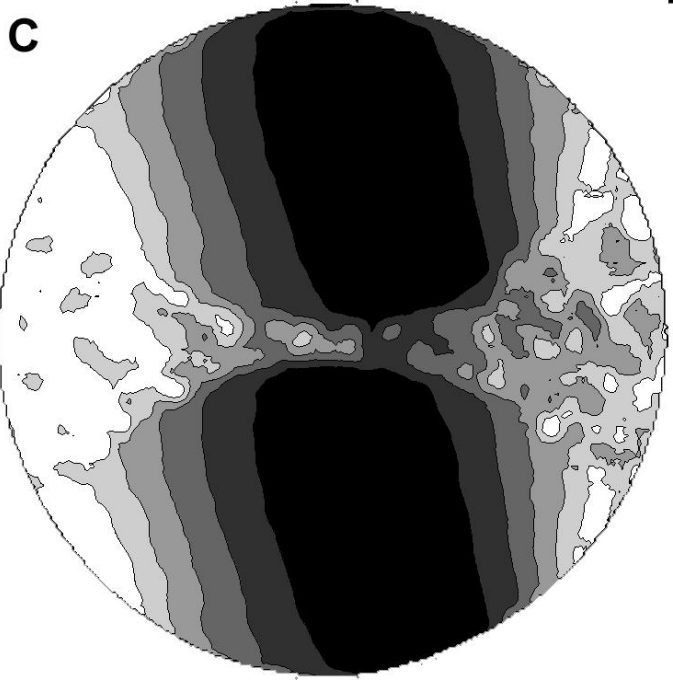
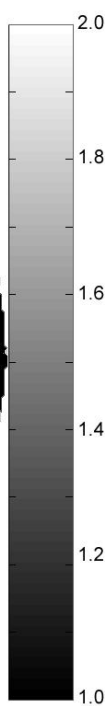
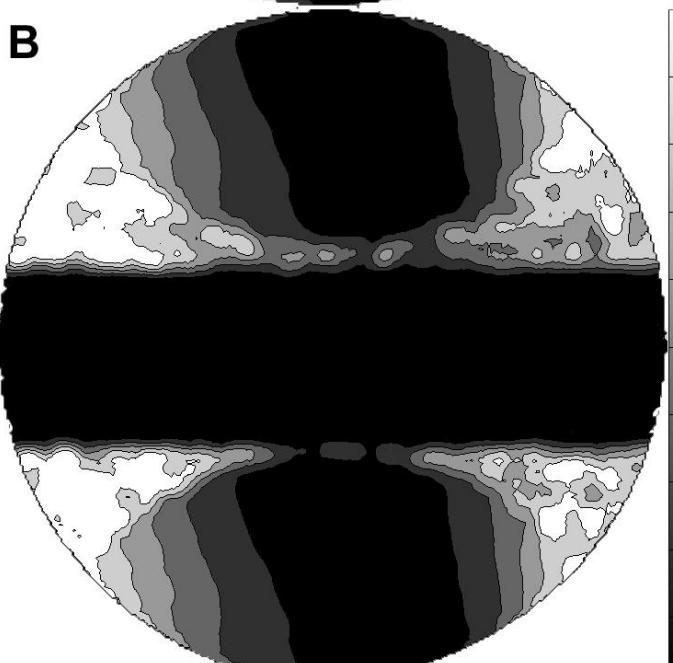
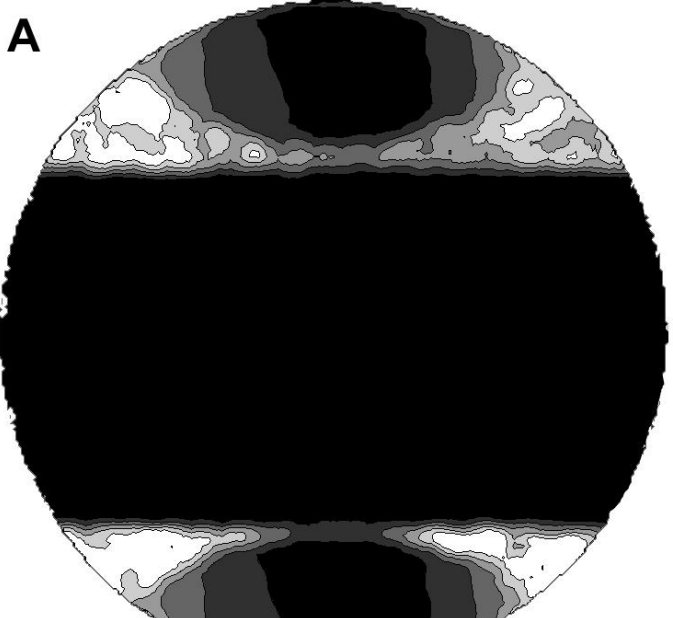
Table A.1: The g-factors of the accelerated SENSE acquisitions at 1.33 (75% of full PE), 1.60 (62.5% of full PE), and 2.0 (50% of full PE). In the table, acceleration is the reciprocal of the ratio between the number of phase encoding line in SENSE acquisition and in full-FOV acquisition

Eq. A2.2. The measured g-factors are listed in Table A1-1. As expected, the median and average g-factors increase when the acceleration factor increases. Figure A1-3 shows the g-factor maps for 3 accelerated acquisitions in Table A1-1.

Figure A1-4 shows an axial slice from a normal volunteer for the full FOV acquisition and SENSE reconstruction using 1.33 fold acceleration (PE=75%) and 2.0 fold acceleration (PE=50%). The top panel shows the two anatomical images from the homogeneous and gradient channel separately. The center of the brain had significant reduced signal in the gradient mode image. The standard deviation across white matter in the brain slice was 19.2% of the mean for the homogeneous mode in the full FOV reference image. The standard deviations of the white matter pixel intensity in the 1.33-fold and 2.0-fold SENSE reconstructions were found to be 20.6% and 21.0% of the mean.

## A.4 DISCUSSIONS

In this study, the uniform and first gradient modes of a birdcage coil are simultaneously detected to enable SENSE acceleration with a traditional birdcage structure. The homogenous mode, which gives uniform FOV coverage, and the gradient mode with its spatially varying  $B_1$  field provide independent views, which can be used for the SENSE reconstruction. Since the maximum acceleration factor is determined by



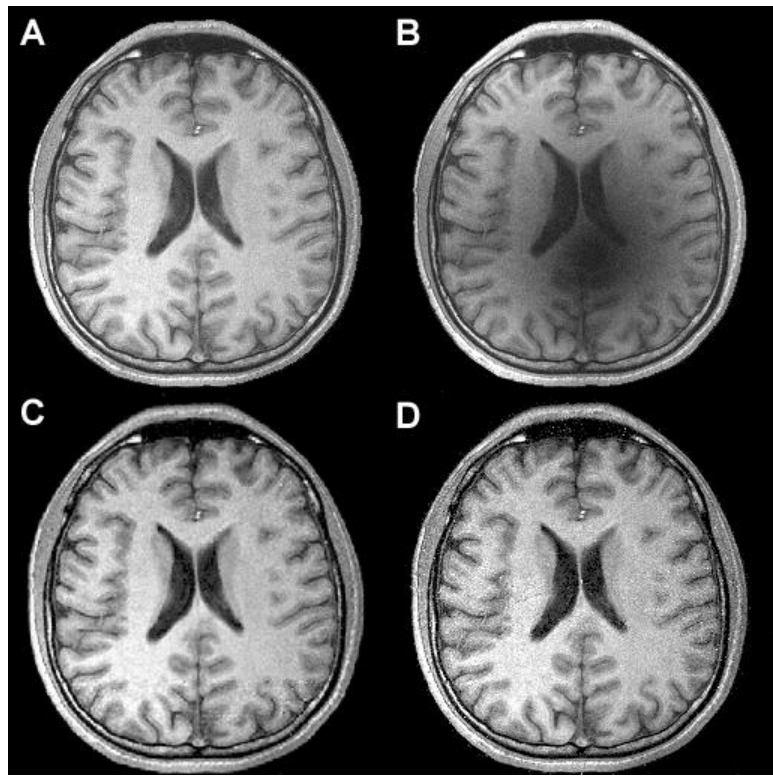


Figure A-4: *In vivo* brain magnitude images from the quadrature homogeneous mode (A) and the gradient mode (B) in full-FOV reference scan. The reconstructed image from 1.3 and 2.0 fold accelerated SENSE acquisition is shown in (C) and (D) respectively.

the number of independent receivers (usually the number of elements in the array), the dual mode birdcage coil is limited to 2-fold SENSE /SMASH acceleration. For an  $n$  rung birdcage there exist  $n/2 + 1$  modes, which could in principle be detected and utilized for increased SENSE accelerations. The higher order modes, however, tend to be similar to the gradient mode in magnitude, but their more complicated spatial distributions of  $B_1$  phase might be useful for SENSE reconstruction. Like the structure demonstrated here to selectively couple into the first gradient mode, dedicated coupling structures that exploit the phase relationship of the higher modes might prove workable.

The aliased air space region in the calculated g-factor maps was found to have a significantly higher G-factor than other areas within the image. This is typical for SENSE reconstruction and results from the ill conditioned matrix inversion when a low signal air-space region is aliased with the brain. The areas with increased g-factor could also be further improved by conditioning the inversion process [23] to decrease the noise amplification in SENSE.

Most coils developed for brain imaging with SENSE reconstruction have utilized traditional overlapped surface coil arrays or gapped surface coil elements. For example, an optimized 8-channel gapped phase array for brain SENSE [8] showed good sensitivity and better g-factor performance than the birdcage demonstrated here, but the uneven spatial SNR distribution may be problematic for clinical applications. The inhomogeneous surface coil image intensity profile may be corrected during or after the SENSE reconstruction [3, 11, 19]. However, the SNR variations across the head are not compensated using this approach. In this work we demonstrate an approach for clinical imaging which allows modest SENSE acceleration factors while preserving the uniform detection efficiency required by many clinical imaging applications.



# References

- [1] D. K. Sodickson and W. J. Manning. Simultaneous acquisition of spatial harmonics (smash): fast imaging with radiofrequency coil arrays. *Magn Reson Med*, 38(4):591–603., 1997.
- [2] K. P. Pruessmann, M. Weiger, M. B. Scheidegger, and P. Boesiger. Sense: sensitivity encoding for fast mri. *Magn Reson Med*, 42(5):952–62., 1999.
- [3] D. K. Sodickson and C. A. McKenzie. A generalized approach to parallel magnetic resonance imaging. *Med Phys*, 28(8):1629–43., 2001.
- [4] C Leussler, J Stimma, and P Roeschmann. The bandpass birdcage resonator modified as a coil array for simultaneous mr acquisition. In *The fifth scientific meeting and exhibition*, Vancouver, British Columbia, Canada, 1997. International Society of Magnetic Resonance in Medicine.
- [5] E. C Wong and W-M Luh. A multimode, single frequency birdcage coil for high sensitivity multichannel whole volume imaging. In *The seventh scientific meeting and exhibition*, Philadelphia, Pennsylvania, USA, 1999. International Society of Magnetic Resonance in Medicine.
- [6] J. W. Carlson and T. Minemura. Imaging time reduction through multiple receiver coil data acquisition and image reconstruction. *Magn Reson Med*, 29(5):681–7, 1993. 93281013 0740-3194 Journal Article.
- [7] D. K. Sodickson. Tailored smash image reconstructions for robust in vivo parallel mr imaging. *Magn Reson Med*, 44(2):243–51., 2000.

- [8] J. A. de Zwart, P. J. Ledden, P. Kellman, P. van Gelderen, and J. H. Duyn. Design of a sense-optimized high-sensitivity mri receive coil for brain imaging. *Magn Reson Med*, 47(6):1218–27, 2002. 22106786 0740-3194 Journal Article.
- [9] L. L. Wald, L. Carvajal, S. E. Moyher, S. J. Nelson, P. E. Grant, A. J. Barkovich, and D. B. Vigneron. Phased array detectors and an automated intensity-correction algorithm for high-resolution mr imaging of the human brain. *Magn Reson Med*, 34(3):433–9., 1995.
- [10] Jr. Maurer, C. R., G. B. Aboutanos, B. M. Dawant, S. Gadamssetty, R. A. Margolin, R. J. Maciunas, and J. M. Fitzpatrick. Effect of geometrical distortion correction in mr on image registration accuracy. *J Comput Assist Tomogr*, 20(4):666–79., 1996.
- [11] M. S. Cohen, R. M. DuBois, and M. M. Zeineh. Rapid and effective correction of rf inhomogeneity for high field magnetic resonance imaging. *Hum Brain Mapp*, 10(4):204–11., 2000.

## **Appendix B**

# **A wavelet based approximation of surface coil sensitivity profiles for correction of image intensity inhomogeneity and parallel imaging reconstruction**

We evaluate a wavelet-based algorithm to estimate the coil sensitivity modulation from surface coils. This information is used to improve the image homogeneity of magnetic resonance imaging when a surface coil is used for reception, and to increase image encoding speed by reconstructing images from under-sampled (aliased) acquisitions using parallel MRI methods for higher spatiotemporal image resolutions. The proposed algorithm estimates the spatial sensitivity profile of surface coils from the original anatomical images directly without using the body coil for additional reference scans or using coil position markers for electromagnetic model-based calculations. No prior knowledge about the anatomy is required for the application of the algorithm. The estimation of the coil sensitivity profile based on the wavelet transform of the original image data was found to provide a robust method for removing

the slowly varying spatial sensitivity pattern of the surface coil image and recovering full FOV images from 2 fold acceleration in 8 channel parallel MRI. The results using bi-orthogonal Daubechies 97 wavelets and other members in this family were evaluated for T1-weighted and T2-weighted brain imaging.

## B.1 INTRODUCTION

Increasing the sensitivity of cortical functional MRI is desirable for either reducing the amount of inter-subject averaging needed to detect subtle cortical activations or for increasing the spatial resolution of the mapping technique. The decrease in detected MR signal at higher resolution is confounded by an accompanying increase in the susceptibility induced spatial distortions in single shot echo planar imaging (EPI) as a percentage of the voxel dimension due to the lengthened readout. Both of these problems can be partially addressed with the use of phased array surface coil detectors which offer the potential to both increase the MR detection sensitivity in the cortex and reduce susceptibility induced image distortions by reducing the length of the EPI readout using the SENSE method [1].

A volume birdcage head coil is conventionally used to achieve homogeneous spatial reception at loci distributed over the whole brain. However, surface coils and surface coil arrays offer the potential for an increase in sensitivity of up to 5 fold in the cortex compared to volume coils at the expense of signal spatial homogeneity [2, 3]. While the phased array technique improves the homogeneity of the images in the plane of the array compared to a single surface coil, the image intensity is still significantly brighter near the coils than deeper in the brain. Thus, the surface coil detector has an inherently inhomogeneous reception profile that leads to a variation in image brightness across the head. This significantly degrades the utility of the images for evaluation of anatomy in the cortex and can also impair automated segmentation of brain structures. For example, in our T1-weighted array images, the signal in the cortex near the coils is approximately 3 fold higher than in the deep gray structures even though these gray structures have similar intensities in a uniform head coil

acquisition. This difference is considerably greater than the contrast between adjacent gray and white matter whose intensities differ only by 22% in a high contrast T1-weighted image.

The surface coil intensity variation is, however, a slowly varying function of position and is amenable to theoretical prediction or measurement. Once the signal intensity changes due to the coil's reception efficiency are determined, the resultant image intensity variations can be greatly reduced by dividing the original images by the coil sensitivity map. Several different methods have been described for determining the surface coil intensity profile [4, 5, 6, 2, 7, 8, 9, 3, 10, 11, 12, 13, 14, 15, 16, 17, 18, 19]. These methods use either a theoretically generated model [2, 9] of the coil or the information in the image itself [4, 6, 3] to generate the expected coil sensitivity map. In the first case, knowledge of the location and orientation of each surface coil is required in addition to a  $B_1$  field map generated from the coil geometry. In the second case, the image variations due to coil fall-off must be separated from those due to anatomical variations. The coil intensity profile can be approximated by a low-pass filtered version of the original image since the coil intensity profile is generally a slowly varying function of position while the anatomic information occurs at higher spatial frequencies. This approach has been demonstrated in a number of different forms [3, 10, 18, 19]. The low-pass filter based approximation of the surface coil profile requires *a priori* knowledge of the anatomy and coil fall-off in order to determine the appropriate cut-off spatial frequency which separates the low frequency variations due to coil fall-off from the higher spatial frequency variations arising from the anatomy.

The largest anatomical artifact incurred when estimating the coil profile based on a low pass filtered version of the original image originates from the air-tissue interface under the coil. This is typically the highest contrast area of the image due to its close proximity to the coil and the complete lack of signal from the air region. Furthermore, the air region is often uniform on the length scale of the low pass filter resulting in an underestimate of the coil map near the skin-air boundary. Similarly, the low pass filtered version of the image generates a poor approximation of the coil sensitivity map near any other large low signal regions such as the lateral ventricles in T1 weighted

images. When this underestimated coil profile map is used to normalize the original image, the result is a residual brightness near the interface.

The approximation of the coil intensity profile can be improved by using a body coil image to determine anatomical content in the original image at the expense of acquisition time [15, 16]. If a body coil image is used, it must have high enough spatial resolution and image contrast to allow the anatomical features of the surface coil image to be extracted. The large anatomical features such as the edge of the head can also be explicitly removed from the image prior to the low pass filtering [3]. This requires some *a priori* knowledge about the location of the high contrast features thus limiting the method's robustness to unexpected features such as large cystic or contrast enhancing regions.

Prior to removing the spatial variations in the detected intensity of the individual array elements, it is beneficial to characterize their spatial information and use this information to decrease the acquisition time of high speed imaging techniques such as EPI. Recent methods which utilize the parallel nature of phased array acquisition to decrease the number of gradient encoding steps needed in the phase encode direction include k-space domain methods such as SMASH [20, 21] and image domain methods such as SENSE [22]. In principle these techniques allow the number of phase encode steps to be reduced by a factor of up to the number of elements in the phased array. The reduced number of phase encode steps (under-sampling in k-space) results in a "folded" or aliased image. The information from the coil sensitivity maps is then used to unfold the aliased images [20, 22, 23]. The shorter image encoding period is beneficial for improving the spatiotemporal resolution of fMRI or reducing the susceptibility induced distortion in EPI. Thus in brain MRI, improvements in the estimation of surface coil sensitivity profiles can be exploited for both homogeneous visualization of the image and decreased encoding times.

Here we propose a method to estimate the surface coil sensitivity profiles using only post-hoc processing of the anatomical surface coil image. This coil sensitivity estimation can be utilized to correct image intensity variations, and to reconstruct full FOV images in parallel MRI for high spatiotemporal resolution brain images. The

method mitigates the effect of edges in the estimation of the coil sensitivity map by using an iterative maximum value projection method to improve the approximation of the coil sensitivity profile near the edge of the head. The slowly varying intensity changes, which comprise the estimated coil sensitivity map, are determined from a filter bank implementation. This method allows the comparison of multiple levels of spatial filtering. The optimum level of filtering is determined by an automated analysis of the coil profile smoothness and the spatial variance in the corrected images.

## B.2 METHOD

The images from a surface coil can be viewed as the product of the true anatomical image and a function representing the spatial modulation imposed on the image by the surface coil reception profile. Thus, the true homogeneous image,  $C[\vec{n}]$ , is modulated by the coil sensitivity,  $S[\vec{n}]$ , to generate the observed inhomogeneous image,  $Y[\vec{n}]$ , where  $\vec{n}$  is the position vector in 3D space. Thus our goal is to get an estimate,  $S[\hat{n}]$ , of the true coil sensitivity profile,  $S[\vec{n}]$ . The intensity-corrected reconstruction image,  $C[\vec{n}]$ , which represents an approximation of the true anatomical image is then expressed in terms of the ratio of the original data,  $Y[\vec{n}]$  and the estimated coil sensitivity profile.

$$\hat{C}[\vec{n}] = \frac{Y[\vec{n}]}{\hat{S}[\vec{n}]}, \vec{n} \in R^3 \quad (B.1)$$

If aliased images are acquired in order to reduce encoding time, an unfolded image is generated by inverting the folding process which is represented by a kspace undersampling matrix. Since kspace is under sampled, the additional spatial information available from the multiple receive channels is needed to complete the matrix inversion. We have applied the standard SENSE reconstruction method and generated a g-factor map depicting the noise added in the unfolding process [22]. The surface coil intensity profile  $S[\hat{n}]$  from the measured image is used as an input for the SENSE unfolding method.

### B.2.1 Multi-resolution analysis

We estimate the coil intensity profile using a hierarchical filter bank structure to efficiently implement a Multi-Resolution Analysis (MRA) [Daubechies I, 1992; Strang G and Nguyen T, 1996; Vaidyanathan PP, 1993] of the original inhomogeneous MRI. In general, MRA decomposes the image into a series of orthogonal "coarse approximations" sub-space and "fine details" sub-space at different spatial resolutions. After breaking down the image into sub-components of different resolution, the original image can be regenerated from the direct sum of the sub-images if desired [Daubechies I, 1992; Strang G and Nguyen T, 1996]. When applied to discrete images, this method is referred to as the discrete-time wavelet transform, DWT. [Vaidyanathan PP, 1993]

In estimating coil sensitivity profiles with the iterative analysis low-pass filter bank, the cut-off spatial frequencies are progressively lowered until very little spatial information is left in the image. Since the coil sensitivity map consists of the slowly varying sensitivity profile of the coil and the details subspace likely contains mainly anatomical information, we estimate  $S[\vec{n}]$  from the low-pass filter data only. This estimate of the coil sensitivity map is computed at each level of the MRA.

In implementation, we use the bi-orthogonal maximally-flat Daubechies' wavelet and scaling functions [24, 25]. The property of symmetric wavelet and scaling functions of this implementation avoids any pixel shift in the filtered data. Also, the Daubechies' bi-orthogonal wavelet family allows the choice of the number of vanishing moments in the filter. This determines the number of zeroes of the discrete digital filters' spectrum; more zeroes provide a higher approximation accuracy. Specifically, we choose Daub97 bi-orthogonal filter banks in our studies. In this notation, the first digit represents the length of analysis filter, which is also the support of the analysis scaling/wavelet function. The second digit describes the length of synthesis filter bank. Daub97 filter banks have 3 zeros at  $\pi$  for the low-pass filter in synthesis filter bank. Thus their approximation power for signal reconstruction is equal to cubic polynomials at each spatial scale.

## B.2.2 Application to coil sensitivity profile estimation

While a given level of the MRA of the original surface coil image could be used alone to estimate the coil sensitivity profile, this leads to an underestimation of the coil sensitivity map in the vicinity of high contrast edges in a similar manner to other low pass filter based estimates. These high contrast features may arise from anatomy inside the brain (e.g. ventricles), or from the air-skin interface. To address this problem, we use an iterative process to improve the estimation near the high contrast edge. This method is applied to each level of the multiple resolution analysis. The generation of the coil sensitivity map at a given MRA level is formed by taking the maximum value projection (MVP) of the approximation subspace (low spatial frequency information) generated by the MRA with the original image. The maximum value projection of two input images is an image whose pixel values are the pixel by pixel maximum of the two input images. Thus the intensity of a given pixel in the maximum value projection image is defined to be that of the greater of the two corresponding pixels in the two input images. In order to form the coil sensitivity estimate from a given level of the MRA, the MRA and maximum value projection are repeated iteratively. In this process the MVP of the output of the MRA and the original image is re-analyzed with the MRA method at a given level. The result of the MRA is then re-compared with the original image using MVP and the output is re-analyzed with MRA at the same level. Thus the input for the  $(i+1)^{th}$  application of the discrete wavelet transform is generated from a maximum value projection of the current result ( $i^{th}$  iteration) and the original image. The process is outlined in Fig. A2-1. We stop the iteration when the total power in the difference image formed from two consecutive iterations is less than 1% of the power in the current iteration.

The iterative MVP process reduces the underestimation of the signal at a high contrast interface (such as the brain-air boundary). An example using 1-dimensional data is illustrated in Fig. A2-2. The projection helps to preserve the original high pixel intensity on the bright side of an edge while increasing the pixel intensity on the darker side of a high contrast edge. The process has the effect of filling in the low

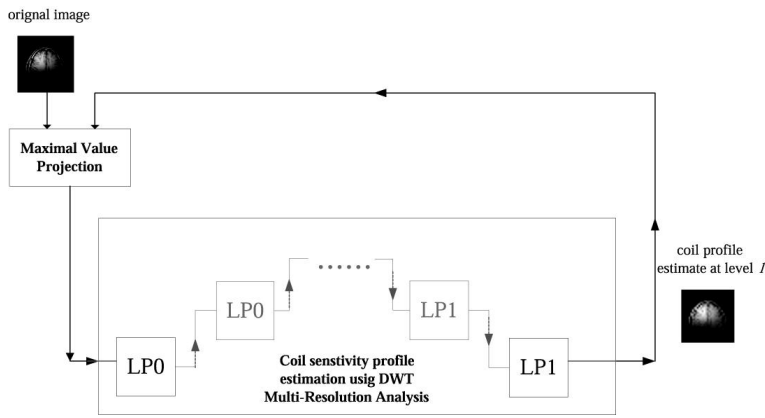


Figure B-1: Schematic diagram of the iterative estimation of coil sensitivity profile at a specific level  $l$  by Discrete-time Wavelet Transform (DWT) based on the Maximum Value Projection (MVP) of the previous estimate and the original inhomogeneous input raw image. LP0 denotes the cascade of a low-pass filter and a 2-fold down-sampler. LP1 denotes the cascade of 2-fold up-sampler and synthesis low-pass filter.

signal intensity regions in a smooth fashion while preserving the local maximum on the tissue side of the interface. Thus, for the edge of the head, the accuracy of the coil map is improved on both sides of the interface.

Once the iterative maximum value projection process converges for a given level of MRA, the process is repeated at the next level. Thus for an image matrix of  $2^n$ ,  $n$  levels of the coil sensitivity profile estimates are generated, each at a different spatial resolution. Each level of estimation employs both the DWT and maximum value projection. Any of these levels of MRA estimation could, in principal, be used as  $\hat{S}[\vec{n}]$  to either generate the corrected version of the original image, or to reconstruct full-FOV images in parallel MRI.

### B.2.3 Automatic selection of optimal reconstruction level

For an image matrix of  $2^n$ , the wavelet-based method provides  $n$  distinct coil sensitivity profiles at different levels of spatial smoothing. For each level, an inhomogeneity-corrected image can be obtained by pixel-by-pixel quotient of the original image over the estimated profile pattern. Automatic selection of the optimal reconstruction level can be achieved by defining a metric of how well the algorithm has done at removing

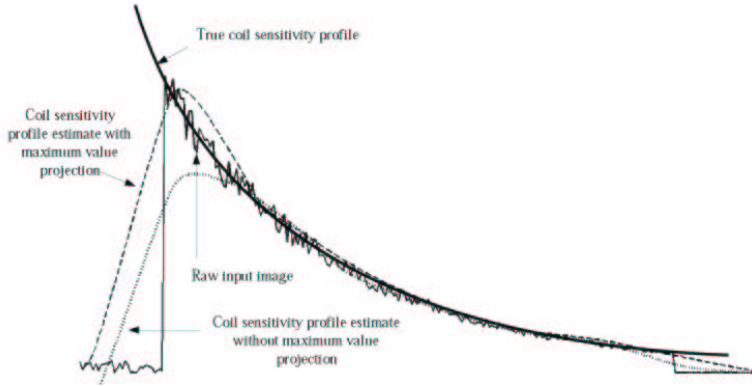


Figure B-2: Simulation of one-dimensional data (thin solid line) with superimposed slowly varying trend (thick solid line) and signal from anatomical contrast. The sharp edge is a simulation of the abrupt signal change at an anatomical boundary such as the air-scalp interface. The first estimation (dotted line) without maximum projection underestimates the sensitivity at the boundary. Iterative maximum projection of the previous estimate and the original data (dashed line) provides better approximation of the global trend in the data, especially in the brain region near the boundary.

the variance in the image due to the coil profile. This metric cannot be a simple measure of image variance since image variance is minimized when both the coil profile and the fine spatial scale anatomic variations are removed from the image. Qualitatively, the optimal reconstruction would contain a high contrast between parenchymal tissue types and low pixel value variance within individual structures. Additionally, the estimated coil sensitivity profile is expected to be spatially smooth due to the electromagnetic properties and the topologies of the coil. We defined an "inhomogeneity index",  $I_l$ , as a metric of how well the algorithm removes the coil profile at each level  $l$ . The MRA level which generates a corrected image with the minimum inhomogeneity index is chosen as the best approximation of the coil profile. The index is a product which attempts to minimize variance  $V_l$  within a loosely defined tissue type, and maximize the smoothness  $\theta_l$  of the coil map and contrast  $C_l$  between tissue types

$$I_l = \frac{V_l}{C_l} \times \theta_l \quad (\text{B.2})$$

Here  $V_l$  denotes the pixels intensity variability within a tissue type in the recon-

structed anatomical image at spatial level  $l$ . And  $C_l$  denotes the contrast between tissue types in the reconstructed anatomical image.  $\theta_l$  is an estimate of the spatial smoothness of the estimated coil sensitivity profile. Thus the inhomogeneity index is computed from both the corrected image and estimated coil profile generated at each spatial level. We use the Gaussian Mixture Model (GMM) [26, 27] to categorize the intensity histogram of the reconstructed images. In GMM, the pixel intensity histogram of an image is assumed to follow multiple Gaussian distributions, each of which is characterized by the unknown mean  $\mu_k$ , variance  $\Sigma_k$  and probability  $p_k$ . The probability of a pixel with value  $\zeta$  is written:

$$p(\xi) = \sum_{k=1}^n p_k \frac{1}{2\pi |\Sigma_k|} \exp\left(\frac{-(\xi - \mu_k)^T \Sigma_k^{-1} (\xi - \mu_k)}{2}\right) \quad (\text{B.3})$$

GMM parameters  $p_k$ ,  $\mu_k$ , and  $\Sigma_k$  can be calculated using Expectation-Maximization (EM) algorithm [4, 26]. The variance in the corrected image,  $V_l$ , is calculated as the sum of all variances ( $\Sigma_k$ ) of the Gaussian models, and the contrast of the corrected image,  $C_l$ , is the difference between the Gaussian distributions with the lowest and the highest mean value as a metric of image contrast. We evaluated the use of 2 to 6 Gaussians in our model. Using 3 Gaussian distributions in T1-weighted images, the histogram of the corrected anatomical image at the optimal level can be approximately partitioned into gray matter, white matter and scalp lipids. The spatial smoothness of the coil  $\theta_l$  is calculated by convoluting a 3-pixel by 3-pixel discrete Laplacian operator over the estimated coil sensitivity profile and summing the pixel values of the resulting map [28].

#### B.2.4 Image acquisition for image intensity inhomogeneity removal

Images were acquired using a 3T scanner (Siemens Medical Solutions, Iselin NJ) with a home built two or four-element bilateral surface coil array. The array elements consisted of 9 cm diameter surface coils. The imaging pulse sequence was an T1-weighted MPRAGE 3D volume exam (TR/TE/flip = 2530ms/3.49ms/70), partition thickness

= 1.33mm, matrix = 256 x 256, 128 partitions, Field of View = 21cm x 21 cm or a T2-weighted Turbo Spin Echo (TSE) sequence (TR/TE/flip = 6000ms/97ms/160o, slice thickness = 3mm, matrix = 512 x 448, Field of View = 22cm x 19.2 cm). The 3D images were cropped to 256\*204 matrix size to minimize the background airspace for visualization purpose before inhomogeneity correction. The array elements were placed over the subject's temporal lobes. To compare the corrected surface coil image with a uniform coil, the nearest anatomical slice prescription and imaging parameters were applied to a birdcage head coil. The utility of the image correction algorithm for rendering surface coil images suitable for automated segmentation algorithms was tested by using the FreeSurfer [Fischl B, et al., 1999] (<http://surfer.mgh.harvard.edu>) segmentation package. Both the original and intensity corrected 3D T1 weighted isotropic 1mm resolution MPRAGE images were processed.

### B.2.5 Parallel MRI acquisition and reconstruction

For parallel MRI acquisition and reconstruction, a home-built 8-channel 3T head array consisting of a linear array of 9cm diameter circular surface coils wrapped around the head was used to test the algorithm for SENSE parallel image reconstruction. Images were under-sampled in the phase-encode direction by 50% (skipping every other phase-encoding line) to achieve 2-fold acceleration. A T1 weighted FLASH sequence (TR/ TE = 450ms/12ms, slice thickness = 3mm, matrix = 256 x 256, Field of View = 19cm x 19cm) was to obtain axial slices through the brain. Given the estimated coil sensitivity maps from each coil acquired with a full FOV reference image, the aliased images were unfolded using a standard SENSE approach [29]. Noise amplification from the geometrical arrangement of the array coil elements is calculated by the G-factor map.

## B.3 RESULTS

The original 256x204x128 uncorrected 3D T1 images were corrected to give 6 distinct coil profile estimations at 6 spatial scales. In the uncorrected image (Fig. A2-3),

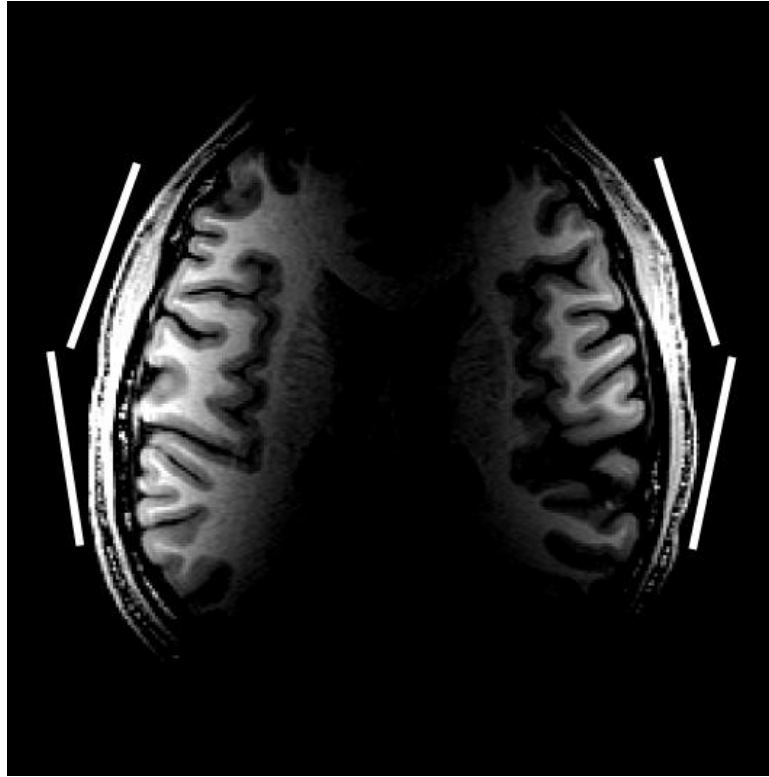


Figure B-3: The raw image acquired from bilateral phased array. White bar shows the location of the elements of the array.

white matter signal intensity is 280% higher near the coils than deeper in the brain. This wide variation in image intensity arises primarily from the coil reception profile. Adjacent gray and white matter regions differ by only 22%. Thus, the coil's reception profile makes most of the anatomy difficult to visualize with a single window and level setting.

Figure A2-4 shows the estimated sensitivity profiles derived from Daubechies-97 (Daub97) filter bank and maximum value projection at each level (1 to 6). The corrected images obtained from each level are shown in Fig. A2-5. Reconstruction using level 1, 2 or 3 fails to preserve the local brain structures because the estimated profile includes anatomical features which are then partially removed during the division step (Eq. A2.1). Level 6 coil profile is too spatially smoothed to effectively remove the coil intensity effects. Each level of corrected image required an average of 4.73 seconds per level of computation for a 256x204 image slice using a 450MHz Intel

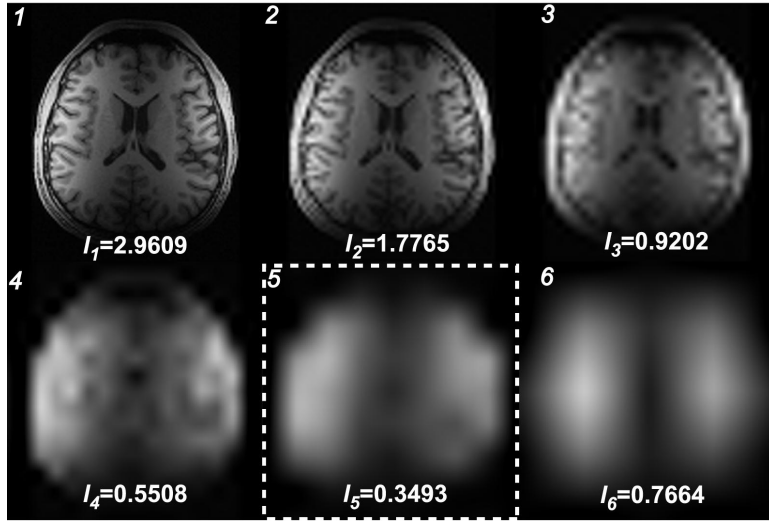


Figure B-4: Estimated sensitivity profiles and inhomogeneity indices for each of the 6 levels of wavelet decomposition and reconstruction. Level 5 (surrounded by the white dashed line box) was found to provide the optimal estimation based on the inhomogeneity index.

PentiumR III processor (Santa Clara, CA).

The optimum level used to estimate the coil sensitivity profile was determined by the quantitative inhomogeneity index in Eq. A2-2. The indexes computed with a 3 Gaussian GMM are shown in Fig. A2-4. Level 5 provided the minimum inhomogeneity index of the 6 levels regardless of the whether 2,3,4,5 or 6 Gaussians were used in the GMM. After correction, visualization of deep sub-cortical structures is considerably improved. The visibility for gray and white matter as well as the contrast between them is maintained for both cortex and deep gray structures at the same window and level. The reconstructed image contained peak-to-peak value white matter differences of 39% compared with differences of 280% in the original image. When the T1-weighted volumetric images were processed with the automated segmentation algorithm, the image intensity normalization was found to be sufficient to allow automated segmentation while the unprocessed surface coil images could not be processed with this package.

The maximum value projection was found to significantly improve the coil profile estimation near high contrast edges. Fig.A2-6 shows one-dimensional profile of the

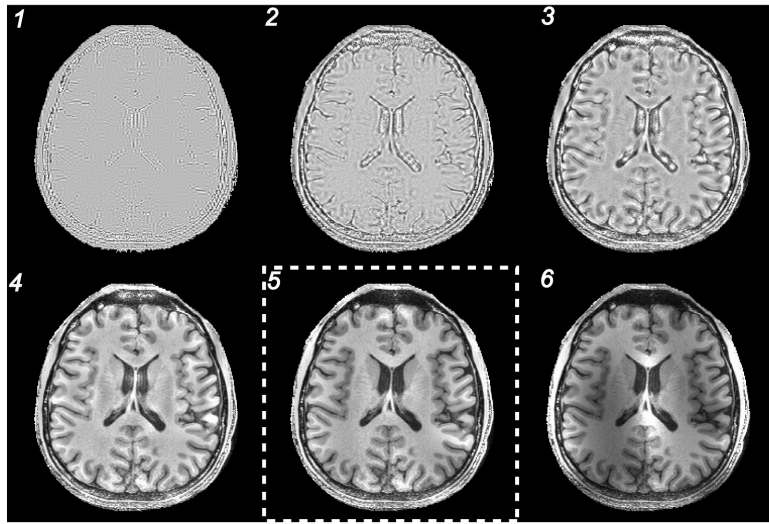


Figure B-5: Six levels of correction by Daub97 filter bank. Reconstruction at level 5 (surrounded by white dashed line box) provided the optimal reconstruction based on a minimization of the inhomogeneity index.

original image through the third ventricle with the coil sensitivity profile estimates with and without maximum intensity projection overlaid. The coil profile generated from a non-iterative, low pass filter based approach is also overlaid. The low pass filter consisted of a 26 mm (32 pixel by 32 pixel) moving-average low-pass kernel filter. This level of spatial smoothing is roughly equivalent to that of the level 5 MRA. Omission of the MVP step resulted in a 50% underestimation of the image data at the edge of the brain. Adding the MVP algorithm with a 1% convergence criteria reduced this error to approximately 5%. Less than 5 iterations of the MVP were required for convergence with a 1% criteria for each spatial level of the MRA. The convergence times for a given level of the wavelet based method with and without the MVP step were a maximum of 6.7 and 2.3 seconds respectively.

Figure A2-7 and A2-8 compares a standard birdcage head coil image with the corrected surface coil image. The uncorrected phased array image temporal lobe white matter SNR ranged from 351% to 466% higher than in the volume head coil birdcage image. For midline structures such as the corpus colossum, the gain was 27%. Figure A2-9 shows application of the method to T2 weighted images.

Figure A2-10 shows the application of the DWT generated coil intensity profiles

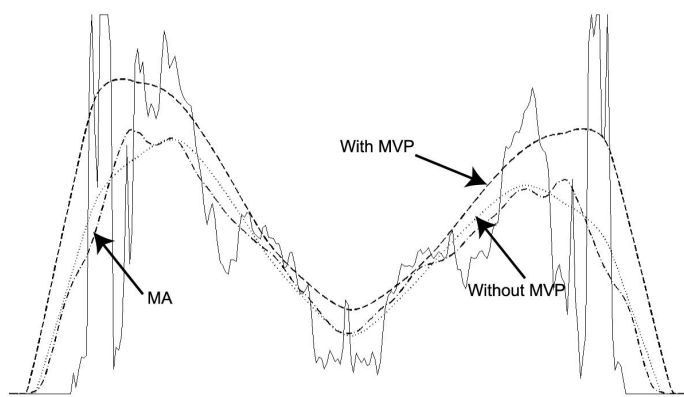


Figure B-6: A cross-section from the unprocessed image data at the location of the 3rd ventricle (solid line) overlaid with the sensitivity profile estimate without maximum intensity projection (MVP) (dotted line), and the sensitivity profile with MVP (thick dashed line). Without iterative MVP, the coil sensitivity profile is under-estimated at the brain-air boundary, as predicted in the simulation (shown in Fig. A2-2). MVP alleviates the underestimation and is more precise at sharp contrast boundary. Also overlaid is a coil intensity profile estimation using a moving-average (MA) low-pass filter with a 32X32 pixel kernel (thin dashed line).

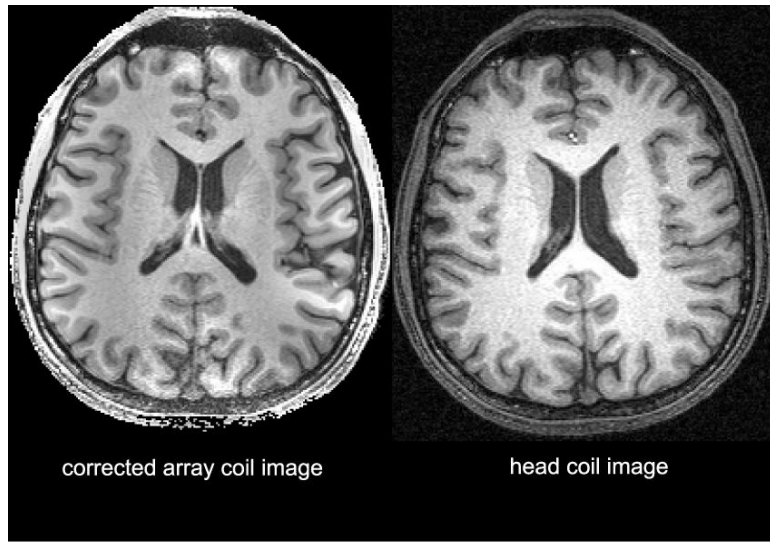


Figure B-7: Comparison of corrected phased array image (left) and volume head coil image (right). The advantage of phased array acquisition for higher SNR at regions near to the array coil is observed. The contrast of the white and gray matter is improved and maintained relatively constant compared to the original array coil image (Fig. A2-3). The inhomogeneity reduction on the array coil image using DWT and maximum value projection even improves the visibility of the deep brain areas at comparable contrast to the head coil image.

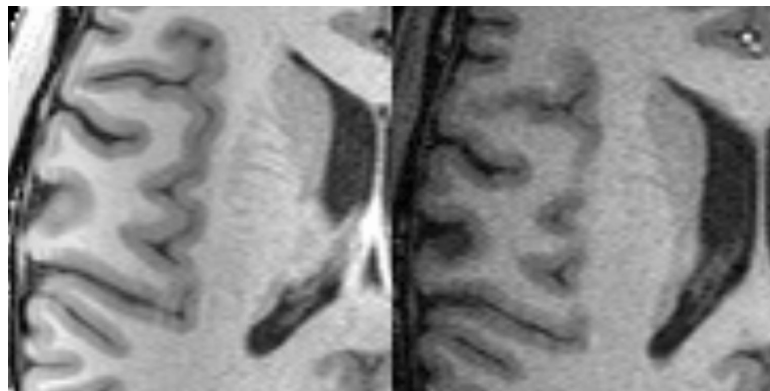


Figure B-8: The detail of the temporal lobe from the corrected phased array surface coil image (left) and the birdcage head coil image (right).

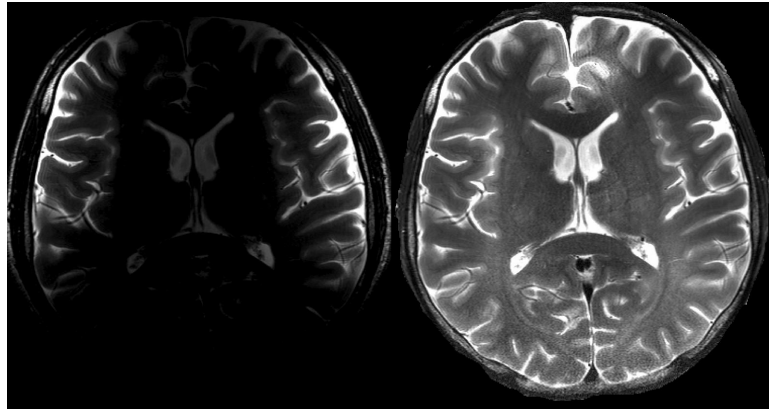


Figure B-9: Application of the DWT estimation of coil sensitivity profile and MVP to a T2-weighted image for inhomogeneity correction. The 2-channel array coil was placed at bi-temporal lobe. The uncorrected image is shown at left. The corrected image (right) shows more details at deep brain compared to the original one.

to the generation of coil sensitivity maps of the individual array coils for parallel reconstruction applications. The coil maps are well matched to the high sensitivity regions of the anatomical images. The reconstructed full-FOV image from a 2 fold undersampled (aliased) image is shown in Figure A2-11. Note that the SENSE reconstructed image is more noisy than the original full-FOV reference image, because in SENSE only 50% of the original k-space data was acquired. This leads to at least degradation of SNR. To further quantify the amplification of noise in SENSE, we provided G-factor map in Figure A2-11. The average G-factor over the whole FOV is 1.15 with standard deviation 0.0952. Maximal G-factor is 1.43, minimal G-factor is 1.0, and the median of G-factor is 1.14.

## B.4 DISCUSSIONS

Improving the sensitivity and encoding time constraints of structural and functional brain imaging is essential for revealing the physiological processes in cognitive, sensory and motor systems. Development of high field scanners and improved brain array coils offer the potential to increase the resolution and sensitivity of non-invasive MR imaging methods. Body coil or volume head (birdcage) coils provide highly homogeneous

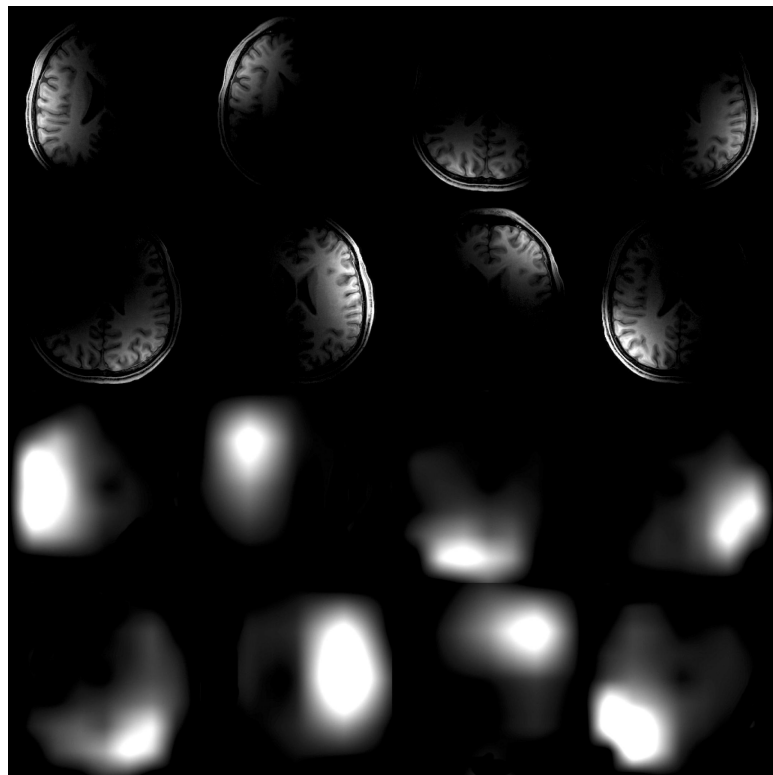


Figure B-10: The full-FOV reference images from an 8-channel array coil (top panel) and their optimal sensitivity profile estimates (lower panel) using DWT and MVP. The sensitivity profiles correlate well to the anatomical images from individual channels in the array as identified by the well-matched localized high sensitivity areas at different angular angles in this domed head array coil.

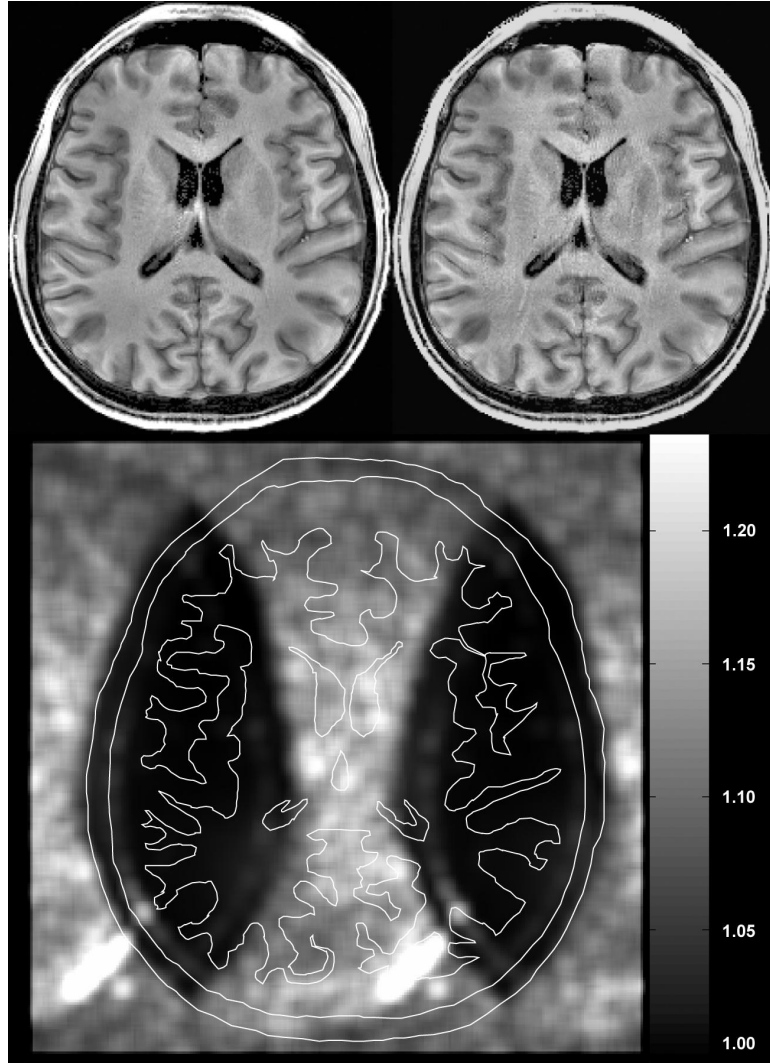


Figure B-11: Reconstructed full-FOV image from an 8-channel array coil using root-mean-square of individual channels (left) and SENSE acquisition with acceleration of 2.0 (right). Reduced-FOV images are acquired from skipping every other line in k-space. Standard SENSE reconstruction was used to unfold the collapsed aliased images from all 8 channels in the array for full-FOV reconstruction. The degraded SNR in the SENSE acquisition is mainly due to subsampling of k-space data by half, and therefore a degradation of SNR at least by  $\sqrt{2}$ . G-factor map associated with the reconstruction of SENSE image was shown to illustrate the noise amplification on top of the SNR degradation resulting from the reduced k-space sampling. In the optimal scenario G-factor would be an uniform matrix with value 1.

MR images. However, the SNR of volume coils in cortical regions is lower than that of surface coils. The image inhomogeneity from surface coils, however, compromises its application in functional imaging because of the intrinsic wide variation of image brightness arising from the coil sensitivity profile. In addition to making the images hard to visualize, the wide dynamic range of the surface coil image confounds the use of automated segmentation measurements of cortical parameters such as thickness and curvature or the automated identification of deep gray structures.[Dale AM, Fischl B, et al., 1999]. If the image inhomogeneity issue is overcome, these applications could potentially benefit from the improved resolution available from the 3 - 4 fold increase in cortical sensitivity of the arrays compared to volume coils since the cortex is relatively poorly resolved on standard (1 mm resolution) structural MRIs.

Array coils are also valuable for decreasing the magnetic field susceptibility distortion in functional imaging by allowing the reconstruction of echoplanar images with reduced encoding times. The susceptibility induced distortion becomes especially problematic for high field (3T and above) studies since the image distortion scales with field strength. The application of parallel imaging methods enables the accelerated image acquisition when multiple receivers are available and therefore a proportional reduction in susceptibility distortion. An estimate of the coil profile is a prerequisite for most of these methods. We show that the wavelet based estimation method can provide this estimate for the reconstruction of 2 fold accelerated SENSE images.

One of the significant features of this method is the iterative maximum value projection (MVP) at each level in multi-resolution analysis of the anatomical image. This method was found to be fast, robust in convergence, and improve the estimate of the coil map near the high contrast air-scalp interface. Without the MVP step, the wavelet transform estimation of the coil profile underestimated the coil profile data by 50% at the edge of the brain. Adding the MVP algorithm with a 1% convergence criteria reduced this error to approximately 5%. While we demonstrate the MVP method in conjunction with a multiresolution wavelet analysis to generate the low-pass filtered image, the iterative MVP approach could be used with other low pass

filter types in order to reduce the underestimation of the coil sensitivity profile near sharp contrast boundaries.

To select the optimal level of the coil sensitivity profile estimation using MRA, we propose a metric of the inhomogeneity index at each spatial level by using measures from the estimated coil sensitivity profile and the inhomogeneity corrected anatomical image. While other metrics might be possible, this method was found to provide the level that subjective analysis of the images would have chosen. The automated method worked for both 2D and 3D images of both T1 and T2 contrast and was found to be insensitive to the number of Gaussians used in the model. While for a certain range of image parameters it might be possible to choose the MRA level 5 based on prior knowledge of 256 matrix images and the coil used, the use of the more general approach does not increase the processing time significantly.

The proposed methods were tested in this study on a 3T MRI scanner using 3 different configurations of phased array coils (2-channel, 4-channel and 8-channels) for images of T1 and T2 weighted contrasts to test the robustness of the wavelet-based approach across image contrast and coil geometries. Since the goal of surface coil imaging is increased sensitivity and resolution, the study concentrated on 3T images. We have also applied the method to 1.5T images (not shown here) with similar results.

In addition to the Daubechies 97 filter banks, which can approximate the input image with precision of the 3rd order approximation at different spatial scales, we also employed other shorter filters of the same filter family to test the different performance. Potentially, shorter filters can save computational time. Using the T2-weighted image in Figure A2-9, Figure A2-12 shows the coil sensitivity estimates and corrected images obtained from Daubechies 53, 75, and 97 bi-orthogonal filter banks. All the filter implementations improve the visualization of the image by showing both cortical and deep brain structures such as the basal ganglia with a single window and level parameter. In all cases level 5 gives the best coil sensitivity estimation. Although the coil sensitivity estimates obtained from the three filter banks are similar in many respects, there are differences. Because the Daubechies 53 synthesis filter bank has support of 3 and 1 vanishing moment at , the approximation ability of

this filter bank is linear functions. Since the surface coil profile drops off faster than linear, the Daub53 filter results in a poorer approximation and produces a highly peaked shape in the estimated sensitivity map with a cross-like artifact. Daub75 and Daub97 have 2 and 3 vanishing moments at in the synthesis filter bank. This enables corresponding scaling functions to have better approximation to the smooth drop off of the surface coil.

Fig. A2-12. Coil sensitivity map estimations (top panel) and reconstruction (bottom panel) using Daub53 filter bank (upper panel), Daub75 filter bank (middle panel) and, Daub 97 filter bank (lower panel)

The accuracy of coil sensitivity estimation has been estimated by analyzing intensity deviations over structures that are known to be homogeneous, such as white matter. An alternative approach is to compare to a theoretical estimation. While a simple Biot-Savart type  $B_1$  field calculation works reasonably well for a single loop coil [9], the geometry of the array is more complicated to even describe. This is especially true of the semi-flexible arrays used in this work. A major confound is the coupling between array elements. This is modulated by both coil geometry, coil loading on the body, and electrical interactions with the preamplifiers. The coupling matrix of the 8-channel array has 28 parameters which depend on how the coil is flexed and how it is placed on the head as well as geometry and preamplifier tuning. All of these factors make it impractical to simply measure these couplings on the bench. In the absence of direct measurement, a realistic model would have too many free parameters to be useful for comparison. Additionally, at dielectric effects in the head are significant (on the 30% level) requiring a full Maxwell equation simulation. While these have been performed for idealized birdcage coils, we are not aware of simulations for surface coil arrays.

Recently, the promising parallel MRI techniques [Pruessmann KP, et al., 1999; Sodickson DK and Manning WJ, 1997; Sodickson DK and McKenzie CA, 2001] enable accelerated image acquisition when multiple receivers are available. The reconstruction of full-FOV image depends on the estimation of coil sensitivity modulation. Using our method, the reconstruction of reduced-FOV images from multiple receivers

is feasible without additional reference scans. Coupling with the regularization technique, we demonstrated initial results of robust parallel MRI reconstruction for brain imaging when our sensitivity profile estimation technique is utilized [30]. The community of brain research can benefit from the proposed algorithm in this study for either the accelerated image acquisition, or the enhanced spatial resolution due to parallel MRI acquisition. Further advantages of the application of parallel MRI in brain imaging include the reduced susceptibility artifacts in Echo planar imaging acquisition because of the shorter read-out time, and the alleviated acoustic noise in fMRI experiment because of the reduced gradient switching required for the k-space trajectory transverse. These are especially important in high field MRI for brain imaging. When the field strength is stronger than 3.0 Tesla, the susceptibility artifacts and unbearable acoustic noise (potentially larger than 130 dB) are so prominent as to challenge the conventional acquisitions. Parallel MRI with the reduced phase-encoding provides one solution to this difficulty. And our automatic coil sensitivity profile estimation method enables the reconstructions of parallel MRI in a convenient and computationally efficient way.

The proposed methods were tested in this study in 3.0 T MRI scanner using 3 different configurations of phased array coils (2-channel, 4-channel and 8-channels) for images of T1 and T2 weighted contrasts. Therefore this wavelet-based approach is robust across the spatial position, sizes and geometries. Concerning the validity of this approach at other field strength, the method is also working for 1.5 T scanner to correct image inhomogeneity when bi-temporal lobe 4-channel surface coils are employed to acquire images in our preliminary studies (not shown here). As the field strength going up to more than 3.0T, it is expected that the acquired images are more inhomogeneous due to an almost 2-fold increase in the  $B_1$  field inhomogeneity [31]. As stated above, parallel imaging may partially address this technical difficulty. Nevertheless, both pos-hoc imaging processing or parallel imaging rely heavily on the estimation of the coil sensitivity profile estimation.

In this study, we proposed a dyadic wavelet decomposition of original surface coil image to estimate the coil sensitivity map. This multi-stage approach is equivalent

to an iterative low-pass filtering, with the cut-off frequency at the current spatial resolution equal to half of the highest frequency in the previous spatial resolution. This division in frequency might be further improved by wavelet packet algorithm [Strang G and Nguyen T, 1996], which divides the input image into both high-pass and low-pass bands at all spatial resolutions. The wavelet packet approach allows for finer division of cut-off frequency at the cost of increased computation time. However, this can be combined with textita priori knowledge about the feasible resolution informed by dyadic DWT to locate the possible "optimal" spatial resolution. The subsequent finer division of spatial resolution might provide even more precise coil sensitivity profile estimation. And this will be the research topic in the near future.

In this study, we demonstrate an automatic method to estimate the coil sensitivity profile and use it to correct the inhomogeneity of surface coil MRI using wavelet transforms as well as for parallel imaging reconstruction using SENSE. The Daubechies maximally flat filter bank was found to have good computational efficiency and approximation of coil sensitivity map. The optimum level could be automatically determined by the defined inhomogeneity index from the corrected image and estimated coil profile. Thus the method uses neither presumed digital filter specifications or the knowledge of the electromagnetic properties and the location of the RF coil. Reconstructed images show both cortical and sub-cortical structures farther away from the surface coil with relatively constant contrast. The corrected surface coil images have both higher SNR than volume coil images and homogeneous contrast and brightness. Surface coil images corrected in this way were found to be usable with automated image segmentation software. The coil sensitivity profile estimation was applied to the accelerated parallel MRI of brain images using an 8-channel array coil to reduce the image encoding time by a factor of 2, allowing for either reduction of susceptibility distortions or increased spatial resolution at given imaging time.

# References

- [1] X. Golay, K. P. Pruessmann, M. Weiger, G. R. Crelier, P. J. Folkers, S. S. Kollias, and P. Boesiger. Presto-sense: an ultrafast whole-brain fmri technique. *Magn Reson Med*, 43(6):779–86, 2000. 20321484 0740-3194 Clinical Trial Journal Article.
- [2] P. B. Roemer, W. A. Edelstein, C. E. Hayes, S. P. Souza, and O. M. Mueller. The nmr phased array. *Magn Reson Med*, 16(2):192–225., 1990.
- [3] L. L. Wald, L. Carvajal, S. E. Moyher, S. J. Nelson, P. E. Grant, A. J. Barkovich, and D. B. Vigneron. Phased array detectors and an automated intensity-correction algorithm for high-resolution mr imaging of the human brain. *Magn Reson Med*, 34(3):433–9., 1995.
- [4] L. Axel, J. Costantini, and J. Listerud. Intensity correction in surface-coil mr imaging. *AJR Am J Roentgenol*, 148(2):418–20., 1987.
- [5] W. W. Brey and P. A. Narayana. Correction for intensity falloff in surface coil magnetic resonance imaging. *Med Phys*, 15(2):241–5., 1988.
- [6] P. A. Narayana, W. W. Brey, M. V. Kulkarni, and C. L. Sievenpiper. Compensation for surface coil sensitivity variation in magnetic resonance imaging. *Magn Reson Imaging*, 6(3):271–4., 1988.
- [7] F. E. Zanella, H. Lanfermann, and J. Bunke. [automatic correction of the signal intensity of surface coils. clinical application and relevance]. *Radiologe*, 30(5):223–7., 1990.

- [8] N. D. Gelber, R. L. Ragland, and J. R. Knorr. Surface coil mr imaging: utility of image intensity correction filter. *AJR Am J Roentgenol*, 162(3):695–7., 1994.
- [9] S. E. Moyher, D. B. Vigneron, and S. J. Nelson. Surface coil mr imaging of the human brain with an analytic reception profile correction. *J Magn Reson Imaging*, 5(2):139–44., 1995.
- [10] P. Irarrazabal, C. H. Meyer, D. G. Nishimura, and A. Macovski. Inhomogeneity correction using an estimated linear field map. *Magn Reson Med*, 35(2):278–82., 1996.
- [11] Jr. Maurer, C. R., G. B. Aboutanos, B. M. Dawant, S. Gadamssetty, R. A. Margolin, R. J. Maciunas, and J. M. Fitzpatrick. Effect of geometrical distortion correction in mr on image registration accuracy. *J Comput Assist Tomogr*, 20(4):666–79., 1996.
- [12] J. W. Murakami, C. E. Hayes, and E. Weinberger. Intensity correction of phased-array surface coil images. *Magn Reson Med*, 35(4):585–90., 1996.
- [13] B. D. Ross, P. Bland, M. Garwood, and C. R. Meyer. Retrospective correction of surface coil mr images using an automatic segmentation and modeling approach. *NMR Biomed*, 10(3):125–8., 1997.
- [14] G. P. Liney, L. W. Turnbull, and A. J. Knowles. A simple method for the correction of endorectal surface coil inhomogeneity in prostate imaging. *J Magn Reson Imaging*, 8(4):994–7., 1998.
- [15] H. Mihara, N. Iriguchi, and S. Ueno. A method of rf inhomogeneity correction in mr imaging. *Magma*, 7(2):115–20., 1998.
- [16] K. R. Thulborn, F. E. Boada, G. X. Shen, J. D. Christensen, and T. G. Reese. Correction of b1 inhomogeneities using echo-planar imaging of water. *Magn Reson Med*, 39(3):369–75., 1998.

- [17] S. H. Lai and M. Fang. A new variational shape-from-orientation approach to correcting intensity inhomogeneities in magnetic resonance images. *Med Image Anal*, 3(4):409–24., 1999.
- [18] K. Van Leemput, F. Maes, D. Vandermeulen, and P. Suetens. Automated model-based bias field correction of mr images of the brain. *IEEE Trans Med Imaging*, 18(10):885–96., 1999.
- [19] M. S. Cohen, R. M. DuBois, and M. M. Zeineh. Rapid and effective correction of rf inhomogeneity for high field magnetic resonance imaging. *Hum Brain Mapp*, 10(4):204–11., 2000.
- [20] D. K. Sodickson and W. J. Manning. Simultaneous acquisition of spatial harmonics (smash): fast imaging with radiofrequency coil arrays. *Magn Reson Med*, 38(4):591–603., 1997.
- [21] D. K. Sodickson, C. A. McKenzie, M. A. Ohliger, E. N. Yeh, and M. D. Price. Recent advances in image reconstruction, coil sensitivity calibration, and coil array design for smash and generalized parallel mri. *Magma*, 13(3):158–63., 2002.
- [22] K. P. Pruessmann, M. Weiger, M. B. Scheidegger, and P. Boesiger. Sense: sensitivity encoding for fast mri. *Magn Reson Med*, 42(5):952–62., 1999.
- [23] D. K. Sodickson. Tailored smash image reconstructions for robust in vivo parallel mr imaging. *Magn Reson Med*, 44(2):243–51., 2000.
- [24] Ingrid Daubechies. *Ten lectures on wavelets*. CBMS-NSF regional conference series in applied mathematics ; 61. Society for Industrial and Applied Mathematics, Philadelphia, Pa., 1992. Ingrid Daubechies. Contains lectures delivered at the CBMS conference organized in June 1990 by the Mathematics Dept. at the University of Lowell, Mass.
- [25] Gilbert Strang and T. Nguyen. *Wavelets and filter banks*. Wellesley-Cambridge Press, Wellesley, MA, 1996. Gilbert Strang and Truong Nguyen.

- [26] Richard A. Redner and Homer F. Walker. Mixture densities, maximum likelihood and the em algorithm. *SIAM Rev*, 26(2):195–239, 1984. Journal-Article Univ of Tulsa, Tulsa, OK, USA SIAM-Review Apr.
- [27] D. M. Titterington, A. F. M. Smith, and U. E. Makov. *Statistical analysis of finite mixture distributions*. Wiley series in probability and mathematical statistics. Applied probability and statistics. Wiley, Chichester ; New York, 1985. D.M. Titterington, A.F.M. Smith, U.E. Makov. Includes index.
- [28] Jae S. Lim. *Two-dimensional signal and image processing*. Prentice-Hall signal processing series. Prentice Hall, Englewood Cliffs, N.J., 1990. Jae S. Lim.
- [29] D. K. Sodickson and C. A. McKenzie. A generalized approach to parallel magnetic resonance imaging. *Med Phys*, 28(8):1629–43., 2001.
- [30] Fa-Hsuan Lin, Kenneth K Kwong, Ying-Jui Chen, John W. Belliveau, and Lawrence L. Wald. Reconstruction of sensitivity encoded images using regularization and discrete time wavelet transform estimates of the coil maps. In *International Society for Magnetic Resonance in Medicine Tenth Sceintific Meeting and Exhibition*, page 2389, Honolulu, Hawaii, USA, 2002. International Society for Magnetic Resonance in Medicine.
- [31] J. T. Vaughan, M. Garwood, C. M. Collins, W. Liu, L. DelaBarre, G. Adriany, P. Andersen, H. Merkle, R. Goebel, M. B. Smith, and K. Ugurbil. 7t vs. 4t: Rf power, homogeneity, and signal-to-noise comparison in head images. *Magn Reson Med*, 46(1):24–30, 2001. 0740-3194 Journal Article.

# Appendix C

## Multivariate linear modeling of brain images

### C.1 Multivariate linear modeling

Assuming the observed spatiotemporal functional imaging data consists of uncorrelated spatiotemporal models and it can be formulated as following:

$$D = M\Lambda N^T + E \quad (\text{C.1})$$

where  $M$  and  $N^T$  are unitary matrices of dimension  $m \times p$  and  $p \times n$  respectively. They represent  $p$  uncorrelated models in time and space, and  $p \leq m, n$ .  $\Lambda$  is a  $p \times p$  diagonal matrix describing the significance of each spatiotemporal model, which consists of one column of  $M$  and one row of  $N^T$ . The residuals are modeled in  $E$ . In the linear modeling framework, we can further decompose the temporal characterization of models,  $M$ , as linear combinations of basis function matrix,  $B$ :

$$M = BC \quad (\text{C.2})$$

Here columns of  $B$  are basis functions to consist each of the temporal models in individual column of  $M$ . And  $C$  is the matrix for basis coefficients. Without loss of generality, we assume the basis functions are orthogonal.

$$B^T B = I \quad (\text{C.3})$$

Here  $I$  denotes an identity matrix.

To achieve orthogonal basis functions, we apply the Singular Value Decomposition (SVD) to an arbitrary set of basis function. The left singular vectors satisfy the orthogonal criterion.

$$\begin{aligned} B_{\text{arbitrary}} &\stackrel{\text{SVD}}{=} U_B S_B V_B^T \\ B &\equiv U_B \end{aligned} \quad (\text{C.4})$$

This basis-whitening process simplifies the basis function selection in most of the experiments. Therefore, we can utilize versatile basis functions to construct spatiotemporal models. The relationship between the whitened and the original bases is a linear transformation:

$$B_{\text{arbitrary}} = BO, \text{ where } O = S_B V_B^T \quad (\text{C.5})$$

Replacing (A3.2), (A3.4) and (A3.5) into (A3.1), we have

$$D = BC\Lambda N^T + E \quad (\text{C.6})$$

And the temporal characterization of the temporal model is written explicitly using either orthonormal bases of an arbitrary basis family.

$$\begin{aligned} M &= BC \\ &= B_{\text{arbitrary}} O^{-1} C \\ &= B_{\text{arbitrary}} V_B S_B^{-1} C \end{aligned} \quad (\text{C.7})$$

To reveal uncorrelated spatiotemporal models, the residual  $E$  is removed by pro-

jecting the data matrix  $D$  into the span of basis functions:

$$\begin{aligned}
D_p &= B(B^T B)^{-1} B^T D \\
&= BB^T(M\Lambda N^T) \\
&= BC\Lambda N^T
\end{aligned} \tag{C.8}$$

Here we use PLS technique to identify coefficients of the bases. An effect space,  $E$ , is constructed by projecting time series of voxels in the data matrix on to these bases. The orthonormality of the bases ensures no biases toward any encoded effect.

$$\begin{aligned}
E &= B^T D_p \\
&= B^T B(B^T B)^{-1} B^T D \\
&= B^T D \\
&= C\Lambda N^T
\end{aligned} \tag{C.9}$$

Assuming that spatiotemporal models are uncorrelated, we can derive that the coefficients of the basis for temporal models are also uncorrelated:

$$\begin{aligned}
I &= M^T M \\
&= C^T B^T B C \\
&= C^T C
\end{aligned} \tag{C.10}$$

Since both model descriptions in both spatial and temporal domains are orthogonal, we can use SVD to decompose the effect space to reveal the basis function coefficients and their spatial loading. Singular Value Decomposition (SVD), which is mathematically equivalent PCA, is applied on the effect space for least-square orthogonal subspaces.

$$\begin{aligned}
E &\stackrel{SVD}{=} C \Lambda N^T \\
C^T C &= I \\
N N^T &= I
\end{aligned} \tag{C.11}$$

Each column of the coefficient matrix  $C$  along with the whitened basis matrix  $B$  constitutes the temporal characterization of a spatiotemporal model. And each row of the matrix  $N^T$  quantifies the spatial loading of the same model. Stemming from the terminology of Partial Least Squares, each column of  $C$  is called a temporal latent variable (temporal LV), and each row of  $N^T$  is called a spatial latent variable (spatial LV). Additionally, we can also derive the "spatial scores" and "temporal scores" as:

$$\begin{aligned}
S_{\text{temporal}} &= BC \\
S_{\text{spatial}} &= DN
\end{aligned} \tag{C.12}$$

Clearly the temporal score is equivalent to the temporal characterization of single spatiotemporal model. Examining both temporal scores and spatial LV using prior knowledge about the experiment design and the neuroanatomical information provides explanatory inferences and confidences of the spatiotemporal models. In the proposed multivariate modeling approach, temporal scores and spatial LVs predict the functional image signals at various conditions and time instants. If the basis functions are continuous, we can further exploit the reveal temporal LVs to interpolate and extrapolate the neuroimaging signals in the whole brain. Singular values are the normalization factors to scale the temporal LVs and spatial LVs to the original data matrix.

## C.2 Robust modeling by cross validation for optimal model selection and statistical inferences

Given a finite set of data, multiple choices of basis functions can fit the data to an arbitrary precision. However, the goodness of fit of the model usually increases at the cost of model complexity. Also the robustness of the model, which is defined here as the inverse of the discrepancy between of the model prediction and new observation, decreases when the model becomes complicated. Based on the limited number of observation, we propose the "leave-k-out" cross-validation scheme to test the robustness of the multivariate model. Basically, we randomly remove k observations, which are rows in data matrix, from the data matrix. Provided with the basis function, temporal LVs, singular values and spatioal LVs, the omitted observations can be predicted from the revealed spatiotemporal models

$$\begin{aligned} D_{cv} &= BC\Lambda N^T \\ &= B_{arbitrary} V_B S_B^{-1} C \Lambda N^T \end{aligned} \quad (\text{C.13})$$

The difference between  $D_{cv}$  and the omitted rows of  $D$ ,  $\mathcal{D}$ , during model identification consists the goodness of fit of the cross validation. Cross validation error is defined as the mean value of the root-mean-squares difference between  $D_{cv}$  and  $\mathcal{D}$ .

$$e_m^{cv} = \sqrt{\|\mathcal{D} - D_{cv}\|_F^2} \quad (\text{C.14})$$

Here  $\|\bullet\|_F^2$  denotes the Frobenius norm, sum of squares of matrix entries.

In addition to cross-validate the whole model, as shown in Eq. (C.14), we can only cross validate the data on the sub-space created by the set of the select indices  $\{\theta\}$ :

$$D_{cv}^{\{\theta\}} = B_{arbitrary} V_B S_B^{-1} C^{\{\theta\}} \Lambda^{\{\theta\}} (N^{\{\theta\}})^T$$

$$\begin{aligned}\Theta &= B_{arbitrary} V_B S_B^{-1} C^{\{\theta\}} \\ \mathcal{D}_{\{\theta\}} &= \Theta(\Theta^T \Theta)^{-1} \Theta^T \mathcal{D}\end{aligned}\quad (\text{C.15})$$

The cross validation error metric allows for the quantitative assessment of the model robustness and model selection among the model family. Iterative random sampling the data matrix along the observation dimension provides the stochastic measurement of robustness and fitting quality for linear models at various orders. Utilizing the computational efficiency of the gPLS algorithm, multiple realizations of the model of can be identified within reasonable time. This leads to the pool of both model-fitting error and cross validation error for each model.

To compare two different models at various order, we can calculate the distributions of the "coefficients",  $\Phi$ , for basis functions.

$$\begin{aligned}D_{cv} &= B_{arbitrary} (V_B S_B^{-1} C \Lambda N^T) \\ &= B_{arbitrary} \Phi\end{aligned}\quad (\text{C.16})$$

Samples of  $\Phi$ 's are generated from the randomized cross-validation process. The statistics to compare two models ( $\Phi_1$  and  $\Phi_2$ ) is the Hotelling's  $T^2$ -statistic

$$T^2 = \frac{n_1 n_2}{(n_1 + n_2)} (\vec{\phi}_1 - \vec{\phi}_2)^T S^{-1} (\vec{\phi}_1 - \vec{\phi}_2) \quad (\text{C.17})$$

Here  $\vec{\phi}_i$  denotes the mean of the column  $i$  of the coefficient matrix.  $n_1$  and  $n_2$  are the number of iterations in cross validation for model.  $o$  represents the order of the basis (the number of entries in the coefficient vector  $\vec{\phi}_i$ ; assuming both  $\vec{\phi}_i$  and  $\vec{\phi}_j$  are of the identical order after padding necessary zero entries). Under the null hypothesis that the two coefficient vectors are of no significant difference, the distribution is of  $T^2$  is given by

$$\frac{n_1 + n_2 - o - 1}{(n_1 + n_2 - 2)o} T^2 \approx F_{o, n_1 + n_2 - o - 1} \quad (\text{C.18})$$